

**Passive Control of the Lateral Critical
Speeds of a Rotating Shaft Using Eccentric
Sleeves**

Antony John Kirk

A thesis submitted in partial fulfilment of the requirements of the University of
Lincoln for the degree of Doctor of Philosophy

2017

It was the best of times, it was the blurst of times.

Abstract

Classical techniques for mitigating vibration in rotating structures are divided into three main categories viz. careful design and manufacture, correct installation and effective control strategies. The balancing sleeves analysed in this thesis were developed as a ‘semi active’ method of vibration control to improve the state of balance of dynamically unstable coupling shafts. However, the addition of the balancing sleeves affects the natural dynamics of the shaft, and requires a detailed understanding of their characteristics and the impact on the overall shaft dynamics in order to be useful in practice. As a first approximation, the sleeves are initially modelled as part of a full coupling shaft using the Extended Hamilton’s Principle. The simulation studies show that the flexibility of the sleeves have little impact upon the dynamics of the system and can therefore be neglected. However, when compared to results from the use of computational finite element methods with different sleeve lengths, discrepancies are identified. Experimental validation using a purpose built high speed test facility is used to show that the difference is due to the lack of appropriate modelling of sleeve flexibility characteristics. A full system model using finite element methods is therefore devised. More widely, a study of the impact of sleeve lengths shows that the classical definition of a ‘shaft mode’ does not encompass sufficient fidelity to discriminate between modes that are initially considered as being shaft dominated and those that are considered as sleeve dominated mode shapes, and the sharp transition that occurs between the two. It is notable that the transition between the two dominant modal contributors occurs at sleeve lengths that impart a natural frequency that is close to that corresponding to the shaft. It is concluded that the mechanism of passive control via use of the sleeves is a combination of softening due to the added mass of the sleeves and coherence of the individual modes of the shaft and sleeves. In this way, it is shown that the sleeves act in a manner similar to a tuned mass-damper. By appropriate design therefore, use of balancing sleeves offer the opportunity to increase the critical speed margin in practical applications and reduce unwanted lateral vibrations.

Acknowledgements

I would like to thank my many supervisors for supporting throughout the period of this thesis. Firstly thanks go to Dr Jill Stewart and Dr Gillian Mara for giving me the opportunity to study for a PhD in the first place. Dr Fotios Georgiadis for giving me the theoretical underpinnings. I thank Professor Ron Bickerton for his role of Chief Engineer, mediator and counsellor. Special thanks go to Professor Chris Bingham for finally getting me over the finishing line.

Grahame Knowles deserves massive credit for his great invention, without which this thesis would never happened and to Siemens Industrial Turbomachinery Ltd. for providing support and funding throughout the project.

I thank Dr Jonathan Griffiths and Dr Mike Riley for being good friends and sounding boards throughout the difficult times.

I thank the University of Lincoln, School of Engineering Technical Team for always providing me with the necessary facilities to do my research.

Publications Resulting from Research Documented in this Thesis

Kirk, Antony and Griffiths, Jonathan David and Bingham, Chris and Knowles, Grahame and Bickerton, Ronald (2016) Passive control of critical speeds of a rotating shaft using eccentric sleeves: model development (GT2016-58155). In: ASME Turbo Expo 2016, 13 - 17 June 2016, Seoul, South Korea.

Kirk, A. and Georgiadis, F. and Bingham, C. (2014) Towards determination of critical speeds of a rotating shaft with eccentric sleeves: equations of motion. In: 9th IFToMM International Conference on Rotor Dynamics, 22 - 25 September 2014, Milan; Italy.

Kirk, Antony and Knowles, Grahame and Stewart, Jill and Bingham, Chris (2013) Mathematical development and modelling of a counter balance compensating sleeve for the suppression of lateral vibrations in high speed flexible couplings. In: ASME Turbo Expo 2013, 3-7 June 2013, San Antonio, Texas, USA.

Knowles, Grahame and Kirk, Antony and Stewart, Jill and Bickerton, Ronald and Bingham, Chris (2014) Theoretical investigation into balancing high-speed flexible shafts, by the use of a novel compensating balancing sleeve. Proceedings of the Institution of Mechanical Engineers, Part C: Journal of Mechanical Engineering Science, 228 (13). pp. 2323-2336. ISSN: 0954-4062.

Contents

Abstract	iii
Acknowledgements	iv
Publications Resulting from Research Documented in this Thesis	v
Contents	vi
List of Figures	x
List of Tables	xiii
Nomenclature	xiv
Chapter 1 Introduction	1
1.1 Problem Background	1
1.2 Application Sectors	2
1.3 Coupling Shafts	3
1.4 Natural Frequency and Critical Speeds	4
1.5 Problem Definition	5
1.6 Research Objectives	7
1.7 Thesis Outline	7
1.8 Research Contributions	8
Chapter 2 Literature Survey	9
2.1 Rotordynamics	9
2.2 Coordinate Systems	10
2.3 Dynamic Effects of Rotation	11
2.3.1 Gyroscopic Effects	11
2.3.2 Bearing Effects	12
2.3.3 Acceleration Effects	13
2.4 Modes of Vibration and Governing Equations	14
2.4.1 Lateral Vibration	14
2.4.2 Whirl	15
2.4.3 Torsional Vibration	16
2.4.4 Longitudinal Vibration	17
2.4.5 Coupling of Vibration Modes	18
2.5 Modal Analysis	19
2.5.1 Mode Shapes	21
2.6 Campbell Diagrams	23

2.7	Methods of Vibration Control in Rotating Shafts	27
2.7.1	Balancing.....	28
2.7.2	Alignment.....	31
2.7.3	Active Control.....	34
2.7.4	Passive Control	38
2.8	Conclusions	41
Chapter 3	Theoretical Model of a Simplified Shaft with Eccentric Sleeves ...	43
3.1	Summary	43
3.2	Chapter Highlights	43
3.3	Introduction	44
3.3.1	Key Adopted Assumptions	44
3.4	Extended Hamilton's Principle.....	46
3.5	Derivation of Simply Supported Rotating Shaft Dynamics	46
3.5.1	Shaft Displacements.....	46
3.5.2	Shaft Position, Velocity and Acceleration Vectors.....	48
3.5.3	Shaft Kinetic Energy.....	48
3.5.4	Shaft Kinetic Energy Boundary Conditions.....	54
3.5.5	Inertia Integration Coefficients	55
3.5.6	Shaft Potential Energy.....	56
3.5.7	Shaft Potential Energy Boundary Conditions	58
3.5.8	Stiffness Integration Coefficients.....	59
3.5.9	Shaft Total Energy Equation.....	60
3.5.10	Comparison with Previously Reported Equations	61
3.6	Derivation of Eccentric Sleeve Dynamics.....	62
3.6.1	Numerical Analysis.....	62
3.6.2	Sleeve Position and Acceleration Vectors	63
3.6.3	Kinetic Energy of Sleeves.....	67
3.7	Torsional Stiffness.....	68
3.8	Equations of Motion.....	68
3.9	Discussion	70
3.10	Conclusions	71
Chapter 4	Dynamic Analysis of a Rotating Shaft with Eccentric Sleeves.....	72
4.1	Summary	72
4.2	Chapter Highlights	72
4.3	Introduction	73

4.4	Theoretical Model	75
4.4.1	Discretisation of Equations of Motion	75
4.4.2	Preparation of Equations for y-plane Lateral Bending	78
4.4.3	Preparation of Equations for z-Plane Lateral Bending	81
4.4.4	Preparation of Equations for Torsional Motion	84
4.4.5	Summation Matrices	86
4.4.6	System Matrices	90
4.4.7	Numerical Solution	92
4.5	Finite Element Analysis	97
4.5.1	Geometry	98
4.5.2	Materials	98
4.5.3	Connections	99
4.5.4	Element Types	101
4.5.5	Meshing	102
4.5.6	Boundary Conditions and Loads	104
4.5.7	Solver Settings	105
4.5.8	Comparison of Proposed (Theoretical) and Finite Element Models..	106
4.6	Modifications to the Finite Element Model	111
4.7	Conclusions	112
Chapter 5	Experimental Validation Study of Rotating Shaft with Eccentric Sleeves	114
5.1	Summary	114
5.2	Chapter Highlights	114
5.3	Experimental Setup and Description	115
5.3.1	Test Methodology	115
5.4	Description of Test Rig	116
5.5	Test Rig Control	117
5.6	Shaft Balancing	118
5.7	Shaft Alignment Process	118
5.8	Instrumentation	119
5.9	Experimental Results	121
5.10	Modifications to FE Model	123
5.11	Comparison of Experimental and Theoretical Results	125
5.12	Relative Sleeve Flexibility	127
5.13	Conclusions	128

Chapter 6	Effect of Variance Study on Critical Speeds of Shaft with Eccentric Sleeves	130
6.1	Summary	130
6.2	Chapter Highlights	131
6.3	Introduction	131
6.4	Mode Classification	132
6.5	Bounds of the Parametric Study	135
6.6	Modal Behaviour	135
6.7	Participation Factor and Effective Mass	143
6.8	Revised Mode Classification	145
6.9	Higher Order Modes	146
6.10	Passive Control of Critical Speeds	152
6.11	Effect of Stiffness and Mass	154
6.12	Conclusions	156
Chapter 7	Conclusions and Recommendations	157
7.1	Research Contributions	157
7.2	Conclusions	157
7.3	Recommendations for Further Work	159
References		161
Appendices		172

List of Figures

Figure 1.1 – SGT-400 core engine	2
Figure 1.2 – Gas turbine layout with driven equipment.....	2
Figure 1.3 – Typical gas turbine coupling	3
Figure 1.4 – Machining of shaft internal diameter.....	4
Figure 1.5 – Eccentric sleeve	6
Figure 2.1 – Effects of clockwise moment about Ox.....	12
Figure 2.2 – Rotor mode shapes with varying support stiffness	12
Figure 2.3 – Critical speed map for three disk shaft	13
Figure 2.4 – Simple torsional vibration rotor model.....	16
Figure 2.5 – Axial behaviour of a multi-disc rotor	17
Figure 2.6 – Modal and frequency domain	20
Figure 2.7 – Input forces and response of a structure related by FRF	21
Figure 2.8 – 1 st bending mode shapes of a shaft with a mounted disc.....	22
Figure 2.9 – 2 nd bending mode shapes of a shaft with a mounted disc.....	22
Figure 2.10 – 3 rd bending mode shapes of a shaft with a mounted disc	22
Figure 2.11 – Example Campbell diagram	23
Figure 2.12 – Campbell diagrams in stationary and rotating coordinate systems	24
Figure 2.13 – 1 st bending mode of simple plain shaft.....	25
Figure 2.14 – 2 nd bending mode of simple plain shaft.....	25
Figure 2.15 – Campbell diagrams for simple plain shaft.....	26
Figure 2.16 – a) Static unbalance b) Dynamic unbalance.....	29
Figure 2.17 – Trial weight location plot	30
Figure 2.18 – Parallel misalignment of coupling shafts.....	32
Figure 2.19 – Angular misalignment of coupling shafts.....	32
Figure 2.20 – Categories of misalignment	33
Figure 2.21 – Feedback control system for active vibration control.....	35
Figure 2.22 – Schematic of an active magnetic bearing	37
Figure 2.23 – Example of a piezo bearing	38
Figure 2.24 – Squeeze film damper configuration.....	40
Figure 2.25 – Effect of tuned mass damper upon system responses and resonant peaks.....	40
Figure 3.1 – Geometry of full shaft with flexible couplings and eccentric sleeves ...	44

Figure 3.2 – Model simplification assumptions	46
Figure 3.3 – Shaft displacements	47
Figure 3.4 – Normalised Campbell Diagram for stiff and flexible sleeves	63
Figure 3.5 – Coordinate system attached to each sleeve and global positions	63
Figure 3.6 – Displacements of eccentric sleeve mass at $x = 0$	64
Figure 4.1 – Convergence error and computation time at 0 rpm	95
Figure 4.2 – Convergence error and computation time at 12000 rpm	95
Figure 4.3 – ANSYS shaft geometry	97
Figure 4.4 – Simplified geometry at shaft end	98
Figure 4.5 – Contact region taken from large area	101
Figure 4.6 – SOLID187 element	101
Figure 4.7 – CONTA174 and TARGE170 elements	102
Figure 4.8 – Refined hub and spacer shaft	102
Figure 4.9 – Refined flexible element mesh	103
Figure 4.10 – Coupling flexible element connection	104
Figure 4.11 – Campbell diagram for theoretical solution	108
Figure 4.12 – Campbell diagram for finite element mode	108
Figure 4.13 – 1 st bending mode of shaft with short sleeve, from FE analysis	110
Figure 4.14 – 1 st bending mode of shaft with medium sleeve, from FE analysis	110
Figure 4.15 – 1 st bending mode of shaft with long sleeve, from FE analysis	110
Figure 4.16 – Finite element model of shaft with point mass replacing the sleeve	111
Figure 4.17 – Campbell diagram for finite element model with point masses	112
Figure 5.1 – Experimental set up	116
Figure 5.2 – Control software screen shot	117
Figure 5.3 – Analogue controller	117
Figure 5.4 – Alignment figures achieved	119
Figure 5.5 – Laser displacement sensors measuring shaft	119
Figure 5.6 – Laser displacement sensors GUI	120
Figure 5.7 – Example complete record measurement	120
Figure 5.8 – Zoom of data record	121
Figure 5.9 – Raw displacement data from shaft for different sleeve configurations	122
Figure 5.10 – Modifications to finite element model to include support structure effects	123
Figure 5.11 – Internal layout of Modifications to finite element model to include support structure effects	124

Figure 5.12 – Critical speed map for first bending mode for no-sleeve configuration	125
Figure 5.13 – Absolute critical speeds for all modelling approaches and experimental	126
Figure 5.14 – Normalised critical speeds for all modelling approaches and experimental	126
Figure 5.15 – Measurements on sleeve and shaft	127
Figure 5.16 – Relative sleeve flexibilities	128
Figure 6.1 – MODE 1: Shaft dominated 1 st bending mode (DR = 0.61)	133
Figure 6.2 – MODE 2: Shaft dominated 2 nd bending mode (DR = 0.43)	133
Figure 6.3 – MODE 3: Shaft dominated 3 rd bending mode (DR = 0.86)	133
Figure 6.4 – Mode 4: 1 st sleeve dominated mode (DR = 22.3)	134
Figure 6.5 – Mode 5: 2 nd sleeve dominated mode (DR = 4.79)	134
Figure 6.6 (a) – Natural frequencies of all modes against sleeve length	136
Figure 6.7 – Natural frequencies of bending for isolated shaft and sleeve	137
Figure 6.8 – Modal analysis of isolated sleeve	138
Figure 6.9 – Displacement ratio (DR) of MODE 1 and MODE 5 for sleeve lengths 76 to 116mm	143
Figure 6.10 – Normalised participation factors for sleeve lengths 76 to 116mm	144
Figure 6.11 – Corrected natural frequencies of MODES 1, 4 and 5 against sleeve length	145
Figure 6.12 – Displacement ratio (DR) of MODE 2 and MODE 4 for sleeve lengths 36 to 66mm	146
Figure 6.13 – Displacement ratio (DR) of MODE 3 and MODE 4 for sleeve lengths 26 to 56mm	149
Figure 6.14 – Critical speeds of all considered modes for sleeve lengths 0 to 136mm	153
Figure 6.15 – Normalised critical speeds of shaft bending modes for sleeve lengths 0 to 136mm	153
Figure 6.16 – First critical speeds including point mass model for sleeve lengths 0 to 136mm	154
Figure 6.17 – Second critical speeds including point mass model for sleeve lengths 0 to 136mm	155
Figure 6.18 – Third critical speeds including point mass model for sleeve lengths 0 to 136mm	155

List of Tables

Table 3-1 – Inertia coefficients	56
Table 3-2 – Stiffness integration coefficients	60
Table 3-3 – Comparison of the variation of generalised coordinates	61
Table 3-4 – Normalised critical speeds of system with flexible/rigid sleeves	62
Table 4-1 – Summation matrix substations.....	88
Table 4-2 – Parameters of simplified shaft	93
Table 4-3 – Computation time for 3 to 30 term solutions.....	94
Table 4-4 – Convergence error at 0 and 12000 rpm	95
Table 4-5 – Material properties.....	99
Table 4-6 – ANSYS contact types	100
Table 4-7 – Sleeve lengths used in analysis.....	107
Table 4-8 – Normalised shaft critical speeds	107
Table 4-9 – Normalised shaft critical speeds for point mass model	111
Table 5-1 – Residual unbalance in test shaft/sleeve configurations	118
Table 5-2 – Experimental critical speeds	122
Table 5-3 – Modified finite element critical speeds.....	124
Table 6-1 – Sleeve lengths used for parametric study	135
Table 6-2 – MODE 1 displacement ratios and mode shapes	140
Table 6-3 – MODE 4 displacement ratios and mode shapes	141
Table 6-4 – MODE 5 displacement ratios and mode shapes	142
Table 6-5 – MODE 2 displacement ratios and mode shapes	147
Table 6-6 – MODE 4 displacement ratios and mode shapes	148
Table 6-7 – MODE 3 displacement ratios and mode shapes	150
Table 6-8 – MODE 5 displacement ratios and mode shapes	151

Nomenclature

All dimensional variables are in SI units unless otherwise stated

A	Cross sectional area
γ_i	Participation factor
D_x, D_y, D_z	Displacements in rotating co-ordinate system
E	Elastic modulus
e_{ij}	Euler strains
$F(t)$	Forcing function of a vibrating system
f_Ω	Frequency of rotational velocity
G	Shear modulus
I	Second moment of area (Moment of inertia)
I_p	Polar inertia
$I_{xx}, I_{yy}, I_{zz}, I_{xy}, I_{xz}, I_{yz}$	Inertia coefficients of sleeve
K_a	Axial stiffness
K_t	Torsional stiffness
k_i	Stiffness coefficients of shaft
δJ	Variation of total energy in continuous system
L	Length of continuum
M_x	Moment about x axis
m_0	Mass per unit area
$M_{i\text{eff}}$	Effective mass
θ	Rotation about x axis
ρ_0	Density
\bar{r}	Position vector in rotating co-ordinate system

r	Position vector in global co-ordinate system
R, R_i, R_o	Continuum radius, Inner, Outer
U	Potential energy in continuous system
δU	Variation of potential energy in system
δU_{TORS}	Variation of potential energy in flexible element
u, v, w	Translational displacements in x, y, z directions
σ_{ij}	Euler stresses
$T(t)$	Applied torque
T	Kinetic energy in continuous system
δT	Variation of kinetic energy in system
$\delta T_1, \delta T_2$	Variation of kinetic energy in attached sleeves
v', w'	Slope of translational displacements in y and z directions
V	Volume of continuum
\bar{v}_i	Eigenvectors/Mode shape
ϕ	Rotational (torsional) displacement
$\phi_i(x) \phi_j(x)$	Trial functions
φ	Cylindrical coordinate system angle
ψ	Rotation about y axis
w_a	Axial displacements
ω	Circular natural frequency
Ω	Rotation about z axis
\cdot	First derivative with respect to time
$\ddot{}$	Second derivative with respect to time
$'$	First derivative with respect to distance
$''$	Second derivative with respect to distance

Matrices

[A]	Rotational transformation matrix
[C]	Damping matrix
[C _{cor}]	Coriolis matrix
[G]	Gyroscopic matrix
[K]	Stiffness matrix
[M]	Mass matrix
[K _{spin}]	Spin softening matrix
{q}	Displacement vector
{ \dot{q} }	Velocity vector
{ \ddot{q} }	Acceleration vector

Chapter 1 Introduction

1.1 Problem Background

Siemens Industrial Turbomachinery Ltd, Lincoln (SITL) produce gas turbine packages for power generation and mechanical drive purposes. Gas turbines are internal combustion engines that use incoming air flow to drive rotors in order to extract mechanical power in the form of rotation. The constituent parts can be grouped into three main sections; compressor, combustion chamber and turbine. Figure 1.1 provides a simplified view of a commercial gas turbine [1].

A continuous flow of air is drawn into the compressor where it is compressed and fed into the combustion chamber. Liquid or gas fuel is then added and the mixture is ignited, creating a hot gas that is channelled and accelerated through a nozzle into a number of turbine stages. This causes the turbine to rotate, converting the thermal energy into mechanical power. Some of the energy is used to drive the compressor that draws in air, with the remainder being traditionally used to provide mechanical power output eg. to feed a generator. In other cases, a proportion of the resulting energy can also be extracted in the form of heat. The highest operating efficiencies for gas turbine are currently around 40% [2].

Compared with reciprocating engines, gas turbines offer high power-to-weight ratios whilst also containing fewer moving parts [2]. Benefits of lower complexity and increased reliability are tempered by the need for careful balancing of the rotor assemblies. Gas turbines are commonly fuelled by natural gas, although, through appropriate design, can be run on various mixtures of liquid fuel which may be native to the installation site.

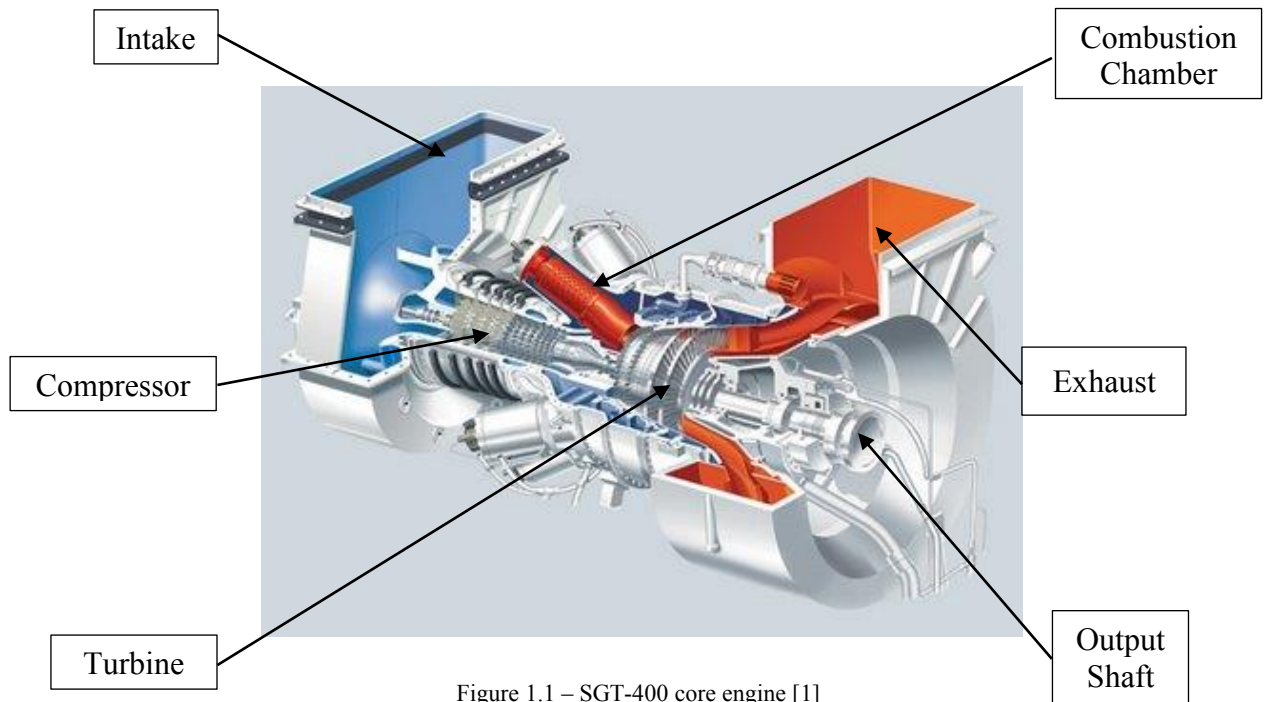


Figure 1.1 – SGT-400 core engine [1]

1.2 Application Sectors

For the aerospace industry, the engine's energy is used to produce thrust either through a rear nozzle or by a front mounted bypass fan. Industrial gas turbines use the power produced by the turbine to drive some form of mechanical equipment/load. Figure 1.2 shows the functional layout of a typical industrial gas turbine. The physical link between the turbine and the driven equipment is the focus of this research.

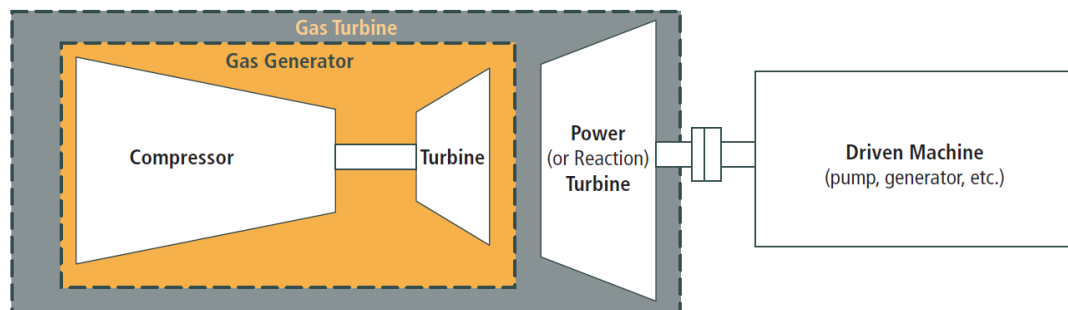


Figure 1.2 – Gas turbine layout with driven equipment [4]

Primarily such equipment is found within the oil and gas industries. The most common uses are for pumping crude oil on offshore platforms and pumping through pipelines for the refining process. Centrifugal compressors also use gas turbines to aid gas processing. Gas pipelines require the generation of sufficient pressure to transfer gas over long distances. Compressors are used to inject gas to boost the pressure. When used for power generation, gas turbines can either directly drive generators or are used in a combined cycle where residual heat is gathered to power steam turbines. A heat exchanger can also be incorporated to use this residual heat to preheat the air entering the combustion chamber, thereby increasing cycle efficiency.

1.3 Coupling Shafts

Gas turbine engine cores are connected to ancillary equipment using a coupling shaft. For high speed applications, the coupling will usually incorporate some form of flexible element; discs or diaphragms. Their flexibility can accommodate some misalignment between the prime mover and load, whilst allowing limited movement due to inertial forces. Figure 1.3 shows a typical gas turbine coupling containing flexible disc elements. The majority of the length of a coupling shaft is made up of a spacer tube.

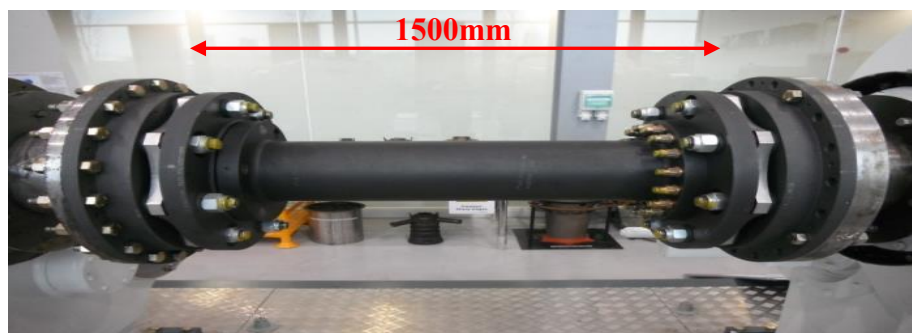


Figure 1.3 – Typical gas turbine coupling

Further increase of coupling lengths mean that tolerance criteria cannot be met. Figure 1.4 shows problems the machining process of the internal diameter of a long shaft can suffer. Misalignment of machining tools can lead to non-uniform thickness of the shaft wall. For instance, a 1500mm coupling shaft with misalignment of 0.5° will cause one machining tool to pass through the side of the shaft by mid-point.

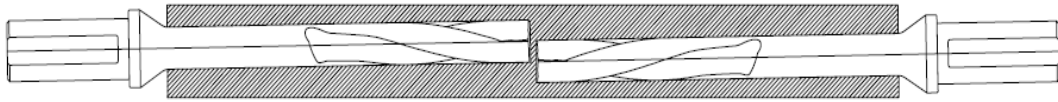


Figure 1.4 – Machining of shaft internal diameter

Due to problems with the machining processes involved with manufacturing these shafts, the dynamic behaviour can be altered away from its desired performance. Machining tolerances cause an uneven distribution of material, and hence mass, around the shaft, resulting in the centre of gravity being positioned away from the neutral axis and thereby creating eccentricity. The magnitude of mass and degree of eccentricity is termed *unbalance*. As the shaft rotates this generates centrifugal force perpendicular to the axis of rotation which is proportional to the square of rotational velocity.

The centrifugal force created by unbalance can induce deflections along the length of the shaft. In thin walled coupling shafts such deflections can be considerable. Since the deflection increases with speed, so does the eccentricity of the centre of mass away from axis of rotation. The effect is cumulative; unbalance causes deflection, deflection increases the eccentricity which increases the unbalance. The resulting centrifugal force is transferred to the support structures as lateral vibration.

1.4 Natural Frequency and Critical Speeds

A natural frequency is considered as a frequency where a system or structure will resonate. A single degree of freedom system will have one natural frequency whereas complex systems with multiple degrees of freedom possess multiple natural frequencies.

Friswell et al [3] describe the dynamics of rotating systems, giving the definition of a critical speed as *a rotational speed of a machine at which some combination of vibration displacement and/or forces reaches a (local) maximum*. Adams [4] becomes more specific describing lateral natural frequencies as being present when a machine is running at a critical speed. This creates an assumption that vibration issues exhibited at critical speed are the result of lateral vibrations. Batrak [5] simply states that *critical speeds coincide with the natural frequencies*

of the shaft whirling vibration. A summarised definition is that a critical speed is a rotational speed at which the frequency of an excitation force, such as unbalance or misalignment, coincides with a natural frequency.

The natural frequency of a system can change with rotational speed due to gyroscopic, damping and support structure dynamics. Careful consideration therefore needs to be taken during design to ensure that the system will run across a broad range of rotational speeds without a natural frequency being excited.

1.5 Problem Definition

Siemens Industrial Turbomachinery Lincoln (SITL) produce four gas turbine models for both power generation and mechanical drive purposes. Output power ranges from 5 to 15MW (approx) depending on model and application. The most recent development unit, the SGT-400, has exhibited vibration problems in the mechanical drive variant (SGT-400-MD). Data from units in field environments have showed high levels of vibration at the rear bearing of the engine and front bearing of driven equipment, resulting in frequent shutdowns. The normal operating speed of the engine is 10,000 rpm. However, to prevent high vibration levels and consequent shutdowns, the engines were routinely operated at lower than optimal running speeds, typically at around 8,000rpm. Increases in speed beyond this have caused large increases in lateral vibration indicating that the engine could be operating close to a shaft critical speed. However, Regulations API671 [6] dictates that for a flexible coupling the lateral safety margin should be 1.5 i.e. a lateral critical speed should be 1.5 times the operating speed. Due to this requirement, critical speeds are ‘designed out’ as part of the development process, suggesting that the source of the problem lies elsewhere.

An alternative cause of the vibration problems has therefore been attributed to machinery layout, which requires long coupling shafts to be employed. Due to the requirement for access between the core engine and driven equipment, a long coupling shaft of up to 2000mm in length needs to be used. To reduce mass, and therefore inertial forces, the wall thickness of these shafts is (in relative terms) extremely thin; 2-3mm on a 250mm diameter shaft, and is therefore susceptible to unbalance induced deflections that cumulatively increase the amount

of unbalance forces. Even operating well away from the designed critical speed might therefore induce high levels of lateral vibration.

In an attempt to solve this problem a novel approach was suggested through collaboration with SITL and the University of Lincoln [7]. The proposed design uses an eccentric sleeve that can be retrofitted to existing coupling shafts, Figure 1.5. The design allows for a balance mass to be added to the shaft to counter any unbalance that may exist. The sleeves are purposely flexible to allow for the eccentric position of the balance mass to increase with speed and therefore increase its counter-balancing effect. However, the successful operation of the design requires prior knowledge of the magnitude and position of the existing unbalance in the shaft. The proposal to use an eccentric sleeve was made prior to the initiation of this research, and is not claimed as part of the research presented in this thesis.

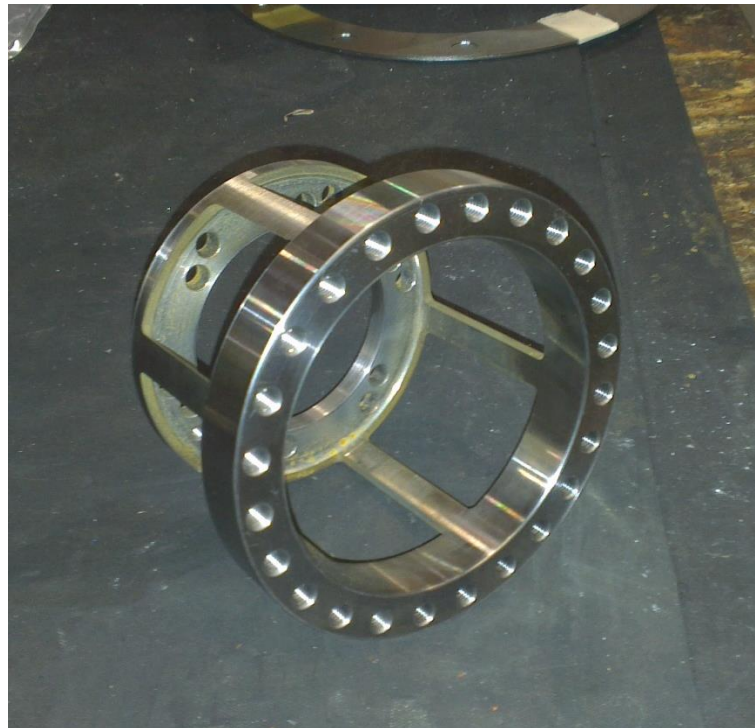


Figure 1.5 – Eccentric sleeve

1.6 Research Objectives

The balancing sleeve is presented as an adaptive passive design to allow for balancing across a range of speeds. By adding mass to the shaft system, in the form of a sleeve, the fundamental natural frequency can be changed, and hence it would be expected that the critical speed of the system would also change. A significant research investigation is therefore required to analyse the behaviour and imparted characteristics of using the sleeves, prior to embedding them into engine units. To investigate the passive control characteristics of the sleeve, a fundamental understanding of the dynamics and effects upon the dynamics of the shaft, is required.

The following research objectives have been pursued in this thesis:

1. Theoretical analysis of the eccentric sleeve design
2. Creation of a finite element model of the full geometry
3. Experimental validation of modelling approaches
4. Parametric study to identify the mechanism and bounds of passive control characteristics of the sleeves

1.7 Thesis Outline

The remainder of the thesis contains the following contributions to knowledge and is organised in the following chapters:

Chapter 2 contains a detailed review of the history of rotordynamics, balancing methods and passive control techniques used in vibration control.

Chapter 3 derives the theoretical equations of motion for the rotating shaft with eccentric sleeves providing similar results to established models but with the inclusion of dynamic boundary conditions due to the inclusion of the eccentric sleeves. Theoretically, the sleeves are treated as rigid bodies and the flexibility is neglected.

Chapter 4 numerically solves the equations of motion and compares the results with those of finite element simulations, and shows a disparity between the two. When included in the finite element model, the flexibility of the sleeves have a greater than expected effect on the natural frequencies and therefore critical speeds of the shaft.

Chapter 5 uses experimental validation using a purpose built test facility to show that the finite element simulations produce the most realistic modelling approach. When including bearing and support characteristics of the test facility, the experimental and finite element results show similar qualitative trends. It is concluded that both the mass and flexibility of the sleeves must be considered in order to proceed with passively controlling the critical speeds of a rotating shaft.

Chapter 6 presents analysis of a wider range of eccentric sleeve configurations and shows that the critical speeds of the shaft can potentially be controlled by altering the stiffness and mass characteristics of the eccentric sleeves. The mechanism by which passive control occurs is a combination of mass damping and coherence of shaft and sleeve natural frequencies. By changing sleeve length it is possible to change the critical speeds of the shaft by up to +10% and -15 % away from the non-sleeve case.

Chapter 7 presents conclusions and outlines further work.

1.8 Research Contributions

- The mechanism by which passive control occurs is a combination of mass damping and coherence of shaft and sleeve natural frequencies
- The effect of adding eccentric balancing sleeves upon the dynamics of a rotating shaft is similar to that of a tuned mass damper
- Sleeve stiffness must be considered as part of the analysis as it has a significant effect upon the critical speeds of the shaft.

Chapter 2 Literature Survey

2.1 Rotordynamics

Much of the underlying principles of rotordynamics were derived between (roughly) 1870 and 1960, with a resurgence in the early 1980's when computing power became readily available to solve complex numerical problems; spawning the development of finite element analysis methods.

The earliest understanding of dynamics of shafts and rotors focused on the description and analysis of vibration that occurs perpendicular to the axis of rotation; known as lateral vibration. Due to extensive work on lateral vibration by pioneers in the subject such as Rankine [8], Dunkerley [9], Weaver [10], Jeffcott [11], Timoshenko [12] and latterly Bishop [13-15] it is a well understood and is a relatively straightforward problem for modern vibration engineers to identify.

Observations by Rankine [8], Föppl [16] and Dunkerley [9] showed that at certain speeds the deflection of a shaft will increase without limit – ‘*The Critical Speed*’. Early developments into rotordynamics suggested that operation above the first critical speed would not be possible. Rankine [8] concluded that a shaft would be stable below the first critical speed and would always be dynamically unstable above it.

Work by de Laval in the late 19th century states that it is possible to design a shaft such that it can operate around critical speeds. The deflection of a flexible shaft will increase as it approaches a critical speed but tend to straighten out once such speeds are exceeded.

In 1894 Dunkerly [9], reported on investigations into whirling and shaft vibration—the formulated empirical equations becoming known as the Dunkerley Method of analysis. However, the study neglected the fact that when a body rotates its natural frequency will

change from when being at rest. Therefore the method overestimates the critical speeds of a rotating body by considerable margins. Chree [17] later reported this phenomenon but was unable to produce a suitable hypothesis.

In 1917 Weaver [10] derived equations describing motions of rotating structures, both qualitatively and quantitatively, and to explain the causes of these motions. This work drew particular criticisms of earlier authors for failing to understand and accurately represent the true physics of what occurs in a shaft when it rotates. Weaver identified that eccentricity of mass along the axis of rotation causes centrifugal forces which induce ‘whirl’. Several previously precluded terms were reported; the shaft arrangement and number of attached disks, the type and number of bearings, the application of power and the presence of torsion, effects of gravity and effects of material damping. A defining observation is the requirement for complex systems to be broken down to more simplified and discrete systems.

A better formulated and quantified analysis of lateral vibrations was published by Jeffcott in 1919 [11]. The Jeffcott Rotor Model considers a uniform, flexible, massless shaft with a centrally mounted single disc, supported by two individual bearings [18]. Later developments to the model brought the inclusion of flexible bearings with variable stiffness and damping coefficients. The Jeffcott rotor model remains in use as basis for modern analysis.

In 1959 Bishop [13] produced a summary of the history of rotordynamics, paying particular attention to the importance and relevance of Jeffcott’s work. An alternative analysis approach was not presented but rather a new solution to solving problems of stability.

2.2 Coordinate Systems

To analyse the dynamics of rotating structures and develop equations of motion, a suitable coordinate system used must be defined. For rotational cases the coordinate system can either be stationary or attached to the spinning object, i.e. a rotating coordinate system.

The choice of coordinates system is dependent upon the rotating body and its support structures. For most simple systems, where the geometry can be considered axis-symmetric, it is common to use a stationary coordinate system regardless of the type of supports. However,

many shafts and rotors are not axis-symmetric, whether through manufacturing imperfections or intentional design. A rotating coordinate system is therefore more useful provided the supports are isotropic.

Instances where a rotating coordinate system is required due to rotational instabilities include: asymmetric rotors with isotropic supports, stability analysis of asymmetric rotors and the effects of internal and external damping. Section 2.6 discusses the impact the chosen coordinate system has upon the calculated natural frequencies of a rotating structure.

2.3 Dynamic Effects of Rotation

A shaft or rotor will not exhibit the same natural behaviour whilst rotating as it does when stationary. This is due to a number of additional forces acting on the rotating structure, with lateral vibrations being dependent both on the speed of rotation due to gyroscopic effects and speed-dependent bearing properties.

2.3.1 Gyroscopic Effects

The gyroscopic effects occur due to coupling between the motions of a body as it rotates. Friswell [3] defines the relationship between the rotations of a disc about three axes in terms of conservation of angular momentum. The disc in Figure 2.1 is rotating about the Oz axis with constant angular speed, Ω .

With a moment (M_x) applied about the x axis, a rotation will occur about the y axis with angular velocity, ψ . For a shaft rotating about its spin axis, if rotation is applied to one of its other axes, a moment will be applied about the third axis to maintain equilibrium. The effect of a rotational axis moving due to an applied moment about another is termed *precession*.

Gyroscopic forces in rotating structures are analysed as damping terms in the system equations of motion. As reported by Green [19] and Föppl [16], these terms are proportional to the rotational speed and are therefore not apparent if the body is stationary. The Coriolis Effect is similar in its analysis to gyroscopic moments and is discussed in Section 2.4.1.

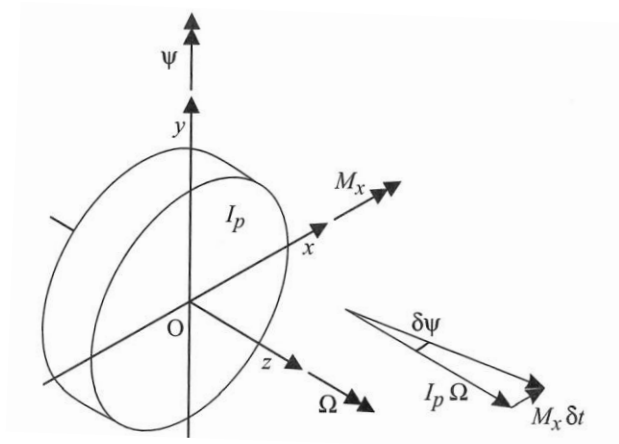


Figure 2.1 – Effects of clockwise moment about Ox [3]

2.3.2 Bearing Effects

All bearings have some degree of flexibility and can absorb energy. Therefore to conduct a comprehensive analysis, it is important to include stiffness and damping forces that may affect the dynamic performance of a rotor system. The stiffness and damping can be speed dependent [20]. For many types of bearings, due to the existence of fluids, the relationship of these is non-linear, making analysis complicated and approximations less inaccurate [15].

The rotor shaft/bearing stiffness ratio will have an effect on the type of motion observed. Where the supports are considered flexible compared to the rotor shaft, the mode shape observed will be circular and uniform in shape; the rotor is effectively undergoing rigid body motion. As bearing stiffness is increased, rigid body motion is prevented causing the rotor shaft to begin to deform. Figure 2.2 compares the first mode shapes at for a shaft rotating at with various levels of bearing stiffness at constant rotational speed.

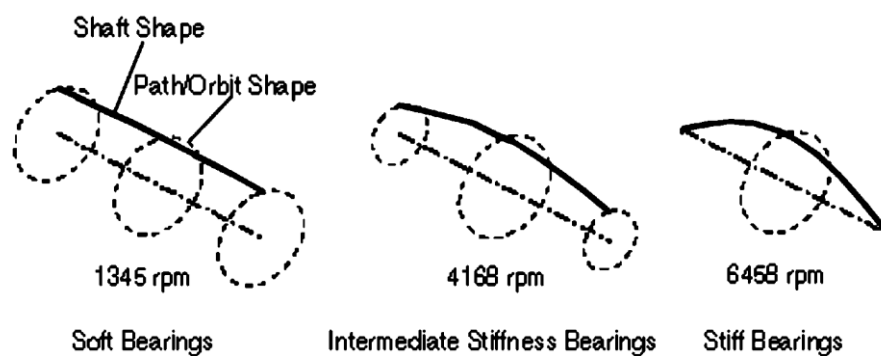


Figure 2.2 – Rotor mode shapes with varying support stiffness [22]

The effect of shaft/bearing stiffness ratio can be particularly important to consider during analysis and design as bearing stiffness cannot always be easily obtained empirically. Parametric studies are often needed to match models to observed behaviour. Figure 2.3 shows a critical speed map, produced in ANSYS [21], for eight modes of a rotating shaft with three mounted disks against varying bearing stiffness.

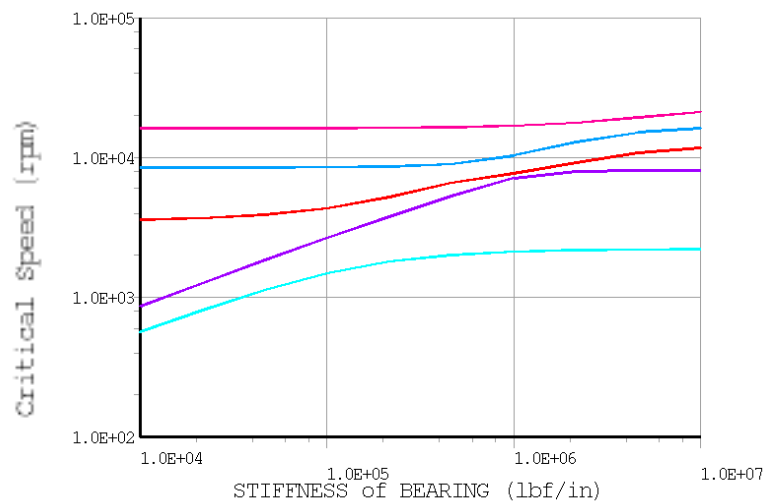


Figure 2.3 – Critical speed map for three disk shaft [21]

When compared with critical speeds measured experimentally, a critical speed map allows the bearing characteristics which produce particular critical speeds to be identified. Tiwari et al [23] conducted an investigation into experimental and theoretical methods of identifying dynamic bearing characteristics. In all incidences, the bearing characteristics obtained are likely to contain inaccuracies.

2.3.3 Acceleration Effects

To run at its operational speed a rotating structure must accelerate from rest. This potentially requires the machine to accelerate through one or more of its lateral critical speeds. Lewis [24] provides an approximate solution to the problem of running a system through its critical speed from rest at a uniform acceleration. The solution shows that the resonant vibration amplitude as it passed through the critical speed is smaller than if the rotor is held there. It is also shown that the critical speed will occur higher than the true critical speed during acceleration but lower than the true critical speed during deceleration.

Sirinivasan et al [25] discuss problems associated with accelerating through a critical speed and limited-torque acceleration. Limited torque acceleration occurs when a rotating machine cannot produce sufficient torque to surpass a critical speed. It is manifested by elevated vibration levels as the machine stalls. It is found that insufficient torque leads to low acceleration rates causing prolonged operation at critical speed and greater levels of vibration. Having sufficient torque therefore allows quicker accelerations and reduced vibration levels when passing through a critical speed.

2.4 Modes of Vibration and Governing Equations

Rotordynamic analysis can be categorised into three different types of motion; lateral, torsional and longitudinal (axial). Each can be discussed and analysed independently, however, it is not always reasonable to do so due to coupling dynamics between them.

2.4.1 Lateral Vibration

Lateral vibration considers motion perpendicular to the axis of rotation and is the primary category of vibration considered when operating high speed machinery. In gas turbine packages excessive lateral vibration can lead to both shaft and bearing wear and eventually failure. Lateral vibration is identified as bending vibration if the rotor shaft is significantly flexible but also rigid body motion if the shaft is rigid compared to the support structures. Key equations of motion for lateral vibration take the standard form of vibration problems. The equations include terms for system mass $[M]$, stiffness $[K]$, damping $[C]$ and also specific terms for gyroscopic effects due to rotation $[G]$. The effects of stiffness and damping in support structures are included in the relevant matrices. For free vibration, the forcing function $F(t)$ is zero.

$$[M]\{\ddot{q}\} + [C + G]\{\dot{q}\} + [K]\{q\} = F(t) \quad (2.1)$$

Gyroscopic terms are added to the damping coefficient matrix. Manipulation of the Equation (2.1) shows that if the rotational speed in the $\{\dot{q}\}$ vector is zero, gyroscopic moments have no effect upon the system dynamics. For any non-zero rotational speed, gyroscopic terms have the effect of splitting the frequencies of the perpendicular motions. The magnitude of the

gyroscopic affect is dependent upon the polar inertia of the body undergoing rotation; therefore for a shaft without a mounted disc, the gyroscopic effect will be limited due to the low polar inertia. When using a rotating coordinate system, the required additional terms due to Coriolis forces $[C_{cor}]$ and spin softening $[K_{spin}]$ are shown in Equation (2.2) [3]:

$$[M]\{\ddot{q}\} + [C + C_{cor}]\{\dot{q}\} + [K - K_{spin}]\{q\} = F(t) \quad (2.2)$$

The Coriolis matrix has a similar effect to the gyroscopic matrix in coupling the lateral displacements; however this is solely the effect of using a rotating coordinate system and not due to the geometry of the body itself [3]. The spin softening matrix accounts for the rotating coordinate system such that the natural frequencies obtained do not include the rotational velocity element [26]. Genta [27] argued using several examples that centrifugal or spin softening is not a real physical effect but merely an artefact of deriving the equations of motion of the system in a rotating coordinate system.

The analysis of lateral vibration using these equations requires knowledge of the mass, stiffness and damping characteristics of the rotor system and bearings. To obtain the forced response, the nature of the excitation function, $F(t)$, must be known.

2.4.2 Whirl

Whirling relates to the deflection in a circular or elliptical motion when a body rotates around the axis of rotation. The direction of whirling is not necessarily determined by the rotational velocity. When the directions of shaft rotation and whirl coincide, it is termed a *forward whirl (FW)*. If the directions are opposite to one another, it is termed *backward whirl (BW)*.

Weaver [10] considered any circular or elliptical motion to be whirling. Downham [28] considers a shaft is whirling when it is rotating at its critical speed. This is opposed by Inman [29] who describes whirling to be *the angular motion of the deflected shaft about the neutral axis of the shaft*. Batrak [5] support Inman's view that whirling can occur at any, non-critical rotational speed. It goes further to define whirl which has speed equal to the rotational speed of the system as *synchronous* whirling. Conversely whirl that occurs at a speed not equal to the rotational speed is defined as *asynchronous* whirling.

A forward whirl excited due to unbalance would be considered a synchronous vibration, however, a backward whirl would not typically be excited due to unbalance. A backward whirl may be excited by an external excitation such as asymmetry or cross coupling in the supports [30].

2.4.3 Torsional Vibration

Torsional vibration is periodic angular motion. Torsional vibrations are considerably simpler to model than lateral vibration as support structures have little influence on torsional natural frequencies [31]. Figure 2.4 shows a rotor system containing several shafts and rotor discs:

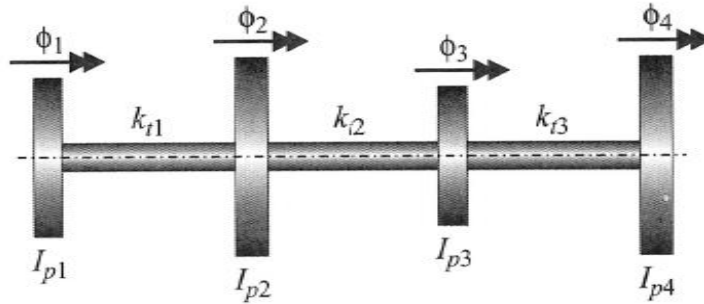


Figure 2.4 – Simple torsional vibration rotor model [3]

Equation 2.3 neglects gyroscopic forces and structural damping. The mass matrix is built using polar second moment of area, I_{pi} and the displacement matrix contains the rotations of the discs, ϕ . The shaft torsional stiffness K_t is determined by Equation (2.4). $T(t)$ is applied torque:

$$[M]\{\ddot{q}\} + [K_t]\{q\} = T(t) \quad (2.3)$$

$$K_{t_i} = \frac{T}{\phi} \quad (2.4)$$

Single rotor shafts are generally unaffected by torsional vibration, with the exceptions of long, rigidly coupled rotors seen in applications such as steam turbines. Single rotors are sufficiently stiff such that the torsional natural frequencies are high enough to avoid excitation through torque transmission. However, by coupling two or more shafts, the overall stiffness of the system is reduced; therefore the torsional natural frequencies are lowered, increasing the possibility of excitation.

Flexible couplings can be affected by torsional vibration. If there is torque ripple, that is where the torque is transferred from one coupled shaft to another and does not remain constant throughout, this can lead to significant torsional excitation. Huang [32] showed that torsional vibration can be excited in the presence of sufficient unbalance and lateral excitation. Conversely torsional vibration could induce bisynchronous lateral vibrations when the shaft is excited at or close to the natural torsional frequency.

2.4.4 Longitudinal Vibration

Longitudinal Vibration concerns translational movement along the axis of rotation and is therefore also referred to as axial vibration. The analysis is of particular importance in rotating machines that are used to provide power by means of thrust through a fan or propeller. In gas turbines, the bearings usually limit the amount of allowable axial movement. Due to this, the analysis of axial vibrations should consider the extension and compression of the rotor shaft material. If a rotor system is analysed for axial vibrations, it can be modelled as a discrete series of spring-mass systems, as shown in Figure 2.5:

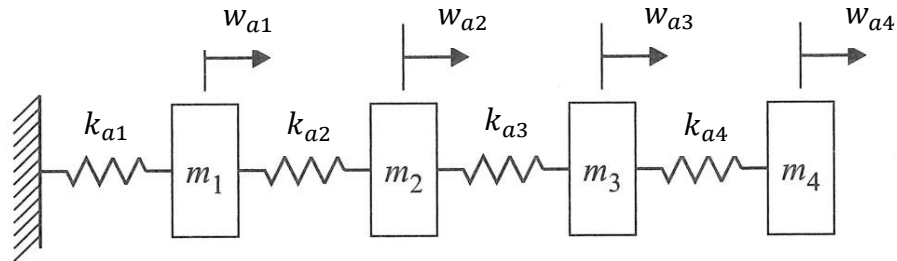


Figure 2.5 – Axial behaviour of a multi-disc rotor [3]

The forced response of the system is given by Equation (2.5) and the axial stiffness by Equation (2.6):

$$[M]\{\ddot{q}\} + [K]\{q\} = F(t) \quad (2.5)$$

$$K_{ai} = \frac{F}{w_{ai}} \quad (2.6)$$

2.4.5 Coupling of Vibration Modes

An awareness and understanding of the mechanisms of how motions are coupled is important. Lateral and torsional vibrations are most commonly analysed individually and whilst it is recognised that both can exist within the same machine, it is generally accepted that they do not significantly interact. Nevertheless, there are exceptions where such coupling can occur:

Lateral – Torsional

Al-Bedoor [33] and Wu and Yang [34] found that interactions between lateral and torsional vibrations can only exist when a shaft or rotor system is not symmetric, and whilst a small amount of eccentricity in any rotating body is sufficient to explain lateral vibrations, it is not a significant factor alone to influence lateral-torsional coupling.

Quin and Mao [35] developed a new shaft element model for coupled torsional-flexural vibration including; translational and rotational inertia, gyroscopic moments, bending, shear and torsional deformations, internal damping and mass eccentricity. Examples analysed included a dual rotor system, a more complex single rotor system, and a spur gear system.

Huang [36] studied the torsional behaviour of a parallel misaligned coupling. This showed that if parallel misalignment occurs, both torsional and lateral natural frequencies are present at the 1x rotating frequency. Although coupling between torsional and lateral vibrations is not specifically mentioned, the results demonstrate that both lateral and torsional vibrations are excited by misalignment. Li and Yu [37] also identify misaligned gear couplings as a source of lateral-torsional vibration.

Gosiewski [38] conducted an analysis of lateral-torsional behaviour of a three mode Jeffcott rotor. Previous work had found that at particular speeds coupled lateral-torsional vibrations led to instability. The regions of instability were found to occur at rotational speeds close to the intersection of lateral and torsional natural frequencies.

Kumar and Roa [39] report on an experimental study of the whirling characteristics of a geared rotor system. The work reached similar conclusions to that of Gosiewski [38] i.e. that lateral vibrations are seen to peak at rotational speeds where the lateral and torsional natural frequencies are close. Shafts connected by gears also influence lateral-torsional coupling, Roa et al [40] and Lee et al [41].

Lateral – Longitudinal

Papadopolous and Dimarogonas [42], [43] examined the lateral – longitudinal vibrations of a non-rotating cracked shaft. Behzad and Bastami [44] demonstrated how centrifugal force can affect the lateral natural frequency through axial forces. The centrifugal force created by rotation causes a radial stress which due to the Poisson effect and the constraining of axial movement in rotors also causes an axial stress. The sum of axial stresses across the rotor shaft cross section produces a net axial force that changes the natural frequency of vibration. The axial force produced by rotation of a shaft and impact upon the lateral natural frequency is comparable with the gyroscopic effect. It was reported that for long shafts at high speed the axial force affect was considerable but at lower speeds negligible.

Lateral – Longitudinal – Torsional

Luo and Sun [45] developed a model for multistage, multi-mesh geared shaft systems which takes into account coupling between torsional-lateral-axial vibrations. It was shown to model some cross coupling at natural frequency that matched observed phenomena.

Darpe et al [46] considered the coupling of all three modes of vibration for a cracked rotating shaft. The coupling between all three motions is evident by excitation of one of the modes and is only seen due to the presence of the crack.

2.5 Modal Analysis

A modal analysis determines the vibration characteristics of a structure; natural frequencies and mode shapes (Section 2.5.1). Modal analysis allows the design of a structure to avoid resonant vibrations or to vibrate at a specified frequency and gives engineers an idea of how the design will respond to different types of dynamic loads. It can also serve as a starting point for another, more detailed, dynamic analysis, such as a transient dynamic analysis, a harmonic analysis, or a spectrum analysis. The natural frequencies and mode shapes are important parameters in the design of a structure for dynamic loading conditions. For a rotating structures, the gyroscopic effects resulting from rotational velocities can be included into the modal system along with damping effects due to the presence of bearings. The evolution of natural frequencies with the rotational velocity can be studied with the aid of Campbell

Diagrams (Section 2.6) [47]. Theoretical modal analysis allows the dynamic characteristics of a structure to be modelled, in terms of equations of motion, and its response predicted.

Modal testing is the process of testing components or structures with the objective of obtaining a mathematical description of their dynamic or vibration behaviour. Doing so allows:

1. Use of the model to predict the structural response at any point
2. Determining the nature and extent of vibration response levels in operation (Determine any unknown input forces)
3. Verification of theoretical models

Ewins [48] states that modal testing requires the integration of three components:

- Understanding of theory of vibration
- Accurate vibration measurement
- Realistic and detailed data analysis

Modal testing uses experimentally obtained data to generate spatially frequency dependent models, Figure 2.6. In the modal domain, the displacement of the structure for each mode is observed against time, whereas in the frequency domain, amplitude spikes occur at the frequency each mode.

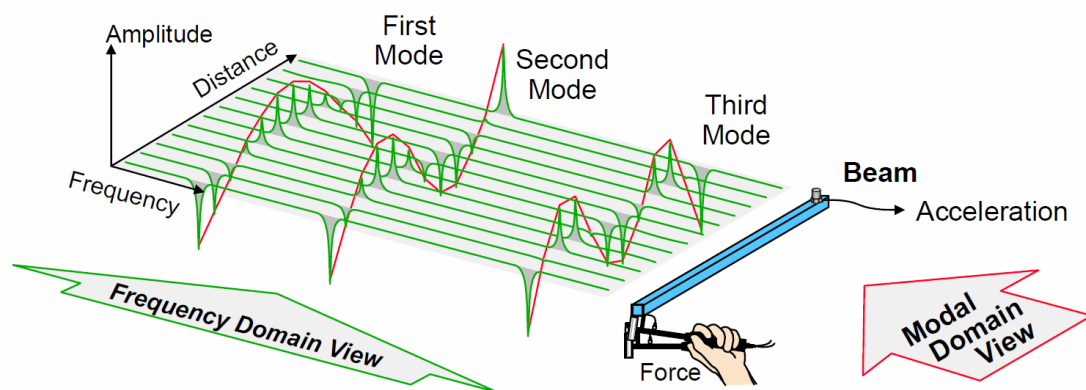


Figure 2.6 – Modal and frequency domain [49]

The relationship between input forces and the system response (X/F) can be modelled as a Frequency Response Function (FRF), Figure 2.7.

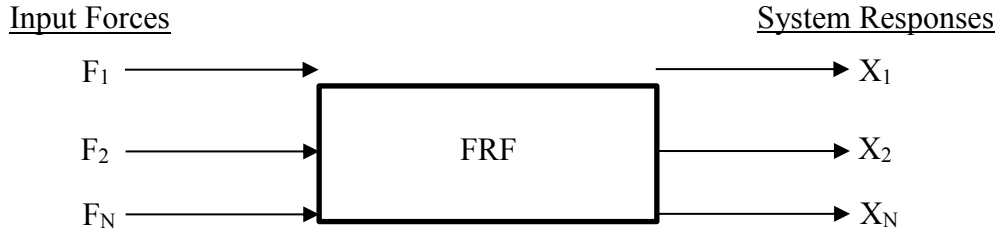


Figure 2.7 – Input forces and response of a structure related by FRF

The general expression for any FRF of a structure can be modelled using Eq (2.7) where: λ_r is the eigenvalue of the r th mode (its natural frequency), $\bar{\mathbf{v}}_{ir}$ is the i th element of the r th eigenvector $\{\bar{\mathbf{v}}_i\}$ (its mode shape) and N is the number of degrees of freedom.

$$H_{ij}(\omega) = \frac{X_i}{F_j} = \sum_{r=1}^N \frac{(\bar{\mathbf{v}}_{ir})(\bar{\mathbf{v}}_{jr})}{\lambda_r^2 - \omega^2} \quad (2.7)$$

This expression forms the foundation of modal analysis: it shows a direct connection between the modal properties of a system and its response characteristics. Using experimental data obtained from a vibrating structure to create an FRF and predict its future behaviour is analogous with using equations of motion and theoretical modal analysis. Furthermore, experimental data can be further used to improve the fit of theoretical models.

2.5.1 Mode Shapes

When excited at a natural frequency, the motion of a system will move with a particular pattern or *mode shape*. The total response of a system will be a combination of all its individual mode shapes from differing contributions. The principle of mode superposition is considered to hold in such studies. The obtained eigenvectors, $\{\bar{\mathbf{v}}\}$, contain the mode shapes of a system.

As previously discussed, due to rotational effects, the natural frequency of a rotating structure will change with rotational speed and, hence, so will the shape taken by a particular mode. As shown in Section 2.3.2, bearing stiffness changes with rotational speed and affect the shape taken by the rotor. Figure 2.8 to Figure 2.10 shows the first three lateral bending mode shapes at critical speed of a shaft with a mounted disc.

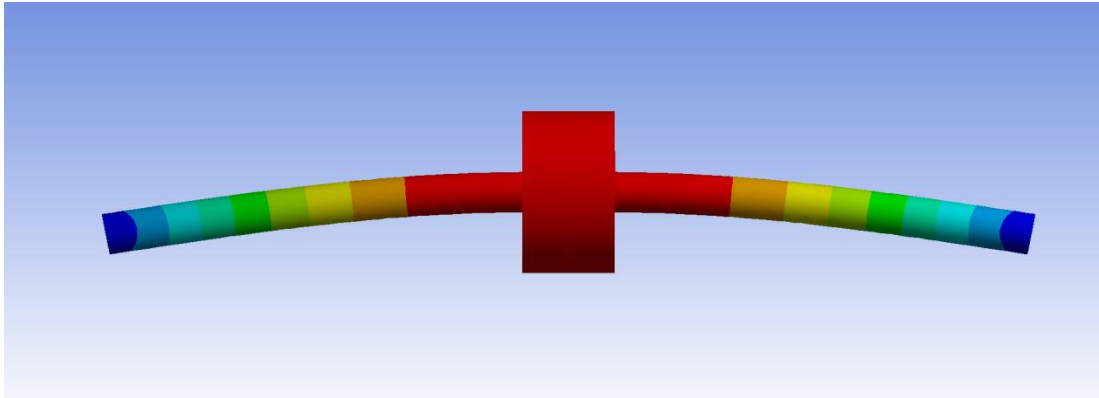


Figure 2.8 – 1st bending mode shapes of a shaft with a mounted disc

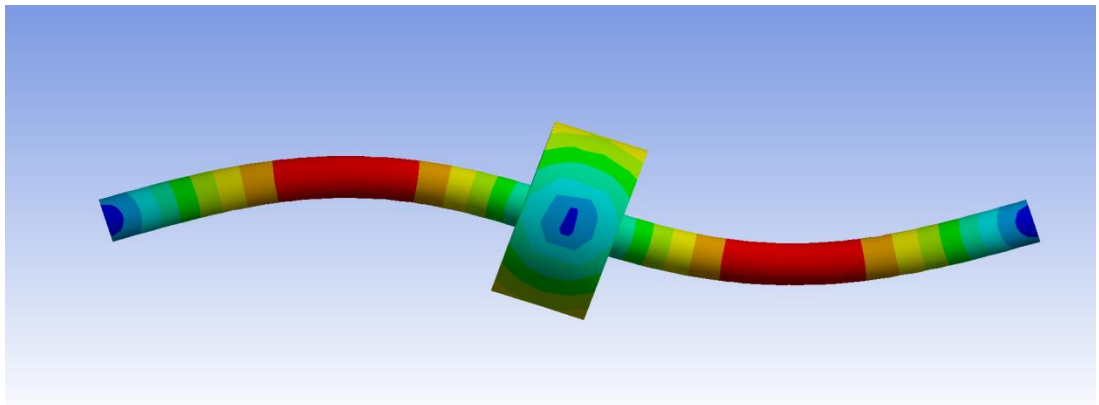


Figure 2.9 – 2nd bending mode shapes of a shaft with a mounted disc

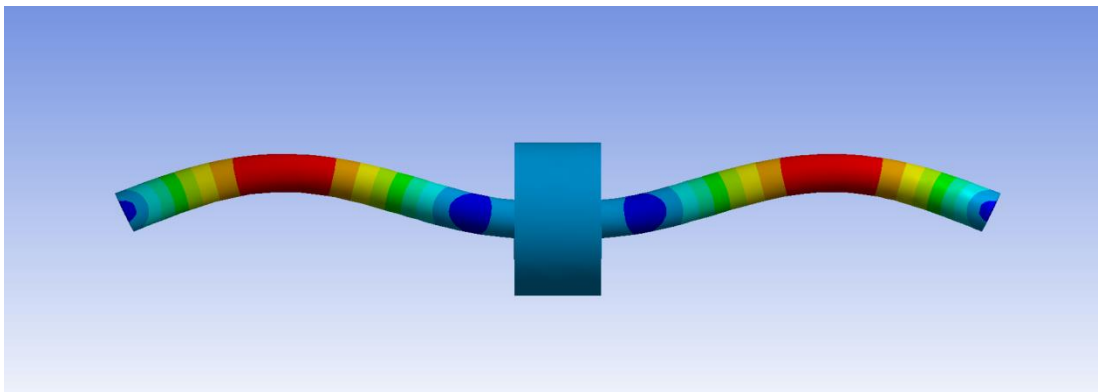


Figure 2.10 – 3rd bending mode shapes of a shaft with a mounted disc

2.6 Campbell Diagrams

An important tool in the analysis of critical speeds is the Campbell Diagram. It is a presentation of resonance frequencies as functions of rotor speeds [4]. The natural frequencies of a machine or system are dependent upon its mass, stiffness and the damping characteristics which are dependent upon rotational speed. It is therefore important to plot these variations of natural frequency with respect to rotational speed. Figure 2.11 shows how the natural frequency (specifically in this instance Ω) varies with rotor speed (ω) for five modes.

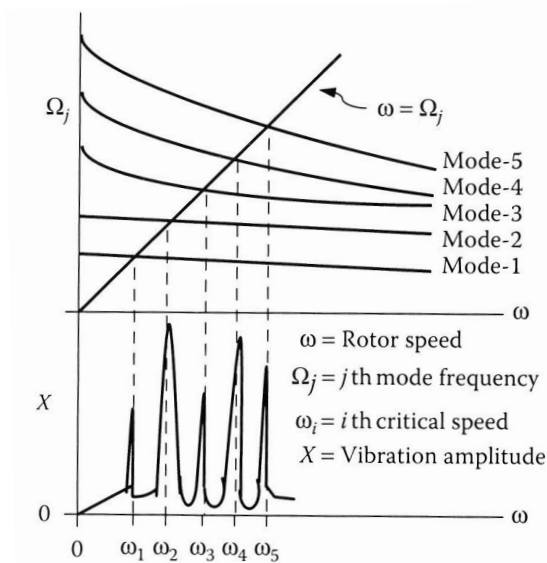


Figure 2.11 – Example Campbell diagram [4]

Rotating bodies are also subject to external excitations. Such forces can be influenced by rotational speed (due to rotor unbalance, misalignment, rotor shaft deformation or cracks). However, they also can be unrelated or be caused by environmental factors; possibly base excitation through foundations and supports. If the frequency of these forces is known, it can be plotted against rotational speed on a Campbell diagram.

When the natural frequency of a mode coincides with frequency of excitation, a critical speed is excited. Critical speeds can be identified by monitoring the system for rotational speeds that cause large vibration amplitude, as shown in the lower part of Figure 2.11. A Campbell Diagram can be used to show gyroscopic effects upon the natural frequencies of modes. Figure 2.12 shows Campbell Diagrams for the shaft in Figure 2.10. The natural frequencies of the first two bending modes are shown as four lines (FW and BW for each mode).

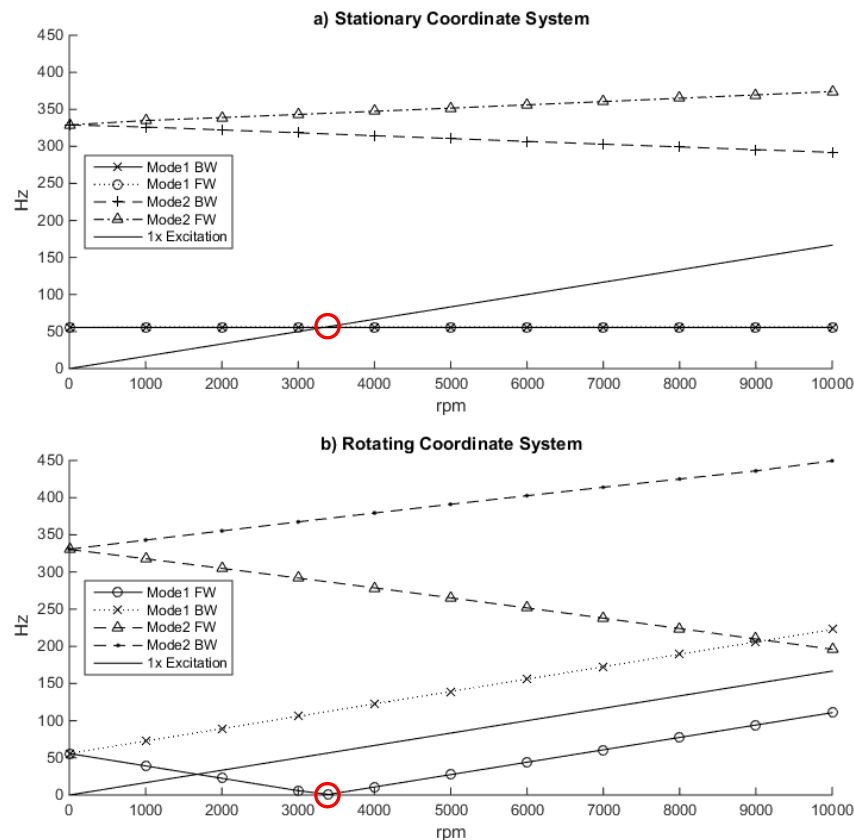


Figure 2.12 – Campbell diagrams in stationary and rotating coordinate systems

For frequencies obtained using a stationary coordinate system, shown in Figure 2.12a, for the first bending mode, the disk is moving with translational motion only; therefore the gyroscopic moment is low, meaning the frequencies of this mode do not significantly deviate. For the second bending mode, the disc is tilting about its own axis; therefore significant gyroscopic moments are induced and there is substantial deviation of the natural frequencies.

How modes appear on a Campbell diagram also vary depending on the type of coordinate system used. Figure 2.12b shows the natural frequencies of the shaft with central disc calculated in a rotating reference frame. The first bending mode shows a clear splitting which is not present in the stationary coordinate system. The second mode shows a greater amount of splitting. Both effects are a result of a combination of the Coriolis spin softening matrices. Figure 2.13 to Figure 2.15 repeats the process for a simple shaft without a centrally mounted disc.

When compared with Figure 2.8 it is clear that the mode shapes of the simple plain shaft are similar to the shaft with centrally mounted disc. However due to the lack of disc and therefore polar inertia, there is a very low gyroscopic moment applied in either the first or second bending modes of the shaft.

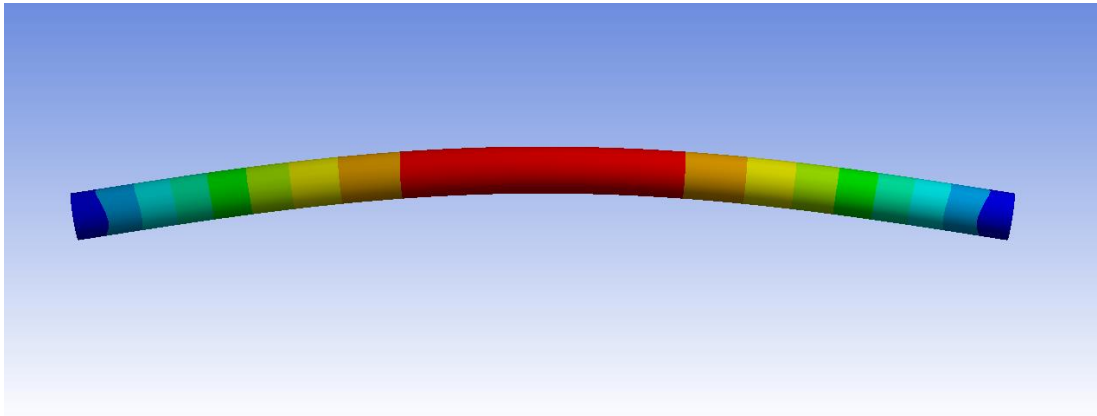


Figure 2.13 – 1st bending mode of simple plain shaft

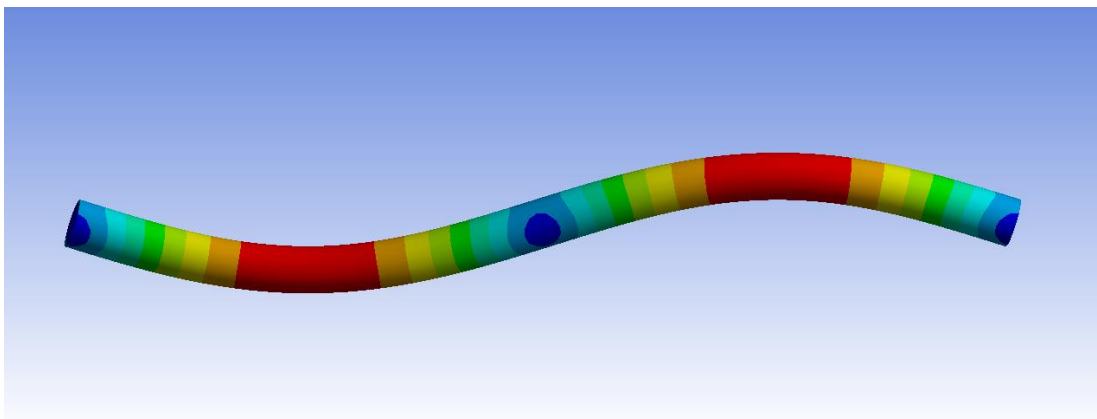


Figure 2.14 – 2nd bending mode of simple plain shaft

Observation of Figure 2.15 shows that in the stationary coordinate system this causes no significant splitting of frequencies. In the rotating coordinate system, the degree of splitting of the frequencies for each mode, due to Coriolis matrix, is almost identical to the shaft with centrally mounted disk.

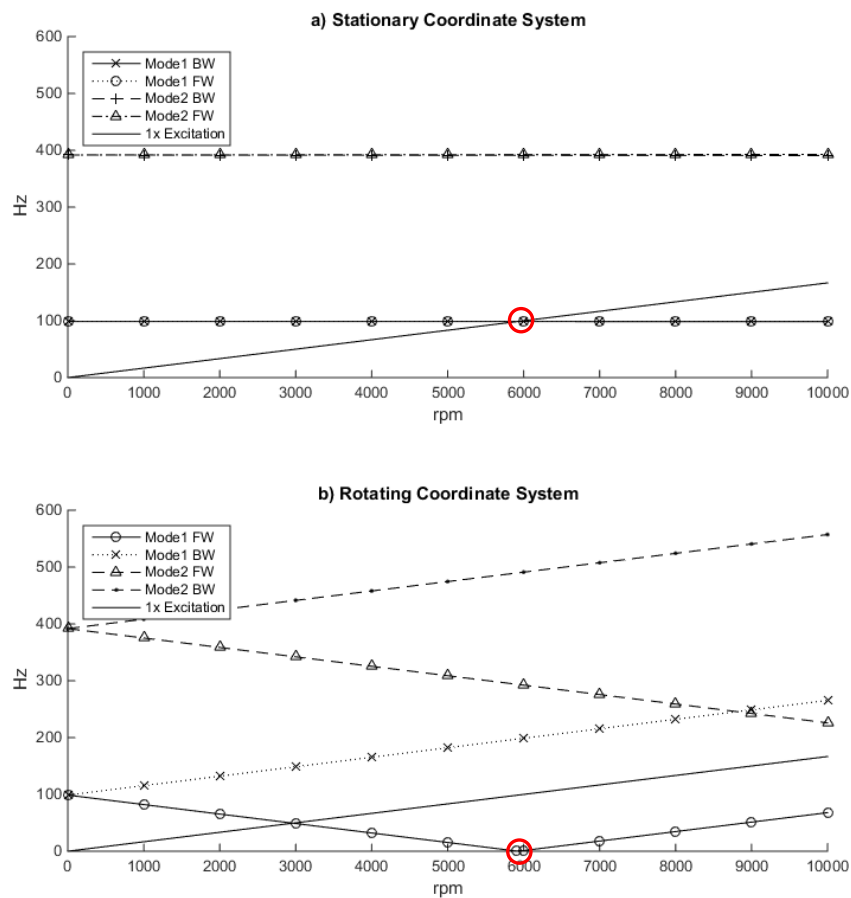


Figure 2.15 – Campbell diagrams for simple plain shaft

From Figure 2.12 and Figure 2.15 there are some clear observations:

1. The natural frequencies of forward whirling modes will increase with rotational velocity and backwards mode frequencies will decrease
2. A forward whirling, synchronous critical speed in a stationary coordinate system is determined by the coincidence of a forward whirling mode with the excitation frequency (circled in Figure 2.12a and Figure 2.15a).
3. When observed in a rotating coordinate system, the same critical speed corresponds to zero frequency [50] (circled in Figure 2.12b and Figure 2.15b).
4. In a rotating coordinate system forward travelling modes have lower frequencies than backward travelling modes [3]

From these observations it is possible to transform between coordinate systems. When observed in a stationary coordinate system, forward travelling modes in a rotating coordinate system have the frequency of the rotational speed (f_{Ω}) added, whilst backward travelling modes have the frequency of rotational velocity subtracted [3]:

$$f_{FW_{stat}} = f_{FW_{rot}} + f_{\Omega} \quad (2.8)$$

$$f_{BW_{stat}} = f_{BW_{rot}} + f_{\Omega} \quad (2.9)$$

Using these equations allows flexibility over the choice of coordinate system used for analysis. There may be instances where one coordinate system should be used in preference to another (asymmetric rotor, anisotropic bearings, and instabilities), however, the results can be transformed between them [26]. This is particularly useful when comparing result from experimental measurements which are usually obtained in a stationary coordinate system [21].

From [3], natural frequencies obtained in a stationary reference frame are not natural frequencies in the usual sense. When equations of motion are converted into a stationary frame of reference, they contain time varying coefficients, such as shaft or support stiffness. Such equations cannot be solved as an eigenvalue problem and do not yield true natural frequencies. Therefore, any natural frequencies obtained in the rotating frame of reference must be transformed into the stationary frame by virtue of Equations (2.8) and (2.9)

2.7 Methods of Vibration Control in Rotating Shafts

Vibration control is the means of reducing the amplitude of vibration exhibited by a structure due to some form of disturbance. This can be carried out in two primary ways: 1) through design and optimal operation to ensure harmful frequencies of vibration are avoided and 2) aggressive mitigation techniques to directly reduce the effects of those vibration frequencies that cannot be avoided.

Through discussion of rotating machinery it is clear that in order to reduce lateral vibration levels, critical speeds should be avoided during operation and exposure minimised during

start-up/run down. Furthermore, to minimise the effect of any residual unbalance that may occur in the rotor field balancing may need to be carried out. To minimise torsional vibration, shafts/rotors and couplings should be designed with suitable stiffness and be correctly aligned when in operation.

Lees et al [51] gave a review of the practices involved in condition monitoring of rotating machines. In addition to the issues of design, unbalance and alignment, the effects of cracked rotors, bearing faults and rotor bow were identified as factors of considerable practical importance.

2.7.1 Balancing

All shafts and rotors contain some degree of residual mass unbalance due to asymmetry and imperfect machining. Such unbalance can lead to significant forces being exerted upon the surroundings; bearings, foundations and casings. It is vitally important to ensure that such forces are controlled by eliminating the geometric unbalance of the rotor where possible. Primarily this is achieved through design and high tolerances in manufacture. Nevertheless, this is frequently insufficient and other means of reducing vibration levels are necessary. Post manufacture, dynamic balancing is achieved by adding or removing the distribution of mass on the rotor such that a state of balance is achieved. This resulting state of balance will still not be perfect as the second moment of area of the rotor will never be symmetric, therefore it is necessary to apply alternative balancing techniques for flexible rotors.

A rigid rotor can be statically unbalanced, where an unbalance force induces a transverse vibration or 'bounce' motion, Figure 2.16a. A static unbalance occurs when there is a single unbalance force present on a rotor. Static unbalance is corrected by single plane balancing, where the addition of a single equal balance weight in the same plane but 180° out of phase in its radial position.

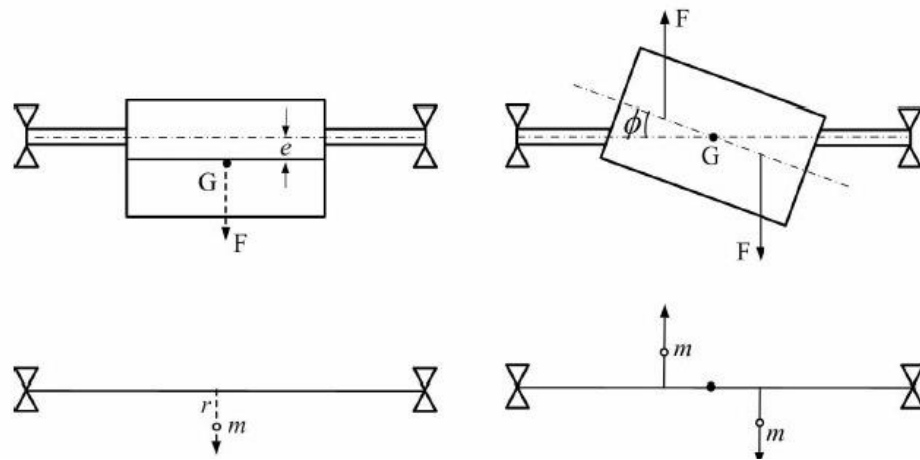


Figure 2.16 – a) Static unbalance b) Dynamic unbalance [2]

Two-plane balancing is required when there are two unbalanced forces acting in two different planes. The vibration induced is a transverse ‘tilting’ motion, although the rotor remains rigid. This is referred to as dynamic unbalance, Figure 2.16b. To balance, two equal balance weights are placed in the same two planes but 180° out of phase in radial positions. If a rigid rotor is balanced using two planes at any speed, it is considered balanced across all speeds. Yu [52] proposes a method whereby two plane balancing of symmetric rotors can be achieved by the use of one trial weight run. Reported results are close to true values obtained by two trial weight runs and are deemed acceptable for field balancing.

Modal balancing was proposed in the 1950s and developed by Bishop and Gladwell [14]. The definition of balancing *involves the addition of small masses at the surface in such a way as to cancel out the effects of eccentricity*. This paper summarised the previously derived mathematics required in order to achieve a ‘*low speed balance*’ and developed the ‘*mode by mode balancing of flexible rotors*’. The underlying mathematics also includes modifications to account for a lack of initial straightness of the rotor shaft.

At low speeds i.e. those below the first critical speed, a flexible rotor can be assumed as a rigid body i.e. there is no deflection due to eccentricity. Despite this there may be considerable increase in centrifugal force transferred to the bearings. The purpose of low speed balancing is to ensure that the mass centre is effectively in line with the axis of rotation. At high speeds i.e. those greater than the first critical speed, balancing as a rigid rotor becomes detrimental.

For each critical speed that a rotor operates above, a different balancing condition will be required and therefore different balance planes are required.

The mathematics developed in [14] allows for the identification of each balance plane, i.e. the axial location where balance weights will have most effect in mitigating vibrations excited at a critical speed. Using the balance plane the position of each balance weight can be found by trial and error using trial weights. When balancing for a particular mode, a trial weight is added to a particular location and the amplitude of vibration is measured close to the critical speed being balanced. The amplitude is plotted against location as seen in Figure 2.17:

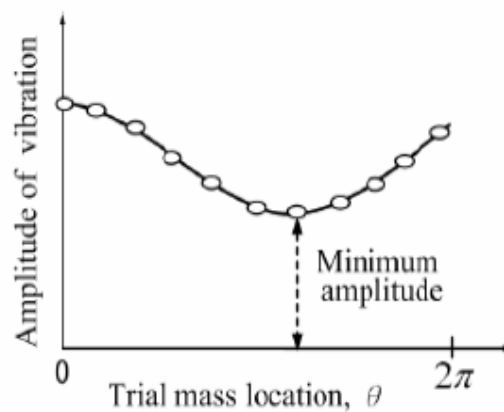


Figure 2.17 – Trial weight location plot [2]

The process is repeated numerous times at different locations until the location is identified where the vibration amplitude is minimum. When the correct location is identified the mass of trial weight can be altered a desired state of balance is achieved. This procedure is clearly tedious and time consuming but yields accurate levels of balance. Morton [53] discussed methods to conduct modal balancing without the use of trial weights. Existing techniques attempt to mathematically model a rotor system based on measured characteristics. However this requires assumptions of the bearings which are difficult to model accurately. Morton's model allowed for the unbalance on a rotating shaft to be calculated from running vibration measurements, and no bearing representation was required. The resulting model offered a reduction in time required running a machine in order to find a state of balance.

Parkinson [54] extensively summarises the theory behind unbalance in rotors with both flexible and rigid shafts. Although written many years after Morton, [53] the principles are similar, although with less mathematical focus. The fundamentals of balancing are reported as well as various balancing procedures; modal balancing, both single and two plane, and influence coefficient balancing. The process selects correction masses in positions to ensure that vibration is zero at a series of locations along the shaft for a series of shaft speeds. It is heavily reliant on computational capability. Parkinson found that modal balancing was made more effective by the use of the influence coefficient computer programmes and made for faster, more sensitive balancing than influence coefficient alone. Influence coefficient balancing does not require the same detailed information regarding critical speeds and mode shapes as the modal method. Assumptions are made concerning how a force or displacement at a particular position on the rotor influences a displacement or force at another position on the rotor. It is suitable for in situ machines where it is not possible to directly balance on the plane of the known unbalance.

Parkinson [54] also discusses ‘automatic balancing’ whereby balance weights have limited movement to allow for balancing across a range of speeds. Such devices have been proposed by many authors, including Rodrigues et al [55]. This research was limited to a rigid rotor where the degree and position unbalance may change over time.

Garvey et al [56] considered rotors that have been balanced in a balancing machine during manufacture. There may be some variability in characteristics between the stator used for balancing and that of the machine in situ. The methods require significant knowledge of the unbalance in order to achieve a robust balance that will overcome the variability which may be experienced. The model may also be useful for rotors where foundation characteristics may change over time.

2.7.2 Alignment

Misalignment is a problem when occurs with the commissioning of turbomachinery. Alignment is important to consider when building a rotor system, ensuring the rotor is aligned correctly in its bearings. The issue becomes more important and the effects of misalignment greater when connecting machines together. To transmit power, rotating machines may require a flexible coupling to be used in order to couple two or more shafts. Manufacturing

tolerances of the shafts and placement of the machines can cause the two shafts to be offset from each another to some degree. If there is a transverse offset between the two shaft lines of rotation, this is referred to as lateral or parallel misalignment, Figure 2.18. However, if the two surfaces being mounted together are not precisely perpendicular, an angular misalignment occurs, Figure 2.19.

‘Correct’ alignment is achieved through ensuring appropriate tolerances are met [6]. Alignment tolerances are usually specified by the coupling manufacturers in line with international standards [57]. Alignment is assessed by four parameters; parallel and angular misalignment in plan and side views. Figure 2.20 refers to these as *vertical and horizontal*. With the misalignment values between the shaft rotation axes known, trigonometry is used to check that the configuration falls within limits.

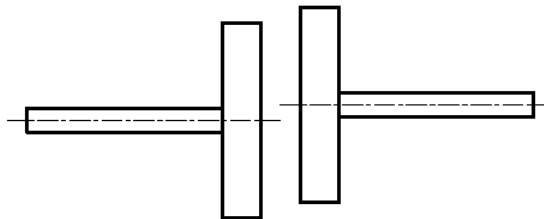


Figure 2.18 – Parallel misalignment of coupling shafts

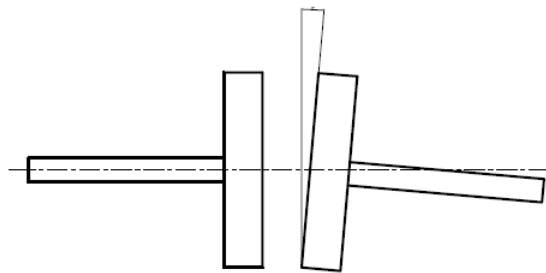


Figure 2.19 – Angular misalignment of coupling shafts

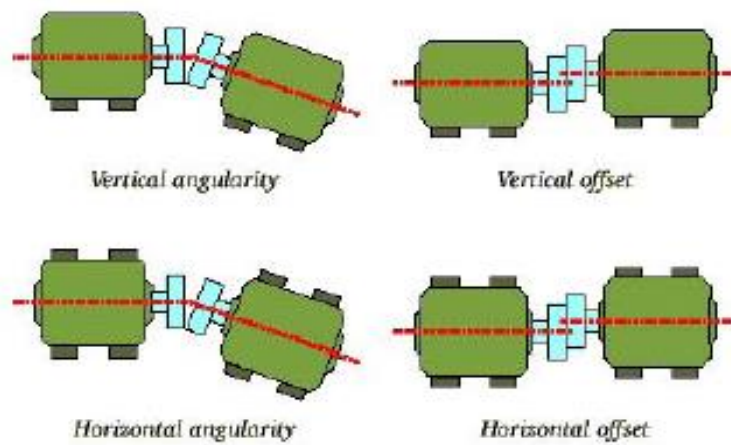


Figure 2.20 – Categories of misalignment

Any misalignment between the shaft rotational axes can result in increased levels of vibration and additional bearing forces. Huang [36] found that if parallel misalignment is present, both lateral and torsional vibrations are excited at several resonance frequencies. This leads to premature wear or even catastrophic failure of bearings, seals, the coupling shaft, or the machine rotors. Misalignment has long been recognized as one of the leading causes of machinery damage. The greater the misalignment, the greater the rate of wear and the likelihood of premature failure. Moreover, misaligned machines absorb more energy and consume more power [58].

Prabhakar et al [59] considered a rotor-coupling-bearing system passing through critical speed using a finite element method (FEM) developed previously. The response of misalignment upon lateral vibrations was analyzed through a parametric study that investigated the time response for varying angular accelerations and types of misalignment. Simple equations of motion are used to build coupling and bearing stiffness matrices. The coupling was either considered as a frictionless joint or one that includes stiffness and damping. Using a continuous wavelet transform (CWT), critical speeds could readily be identified when misalignment was present and at low angular accelerations. The CWT was identified as a useful tool for detecting misalignment when a machine is starting up.

Saavedra and Ramirez published a series of papers on misalignment of couplings [60], [61]. Stiffness data was obtained allowing a FEM stiffness matrix to be constructed. From this, the

vibration caused by misalignment is predicted from simple equations of motion. The effect of misalignment on coupling stiffness can be seen by increased force and vibration levels. To validate the theoretical model a rotor system composed of motor and generator linked by different flexible couplings; a 3-pin and a 3-jaw, was built. The experimental results validated the model and it was proven that vibration characteristics are directly related to the coupling stiffness, i.e. the type of coupling used and amount of misalignment present.

Patel et al [62] analysed the effect of simultaneous crack and coupling misalignment upon the whirl characteristics of a rotor shaft through a parametric study on crack size and location as well as misalignment type and level. Previous research had struggled to identify the vibration response of crack and misalignment when both were present. Using a FEM model, the effect of one upon another was examined and the results were found to be typical for the individual analysis of crack and parallel misalignment faults. Angular misalignment was found to have no impact upon whirl characteristics in the presence of a crack and could not be detected.

Ganesan and Padmanabhan [63] modelled the varying stiffness of a flexible disc coupling used in gas turbine applications. As misalignment increased, the increase in asymmetry caused directional time-variations in stiffness. Disc stiffness was obtained through FE analysis using commercial software. Using the time varying stiffness, equations of motion were developed and a numerical model built to analyse the unbalance response due to misalignment. Sub-critical speed responses were found to exist. Experimental validation was sought that proved the analysis qualitatively; however, discrepancies existed in magnitude of results, the difference due to assumptions regarding the level of unbalance. Nevertheless, despite the inaccuracies the increased credibility to the link between misalignment and increased excitation of subcritical frequencies.

The use of long, flexible couplings allow for a degree of misalignment. This is usually sufficient to absorb any temporary misalignment that may occur due to unbalanced forces whilst machines are traversing the first critical speed.

2.7.3 Active Control

Active vibration control uses an external actuator to provide a change to the dynamic characteristics of the system of which it is a part. Active control requires feedback control so that the change supplied by the actuator is dependent on the response of the system. Actuators

can either be paired with a sensor or can also act as a combined actuator/sensor to provide feedback. The effectiveness of active vibration control is very dependent upon the robustness and response of the feedback system.

Figure 2.21 shows an example control feedback system for an active vibration suppression setup on a structure. The response is measured and an appropriate control signal applied.

Active control in rotordynamics is considered as the application of corrective lateral force to a shaft or rotor. This differs from active or automatic balancing where the mass distribution is adjusted. Automatic balancing of rigid shafts and rotors is limited in its success with high speed flexible shafts operating through numerous modes. Some success is seen in household applications such as washing machines.

Many types of control law have been reported for this purpose. Wang and Inman [64] considered four conventional vibration suppression control laws; positive position feedback (PPF), Proportional Integral Derivative (PID), non-linear control and Linear Quadratic Regulator (LQR) controls, as well as four hybrid modifications to these law for optimal use of actuators in terms of vibration reduction and power consumption. Models were tested on a thin cantilever with a piezoelectric patch. Hybrid control laws show lower power consumption than classical methods. Although only tested on a non-rotating beam, the control laws are considered suitable to control systems for active bearings or other rotating active control systems.

Cole et al [65] developed a real-time algorithm to calculate the amplitude and phase of vibration components with a view to cancelling them using dynamic feedback control. The controller demonstrated the ability to reduce steady state vibration levels as well as responding quickly to excitation

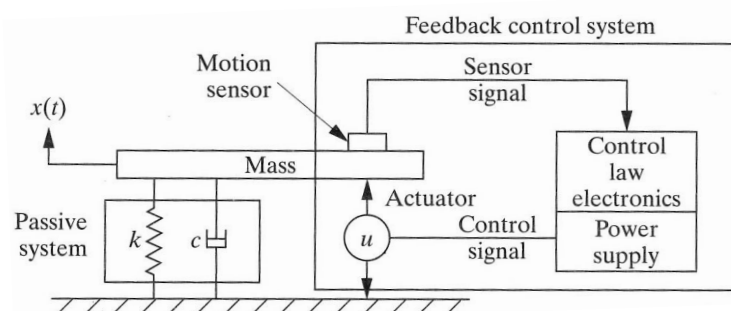


Figure 2.21 – Feedback control system for active vibration control [29]

2.7.3.1 Active Bearings

Zhou and Shi [66] conducted a survey into the special case of active vibration control in rotating machinery. The difference between rotating machinery and other flexible structures is that the dynamics of the rotor changes with the rotational speed of the rotor system. It was identified that the best control performance is obtained if control gains vary with rotational speed. Moreover, since the shaft is a moving element, a noncontact actuator must be used to apply the control force to the rotating shaft. These include electromagnetic, hydraulic and piezoelectric.

Active bearing characteristics can be adapted to reduce vibration levels dependent on the systems response. Burrows et al [67] summarised existing knowledge and current use of active bearings as well as what is required to utilise active bearings to produce so called ‘smart machinery’ that is able to autonomously control vibrations. Again magnetic bearings feature heavily as actuators for future smart machinery; however, greater significance is placed upon effective control and diagnosis of vibration faults.

Magnetic bearings

Magnetic bearings are becoming popular in industry due to their low losses, no requirement for lubricant and long life [3]. Rotordynamics analysts are attracted by the ability to apply a synchronous lateral force to a shaft to control the unbalance response and compensate for vibration displacement of the shaft [66].

An active magnetic bearings are based on electromagnetic suspension that maintain an air gap about the shaft. Figure 2.22 shows the schematic of an active magnetic bearing system and electromagnet assembly; power amplifiers which supply current to the electromagnets, a controller, and sensors to provide the feedback required to control the position of the rotor.

Magnetic bearings are affected by issues of reliability and redundancy, and failure of the magnetic field can result in contact and damage between the bearing and rotor. It is commonplace for magnetic bearings to have a backup set of ‘regular’ bearings to accommodate touchdown—it is known that non-linear vibrations can occur when the rotor falls onto the backup bearings [4]. To maintain a desired rotor position, bearing loads are constantly adjusted through feedback position control. Errors can arise from differences in the placement of sensors and position of the applied bearing force, causing instabilities.

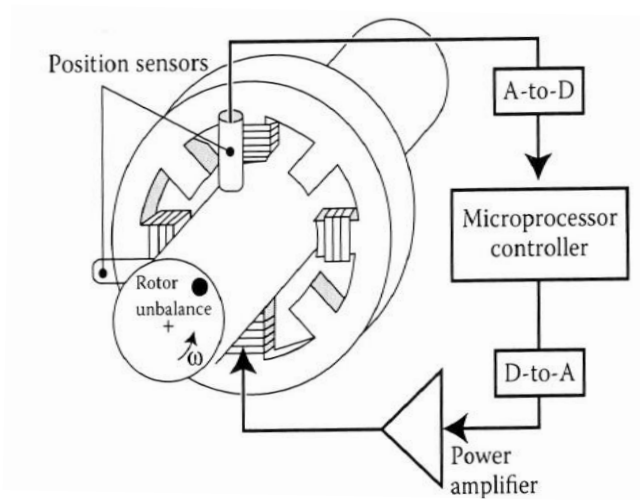


Figure 2.22 – Schematic of an active magnetic bearing [4]

Piezoelectricity – Piezo bearings

Piezoelectric materials undergo mechanical deformation if subjected to an applied voltage. Conversely, they will generate an internal potential difference if subjected to strain. For design purposes. It can be assumed that the force exerted by a piezo actuator is proportional to the applied voltage. Research has been primarily focussed on surface mounted sensors and actuators for mechanical structures such as beams or frames [68-71]. However, effort has been made to use these principles on rotating shafts.

Horst and Wolfel [72] produced an FE model of a rotor system that used shaft mounted piezo actuators to control vibration. The model was validated using experimental testing and demonstrated the ability to achieve active vibration control. However, more robust control techniques need to be sought. Sloetjes and Boer [73] followed [72] by using complex algorithms to model surface mounted piezo sheets mounted to flexible shafts. Four rotor models incorporating piezo functionality are outlined in the study. The model showed that the actuator sheets can be self-powered but with limited function. Despite this, systems using piezo sheets appear feasible with further research.

Piezo bearings use piezoelectric materials to provide actuation instead of magnetic counterparts. In this case, shafts are supported using traditional bearings with piezo sensors and actuators externally mounted. Figure 2.21 shows an example of a piezo bearing with sensors and actuators mounted externally. Control is achieved by adjusting the shaft centre of rotation through adjustment of the bearing position.

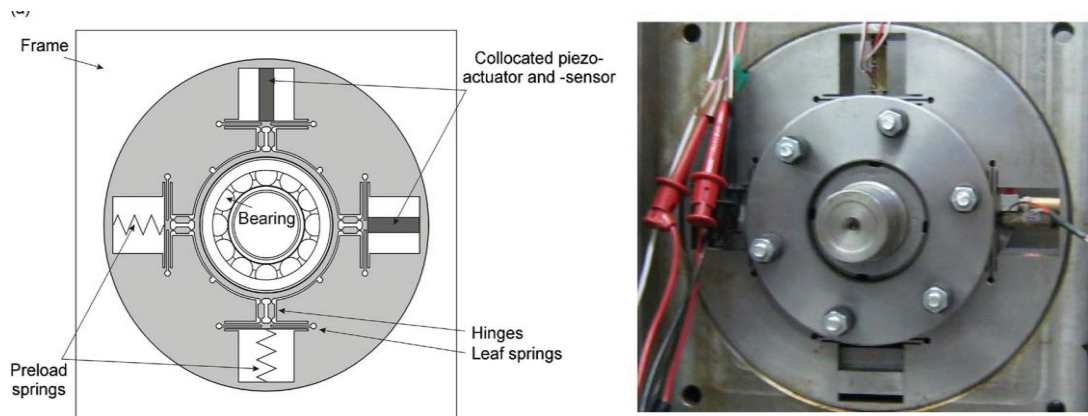


Figure 2.23 – Example of a piezo bearing [72]

Pazzolo et al [74] presented a roller bearing with piezoelectric actuators, whilst Abduljabba et al [75] reported possible control methods for the control of lateral vibration using an active bearing containing piezo actuators; force feedback and robust control. The technical feasibility of the control methods is presented. More recent research by Pinte et al [76] considered the effect of an active piezo bearing on the noise radiated by rotating machinery. Using effective control produces a reduction in radiated sound of 10dB is shown. This effect was due to a reduction in shaft vibrations. However, the degree to which this occurred was not quantified. Proceeding work by the authors also used a bearing that suppressed vibration through the dissipation of electrical energy stored in a piezoelectric transducer [77].

Active control is a promising area of research for performance improvement. However, the limitation of most active bearings is the maximum force the actuators can provide coupled with the bandwidth of actuation.

2.7.4 Passive Control

Whilst it is not always possible to prevent the source of vibration through design, balancing or proper operation, it may be possible to eliminate the effects of vibration through passive modifications by the addition of physical mass, damping or stiffness to the system. This requires permanent changes to the physical system which will not allow for perturbations and changes in system parameters. Wang [78] and Friswell [79] have demonstrated methods of increasing the natural frequency of a structure by altering its stiffness. Wang [78] used an elastic support with varying stiffness to maximise the natural frequency of a cantilever beam. Friswell [75] found the minimum support stiffness required to increase the natural frequency of a two-dimensional plate to its maximum.

It is well established that the vibration of rotating machinery can be reduced by introducing passive devices into the system [64]. A technique which alters the stiffness of a rotating structure is considered by Suherman and Plaut [80]. The reported method adds a flexible support to the structure to increase its stiffness close to the critical speed. Theoretically, the amplitude of resonant vibrations are shown to be reduced by increasing the stiffness of the support which coincidentally increases the critical speed of the shaft away from the running speed.

Vibration Isolation

Vibration isolation through mountings under and around the support structure is intended to reduce the impact of the vibration source on its surroundings. For rotating machinery this will be the stator foundations and prevent coupling to any other machines sharing the same floor space. This does not remove the cause of the problem.

Squeeze Film Dampers

Squeeze film dampers (SFDs) offer dual advantages of dissipation of vibration energy and isolation of structural components, as well as the capability to improve the dynamic stability characteristics of inherently unstable rotor-bearing systems. SFDs are used to provide viscous damping to rolling element bearings or to reduce the bearing stiffness of tilting bad bearings whilst providing additional damping so as to prevent rotordynamic instabilities.

Figure 2.24 shows a typical SFD configuration consisting of an inner nonrotating journal and a stationary outer bearing. The journal is mounted on the external race of a rolling element bearing and fixed to prevent spinning. The annular squeeze film, typically less than 0.25 mm, between the journal and housing is filled lubricant. In operation, as the journal moves due to dynamic forces acting on the system, the fluid is displaced to accommodate the motion. As a result, hydrodynamic squeeze film pressures exert reaction forces on the journal to reduce the rotor amplitude of motion [81].

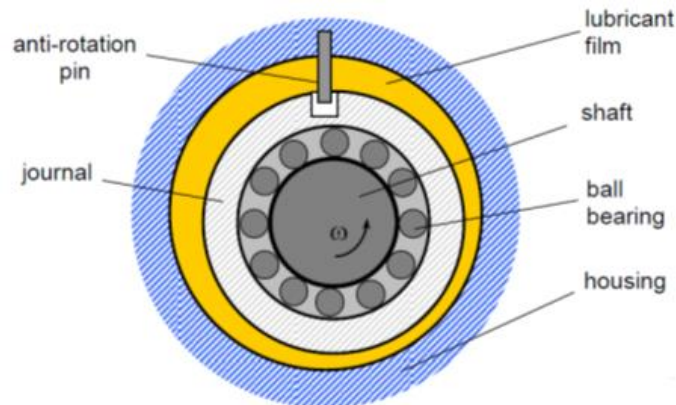


Figure 2.24 – Squeeze film damper configuration [81]

Tuned Mass Dampers

A tuned mass damper (TMD) consists of a mass, spring and a damper that are attached to a structure to reduce the dynamic response. The frequency of the damper is tuned to a particular structural frequency using the mass and spring stiffness. When the specific frequency is excited, the damper will resonate out of phase with the structural motion. Energy is dissipated by the damper inertia force acting on the structure. TMDs are extensively used in civil engineering for the absorption and dissipation of kinetic energy in tall buildings, bridges and power transmission lines [82], [83] and typically have had limited use in rotordynamics but do show potential.

Borghesani [84] showed, at least theoretically, that optimally tuned vibration absorbers can reduce vibration amplitudes on rotating structures but also induce multiple resonance peaks which may have an effect upon the stiffness of main system, Figure 2.25.

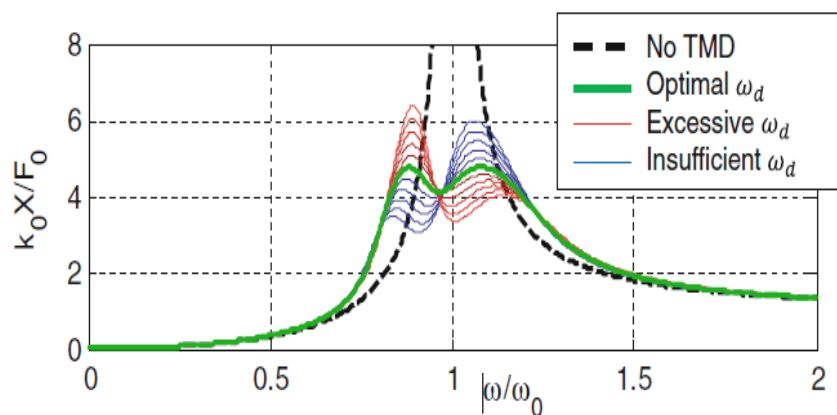


Figure 2.25 - Effect of tuned mass damper upon system responses and resonant peaks [80]

NASA [85] analytically and experimentally demonstrated a self-tuning vibration damper upto 20,000 rpm. The work showed that the frequency of vibration could be increased or decreased depending upon the configuration of the added damper. The self-tuning damper was also shown to have a reduced but noticeable effect away from its design frequency.

A patent application [86] applies a vibration absorber to the outer circumference of the shaft. The absorber is made of a light, elastically deformable inner member with a metal alloy outer shell. Vibration control is theoretically achieved by allowing the heavier outer shell to vibrate with the shaft, thus acting as the inertial mass element of the spring-mass system. A second patent application [87] considers rotating shafts with one free end – drills, borehole operations. A torsional TMD is attached to the rotating body and configured to have a damping frequency that is tuned to a selected natural frequency.

The addition of a TMD to a rotating structure is feasible but the effect upon the system response away from the design frequency must also be considered.

2.8 Conclusions

The analysis and understanding of rotating structures has significant historic grounding dating back to the 19th Century with the development of readily available increased computational power rejuvenating the field in the late 20th Century.

All mechanical systems have an infinite number of frequencies which when excited will cause it to vibrate. When the natural frequencies of rotating systems are excited, usually through unbalanced forces, the speed at which these vibrations occur are called a critical speed. The standard techniques for mitigating vibration in rotating structures are split into three main categories; Careful design and manufacture, correct installation and effective control strategies.

Careful balancing allows the effect of the residual unbalance present in all rotating structures to be minimised. This process can be timely and labour intensive and an effective state of balance difficult to achieve. Furthermore, rotating machines are often only balanced for one optimal operating speed. The proposed sleeve is designed to be flexible to allow for a state of

balance to be achieved across a range of operating speeds without the need to shut down and reconfigure state of balance.

By adding the sleeves to a rotating shaft, its fundamental dynamics will be altered. Therefore it is important that analysis is undertaken to understand the effect of adding the sleeves to the shaft and what, if any, are the practical implications of doing so.

As the response of a structure to any dynamic load is determined by its physical characteristics, a modal analysis should be the first step prior to any further analysis or testing. From the established analysis and understanding of rotating structures, the following path of research will be undertaken:

- Attempt to model the shaft and sleeve system using simplified equations of motion.
- Use theoretical modal analysis to determine the natural frequencies and critical speeds of the system.
- Seek validation and/or model refinement using finite element analysis and experimental tests.

Once a valid model is produced, use this to investigate the effect that the sleeve can have upon the dynamics of the shaft, in particular the critical speeds, and if any significant improvements in performance can be gained.

Chapter 3 Theoretical Model of a Simplified Shaft with Eccentric Sleeves

3.1 Summary

A simplified model of a shaft considering all gyroscopic effects, modelled as an Euler-Bernoulli beam, is derived from first principles, and provides the basis for the proof of concept. A full shaft with eccentric sleeves at each end is modelled as a flexible shaft with simply supported ends and specified boundary conditions; a torsional spring for the flexible coupling and inertia terms of the eccentric sleeves which are modelled as rigid body eccentric masses. The sleeves are modelled as rigid bodies as their flexibility is shown to have little impact upon the critical speed of the shaft; this is demonstrated using finite element simulations that show that the difference in obtained critical speeds for rigid and flexible sleeves is only 1%. The derived equations of motion provide similar results to established models but with the inclusion of dynamic boundary conditions due to the inclusion of the sleeves.

3.2 Chapter Highlights

- Equations of motion for a linear elastic rotating shaft with eccentric sleeves are derived using the Extended Hamilton's Principle
- The resulting equations of motion for the shaft show comparable underpinning characteristics with those reported in literature, but without incorporating the effects of the eccentric sleeves
- The equations neglect the flexibility of the sleeves and only contain mass and inertia terms. Neglecting sleeve flexibility was not anticipated to have a significant effect upon the calculated natural frequencies of the system.

3.3 Introduction

The proposed configuration of the full shaft with flexible coupling elements and eccentric sleeves, is shown in Figure 3.1. In an attempt to describe the model with simplified equations, certain key assumptions are made, as follows.

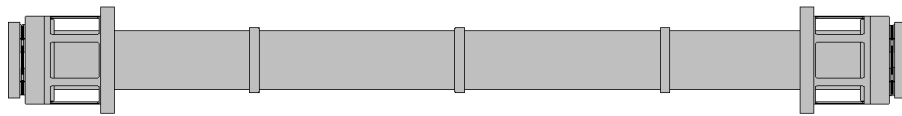


Figure 3.1 – Geometry of full shaft with flexible couplings and eccentric sleeves

3.3.1 Key Adopted Assumptions

- **Simplified Shaft with Euler Bernoulli Theory**

The shaft is modelled as a continuous system with linear elastic behaviour using Euler-Bernoulli beam theory. The complexity of the full geometry is replaced with approximate cross-sectional areas and uniform material properties. Therefore, when determining the kinetic and potential energies of the system, established displacement and stress-strain equations can be used.

The Euler-Bernoulli theory assumes that the displacements of the shaft are considered to be sufficiently small to have negligible effect on the dynamics of the system, therefore higher order terms (arising from the product of the generalised coordinates), and nonlinear terms that arise in the derivation, such as rotary inertia are neglected [88].

Certain limitations apply, however viz. the Euler-Bernoulli beam theory is only applicable for slender beams with small displacements and tends to overestimate natural frequencies, in particular, with higher order modes [18].

- **Dynamic Boundary Conditions**

The ends of the shaft are considered to be constrained translationally, rendering the strong boundary conditions of the shaft to be simply supported. However, due to the addition of the eccentric sleeves and subsequent derivation, the weak boundary conditions contain dynamic terms which are dependent upon the eccentric sleeves.

- **Flexible Elements Have Flexibility and Resistance to Bending**

A common assumption made in the determination of critical speeds of shafts and rotors with flexible coupling elements is that they are considered as simply supported ends [89]. However, in practice this is not truly the case and it is recognised that the flexible elements provide a degree of bending resistance in both lateral directions. The stiffness of such elements can be obtained through experiment and finite element analysis when necessary.

- **No Shear Deformation**

Theory based on Euler-Bernoulli techniques assume that, as the displacements are considered small, the cross-sectional area remains perpendicular to the bending axis i.e. there is no shear deformation in the underlying theory. Non-inclusion of such terms will dictate that there are bounds of applicability for the generated model which will ultimately be examined under experimental testing and parametric studies. [note: If the assumption of no shear deformation significantly impacts on the usefulness of the analytical model, Timoshenko beam theory can be considered as an alternative for modelling [90] — as is often employed in beam element analyses in commercial finite element packages such as ANSYS.]

- **Rigid Body Sleeves**

The sleeves themselves are considered to have no flexibility, therefore only the kinetic energies are derived. Initial simulations show that the flexibility of the sleeves has negligible effect upon the critical speeds of the shaft and are discussed in more detail in Section 3.6.1

The above assumptions are summarised in Figure 3.2; the material properties are constant, the sleeves are considered as rigid bodies, and the flexible elements show resistance to bending in the lateral directions.

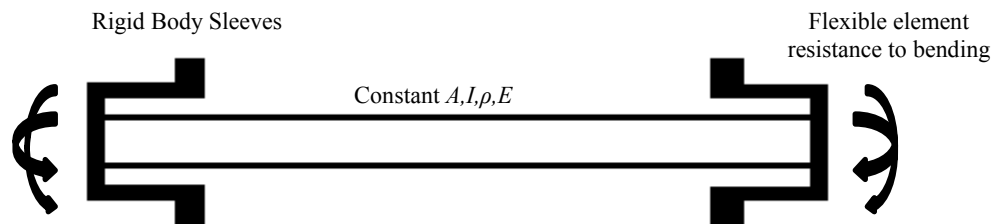


Figure 3.2 – Model simplification assumptions

3.4 Extended Hamilton's Principle

Using the assumptions in Section 3.3.1, the 'simply supported' Euler-Bernoulli elastic shaft is considered with boundary conditions to include the effects of the attached eccentric sleeves and torsional springs due to the flexible end couplings. The least action by the Extended Hamilton's Principle is given by:

$$\delta J = \int_{t_1}^{t_2} (\delta T - \delta U + \delta T_1 + \delta T_2 - \delta U_{\text{TORS}}) dt = 0 \quad (3.1)$$

The additional terms δT_1 and δT_2 account for the eccentric sleeves fixed at either end of the shaft. δU_{TORS} is the torsional stiffness of the flexible elements in both the lateral directions.

3.5 Derivation of Simply Supported Rotating Shaft Dynamics

3.5.1 Shaft Displacements

A shaft is considered to be rotating about its x-axis with instantaneous angle, θ , Figure 3.3. A coordinate system is attached to and rotates with the shaft. The position vector of location on shaft in rotating co-ordinate system, \vec{r} , is determined by an initial position (x, y, z) plus any displacements (D_x, D_y, D_z).

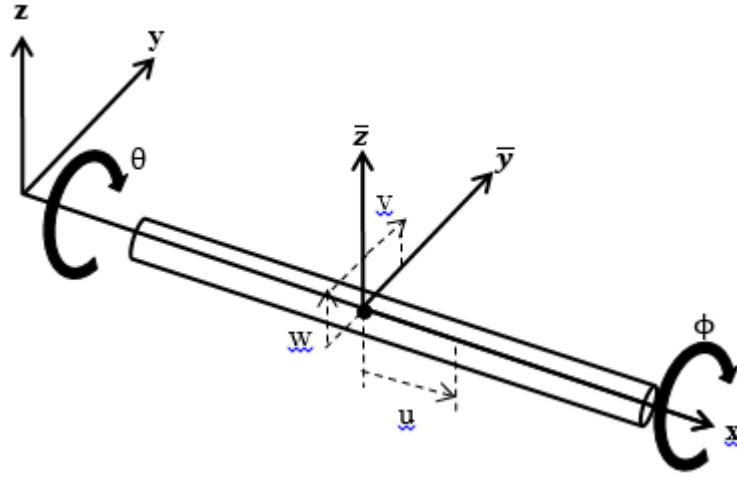


Figure 3.3 – Shaft displacements

Figure 3.3 also shows the axial and lateral displacements of the shaft as it rotates. The translational displacements of any point along x , y , z axes are respectively, u , v , w . The slope of translation displacements v and w are denoted v' and w' . Torsion in the shaft is denoted by ϕ . Librescu [91] defines the total displacements, as in Equation (3.2).

$$\bar{\mathbf{r}} = \begin{Bmatrix} \bar{r}_x \\ \bar{r}_y \\ \bar{r}_z \end{Bmatrix} = \begin{Bmatrix} x + D_x \\ y + D_y \\ z + D_z \end{Bmatrix} = \begin{Bmatrix} x + u - yv' - zw' \\ y + v - z\phi \\ z + w + y\phi \end{Bmatrix} \quad (3.2)$$

The first and second time derivatives of the displacements yield velocity and acceleration vectors. Initial positions remain constant:

$$\dot{\bar{\mathbf{r}}} = \begin{Bmatrix} \dot{\bar{r}}_x \\ \dot{\bar{r}}_y \\ \dot{\bar{r}}_z \end{Bmatrix} = \begin{Bmatrix} \dot{u} - y\dot{v}' - z\dot{w}' \\ \dot{v} - z\dot{\phi} \\ \dot{w} + y\dot{\phi} \end{Bmatrix} \quad (3.3a)$$

$$\ddot{\bar{\mathbf{r}}} = \begin{Bmatrix} \ddot{\bar{r}}_x \\ \ddot{\bar{r}}_y \\ \ddot{\bar{r}}_z \end{Bmatrix} = \begin{Bmatrix} \ddot{u} - y\ddot{v}' - z\ddot{w}' \\ \ddot{v} - z\ddot{\phi} \\ \ddot{w} + y\ddot{\phi} \end{Bmatrix} \quad (3.3b)$$

3.5.2 Shaft Position, Velocity and Acceleration Vectors

A position vector in the global co-ordinate system is given by; $r = [A][\bar{r}]$; where $[A]$ is rotational transformation matrix, specific for rotation about the x axis:

$$r = \begin{bmatrix} 1 & 0 & 0 \\ 0 & \cos \theta & -\sin \theta \\ 0 & \sin \theta & \cos \theta \end{bmatrix} \begin{Bmatrix} \bar{r}_x \\ \bar{r}_y \\ \bar{r}_z \end{Bmatrix} = \begin{Bmatrix} \bar{r}_x \\ \bar{r}_y \cos \theta - \bar{r}_z \sin \theta \\ \bar{r}_z \cos \theta + \bar{r}_y \sin \theta \end{Bmatrix} \quad (3.4)$$

The velocity and acceleration vectors are obtained from the first (\dot{r}) and second (\ddot{r}) time derivatives of r (using product rule). See Appendix A for the derivatives of the transformation matrices.

$$\dot{r} = [A]\{\dot{\bar{r}}\} + [\dot{A}]\{\bar{r}\} = \begin{Bmatrix} \dot{\bar{r}}_x \\ \dot{\bar{r}}_y \cos \theta - \dot{\bar{r}}_z \sin \theta \\ \dot{\bar{r}}_z \cos \theta + \dot{\bar{r}}_y \sin \theta \end{Bmatrix} + \dot{\theta} \begin{Bmatrix} 0 \\ -\bar{r}_z \cos \theta - \bar{r}_y \sin \theta \\ \bar{r}_y \cos \theta - \bar{r}_z \sin \theta \end{Bmatrix} \quad (3.5)$$

$$\begin{aligned} \ddot{r} &= [\ddot{A}]\{\bar{r}\} + 2[\dot{A}]\{\dot{\bar{r}}\} + [A]\{\ddot{\bar{r}}\} \\ &= \dot{\theta}^2 \begin{Bmatrix} 0 \\ -\bar{r}_y \cos \theta + \bar{r}_z \sin \theta \\ -\bar{r}_z \cos \theta - \bar{r}_y \sin \theta \end{Bmatrix} + \ddot{\theta} \begin{Bmatrix} 0 \\ -\bar{r}_z \cos \theta - \bar{r}_y \sin \theta \\ \bar{r}_y \cos \theta - \bar{r}_z \sin \theta \end{Bmatrix} \\ &\quad + 2\dot{\theta} \begin{Bmatrix} 0 \\ -\dot{\bar{r}}_z \cos \theta - \dot{\bar{r}}_y \sin \theta \\ \dot{\bar{r}}_y \cos \theta - \dot{\bar{r}}_z \sin \theta \end{Bmatrix} + \begin{Bmatrix} \ddot{\bar{r}}_x \\ \ddot{\bar{r}}_y \cos \theta - \ddot{\bar{r}}_z \sin \theta \\ \ddot{\bar{r}}_z \cos \theta + \ddot{\bar{r}}_y \sin \theta \end{Bmatrix} \end{aligned} \quad (3.6)$$

In Equation (3.6), the terms refer to centrifugal acceleration; non-constant rotating speed, Coriolis acceleration and translational acceleration respectively.

3.5.3 Shaft Kinetic Energy

The kinetic energy of a continuous system is given by [91] where ρ_0 is mass per unit area and V is the volume of the body:

$$T = \frac{1}{2} \int_V \rho_0 \vec{r} \cdot \dot{\vec{r}} \, dV = \frac{1}{2} \int_V \rho_0 \dot{r}^T \dot{r} \, dV \quad (3.7)$$

Therefore the variation of kinetic energy is:

$$\int_{t_1}^{t_2} \delta T dt = \frac{1}{2} \int_{t_1}^{t_2} \int_V \rho_0 \delta(\dot{r}^T \dot{r}) dV dt \quad (3.8)$$

Through integration by parts:

$$\int_{t_1}^{t_2} \delta T dt = -\rho_0 [\dot{r}^T \delta r]_{t=t_1}^{t=t_2} - \int_{t_1}^{t_2} \int_V \rho_0 \ddot{r}^T \delta r dV dt \quad (3.9)$$

At $t = t_1$ and t_2 , $\delta r = 0 \therefore -\rho_0 [\dot{r}^T \delta r]_{t=t_1}^{t=t_2} = 0$ at initial conditions:

$$\therefore \int_{t_1}^{t_2} \delta T dt = - \int_{t_1}^{t_2} \int_V \rho_0 \ddot{r}^T \delta r dV dt \quad (3.10)$$

To determine the variation of kinetic energy (δT), the terms for variation of the position vector (δr) and acceleration vector (\ddot{r}^T) are required. δr is described by a series of equations that individually describe the variation of the generalised coordinates $r = f(u, v, w, v', w', \phi, \theta)$:

$$\therefore \delta r = \frac{\partial r}{\partial u} \delta u + \frac{\partial r}{\partial v} \delta v + \frac{\partial r}{\partial w} \delta w + \frac{\partial r}{\partial v'} \delta v' + \frac{\partial r}{\partial w'} \delta w' + \frac{\partial r}{\partial \phi} \delta \phi + \frac{\partial r}{\partial \theta} \delta \theta \quad (3.11)$$

Using the explicit form of r from Equations (3.3) and (3.6) to include displacements:

$$\begin{aligned} \frac{\partial r}{\partial u} &= \begin{Bmatrix} 1 \\ 0 \\ 0 \end{Bmatrix} \\ \frac{\partial r}{\partial v} &= \begin{Bmatrix} 0 \\ \cos \theta \\ \sin \theta \end{Bmatrix} \\ \frac{\partial r}{\partial w} &= \begin{Bmatrix} 0 \\ -\sin \theta \\ \cos \theta \end{Bmatrix} \\ \frac{\partial r}{\partial v'} &= \begin{Bmatrix} -y \\ 0 \\ 0 \end{Bmatrix} \end{aligned} \quad (3.12a-d)$$

$$\begin{aligned}\frac{\partial \mathbf{r}}{\partial w'} &= \begin{Bmatrix} -z \\ 0 \\ 0 \end{Bmatrix} \\ \frac{\partial \mathbf{r}}{\partial \Phi} &= \begin{Bmatrix} 0 \\ -z \cos \theta - y \sin \theta \\ y \cos \theta - z \sin \theta \end{Bmatrix} \\ \frac{\partial \mathbf{r}}{\partial \theta} &= \begin{Bmatrix} 0 \\ -(z+w+y\phi) \cos \theta - (y+v-z\phi) \sin \theta \\ (y+v-z\phi) \cos \theta - (z+w+y\phi) \sin \theta \end{Bmatrix} = \begin{Bmatrix} 0 \\ -\bar{r}_z \cos \theta - \bar{r}_y \sin \theta \\ \bar{r}_y \cos \theta - \bar{r}_z \sin \theta \end{Bmatrix}\end{aligned}\quad (3.12e-g)$$

$\{\ddot{\mathbf{r}}\}^T \delta \mathbf{r}$ is equivalent to:

$$\begin{aligned}\{\ddot{\mathbf{r}}\}^T \frac{\partial \mathbf{r}}{\partial u} \delta u + \{\ddot{\mathbf{r}}\}^T \frac{\partial \mathbf{r}}{\partial v} \delta v + \{\ddot{\mathbf{r}}\}^T \frac{\partial \mathbf{r}}{\partial w} \delta w + \{\ddot{\mathbf{r}}\}^T \frac{\partial \mathbf{r}}{\partial v'} \delta v' + \{\ddot{\mathbf{r}}\}^T \frac{\partial \mathbf{r}}{\partial w'} \delta w' \\ + \{\ddot{\mathbf{r}}\}^T \frac{\partial \mathbf{r}}{\partial \Phi} \delta \Phi + \{\ddot{\mathbf{r}}\}^T \frac{\partial \mathbf{r}}{\partial \theta} \delta \theta\end{aligned}\quad (3.13)$$

$\{\ddot{\mathbf{r}}\}^T$ is separated into components to produce four individual vectors corresponding to centrifugal, non-constant rotation, Coriolis and translational accelerations:

$$\{\ddot{\mathbf{r}}\}^T = \{\ddot{\mathbf{r}}_1\}^T + \{\ddot{\mathbf{r}}_2\}^T + \{\ddot{\mathbf{r}}_3\}^T + \{\ddot{\mathbf{r}}_4\}^T \quad (3.14)$$

The individual components of $\{\ddot{\mathbf{r}}\}^T \delta \mathbf{r}$ are obtained through multiplication of Equations (3.12) and (3.14):

δu

$$\begin{aligned}\{\ddot{\mathbf{r}}_1\}^T \frac{\partial \mathbf{r}}{\partial u} &= \dot{\theta}^2 \{0, \quad -\bar{r}_y \cos \theta + \bar{r}_z \sin \theta, \quad -\bar{r}_z \cos \theta - \bar{r}_y \sin \theta\} \begin{Bmatrix} 1 \\ 0 \\ 0 \end{Bmatrix} \delta u = 0 \\ \{\ddot{\mathbf{r}}_2\}^T \frac{\partial \mathbf{r}}{\partial u} &= \ddot{\theta} \{0, \quad -\bar{r}_z \cos \theta - \bar{r}_y \sin \theta, \quad \bar{r}_y \cos \theta - \bar{r}_z \sin \theta\} \begin{Bmatrix} 1 \\ 0 \\ 0 \end{Bmatrix} \delta u = 0 \\ \{\ddot{\mathbf{r}}_3\}^T \frac{\partial \mathbf{r}}{\partial u} &= 2\dot{\theta} \{0, \quad -\dot{\bar{r}}_z \cos \theta - \dot{\bar{r}}_y \sin \theta, \quad \dot{\bar{r}}_y \cos \theta - \dot{\bar{r}}_z \sin \theta\} \begin{Bmatrix} 1 \\ 0 \\ 0 \end{Bmatrix} \delta u = 0 \\ \{\ddot{\mathbf{r}}_4\}^T \frac{\partial \mathbf{r}}{\partial u} &= \{\ddot{\mathbf{r}}_x, \quad \ddot{\bar{r}}_y \cos \theta - \ddot{\bar{r}}_z \sin \theta, \quad \ddot{\bar{r}}_z \cos \theta + \ddot{\bar{r}}_y \sin \theta\} \begin{Bmatrix} 1 \\ 0 \\ 0 \end{Bmatrix} \delta u = \ddot{\mathbf{r}}_x \delta u\end{aligned}$$

$$\therefore \{\ddot{\mathbf{r}}\}^T \delta u = \ddot{\mathbf{r}}_x \delta u \quad (3.15)$$

δv

$$\begin{aligned}
\{\ddot{r}_1\}^T \frac{\partial r}{\partial v} \delta v &= \dot{\theta}^2 \{0, -\bar{r}_y \cos \theta + \bar{r}_z \sin \theta, -\bar{r}_z \cos \theta - \bar{r}_y \sin \theta\} \begin{Bmatrix} 0 \\ \cos \theta \\ \sin \theta \end{Bmatrix} \delta v \\
&= \dot{\theta}^2 (-\bar{r}_y (\cos^2 \theta + \sin^2 \theta)) \delta v = -\dot{\theta}^2 \bar{r}_y \delta v \\
\{\ddot{r}_2\}^T \frac{\partial r}{\partial v} \delta v &= \ddot{\theta} \{0, -\bar{r}_z \cos \theta - \bar{r}_y \sin \theta, \bar{r}_y \cos \theta - \bar{r}_z \sin \theta\} \begin{Bmatrix} 0 \\ \cos \theta \\ \sin \theta \end{Bmatrix} \delta v \\
&= \ddot{\theta} (-\bar{r}_z (\cos^2 \theta + \sin^2 \theta)) \delta v = -\ddot{\theta} \bar{r}_z \delta v \\
\{\ddot{r}_3\}^T \frac{\partial r}{\partial v} \delta v &= 2\dot{\theta} \{0, -\dot{r}_z \cos \theta - \dot{r}_y \sin \theta, \dot{r}_y \cos \theta - \dot{r}_z \sin \theta\} \begin{Bmatrix} 0 \\ \cos \theta \\ \sin \theta \end{Bmatrix} \delta v \\
&= 2\dot{\theta} (-\dot{r}_z (\cos^2 \theta + \sin^2 \theta)) \delta v = -2\dot{\theta} \dot{r}_z \delta v \\
\{\ddot{r}_4\}^T \frac{\partial r}{\partial v} \delta v &= \{\ddot{r}_x, \ddot{r}_y \cos \theta - \ddot{r}_z \sin \theta, \ddot{r}_z \cos \theta + \ddot{r}_y \sin \theta\} \begin{Bmatrix} 0 \\ \cos \theta \\ \sin \theta \end{Bmatrix} \delta v \\
&= \ddot{r}_y (\cos^2 \theta + \sin^2 \theta) \delta v = \ddot{r}_y \delta v \\
\therefore \{\ddot{r}\}^T \delta v &= -\dot{\theta}^2 \bar{r}_y - \ddot{\theta} \bar{r}_z - 2\dot{\theta} \dot{r}_z + \ddot{r}_y \delta v \tag{3.16}
\end{aligned}$$

 δw

$$\begin{aligned}
\{\ddot{r}_1\}^T \frac{\partial r}{\partial w} \delta w &= \dot{\theta}^2 \{0, -\bar{r}_y \cos \theta + \bar{r}_z \sin \theta, -\bar{r}_z \cos \theta - \bar{r}_y \sin \theta\} \begin{Bmatrix} 0 \\ -\sin \theta \\ \cos \theta \end{Bmatrix} \delta w \\
&= \dot{\theta}^2 [-\bar{r}_z (\cos^2 \theta + \sin^2 \theta)] \delta w = -\dot{\theta}^2 \bar{r}_z \delta w \\
\{\ddot{r}_2\}^T \frac{\partial r}{\partial w} \delta w &= \ddot{\theta} \{0, -\bar{r}_z \cos \theta - \bar{r}_y \sin \theta, \bar{r}_y \cos \theta - \bar{r}_z \sin \theta\} \begin{Bmatrix} 0 \\ -\sin \theta \\ \cos \theta \end{Bmatrix} \delta w \\
&= \ddot{\theta} [\bar{r}_y (\cos^2 \theta + \sin^2 \theta)] \delta w = \ddot{\theta} \bar{r}_y \delta w \\
\{\ddot{r}_3\}^T \frac{\partial r}{\partial w} \delta w &= 2\dot{\theta} \{0, -\dot{r}_z \cos \theta - \dot{r}_y \sin \theta, \dot{r}_y \cos \theta - \dot{r}_z \sin \theta\} \begin{Bmatrix} 0 \\ -\sin \theta \\ \cos \theta \end{Bmatrix} \delta w \\
&= 2\dot{\theta} [\dot{r}_y (\cos^2 \theta + \sin^2 \theta)] \delta w = 2\dot{\theta} \dot{r}_y \delta w \\
\{\ddot{r}_4\}^T \frac{\partial r}{\partial w} \delta w &= \{\ddot{r}_x, \ddot{r}_y \cos \theta - \ddot{r}_z \sin \theta, \ddot{r}_z \cos \theta + \ddot{r}_y \sin \theta\} \begin{Bmatrix} 0 \\ -\sin \theta \\ \cos \theta \end{Bmatrix} \delta w \\
&= \ddot{r}_z (\cos^2 \theta + \sin^2 \theta) \delta w = \ddot{r}_z \delta w \\
\therefore \{\ddot{r}\}^T \delta w &= -\dot{\theta}^2 \bar{r}_z + \ddot{\theta} \bar{r}_y + 2\dot{\theta} \dot{r}_y + \ddot{r}_z \delta w \tag{3.17}
\end{aligned}$$

$\delta \mathbf{v}'$

$$\{\ddot{\mathbf{r}}_1\}^T \frac{\partial \mathbf{r}}{\partial \mathbf{v}'} \delta \mathbf{v}' = \dot{\theta}^2 \{0, -\bar{r}_y \cos \theta + \bar{r}_z \sin \theta, -\bar{r}_z \cos \theta - \bar{r}_y \sin \theta\} \begin{Bmatrix} -y \\ 0 \\ 0 \end{Bmatrix} \delta \mathbf{v}' = 0$$

$$\{\ddot{\mathbf{r}}_2\}^T \frac{\partial \mathbf{r}}{\partial \mathbf{v}'} \delta \mathbf{v}' = \ddot{\theta} \{0, -\bar{r}_z \cos \theta - \bar{r}_y \sin \theta, \bar{r}_y \cos \theta - \bar{r}_z \sin \theta\} \begin{Bmatrix} -y \\ 0 \\ 0 \end{Bmatrix} \delta \mathbf{v}' = 0$$

$$\{\ddot{\mathbf{r}}_3\}^T \frac{\partial \mathbf{r}}{\partial \mathbf{v}'} \delta \mathbf{v}' = 2\dot{\theta} \{0, -\dot{\bar{r}}_z \cos \theta - \dot{\bar{r}}_y \sin \theta, \dot{\bar{r}}_y \cos \theta - \dot{\bar{r}}_z \sin \theta\} \begin{Bmatrix} -y \\ 0 \\ 0 \end{Bmatrix} \delta \mathbf{v}' = 0$$

$$\{\ddot{\mathbf{r}}_4\}^T \frac{\partial \mathbf{r}}{\partial \mathbf{v}'} \delta \mathbf{v}' = \{\ddot{\mathbf{r}}_x, \ddot{\bar{r}}_y \cos \theta - \ddot{\bar{r}}_z \sin \theta, \ddot{\bar{r}}_z \cos \theta + \ddot{\bar{r}}_y \sin \theta\} \begin{Bmatrix} -y \\ 0 \\ 0 \end{Bmatrix} \delta \mathbf{v}' = -y \ddot{\mathbf{r}}_x \delta \mathbf{v}'$$

$$\therefore \{\ddot{\mathbf{r}}\}^T \delta \mathbf{v}' = -y \ddot{\mathbf{r}}_x \delta \mathbf{v}' \quad (3.18)$$

 $\delta \mathbf{w}'$

$$\{\ddot{\mathbf{r}}_1\}^T \frac{\partial \mathbf{r}}{\partial \mathbf{w}'} \delta \mathbf{w}' = \dot{\theta}^2 \{0, -\bar{r}_y \cos \theta + \bar{r}_z \sin \theta, -\bar{r}_z \cos \theta - \bar{r}_y \sin \theta\} \begin{Bmatrix} -z \\ 0 \\ 0 \end{Bmatrix} \delta \mathbf{w}' = 0$$

$$\{\ddot{\mathbf{r}}_2\}^T \frac{\partial \mathbf{r}}{\partial \mathbf{w}'} \delta \mathbf{w}' = \ddot{\theta} \{0, -\bar{r}_z \cos \theta - \bar{r}_y \sin \theta, \bar{r}_y \cos \theta - \bar{r}_z \sin \theta\} \begin{Bmatrix} -z \\ 0 \\ 0 \end{Bmatrix} \delta \mathbf{w}' = 0$$

$$\{\ddot{\mathbf{r}}_3\}^T \frac{\partial \mathbf{r}}{\partial \mathbf{w}'} \delta \mathbf{w}' = 2\dot{\theta} \{0, -\dot{\bar{r}}_z \cos \theta - \dot{\bar{r}}_y \sin \theta, \dot{\bar{r}}_y \cos \theta - \dot{\bar{r}}_z \sin \theta\} \begin{Bmatrix} -z \\ 0 \\ 0 \end{Bmatrix} \delta \mathbf{w}' = 0$$

$$\{\ddot{\mathbf{r}}_4\}^T \frac{\partial \mathbf{r}}{\partial \mathbf{w}'} \delta \mathbf{w}' = \{\ddot{\mathbf{r}}_x, \ddot{\bar{r}}_y \cos \theta - \ddot{\bar{r}}_z \sin \theta, \ddot{\bar{r}}_z \cos \theta + \ddot{\bar{r}}_y \sin \theta\} \begin{Bmatrix} -z \\ 0 \\ 0 \end{Bmatrix} \delta \mathbf{w}' = -z \ddot{\mathbf{r}}_x \delta \mathbf{w}'$$

$$\therefore \{\ddot{\mathbf{r}}\}^T \delta \mathbf{w}' = -z \ddot{\mathbf{r}}_x \delta \mathbf{w}' \quad (3.19)$$

 $\delta \phi$

$$\begin{aligned} \{\ddot{\mathbf{r}}_1\}^T \frac{\partial \mathbf{r}}{\partial \phi} \delta \phi &= \dot{\theta}^2 \{0, -\bar{r}_y \cos \theta + \bar{r}_z \sin \theta, -\bar{r}_z \cos \theta - \bar{r}_y \sin \theta\} \begin{Bmatrix} 0 \\ -z \cos \phi - y \sin \phi \\ y \cos \phi - z \sin \phi \end{Bmatrix} \delta \phi \\ &= \dot{\theta}^2 (\bar{r}_y z (\cos^2 \theta + \sin^2 \theta) - \bar{r}_z y (\cos^2 \theta + \sin^2 \theta)) \delta \phi = \dot{\theta}^2 (\bar{r}_y z - \bar{r}_z y) \delta \phi \end{aligned}$$

$$\begin{aligned} \{\ddot{\mathbf{r}}_2\}^T \frac{\partial \mathbf{r}}{\partial \phi} \delta \phi &= \ddot{\theta} \{0, -\bar{r}_z \cos \theta - \bar{r}_y \sin \theta, \bar{r}_y \cos \theta - \bar{r}_z \sin \theta\} \begin{Bmatrix} 0 \\ -z \cos \phi - y \sin \phi \\ y \cos \phi - z \sin \phi \end{Bmatrix} \delta \phi \\ &= \ddot{\theta} (\bar{r}_z z (\cos^2 \theta + \sin^2 \theta) + \bar{r}_y y (\cos^2 \theta + \sin^2 \theta)) \delta \phi = \ddot{\theta} (\bar{r}_z z + \bar{r}_y y) \delta \phi \end{aligned}$$

$$\begin{aligned} \{\dot{\mathbf{r}}_3\}^T \frac{\partial \mathbf{r}}{\partial \phi} \delta \phi &= 2\dot{\theta} \left\{ 0, \quad -\dot{\mathbf{r}}_z \cos \theta - \dot{\mathbf{r}}_y \sin \theta, \quad \dot{\mathbf{r}}_y \cos \theta - \dot{\mathbf{r}}_z \sin \theta \right\} \begin{Bmatrix} 0 \\ -z \cos \phi - y \sin \phi \\ y \cos \phi - z \sin \phi \end{Bmatrix} \delta \phi \\ &= 2\dot{\theta} (\dot{\mathbf{r}}_z z (\cos^2 \theta + \sin^2 \theta) + \dot{\mathbf{r}}_y y (\cos^2 \theta + \sin^2 \theta)) \delta \phi = 2\dot{\theta} (\dot{\mathbf{r}}_z z + \dot{\mathbf{r}}_y y) \delta \phi \end{aligned}$$

$$\begin{aligned} \{\dot{\mathbf{r}}_4\}^T \frac{\partial \mathbf{r}}{\partial \phi} \delta \phi &= \{\ddot{\mathbf{r}}_x, \quad \ddot{\mathbf{r}}_y \cos \theta - \ddot{\mathbf{r}}_z \sin \theta, \quad \ddot{\mathbf{r}}_z \cos \theta + \ddot{\mathbf{r}}_y \sin \theta\} \begin{Bmatrix} 0 \\ -z \cos \phi - y \sin \phi \\ y \cos \phi - z \sin \phi \end{Bmatrix} \delta \phi \\ &= \ddot{\mathbf{r}}_z y (\cos^2 \theta + \sin^2 \theta) - \ddot{\mathbf{r}}_y z (\cos^2 \theta + \sin^2 \theta) \delta \phi = \ddot{\mathbf{r}}_z y - \ddot{\mathbf{r}}_y z \delta \phi \end{aligned}$$

$$\therefore \{\ddot{\mathbf{r}}\}^T \delta \phi = (\dot{\theta}^2 (\bar{\mathbf{r}}_y z - \bar{\mathbf{r}}_z y) + \ddot{\theta} (\bar{\mathbf{r}}_z z + \bar{\mathbf{r}}_y y) + 2\dot{\theta} (\dot{\mathbf{r}}_z z + \dot{\mathbf{r}}_y y) + \ddot{\mathbf{r}}_z y - \ddot{\mathbf{r}}_y z) \delta \phi \quad (3.20)$$

$\delta \theta$

$$\{\dot{\mathbf{r}}_1\}^T \frac{\partial \mathbf{r}}{\partial \theta} \delta \theta = \dot{\theta}^2 \left\{ 0, \quad -\bar{\mathbf{r}}_y \cos \theta + \bar{\mathbf{r}}_z \sin \theta, \quad -\bar{\mathbf{r}}_z \cos \theta - \bar{\mathbf{r}}_y \sin \theta \right\} \begin{Bmatrix} 0 \\ -\bar{\mathbf{r}}_z \cos \phi - \bar{\mathbf{r}}_y \sin \phi \\ \bar{\mathbf{r}}_y \cos \phi - \bar{\mathbf{r}}_z \sin \phi \end{Bmatrix} \delta \theta = 0$$

$$\begin{aligned} \{\dot{\mathbf{r}}_2\}^T \frac{\partial \mathbf{r}}{\partial \theta} \delta \theta &= \ddot{\theta} \left\{ 0, \quad -\bar{\mathbf{r}}_z \cos \theta - \bar{\mathbf{r}}_y \sin \theta, \quad \bar{\mathbf{r}}_y \cos \theta - \bar{\mathbf{r}}_z \sin \theta \right\} \begin{Bmatrix} 0 \\ -\bar{\mathbf{r}}_z \cos \phi - \bar{\mathbf{r}}_y \sin \phi \\ \bar{\mathbf{r}}_y \cos \phi - \bar{\mathbf{r}}_z \sin \phi \end{Bmatrix} \delta \theta \\ &= \ddot{\theta} (\bar{\mathbf{r}}_z^2 (\cos^2 \theta + \sin^2 \theta) + \bar{\mathbf{r}}_y^2 (\cos^2 \theta + \sin^2 \theta)) \delta \theta = \ddot{\theta} (\bar{\mathbf{r}}_z^2 + \bar{\mathbf{r}}_y^2) \delta \theta \end{aligned}$$

$$\begin{aligned} \{\dot{\mathbf{r}}_3\}^T \frac{\partial \mathbf{r}}{\partial \theta} \delta \theta &= 2\dot{\theta} \left\{ 0, \quad -\dot{\mathbf{r}}_z \cos \theta - \dot{\mathbf{r}}_y \sin \theta, \quad \dot{\mathbf{r}}_y \cos \theta - \dot{\mathbf{r}}_z \sin \theta \right\} \begin{Bmatrix} 0 \\ -\bar{\mathbf{r}}_z \cos \phi - \bar{\mathbf{r}}_y \sin \phi \\ \bar{\mathbf{r}}_y \cos \phi - \bar{\mathbf{r}}_z \sin \phi \end{Bmatrix} \delta \theta \\ &= 2\dot{\theta} (\dot{\mathbf{r}}_y \bar{\mathbf{r}}_y (\cos^2 \theta + \sin^2 \theta) + \dot{\mathbf{r}}_z \bar{\mathbf{r}}_z (\cos^2 \theta + \sin^2 \theta)) \delta \theta = 2\dot{\theta} (\dot{\mathbf{r}}_y \bar{\mathbf{r}}_y + \dot{\mathbf{r}}_z \bar{\mathbf{r}}_z) \delta \theta \end{aligned}$$

$$\begin{aligned} \{\dot{\mathbf{r}}_4\}^T \frac{\partial \mathbf{r}}{\partial \theta} \delta \theta &= \{\ddot{\mathbf{r}}_x, \quad \ddot{\mathbf{r}}_y \cos \theta - \ddot{\mathbf{r}}_z \sin \theta, \quad \ddot{\mathbf{r}}_z \cos \theta + \ddot{\mathbf{r}}_y \sin \theta\} \begin{Bmatrix} 0 \\ -\bar{\mathbf{r}}_z \cos \phi - \bar{\mathbf{r}}_y \sin \phi \\ \bar{\mathbf{r}}_y \cos \phi - \bar{\mathbf{r}}_z \sin \phi \end{Bmatrix} \delta \theta \\ &= \ddot{\mathbf{r}}_z \bar{\mathbf{r}}_y (\cos^2 \theta + \sin^2 \theta) - \ddot{\mathbf{r}}_y \bar{\mathbf{r}}_z (\cos^2 \theta + \sin^2 \theta) \delta \theta = \ddot{\mathbf{r}}_z \bar{\mathbf{r}}_y - \ddot{\mathbf{r}}_y \bar{\mathbf{r}}_z \delta \theta \end{aligned}$$

$$\therefore \{\ddot{\mathbf{r}}\}^T \delta \theta = \ddot{\theta} (\bar{\mathbf{r}}_z^2 + \bar{\mathbf{r}}_y^2) + 2\dot{\theta} (\dot{\mathbf{r}}_y \bar{\mathbf{r}}_y + \dot{\mathbf{r}}_z \bar{\mathbf{r}}_z) - \ddot{\mathbf{r}}_z \bar{\mathbf{r}}_y - \ddot{\mathbf{r}}_y \bar{\mathbf{r}}_z \delta \theta \quad (3.21)$$

Summing together Equations (3.15) to (3.21) and using the explicit form for r from (3.3):

$$\begin{aligned}
\{\ddot{r}\}^T \delta r = & ((\ddot{u} - y\ddot{v}' - z\ddot{w}')\delta u) + (-\dot{\theta}^2(y + v - z\phi) - \ddot{\theta}(z + w + y\phi) - \\
& 2\dot{\theta}(\dot{w} + y\dot{\phi}) + (\ddot{v} - z\ddot{\phi})\delta v) + (-\dot{\theta}^2(z + w + y\phi) + \ddot{\theta}(y + v - z\phi) + 2\dot{\theta}(\dot{v} - \\
& z\dot{\phi}) + (\ddot{w} + y\ddot{\phi})\delta w - (y\ddot{u} - y^2\ddot{v}' - yz\ddot{w}')\delta v') - (z\ddot{u} - yz\ddot{v}' - z^2\ddot{w}')\delta w' + \\
& (\dot{\theta}^2(yz + zv - z^2\phi - yz - yw - y^2\phi) + \ddot{\theta}(z^2 + zw + y^2 + yv) + 2\dot{\theta}(z\dot{w} + \\
& y\dot{v}) + (y\ddot{w} + y^2\ddot{\phi} - z\ddot{v} + z^2\ddot{\phi})\delta\phi) + (\ddot{\theta}(y^2 + z^2 + v^2 + w^2 + y^2\phi^2 + z^2\phi^2 + \\
& 2wz + 2vy + 2wy\phi - 2vz\phi - 2yz\phi + 2yz\phi) + 2\dot{\theta}(\dot{v}y + \dot{v}z - \dot{v}z\phi - yz\dot{\phi} - \\
& vz\dot{\phi} + z^2\phi\dot{\phi} + \dot{w}z + \dot{w}w + \dot{w}y\phi + yz\dot{\phi} + wy\dot{\phi} + y^2\phi\dot{\phi}) - (\ddot{w}y + \ddot{w}v - \ddot{w}z\phi + \\
& yy\ddot{\phi} + vy\ddot{\phi} - yz\phi\ddot{\phi} - \ddot{v}w - \ddot{v}z - \ddot{v}y\phi + zz\ddot{\phi} + wz\ddot{\phi} + yz\phi\ddot{\phi})\delta\theta)
\end{aligned} \tag{3.22}$$

To simplify the solution of these equations, any higher order terms are neglected at this stage. Due to the small displacements under consideration, the effects of these term are expected to be minimal. Only $\delta\theta$ contains higher order terms, therefore Equation (3.22) becomes:

$$\begin{aligned}
& \ddot{\theta}(y^2 + z^2 + 2wz + 2vy + 2yz\phi - 2yz\phi) + 2\dot{\theta}(\dot{v}y + \dot{w}z - yz\dot{\phi} + yz\dot{\phi}) \\
& - (\ddot{w}y - \ddot{v}z + y^2\ddot{\phi} + z^2\ddot{\phi})\delta\theta
\end{aligned} \tag{3.22a}$$

3.5.4 Shaft Kinetic Energy Boundary Conditions

To incorporate $\delta v'$ and $\delta w'$ into the energy equation, the relevant components of Equation (3.22) must be integrated by parts. Two boundary conditions are obtained (one for $\delta v'$ and one for $\delta w'$) as follows:

$\delta v'$ by parts:

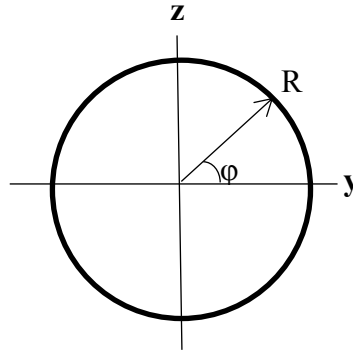
$$\begin{aligned}
& - \int_V \rho_0 (y\ddot{u} - y^2\ddot{v}' - yz\ddot{w}') \delta v' \, dV \\
& = \int_A -\rho_0 [(y\ddot{u} - y^2\ddot{v}' - yz\ddot{w}') \delta v]_{x=0}^{x=l} dA + \int_V \rho_0 (y\ddot{u} - y^2\ddot{v}' - yz\ddot{w}')' \delta v \, dV
\end{aligned} \tag{3.23}$$

$\delta w'$ by parts:

$$\begin{aligned}
& - \int_V \rho_0 (z\ddot{u} - yz\ddot{v}' - z^2\ddot{w}') \delta w' \, dV \\
& = \int_A -\rho_0 [(z\ddot{u} - yz\ddot{v}' - z^2\ddot{w}') \delta w]_{x=0}^{x=L} \, dA + \int_V \rho_0 (z\ddot{u} - yz\ddot{v}' - z^2\ddot{w}')' \delta w \, dV \quad (3.24)
\end{aligned}$$

3.5.5 Inertia Integration Coefficients

By Equation (3.10), the variation of kinetic energy is given by integrating $\rho_0 \{\ddot{r}\}^T \delta r$ through the volume of the shaft. To use only the generalised co-ordinates, the terms x, y, z, yz, yz^2, z^2 are integrated to obtain relevant inertia coefficients. The integration of volume is conducted using cylindrical co-ordinates:



Where:

$$dV = dx dy dz = R dR d\varphi \, dx \quad y = R \cos \varphi \quad z = R \sin \varphi$$

Considering the cross section of the shaft, the integration is restricted to area; therefore dV becomes $dA = R dR d\varphi$. The per unit area terms are integrated along the length of the shaft in the main energy equation. The shaft is assumed to have a constant tubular cross section with inner and outer radii (R_i and R_o). Integrating for $0 < \varphi < 2\pi$, The specific inertia coefficients are given in Table 3-1. Appendix B.1 gives the full derivation for the terms.

Table 3-1 – Inertia coefficients

Integral	Equivalent	Value	True Value
$\iint \rho_0 dA$	I_1	$\pi\rho_0(R_o^2 - R_i^2)$	m_0
$\iint \rho_0 y dA$	I_2	0	
$\iint \rho_0 z dA$	I_3	0	
$\iint \rho_0 yz dA$	I_4	0	
$\iint \rho_0 y^2 dA$	I_5	$\pi\rho_0 \left(\frac{R_o^4 - R_i^4}{4} \right)$	$\rho_0 I$
$\iint \rho_0 z^2 dA$	I_6	$\pi\rho_0 \left(\frac{R_o^4 - R_i^4}{4} \right)$	$\rho_0 I$

Using Table 3-1 to substitute values into Equations (3.22) through (3.24), the variation of kinetic energy, including boundary conditions is given by:

$$\begin{aligned}
\delta T = & - \int_0^L I_1 \ddot{u} \delta u - \dot{\theta}^2 I_1 v - \ddot{\theta} I_1 w - 2\dot{\theta} I_1 \dot{w} + I_1 \ddot{v} - I_5 \ddot{v}' \delta v - \dot{\theta}^2 I_1 w + \ddot{\theta} I_1 v \\
& + 2\dot{\theta} I_1 \dot{v} + I_1 \ddot{w} - I_6 \ddot{w}' \delta w - \dot{\theta}^2 (I_6 \phi + I_5 \phi) + \ddot{\theta} (I_6 + I_5) \\
& + I_5 \ddot{\phi} + I_6 \ddot{\phi} \delta \phi + \ddot{\theta} (I_5 + I_6) + I_5 \ddot{\phi} + I_6 \ddot{\phi} \delta \theta \, dx \\
& - [(I_5 \ddot{v}') \delta v]_{x=0}^{x=L} - [(I_6 \ddot{w}') \delta w]_{x=0}^{x=L}
\end{aligned} \quad (3.25)$$

3.5.6 Shaft Potential Energy

From Nayfeh & Pai [92], the variation of potential energy of an Euler Bernoulli beam is given by the relationship of stresses (σ) and the variation of strains (e):

$$\delta U = \int_V (\sigma_{xx} \delta e_{xx} + \sigma_{yy} \delta e_{yy} + \sigma_{zz} \delta e_{zz} + \sigma_{yz} \delta e_{yz} + 2\sigma_{xy} \delta e_{xy} + 2\sigma_{xz} \delta e_{xz}) dV \quad (3.26)$$

The derivation of stresses and strains is straightforward, considering that the shaft is made of linear elastic isotropic material and the displacements of an Euler-Bernoulli beam are already given in Equation (3.3). The strain-displacement relationships are given by [92]:

$$\begin{aligned}
 \frac{\partial D_x}{\partial x} &= u' - yv'' - zw'' & \frac{\partial D_y}{\partial x} &= v' - z\phi' & \frac{\partial D_z}{\partial x} &= w' + y\phi' \\
 \frac{\partial D_x}{\partial y} &= -v' & \frac{\partial D_y}{\partial y} &= 0 & \frac{\partial D_z}{\partial y} &= \phi \\
 \frac{\partial D_x}{\partial z} &= -w' & \frac{\partial D_y}{\partial z} &= -\phi & \frac{\partial D_z}{\partial z} &= 0
 \end{aligned} \tag{3.27 a-f}$$

The strain tensors, e_{ij} are given in Equation 3.28 [11]:

$$\begin{aligned}
 e_{xx} &= \frac{\partial D_x}{\partial x} = u' - yv'' - zw'' \\
 e_{yy} &= \frac{\partial D_y}{\partial y} = 0 \\
 e_{zz} &= \frac{\partial D_z}{\partial z} = 0 \\
 e_{xy} &= \frac{1}{2} \left(\frac{\partial D_x}{\partial y} + \frac{\partial D_y}{\partial x} \right) = \frac{-v' + v' - z\phi'}{2} = \frac{-z\phi'}{2} \\
 e_{xz} &= \frac{1}{2} \left(\frac{\partial D_x}{\partial z} + \frac{\partial D_z}{\partial x} \right) = \frac{-w' + w' + y\phi'}{2} = \frac{y\phi'}{2} \\
 e_{yz} &= \frac{1}{2} \left(\frac{\partial D_y}{\partial z} + \frac{\partial D_z}{\partial y} \right) = \frac{-\phi + \phi}{2} = 0
 \end{aligned} \tag{3.28 a-f}$$

These lead to the variations of strains in Equations (3.29) to (3.31):

$\delta e_{xx} = f(u', v'', w'')$:

$$\delta e_{xx} = \frac{\partial e_{xx}}{\partial u'} \delta u' + \frac{\partial e_{xx}}{\partial v''} \delta v'' + \frac{\partial e_{xx}}{\partial w''} \delta w'' = \delta u' - y \delta v'' - z \delta w'' \tag{3.29}$$

$\delta \mathbf{e}_{xy} = \mathbf{f}(\phi')$:

$$e_{xy} = \frac{\partial e_{xy}}{\partial \phi'} \delta \phi' = -\frac{z}{2} \delta \phi' \quad (3.30)$$

$\delta \mathbf{e}_{xz} = \mathbf{f}(\phi')$:

$$\delta e_{xz} = \frac{\partial e_{xz}}{\partial \phi'} \delta \phi' = \frac{y}{2} \delta \phi' \quad (3.31)$$

For an isotropic material, the stress-strain relationship is determined by [92]:

$$\begin{Bmatrix} \sigma_{xx} \\ \sigma_{xy} \\ \sigma_{xz} \end{Bmatrix} = \begin{bmatrix} E & 0 & 0 \\ 0 & G & 0 \\ 0 & 0 & G \end{bmatrix} \begin{Bmatrix} e_{xx} \\ e_{xy} \\ e_{xz} \end{Bmatrix} = \begin{Bmatrix} E(u' - yv'' - zw'') \\ G\left(\frac{-z\phi'}{2}\right) \\ G\left(\frac{y\phi'}{2}\right) \end{Bmatrix} \quad (3.32)$$

Combining Equations 3.29 to 3.32 into 3.26, derives the variation of potential energy:

$$\begin{aligned} \delta U = \int_V \left([E(u' - yv'' - zw'')] \delta u' \right) &- [Ey(u' - yv'' - zw'')] \delta v'' \\ &- [Ez(u' - yv'' - zw'')] \delta w'' + \left[\left(\frac{Gz^2 \phi'}{2} + \frac{Gy^2 \phi'}{2} \right) \delta \phi' \right] \right) dV \end{aligned} \quad (3.33)$$

3.5.7 Shaft Potential Energy Boundary Conditions

To incorporate $\delta u'$, $\delta v''$, $\delta w''$ and $\delta \phi''$ into the energy equation for δv and δw , the required components of Equation 3.33 are integrated by parts. Six boundary conditions are obtained (one for each of $\delta u'$, δv , $\delta v'$, δw , $\delta w'$ and $\delta \phi''$):

$\delta u'$ by parts once:

$$\begin{aligned} \int_V E(u' - yv'' - zw'') \delta u' dV \\ = [E(u' - yv'' - zw'')] \delta u \Big|_x=0^x=L - \int_V E(u' - yv'' - zw'')' \delta u dV \end{aligned} \quad (3.34)$$

δv by parts twice:

$$\begin{aligned}
& - \int_V Ey(u' - yv'' - zw'')\delta v'' dV \\
& = -[Ey(u' - yv'' - zw'')\delta v']_{x=0}^{x=L} + \int_V [Ey(u' - yv'' - zw'')]'\delta v' dV \quad (3.35) \\
& = -[Ey(u' - yv'' - zw'')\delta v']_{x=0}^{x=L} + [Ey(u' - yv'' - zw'')\delta v]_{x=0}^{x=L} \\
& \quad - \int_V [Ey(u' - yv'' - zw'')]'\delta v dV
\end{aligned}$$

δw'' by parts twice:

$$\begin{aligned}
& - \int_V Ez(u' - yv'' - zw'')\delta w'' dV \\
& = -[Ez(u' - yv'' - zw'')\delta w']_{x=0}^{x=L} + \int_V [Ez(u' - yv'' - zw'')]'\delta w' dV \quad (3.36) \\
& = -[Ez(u' - yv'' - zw'')\delta w']_{x=0}^{x=L} + [Ez(u' - yv'' - zw'')\delta w]_{x=0}^{x=L} \\
& \quad - \int_V [Ez(u' - yv'' - zw'')]'\delta w dV
\end{aligned}$$

δφ' by parts once:

$$\begin{aligned}
& \int_V \frac{Gz^2\phi'}{2} + \frac{Gy^2\phi'}{2} \delta\phi' dV \\
& = \left[\frac{Gz^2\phi'}{2} + \frac{Gy^2\phi'}{2} \delta\phi \right]_{x=0}^{x=L} - \int_V \left(\frac{Gz^2\phi'}{2} + \frac{Gy^2\phi'}{2} \right)' \delta\phi dV \quad (3.37)
\end{aligned}$$

3.5.8 Stiffness Integration Coefficients

In order to use just the generalised co-ordinates, the integration of volume is done using cylindrical co-ordinates restricted to over area (Appendix B.2 gives the full derivation for the terms). The specific stiffness coefficients are given in Table 3-2 and substituted into Equations (3.33) to (3.37) to give the variation of potential energy, including BCs:

$$\begin{aligned}
\delta U = \int_L & -k_1 u'' \delta u + k_5 v'''' \delta v + k_6 w'''' \delta w - \left(\frac{k_7 \phi''}{2} + \frac{k_8 \phi''}{2} \right) \delta \phi dx \\
& + [k_1 u' \delta u]_{x=0}^{x=L} + [k_5 v'' \delta v']_{x=0}^{x=L} - [k_5 v'' \delta v]_{x=0}^{x=L} \quad (3.38) \\
& + [k_6 w'' \delta w']_{x=0}^{x=L} - [k_6 w'' \delta w]_{x=0}^{x=L} + \left[\frac{k_7 \phi'}{2} + \frac{k_8 \phi'}{2} \delta \phi \right]_{x=0}^{x=L}
\end{aligned}$$

Table 3-2 – Stiffness integration coefficients

Integral	Equivalent	Value	True Value
$\iint E \, dA$	k_1	$E\pi(R_o^2 - R_i^2)$	EA
$\iint E y \, dA$	k_2	0	
$\iint E z \, dA$	k_3	0	
$\iint E y z \, dA$	k_4	0	
$\iint E y^2 \, dA$	k_5	$E\pi\left(\frac{R_o^4 - R_i^4}{4}\right)$	EI
$\iint E z^2 \, dA$	k_6	$E\pi\left(\frac{R_o^4 - R_i^4}{4}\right)$	EI
$\iint G y^2 \, dA$	k_7	$G\pi\left(\frac{R_o^4 - R_i^4}{4}\right)$	GI
$\iint G z^2 \, dA$	k_8	$G\pi\left(\frac{R_o^4 - R_i^4}{4}\right)$	GI

3.5.9 Shaft Total Energy Equation

Reviewing Equation (3.1), the kinetic (3.25) and potential (3.38) energy terms for the shaft have been derived. The total variation of energy in the shaft is therefore given by:

$$\begin{aligned}
\delta J = \int_0^L & \left((-I_1 \ddot{u} + k_1 u'' \delta u) + (\dot{\theta}^2 I_1 v + \ddot{\theta} I_1 w + 2\dot{\theta} I_1 \dot{w} - I_1 \dot{v} + I_5 \dot{v}'' - k_5 v'''' \delta v \right. \\
& + (\dot{\theta}^2 I_1 w - \ddot{\theta} I_1 v - 2\dot{\theta} I_1 \dot{v} - I_1 \dot{w} + I_6 \dot{w}'' - k_6 w'''' \delta w) \\
& + \left(\dot{\theta}^2 (I_6 \phi + I_5 \phi) - \ddot{\theta} (I_6 + I_5) - I_5 \ddot{\phi} - I_6 \ddot{\phi} \right. \\
& \left. + \left(\frac{k_7 \phi''}{2} + \frac{k_8 \phi''}{2} \right) \delta \phi \right) + (-\ddot{\theta} (I_5 + I_6) - I_5 \ddot{\phi} - I_6 \ddot{\phi} \delta \theta) dx \quad (3.39) \\
& - [k_1 u' \delta u]_{x=0}^{x=L} + [I_5 \dot{v}' \delta v]_{x=0}^{x=L} + [I_6 \dot{w}' \delta w]_{x=0}^{x=L} + [k_5 v'' \delta v]_{x=0}^{x=L} \\
& + [k_6 w'' \delta w]_{x=0}^{x=L} - [k_5 v'' \delta v']_{x=0}^{x=L} - [k_6 w'' \delta w']_{x=0}^{x=L} \\
& - \left[\frac{k_7 \phi'}{2} + \frac{k_8 \phi'}{2} \delta \phi \right]_{x=0}^{x=L}
\end{aligned}$$

3.5.10 Comparison with Previously Reported Equations

Using the shaft energy Equation (3.39), it is possible to compare the energy variation equation with those previously reported in existing literature. Suherman [80] conducted a derivation using a similar procedure for a different method of controlling shaft vibration; an internal support to change the stiffness and boundary conditions of the system.

Table 3-3 contains the variation of the individual generalised coordinates from both derivations. The equations of motion derived in [80] consider non-constant rotating speed, gravity, energy dissipation and eccentricity but neglect torsional vibration of shaft and rotary inertia terms. Under the same assumptions, i.e neglecting the effects of the eccentric sleeves and internal support, both sets of equations show similar form. In particular, the centrifugal, Coriolis, non-constant rotating speed and stiffness terms for variation of lateral displacement (δv and δw) are identical. Any differences in the two sets of equations stem from consideration of different systems therefore this method will not be used for further comparison.

Table 3-3 – Comparison of the variation of generalised coordinates

	Kirk	Suherman [80]
δu	$k_1 u'' - I_1 \ddot{u} = 0$	
δv	$\dot{\theta}^2 I_1 v + \ddot{\theta} I_1 w + 2\dot{\theta} I_1 \dot{w} - I_1 \ddot{v} + I_5 \ddot{v}'' - k_5 v'''' = 0$	$\mu(\dot{\theta}^2 v + \ddot{\theta} w + 2\dot{\theta} \dot{w} - \ddot{v} + g \sin \theta) - EI v'''' - d_i EI \dot{v}'''' + d_e \mu(\dot{v} + \dot{\theta} w) = 0$
δw	$\dot{\theta}^2 I_1 w - \ddot{\theta} I_1 v - 2\dot{\theta} I_1 \dot{v} - I_1 \ddot{w} + I_6 \ddot{w}'' - k_6 w'''' = 0$	$\mu(\dot{\theta}^2 w - \ddot{\theta} v - 2\dot{\theta} \dot{v} - \ddot{w} + g \cos \theta) - EI w'''' - d_i EI \dot{w}'''' - d_e \mu(\dot{w} + \dot{\theta} v) = 0$
$\delta \phi$	$\dot{\theta}^2 (I_6 \phi + I_5 \phi) - \ddot{\theta} (I_6 + I_5) - I_5 \ddot{\phi} - I_6 \ddot{\phi} + \left(\frac{k_7 \phi''}{2} + \frac{k_8 \phi''}{2} \right) = 0$	
$\delta \theta$	$-\ddot{\theta} (I_5 + I_6) - I_5 \ddot{\phi} - I_6 \ddot{\phi} = 0$	$\mu \left(-\ddot{v} w + v \ddot{w} + 2\dot{\theta} (v \dot{v} + w \dot{w}) + \ddot{\theta} (v^2 + w^2) \right) - \mu g v \cos \theta + \mu g v \sin \theta + \frac{1}{2} d_e \mu r_s^2 \dot{\theta} = 0$

3.6 Derivation of Eccentric Sleeve Dynamics

The procedure used for the derivation of the shaft equations of motion is repeated for each of the eccentric sleeves.

3.6.1 Numerical Analysis

If the flexibility of the sleeve is shown to have little effect on the critical speeds of the system, the potential energy can be neglected. Therefore, to minimise the complexity of the modelling process for the sleeves, only the kinetic energies are initially considered. To determine the impact of sleeve flexibility, numerical determination of critical speeds is performed for two models using ANSYS. In the first, the sleeves are modelled with flexibility (the full geometry as is intended for the ‘semi-active’ method of vibration control), and in the second, the sleeves are considered as rigid bodies. In this case, the flexible sleeves are removed from the geometry and replaced with point masses with equal mass and inertia coefficients. Figure 3.4 depicts the normalised natural frequencies of the 1st and 2nd modes (FW and BW) in lateral bending vibration for both models. Considering the rigid body assumption there is approximately 1% difference in the determination of critical speed—see Table 3-4.

Table 3-4 – Normalised critical speeds of system with flexible/rigid sleeves

Sleeve Type	Normalised Critical Speed
Rigid	1.000
Flexible	0.989

Hence the assumption of zero sleeve flexibility is suitable for the analysis of critical speeds of the shaft.

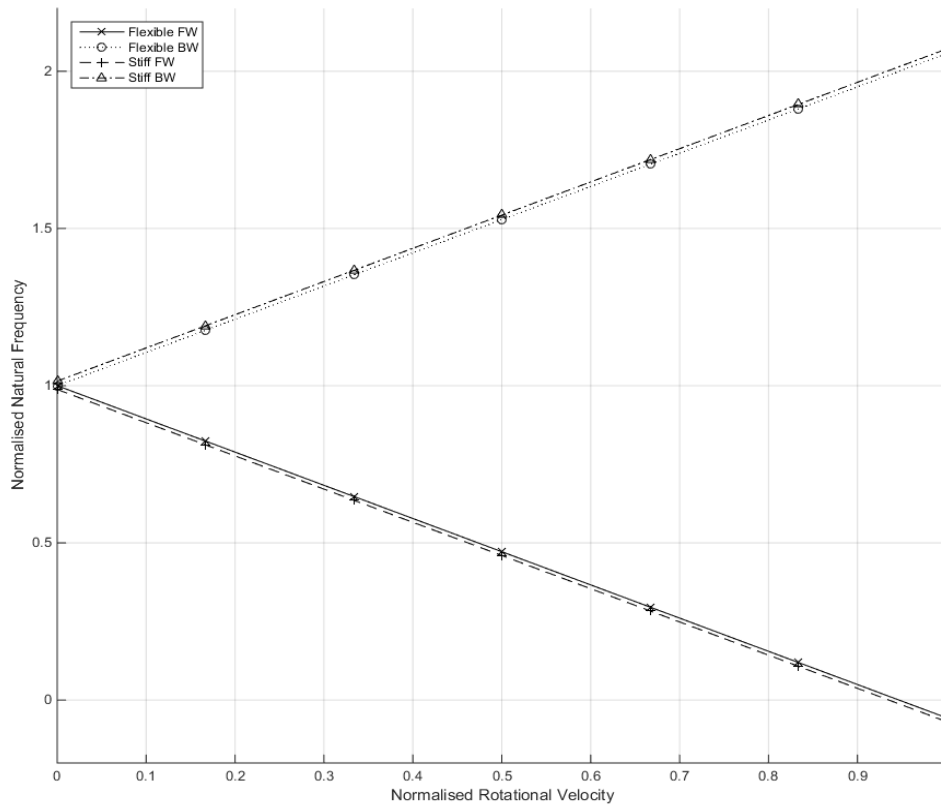


Figure 3.4 – Normalised Campbell Diagram for stiff and flexible sleeves

3.6.2 Sleeve Position and Acceleration Vectors

Since the sleeves are fixed to the shaft, they are considered to be rotating in the same rotating coordinate system. Additionally, the eccentric mass of each sleeve, denoted by the red circle in

Figure 3.5 and Figure 3.6, has motion in three dimensions – v' , w' and ϕ describe the rotation of the sleeve eccentric mass about the y and z axes and torsion and rotation about the x axis. The coordinate system is attached to the shaft in locations $x = 0$ and $x = L$.

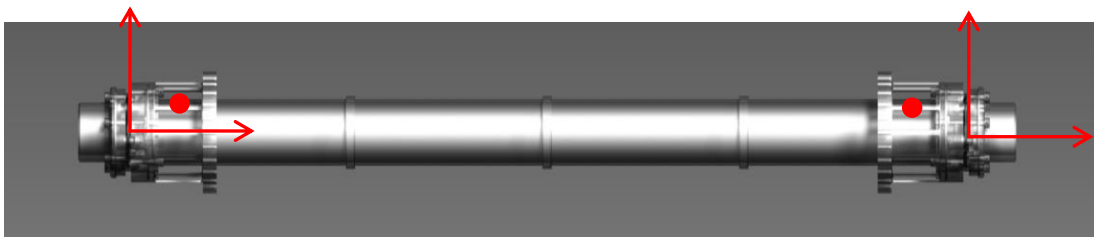
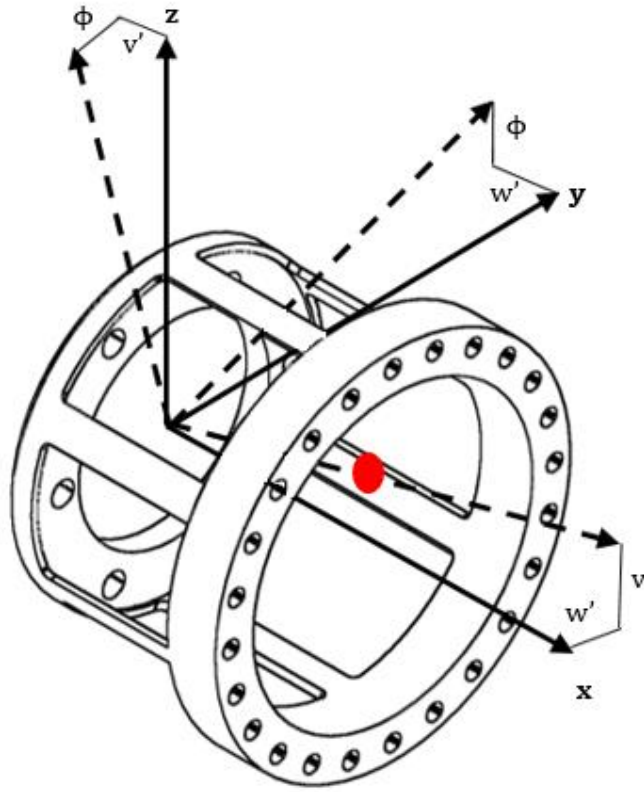


Figure 3.5 – Coordinate system attached to each sleeve and global positions

Figure 3.6 – Displacements of eccentric sleeve mass at $x = 0$

The position vector of each sleeve in the global co-ordinate system ($r = [A][\bar{r}]$) is obtained through transformations. The total transformation matrix for the motions (neglecting higher order terms) is shown in Equation (3.40) and describes four successive transformations; rotation about each axis of deformation, v' , w' , ϕ and the total rotation of the shaft, θ . The term (c,t) is used to denote $x = 0$ or $x=L$.

$$\begin{aligned}
 [A] &= [A_{v'}][A_{w'}][A_{\phi}][A_{\theta}] \\
 &= \begin{bmatrix} 1 & v'(c,t) & 0 \\ -v'(c,t) & 1 & 0 \\ 0 & 0 & 1 \end{bmatrix} \begin{bmatrix} 1 & 0 & w'(c,t) \\ 0 & 1 & 0 \\ -w'(c,t) & 0 & 1 \end{bmatrix} \begin{bmatrix} 1 & 0 & 0 \\ 0 & 1 & \phi \\ 0 & -\phi & 1 \end{bmatrix} \begin{bmatrix} 1 & 0 & 0 \\ 0 & \cos \theta & -\sin \theta \\ 0 & \sin \theta & \cos \theta \end{bmatrix} \\
 &= \begin{bmatrix} 1 & 0 & 0 \\ 0 & \cos \theta & -\sin \theta \\ 0 & \sin \theta & \cos \theta \end{bmatrix} \begin{bmatrix} 1 & v'(c,t) & w'(c,t) \\ -v'(c,t) & 1 & \phi \\ -w'(c,t) & -\phi & 1 \end{bmatrix} \\
 &= \begin{bmatrix} 1 & v'(c,t) & w'(c,t) \\ -v'(c,t)\cos \theta + w'(c,t)\sin \theta & \cos \theta + \phi \sin \theta & -\sin \theta + \phi \cos \theta \\ -w'(c,t)\cos \theta - v'(c,t)\sin \theta & \sin \theta - \phi \cos \theta & \cos \theta + \phi \sin \theta \end{bmatrix} \quad (3.40)
 \end{aligned}$$

The local position vector of the sleeves account for the axial position and eccentricity of the sleeve masses. Using the coordinate system established in Figure 3.5, fixed at $x=0$ and $x=L$, the axial position of the second sleeve is in the negative X direction. Therefore the position vectors for each sleeve are:

$$\bar{r}_1 = \begin{Bmatrix} \bar{r}_x \\ \bar{r}_y \\ \bar{r}_z \end{Bmatrix} = \begin{Bmatrix} x + L \\ y + e_y \\ z + e_z \end{Bmatrix} \quad (3.41)$$

$$\bar{r}_2 = \begin{Bmatrix} -\bar{r}_x \\ \bar{r}_y \\ \bar{r}_z \end{Bmatrix} = \begin{Bmatrix} -x - L \\ y + e_y \\ z + e_z \end{Bmatrix} \quad (3.42)$$

The position vector in the global coordinate system is obtained by considering all transformation matrices in Equation (3.40); the rotation of the system about x -axis and the angular deformations of the shaft in boundary conditions in all directions. The resulting position vectors for the first (r_1) and second (r_2) sleeves in the global frame are therefore:

$$r_1 = \begin{Bmatrix} \bar{r}_x + \bar{r}_y v'(0, t) + \bar{r}_z w'(0, t) \\ -\bar{r}_x (v'(0, t) \cos \theta - w'(0, t) \sin \theta) + \bar{r}_y (\cos \theta + \phi \sin \theta) - \bar{r}_z (\sin \theta - \phi \cos \theta) \\ -\bar{r}_x (w'(0, t) \cos \theta + v'(0, t) \sin \theta) + \bar{r}_y (\sin \theta - \phi \cos \theta) + \bar{r}_z (\cos \theta + \phi \sin \theta) \end{Bmatrix} \quad (3.43)$$

$$r_2 = \begin{Bmatrix} -\bar{r}_x + \bar{r}_y v'(L, t) + \bar{r}_z w'(L, t) \\ \bar{r}_x (v'(L, t) \cos \theta - w'(L, t) \sin \theta) + \bar{r}_y (\cos \theta + \phi \sin \theta) - \bar{r}_z (\sin \theta - \phi \cos \theta) \\ \bar{r}_x (w'(L, t) \cos \theta + v'(L, t) \sin \theta) + \bar{r}_y (\sin \theta - \phi \cos \theta) + \bar{r}_z (\cos \theta + \phi \sin \theta) \end{Bmatrix} \quad (3.44)$$

Following a similar procedure as in Section 3.5, appropriate manipulation of the position vectors produces the acceleration vectors of the sleeves, Equations (3.45) and (3.46). As with the shaft acceleration vector, Equation (3.8), the first component of the acceleration vector is due to centrifugal acceleration, the second component is due to non-constant rotating speed, the third is due to Coriolis acceleration, and the final component is due to translational acceleration.

$$\begin{aligned}
& \ddot{r}_1 \\
&= \dot{\theta}^2 \left\{ \begin{array}{c} 0 \\ \bar{r}_x(v'(0,t)\cos\theta - w'(0,t)\sin\theta) + \bar{r}_y(-\phi\sin\theta - \cos\theta) + \bar{r}_z(-\phi\cos\theta + \sin\theta) \\ \bar{r}_x(w'(0,t)\cos\theta + v'(0,t)\sin\theta) + \bar{r}_y(\phi\cos\theta - \sin\theta) + \bar{r}_z(-\phi\sin\theta - \cos\theta) \end{array} \right\} \\
&- \ddot{\theta} \left\{ \begin{array}{c} 0 \\ -\bar{r}_x(v'(0,t)\sin\theta + w'(0,t)\cos\theta) - \bar{r}_y(\phi\cos\theta - \sin\theta) - \bar{r}_z(-\phi\sin\theta - \cos\theta) \\ \bar{r}_x(-w'(0,t)\sin\theta + v'(0,t)\cos\theta) + \bar{r}_y(-\phi\sin\theta - \cos\theta) - \bar{r}_z(\phi\cos\theta - \sin\theta) \end{array} \right\} \\
&- 2\dot{\theta} \left\{ \begin{array}{c} 0 \\ -\bar{r}_x(\dot{v}'(0,t)\sin\theta + \dot{w}'(0,t)\cos\theta) - \bar{r}_y\dot{\phi}\cos\theta + \bar{r}_z\dot{\phi}\sin\theta \\ \bar{r}_x(-\dot{w}'(0,t)\sin\theta + \dot{v}'(0,t)\cos\theta) - \bar{r}_y\dot{\phi}\sin\theta - \bar{r}_z\dot{\phi}\cos\theta \end{array} \right\} \quad (3.45) \\
&+ \left\{ \begin{array}{c} \bar{r}_y\ddot{v}' + \bar{r}_z\ddot{w}' \\ \bar{r}_x(\ddot{v}'(L,t)\cos\theta - \ddot{w}'(L,t)\sin\theta) + \bar{r}_y\ddot{\phi}\sin\theta + \bar{r}_z\ddot{\phi}\cos\theta \\ \bar{r}_x(\ddot{w}'(L,t)\cos\theta + \ddot{v}'(L,t)\sin\theta) - \bar{r}_y\ddot{\phi}\cos\theta + \bar{r}_z\ddot{\phi}\sin\theta \end{array} \right\}
\end{aligned}$$

$$\begin{aligned}
& \ddot{r}_2 \\
&= \dot{\theta}^2 \left\{ \begin{array}{c} 0 \\ -\bar{r}_x(v'(L,t)\cos\theta - w'(L,t)\sin\theta) + \bar{r}_y(-\phi\sin\theta - \cos\theta) + \bar{r}_z(-\phi\cos\theta + \sin\theta) \\ -\bar{r}_x(w'(L,t)\cos\theta + v'(L,t)\sin\theta) + \bar{r}_y(\phi\cos\theta - \sin\theta) + \bar{r}_z(-\phi\sin\theta - \cos\theta) \end{array} \right\} \\
&- \ddot{\theta} \left\{ \begin{array}{c} 0 \\ \bar{r}_x(v'(L,t)\sin\theta + w'(L,t)\cos\theta) - \bar{r}_y(\phi\cos\theta - \sin\theta) - \bar{r}_z(-\phi\sin\theta - \cos\theta) \\ -\bar{r}_x(-w'(L,t)\sin\theta + v'(L,t)\cos\theta) + \bar{r}_y(-\phi\sin\theta - \cos\theta) - \bar{r}_z(\phi\cos\theta - \sin\theta) \end{array} \right\} \\
&- 2\dot{\theta} \left\{ \begin{array}{c} 0 \\ \bar{r}_x(\dot{v}'(L,t)\sin\theta + \dot{w}'(L,t)\cos\theta) - \bar{r}_y\dot{\phi}\cos\theta + \bar{r}_z\dot{\phi}\sin\theta \\ -\bar{r}_x(-\dot{w}'(L,t)\sin\theta + \dot{v}'(L,t)\cos\theta) - \bar{r}_y\dot{\phi}\sin\theta - \bar{r}_z\dot{\phi}\cos\theta \end{array} \right\} \quad (3.46) \\
&+ \left\{ \begin{array}{c} \bar{r}_y\ddot{v}' + \bar{r}_z\ddot{w}' \\ \bar{r}_x(\ddot{v}'(L,t)\cos\theta - \ddot{w}'(L,t)\sin\theta) + \bar{r}_y\ddot{\phi}\sin\theta + \bar{r}_z\ddot{\phi}\cos\theta \\ \bar{r}_x(\ddot{w}'(L,t)\cos\theta + \ddot{v}'(L,t)\sin\theta) - \bar{r}_y\ddot{\phi}\cos\theta + \bar{r}_z\ddot{\phi}\sin\theta \end{array} \right\}
\end{aligned}$$

3.6.3 Kinetic Energy of Sleeves

The process for driving the variation of kinetic energy is repeated for each sleeve. The full derivation is listed in Appendix C with the variation of kinetic energy for the two sleeves given in Equations (3.47) and (3.48):

$$\begin{aligned}
\delta T_1 = & - \left(\left(-\ddot{\theta} \left(I_{yy} + I_{zz} - I_{yz} \phi(0, t) - 2 \left(I_{xy} v'(0, t) + I_{xz} w'(0, t) \right) \right) - \right. \\
& 2\dot{\theta} \left(I_{xy} \dot{v}'(0, t) + I_{xz} \dot{w}'(0, t) \right) + I_{xy} \ddot{w}'(0, t) - I_{xz} \ddot{v}'(0, t) + I_{yy} \ddot{\phi}(0, t) + \\
& I_{zz} \ddot{\phi}(0, t) \delta\theta \left. \right) + \left(\dot{\theta}^2 \left(-I_{xx} v'(0, t) + I_{xy} + I_{xz} \phi(0, t) \right) - \ddot{\theta} \left(I_{xx} w'(0, t) + \right. \right. \\
& I_{xy} \phi(0, t) - I_{xz} \left. \right) - 2\dot{\theta} \left(I_{xx} \dot{w}'(0, t) + I_{xy} \dot{\phi}(0, t) \right) + I_{yy} \ddot{v}'(0, t) + I_{yz} \ddot{w}'(0, t) + \\
& I_{xx} \ddot{v}'(0, t) - I_{xz} \ddot{\phi}(0, t) \delta v'(0, t) \left. \right) + \left(\dot{\theta}^2 \left(-I_{xx} w'(0, t) - I_{xy} \phi(0, t) + I_{xz} \right) - \right. \\
& \ddot{\theta} \left(-I_{xx} v'(0, t) + I_{xy} + I_{xz} \phi(0, t) \right) - 2\dot{\theta} \left(-I_{xx} \dot{v}'(0, t) + I_{xz} \dot{\phi}(0, t) \right) + \\
& I_{yz} \ddot{v}'(0, t) + I_{zz} \ddot{w}'(0, t) + I_{xx} \ddot{w}'(0, t) + I_{xy} \ddot{\phi}(0, t) \delta w'(0, t) \left. \right) + \\
& \left(\dot{\theta}^2 \left(-I_{xy} w'(0, t) - I_{yy} \phi(0, t) + I_{xz} v'(0, t) - I_{zz} \phi(0, t) \right) - \ddot{\theta} \left(-I_{xy} v'(0, t) + \right. \right. \\
& I_{yy} - I_{xz} w'(0, t) + I_{zz} \left. \right) - 2\dot{\theta} \left(-I_{xy} \dot{v}'(0, t) - I_{xz} \dot{w}'(0, t) \right) + I_{xy} \ddot{w}'(0, t) + \\
& \left. I_{yy} \ddot{\phi}(0, t) - I_{xz} \ddot{v}'(0, t) + I_{zz} \ddot{\phi}(0, t) \delta\phi(0, t) \right) \left. \right) \tag{3.47}
\end{aligned}$$

$$\begin{aligned}
\delta T_2 = & - \left(\left(-\ddot{\theta} \left(-I_{yy} - I_{zz} + I_{yz} \phi(L, t) - 2 \left(I_{xy} v'(L, t) + I_{xz} w'(L, t) \right) \right) - \right. \\
& 2\dot{\theta} \left(-I_{xy} \dot{v}'(L, t) - I_{xz} \dot{w}'(L, t) \right) + I_{xy} \ddot{w}'(L, t) - I_{xz} \ddot{v}'(L, t) - I_{yy} \ddot{\phi}(L, t) - \\
& I_{zz} \ddot{\phi}(L, t) \delta\theta \left. \right) + \left(\dot{\theta}^2 \left(-I_{xx} v'(L, t) - I_{xy} - I_{xz} \phi(L, t) \right) - \ddot{\theta} \left(I_{xx} w'(L, t) - \right. \right. \\
& I_{xy} \phi(L, t) + I_{xz} \left. \right) - 2\dot{\theta} \left(I_{xx} \dot{w}'(L, t) - I_{xy} \dot{\phi}(L, t) \right) + I_{yy} \ddot{v}'(L, t) + I_{yz} \ddot{w}'(L, t) + \\
& I_{xx} \ddot{v}'(L, t) + I_{xz} \ddot{\phi}(L, t) \delta v'(L, t) \left. \right) + \left(\dot{\theta}^2 \left(-I_{xx} w'(L, t) + I_{xy} \phi(L, t) - I_{xz} \right) - \right. \\
& \ddot{\theta} \left(-I_{xx} v'(L, t) - I_{xy} - I_{xz} \phi(L, t) \right) - 2\dot{\theta} \left(-I_{xx} \dot{v}'(L, t) - I_{xz} \dot{\phi}(L, t) \right) + \\
& \left(I_{yz} \ddot{v}'(L, t) + I_{zz} \ddot{w}'(L, t) + I_{xx} \ddot{w}'(L, t) - I_{xy} \ddot{\phi}(L, t) \right) \delta w'(L, t) \left. \right) + \\
& \left(\dot{\theta}^2 \left(I_{xy} w'(L, t) - I_{yy} \phi(L, t) - I_{xz} v'(L, t) - I_{zz} \phi(L, t) \right) - \ddot{\theta} \left(I_{xy} v'(L, t) + I_{yy} + \right. \right. \\
& I_{xz} w'(L, t) + I_{zz} \left. \right) - 2\dot{\theta} \left(I_{xy} \dot{v}'(L, t) + I_{xz} \dot{w}'(L, t) \right) - I_{xy} \ddot{w}'(L, t) + I_{yy} \ddot{\phi}(L, t) + \\
& \left. I_{xz} \ddot{v}'(L, t) + I_{zz} \ddot{\phi}(L, t) \delta\phi(L, t) \right) \left. \right) \tag{3.48}
\end{aligned}$$

3.7 Torsional Stiffness

Considering torsional stiffness of the flexible elements, additional boundary condition terms need to be included for $\delta v'$ and $\delta w'$ at $x = 0$ and $x = L$. Assuming a constant torsional stiffness, k , in both v' and w' directions, the strain energy is given by:

$$U_{\text{TORS}} = \frac{1}{2}kv'(0, t)^2 + \frac{1}{2}kw'(0, t)^2 + \frac{1}{2}kv'(L, t)^2 + \frac{1}{2}kw'(L, t)^2$$

Therefore the variation of the strain energy due to torsional stiffness is:

$$\delta U_{\text{TORS}} = kv'(0, L)\delta v' + kw'(0, L)\delta w' \quad (3.49)$$

3.8 Equations of Motion

Using the Extended Hamilton Principle (3.1) and the derived individual variations of the kinetic and potential energies of the system (3.39, 3.47, 3.48, 3.49) the equations of motion and associated boundary conditions are given in Equations (3.50) through (3.56). The real values of the equivalent integration coefficients from Tables 3.3 and 3.4 are applied. The underlined terms represent those that are coupled by the non-constant rotating speed.

Axial Motion δu :

$$-m_0\ddot{u} + EAu'' = 0 \quad (3.50)$$

Y Lateral Bending δv :

$$\dot{\theta}^2 m_0 v + \underline{\ddot{\theta} m_0 w} + 2\dot{\theta} m_0 \dot{w} - m_0 \ddot{v} + \rho_0 I \ddot{v}'' - EIv'''' = 0 \quad (3.51)$$

Z Lateral Bending δw :

$$\dot{\theta}^2 m_0 w - \underline{\ddot{\theta} m_0 v} - 2\dot{\theta} m_0 \dot{v} - m_0 \ddot{w} + \rho_0 I \ddot{w}'' - EIw'''' = 0 \quad (3.52)$$

Torsion $\delta\phi$:

$$\dot{\theta}^2(2\rho_0 I\phi) - \ddot{\theta}(2\rho_0 I) - 2\rho_0 I\ddot{\phi} + GI\phi'' = 0 \quad (3.53)$$

Non-constant Rotating Speed $\delta\theta$:

$$\begin{aligned} & -\int_0^L \ddot{\phi}(2\rho_0 I) + \ddot{\theta}(2\rho_0 I) dx - \left(-\ddot{\theta} \left(I_{yy} + I_{zz} - I_{yz}\phi(0,t) - 2 \left(I_{xy}v'(0,t) + \right. \right. \right. \\ & \left. \left. \left. I_{xz}w'(0,t) \right) \right) - 2\dot{\theta} \left(I_{xy}\dot{v}'(0,t) + I_{xz}\dot{w}'(0,t) \right) + I_{xy}\ddot{w}'(0,t) - I_{xz}\ddot{v}'(0,t) + \right. \\ & \left. I_{yy}\ddot{\phi}(0,t) + I_{zz}\ddot{\phi}(0,t) \delta\theta \right) - \left(-\ddot{\theta} \left(-I_{yy} - I_{zz} + I_{yz}\phi(L,t) - 2 \left(I_{xy}v'(L,t) + \right. \right. \right. \\ & \left. \left. \left. I_{xz}w'(L,t) \right) \right) - 2\dot{\theta} \left(-I_{xy}\dot{v}'(L,t) - I_{xz}\dot{w}'(L,t) \right) + I_{xy}\ddot{w}'(L,t) - I_{xz}\ddot{v}'(L,t) - \right. \\ & \left. I_{yy}\ddot{\phi}(L,t) - I_{zz}\ddot{\phi}(L,t) \delta\theta \right) = 0 \end{aligned} \quad (3.54)$$

Strong BCs arising from geometry of the problem:

$$\begin{aligned} u(0,t) = u(L,t) &= 0 \\ v(0,t) = v(L,t) &= 0 \\ w(0,t) = w(L,t) &= 0 \end{aligned} \quad \begin{array}{l} (3.55) \\ \\ \text{a-c)} \end{array}$$

Weak BCs arising from the variational formulation: **$x=0, \delta v'$:**

$$\begin{aligned} EIv'' - \left(-\ddot{\theta} \left(I_{xx}w'(0,t) + I_{xy}\phi(0,t) - I_{xz} \right) + \dot{\theta}^2 \left(-I_{xx}v'(0,t) + I_{xy} + \right. \right. \\ \left. \left. I_{xz}\phi(0,t) \right) - 2\dot{\theta} \left(I_{xx}\dot{w}'(0,t) + I_{xy}\dot{\phi}(0,t) \right) + I_{yy}\ddot{v}'(0,t) + I_{yz}\ddot{w}'(0,t) + \right. \\ \left. I_{xx}\ddot{v}'(0,t) - I_{xz}\ddot{\phi}(0,t) \right) - kv'(0,t) = 0 \end{aligned} \quad (3.56)$$

 $x=L, \delta v'$

$$\begin{aligned} -EIv'' - \left(-\ddot{\theta} \left(I_{xx}w'(L,t) - I_{xy}\phi(L,t) + I_{xz} \right) + \dot{\theta}^2 \left(-I_{xx}v'(L,t) - I_{xy} - \right. \right. \\ \left. \left. I_{xz}\phi(L,t) \right) - 2\dot{\theta} \left(I_{xx}\dot{w}'(L,t) - I_{xy}\dot{\phi}(L,t) \right) + I_{yy}\ddot{v}'(L,t) + I_{yz}\ddot{w}'(L,t) + \right. \\ \left. I_{xx}\ddot{v}'(L,t) + I_{xz}\ddot{\phi}(L,t) \right) - kv'(L,t) = 0 \end{aligned} \quad \text{a-b)}$$

$x=0, \delta w'$:

$$EIw'' - \left(\underline{-\ddot{\theta}(-I_{xx}v'(0,t) + I_{xy} + I_{xz}\phi(0,t))} + \dot{\theta}^2(-I_{xx}w'(0,t) - I_{xy}\phi(0,t) + I_{zz}) - 2\dot{\theta}(-I_{xx}\dot{v}'(0,t) + I_{xz}\dot{\phi}(0,t)) + I_{yz}\ddot{v}'(0,t) + I_{zz}\ddot{w}'(0,t) + I_{xx}\ddot{w}'(0,t) + I_{xy}\ddot{\phi}(0,t) \right) - kw'(0,t) = 0$$

$x=L, \delta w'$:

$$-EIw'' - \left(\underline{-\ddot{\theta}(-I_{xx}v'(L,t) - I_{xy} - I_{xz}\phi(L,t))} + \dot{\theta}^2(-I_{xx}w'(L,t) + I_{xy}\phi(L,t) - I_{zz}) - 2\dot{\theta}(-I_{xx}\dot{v}'(L,t) - I_{xz}\dot{\phi}(L,t)) + I_{yz}\ddot{v}'(L,t) + I_{zz}\ddot{w}'(L,t) + I_{xx}\ddot{w}'(L,t) - I_{xy}\ddot{\phi}(L,t) \right) - kw'(L,t) = 0 \quad (3.56)$$

c-f)

$x=0, \delta \phi$:

$$GI\phi' - \left(\underline{-\ddot{\theta}(-I_{xy}v'(0,t) + I_{yy} - I_{xz}w'(0,t) + I_{zz})} + \dot{\theta}^2(-I_{xy}w'(0,t) - I_{yy}\phi(0,t) + I_{xz}v'(0,t) - I_{zz}\phi(0,t)) - 2\dot{\theta}(-I_{xy}\dot{v}'(0,t) - I_{xz}\dot{w}'(0,t)) + I_{xy}\ddot{w}'(0,t) + I_{yy}\ddot{\phi}(0,t) - I_{xz}\ddot{v}'(0,t) + I_{zz}\ddot{\phi}(0,t) \right) = 0$$

$x=L, \delta \phi$:

$$-GI\phi' - \left(\underline{-\ddot{\theta}(I_{xy}v'(L,t) + I_{yy} + I_{xz}w'(L,t) + I_{zz})} + \dot{\theta}^2(I_{xy}w'(L,t) - I_{yy}\phi(L,t) - I_{xz}v'(L,t) - I_{zz}\phi(L,t)) - 2\dot{\theta}(I_{xy}\dot{v}'(L,t) + I_{xz}\dot{w}'(L,t)) - I_{xy}\ddot{w}'(L,t) + I_{yy}\ddot{\phi}(L,t) + I_{xz}\ddot{v}'(L,t) + I_{zz}\ddot{\phi}(L,t) \right) = 0$$

3.9 Discussion

From the derivation of the equations of motion, it is seen that the lateral bending vibrations, (3.51 and 3.52) and the torsional motions (3.53) are coupled by the non-constant rotating speed component. Also these equations are coupled with the main non-constant rotating speed (3.54).

Considering the system rotating at a constant speed (neglecting the underlined terms), the angular velocity becomes a parameter. In this case, the equations of motion describing the

lateral bending vibrations (3.51 and 3.52) are coupled due to Coriolis forces only, and are decoupled for the rest of the main equations of motion. However, through manipulation, it is seen that due to applied bending moment of the eccentric sleeves, all the motions (apart from the axial) are coupled through the weak boundary conditions, Equations (3.56a-f).

It is shown, through numerical simulations, that the natural frequencies of the shaft are only be affected by the mass and inertia of the sleeve and that sleeve stiffness has no impact. Therefore the presented model neglects the potential energy and therefore the stiffness of the sleeves. Hence, the impact of sleeve stiffness on the natural frequencies of the shaft cannot be observed. The use of more complex computational models and experimental data will therefore test the validity of this assumption for modelling the eccentric sleeves.

3.10 Conclusions

The equations of motion of an elastic shaft are derived with the associated dynamic boundary conditions due to the existence of eccentric sleeves and torsional springs. In the case of non-constant rotating speed, the equations of motion form a nonlinear system of partial differential equations. In the case of constant rotating speed, then the lateral bending vibrations are coupled together by Coriolis forces and with the torsional motion through the boundary conditions. Preliminary numerical simulations are used to validate the approach of considering the sleeves as rigid bodies in deriving the equations of motion; having less than 1% difference in the determination of the critical speeds in the specific case considered

Chapter 4 Dynamic Analysis of a Rotating Shaft with Eccentric Sleeves

4.1 Summary

Here, the equations of motion of a simplified rotating shaft with rigid body eccentric sleeves are discretised using the Galerkin technique. Manipulation of system matrices allow modal analysis to be conducted and the theoretical natural frequencies of the system to be obtained. For comparison purposes, a three-dimensional finite element model of the full shaft-sleeve geometry is created. Through use of Campbell diagrams, the critical speeds for both models are obtained for four practical cases viz. a shaft with no sleeve, and short, medium and long sleeves. When considering the relative difference in shaft critical speeds as the sleeve length is changed, a discrepancy between the two approaches is observed. Modifications to the finite element model to remove the sleeve flexibility but leave the mass/inertia produces results much similar to the theoretical model. Sleeve flexibility is therefore found to have a greater than anticipated effect upon the critical speeds of the shaft. Furthermore, sleeve flexibility has progressively more impact as sleeve length increases.

4.2 Chapter Highlights

- Equations of motion discretised and system matrices assembled
- Finite element model of full geometry created
- Results from the two compared – sleeve flexibility found to be important factor in passively controlling shaft critical speeds

4.3 Introduction

When employing relatively basic analytical models it is often possible to find exact, closed form solutions. However, for more complicated models, in particular those cases containing partial differential equations, such as when considering the vibration of continuous systems containing spatial and time dependent components, approximate methods are often required.

To obtain an approximate solution for a continuous system it is often desirable to discretise the model into a finite number of elements. Each element possesses a simplified algebraic equation representing that particular subdivision of the entire continuum. The summation of these equations gives an approximation of the entire system that can then be solved numerically. Using a higher number of elements generally increases the accuracy of the solution at the expense of computation complexity and overhead.

The process of obtaining an approximated solution for a complex problem through discretisation, regardless of the specific technique used, is commonly referred to as the finite element method (FEM). Considerable research has given rise to a familiar and relatively standardised procedure for applying the FEM [93]:

1. *Divide the structure into discrete elements*
2. *Select a displacement function*
3. *Derive element matrices*
4. *Assemble system matrices*
5. *Obtain solution*

Commonly used methods of discretisation are the variational approach and method of weighted residuals. The Rayleigh-Ritz method is a variational tool that uses the principle of minimum energy to find an admissible function that approximates the displacements of the region of interest. The accuracy of the solution is determined by the suitability of the chosen displacement function to satisfy the differential equations of the continuum.

The method of weighted residuals uses the differential equation and the boundary conditions of the problem to obtain a solution. A weighted residual is applied to the differential equation and a solution is obtained where the error between the approximation and the differential

equation approaches zero: the integral of the residual is zero. The method uses trial functions to determine an approximate solution that, on average, satisfies the differential equations over the region of interest. However, the selected functions must also satisfy the boundary conditions of the problem. The Galerkin method is a commonly employed technique that uses a weighted residual that is equal to the selected trial function.

Once the system is discretised, the elements are connected via nodes. The combined structure of elements and nodes being known as a mesh. To determine the relative nodal displacements, (displacement) functions are applied to interpolate the displacements within the elements. The type of geometry under consideration affects the type of element and the complexity of the displacement functions that can be used. For instance, a one-dimensional problem can be solved with a bar element that uses a linear shape function. More complicated geometries require the use of elements with complex displacement interpolations in two (beam element) or three (solid element) dimensions. Nandi [94] showed how using 3D solid elements offered improved prediction of rotor critical speeds and responses than existing analytical and 2D methods. This was due to the capability of the elements to model complex geometry.

Finite element analysis (FEA) now commonly refers to the use of computer packages and computational solvers that allow FEMs to be applied to a broad range of engineering problems including; structural mechanics, heat transfer, transient situations, nonlinearities and electromagnetics. As discussed in Chapter 2, section 3, rotating structures are subjected to gyroscopic loads which are not present in static structures. Therefore analysis techniques must account for these to yield a fully representative and accurate solution. Ruffini [95] conducted a review of existing finite element software packages and considered the effectiveness of capturing the full range of gyroscopic loads that occur in rotating structures. All packages were found to account for gyroscopic motions but discrepancies arise at high speeds, where gyroscopic forces are greater, and in the vicinity of instabilities.

Here it is used to conduct modal analysis to obtain the natural frequencies of rotating shaft a rotating shaft with attached eccentric sleeves.

4.4 Theoretical Model

Chapter 3 derived the equations of motion of a rotating shaft that incorporated the effects of the eccentric sleeves as dynamic boundary conditions (Chapter 3, Section 8, Equations (3.50) to (3.56)). The model used a rotating coordinate system to analyse the simplified shaft geometry with approximate cross-sectional areas and uniform material properties. Due to the complex geometry of the eccentric sleeves, only their kinetic energy contribution is considered in the model. Nonlinear terms arising from the derivation are neglected as a result of displacements being considered to be sufficiently small. In this case, the terms for non-constant rotating speed are also neglected. Therefore any comparative analysis, either computational or experimental, is undertaken at steady state speeds.

4.4.1 Discretisation of Equations of Motion

The equations of motion are discretised in space and the system matrices are formulated using the Galerkin method. In this instance, the Galerkin method gives a good approximation of the equations of motion and it is possible to find suitable functions that satisfy the boundary conditions. Moreover, it requires a relatively small number of terms to obtain a convergent solution. Using the Galerkin method, discretisation of the equations of motion is achieved using the following steps:

1. Integrate the main equations over the length of the shaft
 - a. Symmetrise the terms by integration by parts
 - b. Combine the BCs and main equations
2. Apply the displacement functions and solutions
3. Formulate system matrices

Using the Galerkin method, the general form of the mass (m_{ij}) and stiffness (k_{ij}) matrices is given in Equations (4.1) and (4.2) [96]:

$$m_{ij} = \int_0^L m \tilde{\Phi}_i(x) \tilde{\Phi}_j(x) dx \quad (4.1)$$

$$k_{ij} = \int_0^L \tilde{\Phi}_i(x) L \tilde{\Phi}_j(x) dx \quad (4.2)$$

In this case the trial functions $\tilde{\Phi}_i$ and $\tilde{\Phi}_j$ are spatial functions; $Y_i(x)$, $Y_j(x)$, $Z_i(x)$, $Z_j(x)$ and $\Phi_i(x)$, corresponding to y and z plane bending and torsional displacements, respectively. Approximate displacement functions for these are given in Equations (4.3) to (4.5). They contain a spatial and a time component along with corresponding eigenvectors $\{\bar{\mathbf{v}}_i\}$ [97].

$$v(x, t) = \sum_{i=1}^N Y_i(x) q_v(t) \{\bar{\mathbf{v}}_i\} \quad (4.3)$$

$$w(x, t) = \sum_{i=1}^N Z_i(x) q_w(t) \{\bar{\mathbf{v}}_i\} \quad (4.4)$$

$$\phi(x, t) = \sum_{i=1}^N \Phi_i(x) q_\phi(t) \{\bar{\mathbf{v}}_i\} \quad (4.5)$$

Approximate solutions for the displacement functions can be of the form $\sin \frac{i\pi x}{L}$ or $\cos \frac{i\pi x}{L}$ [89]. To achieve a solution, the selected function must satisfy the strong boundary conditions in Equation (3.55).

y plane lateral bending ($v/Y_i(x)/Y_j(x)$)

Strong BCs:

$$v(0, t) = v(L, t) = 0$$

Using $\sin \frac{i\pi x}{L}$:

$$Y_i(0) = \sin 0 = 0$$

$$Y_i(L) = \sin \pi = 0$$

$$\text{Therefore } \sin \frac{i\pi x}{L} \text{ is suitable for } Y_i(x)/Y_j(x) \quad (4.6)$$

z plane lateral bending ($w/Z_i(x)/Z_j(x)$)**Strong BCs:**

$$w(0, t) = w(L, t) = 0$$

Using $\sin \frac{i\pi x}{L}$:

$$Z_i(0) = \sin 0 = 0$$

$$Z_i(L) = \sin \pi = 0$$

$$\text{Therefore } \sin \frac{i\pi x}{L} \text{ is suitable for } Z_i(x)/Z_j(x) \quad (4.7)$$

Torsional motion ($\Phi/\Phi_i(x)/\Phi_j(x)$)

No strong boundary conditions from physical shaft, therefore the weak boundary conditions must be considered from the formulation:

$$\pm GI\phi' = 0$$

From Equation (3.71) $\phi' = 0$, requiring:

$$\phi'(0) = 0 = \sin 0$$

$$\phi'(L) = 0 = \sin \pi$$

Through integration:

$$\phi(0) = \cos 0$$

$$\phi(L) = \cos \pi$$

$$\text{Therefore, } \Phi_i(x) \text{ must be in the form of } \cos \frac{i\pi x}{L} \quad (4.8)$$

4.4.2 Preparation of Equations for y-plane Lateral Bending

To integrate the main equation for y-plane lateral bending and include the boundary conditions, Equation (3.51) is multiplied by functions $Y_j(x)$, $Z_j(x)$ and integrated over the length of the shaft. If the displacements and trial functions are non-symmetrical (the derivatives of the displacements and the spatial functions are not equal), then the terms are symmetrised using integration by parts:

$$\begin{aligned} \dot{\theta}^2 m_0 \int_0^L v Y_j(x) dx + 2\dot{\theta} m_0 \int_0^L \dot{w} Z_j(x) dx - m_0 \int_0^L \ddot{v} Y_j(x) dx + \rho I \int_0^L \ddot{v}'' Y_j(x) dx \\ - EI \int_0^L v'''' Y_j(x) dx = 0 \end{aligned} \quad (4.9)$$

The terms $\rho I \int_0^L \ddot{v}'' Y_j(x) dx$ and $-EI \int_0^L v'''' Y_j(x) dx$ in Equation (4.9) are non-symmetrical and require integration by parts.

$\rho I \int_0^L \ddot{v}'' Y_j(x) dx$ is integrated by parts once:

$$= [\rho I \dot{v}' Y_j(x)]_{x=0}^{x=L} - \rho I \int_0^L \dot{v}' Y_j'(x) dx$$

Applying the strong BCs from Equation (3.55):

$$\rho I \int_0^L \ddot{v}'' Y_j(x) dx = -\rho I \int_0^L \dot{v}' Y_j'(x) dx \quad (4.10)$$

$-EI \int_0^L v'''' Y_j(x) dx$ is integrated by parts twice:

$$\begin{aligned} &= -[EI v'''' Y_j(x)]_{x=0}^{x=L} + EI \int_0^L v'''' Y_j'(x) dx \\ &= -[EI v'''' Y_j(x)]_{x=0}^{x=L} + [EI v'''' Y_j'(x)]_{x=0}^{x=L} - EI \int_0^L v'''' Y_j''(x) dx \end{aligned}$$

Applying the strong BCs from Equation (3.55):

$$-EI \int_0^L v'''' Y_j(x) dx = [EI v'' Y_j'(x)]_{x=0}^{x=L} - EI \int_0^L v'' Y_j''(x) dx \quad (4.11)$$

Rearranging the weak boundary condition equations to allow for inclusion in the main equation:

$$\begin{aligned} v''(0) = \frac{1}{EI} & \left(\dot{\theta}^2 \left(-I_{xx} v'(0, t) + I_{xy} + I_{xz} \phi(0, t) \right) \right. \\ & - 2\dot{\theta} \left(I_{xx} \dot{w}'(0, t) + I_{xy} \dot{\phi}(0, t) \right) + I_{yy} \ddot{v}'(0, t) + I_{yz} \ddot{w}'(0, t) \\ & \left. + I_{xx} \ddot{v}'(0, t) - I_{xz} \ddot{\phi}(0, t) + kv'(0, t) \right) \end{aligned} \quad (4.12)$$

$$\begin{aligned} v''(L) = -\frac{1}{EI} & \left(\dot{\theta}^2 \left(-I_{xx} v'(L, t) - I_{xy} - I_{xz} \phi(L, t) \right) \right. \\ & - 2\dot{\theta} \left(I_{xx} \dot{w}'(L, t) - I_{xy} \dot{\phi}(L, t) \right) + I_{yy} \ddot{v}'(L, t) + I_{yz} \ddot{w}'(L, t) \\ & \left. + I_{xx} \ddot{v}'(L, t) + I_{xz} \ddot{\phi}(L, t) + kv'(L, t) \right) \end{aligned} \quad (4.13)$$

Combining (4.10) through (4.13):

$$\begin{aligned} & \left(\dot{\theta}^2 m_0 \int_0^L v Y_j(x) dx + 2\dot{\theta} m_0 \int_0^L \dot{w} Z_j(x) dx - m_0 \int_0^L \ddot{v} Y_j(x) dx \right. \\ & \quad \left. - \rho I \int_0^L \ddot{v}' Y_j'(x) dx - EI \int_0^L v'' Y_j''(x) dx \right. \\ & \quad \left. - Y_j'(L) \begin{pmatrix} \dot{\theta}^2 \left(-I_{xx} v'(L, t) - I_{xy} - I_{xz} \phi(L, t) \right) \\ -2\dot{\theta} \left(I_{xx} \dot{w}'(L, t) - I_{xy} \dot{\phi}(L, t) \right) \\ + I_{yy} \ddot{v}'(L, t) + I_{yz} \ddot{w}'(L, t) + I_{xx} \ddot{v}'(L, t) \\ + I_{xz} \ddot{\phi}(L, t) + kv'(L, t) \end{pmatrix} \right. \\ & \quad \left. - Y_j'(0) \begin{pmatrix} \dot{\theta}^2 \left(-I_{xx} v'(0, t) + I_{xy} + I_{xz} \phi(0, t) \right) \\ -2\dot{\theta} \left(I_{xx} \dot{w}'(0, t) + I_{xy} \dot{\phi}(0, t) \right) \\ + I_{yy} \ddot{v}'(0, t) + I_{yz} \ddot{w}'(0, t) + I_{xx} \ddot{v}'(0, t) \\ - I_{xz} \ddot{\phi}(0, t) + kv'(0, t) \end{pmatrix} \right) = 0 \end{aligned} \quad (4.14)$$

Application of the displacement function solutions Equations (4.3 through 4.5) into Equation (4.14) gives the final form of the equations for Y plane lateral bending prior to application of the displacement function solutions and arrangement into matrices:

$$\begin{aligned}
& \left(\dot{\theta}^2 m_0 \int_0^L \sum_{i=1}^N Y_i(x) Y_j(x) q_v(t) \{ \bar{v}_i \} dx + 2 \dot{\theta} m_0 \int_0^L \sum_{i=1}^N Z_i(x) Z_j(x) \dot{q}_w(t) \{ \bar{v}_i \} dx \right. \\
& \quad - m_0 \int_0^L \sum_{i=1}^N Y_i(x) Y_j(x) \ddot{q}_v(t) \{ \bar{v}_i \} dx - \rho I \int_0^L \sum_{i=1}^N Y_i'(x) Y_j'(x) \ddot{q}_v(t) \{ \bar{v}_i \} dx \\
& \quad \quad \quad \left. - EI \int_0^L \sum_{i=1}^N Y_i''(x) Y_j''(x) q_v(t) \{ \bar{v}_i \} \right. \\
- Y_j'(L) & \left. \begin{array}{l} \left(-\dot{\theta}^2 \left(I_{xx} \sum_{i=1}^N Y_i'(L) q_v(t) \{ \bar{v}_i \} + I_{xy} - I_{xz} \sum_{i=1}^N \Phi_i(L) q_\phi(t) \{ \bar{v}_i \} \right) \right) \\ \left(-2 \dot{\theta} \left(I_{xx} \sum_{i=1}^N Z_i'(L) \dot{q}_w(t) \{ \bar{v}_i \} - I_{xy} \sum_{i=1}^N \Phi_i(L) \dot{q}_\phi(t) \{ \bar{v}_i \} \right) \right) \\ + I_{yy} \sum_{i=1}^N Y_i'(L) \ddot{q}_v(t) \{ \bar{v}_i \} + I_{yz} \sum_{i=1}^N Z_i'(L) \ddot{q}_w(t) \{ \bar{v}_i \} \\ + I_{xx} \sum_{i=1}^N Y_i'(L) \ddot{q}_v(t) \{ \bar{v}_i \} + I_{xz} \sum_{i=1}^N \Phi_i(L) \ddot{q}_\phi(t) \{ \bar{v}_i \} \\ + k \sum_{i=1}^N Y_i'(L) q_v(t) \{ \bar{v}_i \} \end{array} \right) \\
- Y_j'(0) & \left. \begin{array}{l} \left(-\dot{\theta}^2 \left(I_{xx} \sum_{i=1}^N Y_i'(0) q_v(t) \{ \bar{v}_i \} - I_{xy} + I_{xz} \sum_{i=1}^N \Phi_i(0) q_\phi(t) \{ \bar{v}_i \} \right) \right) \\ \left(-2 \dot{\theta} \left(I_{xx} \sum_{i=1}^N Z_i'(0) \dot{q}_w(t) \{ \bar{v}_i \} + I_{xy} \sum_{i=1}^N \Phi_i(0) \dot{q}_\phi(t) \{ \bar{v}_i \} \right) \right) \\ + I_{yy} \sum_{i=1}^N Y_i'(0) \ddot{q}_v(t) \{ \bar{v}_i \} + I_{yz} \sum_{i=1}^N Z_i'(0) \ddot{q}_w(t) \{ \bar{v}_i \} \\ + I_{xx} \sum_{i=1}^N Y_i'(0) \ddot{q}_v(t) \{ \bar{v}_i \} - I_{xz} \sum_{i=1}^N \Phi_i(0) \ddot{q}_\phi(t) \{ \bar{v}_i \} \\ + k \sum_{i=1}^N Y_i'(0) q_v(t) \{ \bar{v}_i \} \end{array} \right) = 0
\end{aligned} \tag{4.15}$$

4.4.3 Preparation of Equations for z-Plane Lateral Bending

Equation (3.52) is multiplied by $Y_j(x)$, $Z_j(x)$ and integrated over the length of the shaft:

$$\begin{aligned} \dot{\theta}^2 m_0 \int_0^L w Z_j(x) dx - 2\dot{\theta} m_0 \int_0^L \dot{v} Y_j(x) dx - m_0 \int_0^L \ddot{w} Z_j(x) dx + \rho I \int_0^L \ddot{w}'' Z_j(x) dx \\ - EI \int_0^L w'''' Z_j(x) dx = 0 \end{aligned} \quad (4.16)$$

The terms $\rho I \int_0^L \ddot{w}'' Z_j(x) dx$ and $-EI \int_0^L w'''' Z_j(x) dx$ in Equation (4.16) are non-symmetrical and require integration by parts:

$\rho I \int_0^L \ddot{w}'' Z_j(x) dx$ integrated by parts once:

$$= [\rho I \dot{w}' Z_j(x)]_{x=0}^{x=L} - \rho I \int_0^L \dot{w}' Z_j'(x) dx$$

Applying the strong BCs from Equation (3.55):

$$\rho I \int_0^L \ddot{w}'' Z_j(x) dx = -\rho I \int_0^L \dot{w}' Z_j'(x) dx \quad (4.17)$$

$-EI \int_0^L w'''' Z_j(x) dx$ integrated by parts twice:

$$\begin{aligned} = -[EI w'''' Z_j(x)]_{x=0}^{x=L} + EI \int_0^L w'''' Z_j'(x) dx \\ = -[EI w'''' Z_j(x)]_{x=0}^{x=L} + [EI w'' Z_j'(x)]_{x=0}^{x=L} - EI \int_0^L w'' Z_j''(x) dx \end{aligned}$$

Applying the strong BCs from Equation (3.55):

$$-EI \int_0^L w'''' Z_j(x) dx = [EI w'' Z_j'(x)]_{x=0}^{x=L} - EI \int_0^L w'' Z_j''(x) dx \quad (4.18)$$

Rearranging the weak boundary condition equations to allow for inclusion in the main equation:

$$\begin{aligned}
w''(0) = \frac{1}{EI} & \left(\dot{\theta}^2 (-I_{xx}w'(0,t) - I_{xy}\phi(0,t) + I_{xz}) \right. \\
& - 2\dot{\theta} \left(-I_{xx}\dot{v}'(0,t) + I_{xz}\dot{\phi}(0,t) \right) + I_{yz}\ddot{v}'(0,t) + I_{zz}\ddot{w}'(0,t) \\
& \left. + I_{xx}\ddot{w}'(0,t) + I_{xy}\ddot{\phi}(0,t) + kw'(0,t) \right) \quad (4.19)
\end{aligned}$$

$$\begin{aligned}
w''(L) = -\frac{1}{EI} & \left(\dot{\theta}^2 (-I_{xx}w'(L,t) + I_{xy}\phi(L,t) - I_{xz}) \right. \\
& - 2\dot{\theta} \left(-I_{xx}\dot{v}'(L,t) - I_{xz}\dot{\phi}(L,t) \right) + I_{yz}\ddot{v}'(L,t) + I_{zz}\ddot{w}'(L,t) \\
& \left. + I_{xx}\ddot{w}'(L,t) - I_{xy}\ddot{\phi}(L,t) + kw'(L,t) \right) \quad (4.20)
\end{aligned}$$

Combining Equations (4.17) through (4.20):

$$\begin{aligned}
& \left(\dot{\theta}^2 m_0 \int_0^L w Z_j(x) dx - 2\dot{\theta} m_0 \int_0^L \dot{v} Y_j(x) dx - m_0 \int_0^L \ddot{w} Z_j(x) dx \right. \\
& \quad \left. - \rho I \int_0^L \ddot{w}' Z_j'(x) dx - EI \int_0^L w'' Z_j''(x) dx \right. \\
& \quad \left. - Z_j'(L) \begin{pmatrix} \dot{\theta}^2 (-I_{xx}w'(L,t) - I_{xz} + I_{xy}\phi(L,t)) \\ -2\dot{\theta} (-I_{xx}\dot{v}'(L,t) - I_{xz}\dot{\phi}(L,t)) \\ + I_{yz}\ddot{v}'(L,t) + I_{zz}\ddot{w}'(L,t) + I_{xx}\ddot{w}'(L,t) \\ -I_{xy}\ddot{\phi}(L,t) + kw'(L,t) \end{pmatrix} \right) \\
& \quad \left. - Z_j'(0) \begin{pmatrix} \dot{\theta}^2 (-I_{xx}w'(0,t) + I_{xz} - I_{xy}\phi(0,t)) \\ -2\dot{\theta} (-I_{xx}\dot{v}'(0,t) + I_{xz}\dot{\phi}(0,t)) \\ + I_{yz}\ddot{v}'(0,t) + I_{zz}\ddot{w}'(0,t) + I_{xx}\ddot{w}'(0,t) \\ + I_{xy}\ddot{\phi}(0,t) + kw'(0,t) \end{pmatrix} \right) = 0 \quad (4.21)
\end{aligned}$$

Application of the displacement function solutions Equations (4.3 through 4.5) into (4.21) gives the final form of the equations for Z plane lateral bending prior to application of the displacement function solutions and arrangement into matrices:

$$\begin{aligned}
& \left(\dot{\theta}^2 m_0 \int_0^L \sum_{i=1}^N Z_i(x) Z_j(x) q_w(t) \{ \bar{\mathbf{v}}_i \} dx - 2 \dot{\theta} m_0 \int_0^L \sum_{i=1}^N Y_i(x) Y_j(x) \dot{q}_v(t) \{ \bar{\mathbf{v}}_i \} dx \right. \\
& \quad - m_0 \int_0^L \sum_{i=1}^N Z_i(x) Z_j(x) \ddot{q}_w(t) \{ \bar{\mathbf{v}}_i \} dx - \rho I \int_0^L \sum_{i=1}^N Z_i'(x) Z_j'(x) \ddot{q}_w(t) \{ \bar{\mathbf{v}}_i \} dx \\
& \quad \quad \quad \left. - EI \int_0^L \sum_{i=1}^N Z_i''(x) Z_j''(x) q_w(t) \{ \bar{\mathbf{v}}_i \} dx \right) \\
& - Z_j'(L) \left(\begin{aligned} & -\dot{\theta}^2 \left(I_{xx} \sum_{i=1}^N Z_i'(L) q_w(t) \{ \bar{\mathbf{v}}_i \} + I_{xz} + I_{xy} \sum_{i=1}^N \Phi_i(L) q_\phi(t) \{ \bar{\mathbf{v}}_i \} \right) \\ & + 2\dot{\theta} \left(I_{xx} \sum_{i=1}^N Y_i'(L) \dot{q}_v(t) \{ \bar{\mathbf{v}}_i \} + I_{xz} \sum_{i=1}^N \Phi_i(L) \dot{q}_\phi(t) \{ \bar{\mathbf{v}}_i \} \right) \\ & + I_{yz} \sum_{i=1}^N Y_i'(L) \ddot{q}_v(t) \{ \bar{\mathbf{v}}_i \} + I_{zz} \sum_{i=1}^N Z_i'(L) \ddot{q}_w(t) \{ \bar{\mathbf{v}}_i \} \\ & + I_{xx} \sum_{i=1}^N Z_i'(L) \ddot{q}_w(t) \{ \bar{\mathbf{v}}_i \} - I_{xy} \sum_{i=1}^N \Phi_i(L) \ddot{q}_\phi(t) \{ \bar{\mathbf{v}}_i \} \\ & \quad \quad \quad + k \sum_{i=1}^N Z_i'(L) q_w(t) \{ \bar{\mathbf{v}}_i \} \end{aligned} \right) \tag{4.22} \\
& - Z_j'(0) \left(\begin{aligned} & -\dot{\theta}^2 \left(I_{xx} \sum_{i=1}^N Z_i'(0) q_w(t) \{ \bar{\mathbf{v}}_i \} - I_{xz} - I_{xy} \sum_{i=1}^N \Phi_i(0) q_\phi(t) \{ \bar{\mathbf{v}}_i \} \right) \\ & + 2\dot{\theta} \left(I_{xx} \sum_{i=1}^N Y_i'(0) \dot{q}_v(t) \{ \bar{\mathbf{v}}_i \} - I_{xz} \sum_{i=1}^N \Phi_i(0) \dot{q}_\phi(t) \{ \bar{\mathbf{v}}_i \} \right) \\ & + I_{yz} \sum_{i=1}^N Y_i'(0) \ddot{q}_v(t) \{ \bar{\mathbf{v}}_i \} + I_{zz} \sum_{i=1}^N Z_i'(0) \ddot{q}_w(t) \{ \bar{\mathbf{v}}_i \} \\ & + I_{xx} \sum_{i=1}^N Z_i'(0) \ddot{q}_w(t) \{ \bar{\mathbf{v}}_i \} + I_{xy} \sum_{i=1}^N \Phi_i(0) \ddot{q}_\phi(t) \{ \bar{\mathbf{v}}_i \} \\ & \quad \quad \quad + k \sum_{i=1}^N Z_i'(0) q_w(t) \{ \bar{\mathbf{v}}_i \} \end{aligned} \right) = 0
\end{aligned}$$

4.4.4 Preparation of Equations for Torsional Motion

Equation (3.53) is multiplied by functions $\Phi_j(x)$ and integrated over the length of the shaft.

$$\dot{\theta}^2 2\rho I \int_0^L \phi \Phi_j(x) dx - 2\rho I \int_0^L \ddot{\phi} \Phi_j(x) dx + GI \int_0^L \phi'' \Phi_j(x) dx = 0 \quad (4.23)$$

The $GI \int_0^L \phi'' \Phi_j(x) dx$ term in Equation (4.23) is non-symmetrical and requires integration by parts:

$GI \int_0^L \phi'' \Phi_j(x) dx$ integrated by parts once:

$$= [GI \phi' \Phi_j(x)]_{x=0}^{x=L} - GI \int_0^L \phi' \Phi_j'(x) dx$$

There are no strong BCs, therefore those from formulation must be used:

$$GI \int_0^L \phi'' \Phi_j(x) dx = [GI \phi' \Phi_j(x)]_{x=0}^{x=L} - GI \int_0^L \phi' \Phi_j'(x) dx \quad (4.24)$$

Rearranging the weak boundary condition equations to allow for inclusion in the main equation:

$$\begin{aligned} \phi'(0) = & \frac{1}{GI} \left(\dot{\theta}^2 (-I_{xy} w'(0, t) - I_{yy} \phi(0, t) + I_{xz} v'(0, t) - I_{zz} \phi(0, t)) - \right. \\ & 2\dot{\theta} \left(-I_{xy} \dot{v}'(0, t) - I_{xz} \dot{w}'(0, t) \right) + I_{xy} \ddot{w}'(0, t) + I_{yy} \ddot{\phi}(0, t) - I_{xz} \dot{v}'(0, t) + \\ & \left. I_{zz} \ddot{\phi}(0, t) \right) \end{aligned} \quad (4.25)$$

$$\begin{aligned} \phi'(L) = & -\frac{1}{GI} \left(\dot{\theta}^2 \left(I_{xy} w'(L, t) - I_{yy} \phi(L, t) - I_{xz} v'(L, t) - I_{zz} \phi(L, t) \right) - \right. \\ & 2\dot{\theta} \left(I_{xy} \dot{v}'(L, t) + I_{xz} \dot{w}'(L, t) \right) - I_{xy} \ddot{w}'(L, t) + I_{yy} \ddot{\phi}(L, t) + I_{xz} \dot{v}'(L, t) + \\ & \left. I_{zz} \ddot{\phi}(L, t) \right) \end{aligned} \quad (4.26)$$

Combining Equations (4.24) through (4.26):

$$\begin{aligned}
& \left(\dot{\theta}^2 2\rho I \int_0^L \phi \Phi_j(x) dx - 2\rho I \int_0^L \ddot{\phi} \Phi_j(x) dx - GI \int_0^L \phi' \Phi_j'(x) dx \right. \\
& - \Phi_j(L) \left(\begin{array}{c} \dot{\theta}^2 (I_{xy} w'(L, t) - I_{yy} \phi(L, t) - I_{xz} v'(L, t) - I_{zz} \phi(L, t)) \\ -2\dot{\theta} (I_{xy} \dot{v}'(L, t) + I_{xz} \dot{w}'(L, t)) \\ -I_{xy} \ddot{w}'(L, t) + I_{yy} \ddot{\phi}(L, t) + I_{xz} \ddot{v}'(L, t) + I_{zz} \ddot{\phi}(L, t) \end{array} \right) \\
& \left. - \Phi_j(0) \left(\begin{array}{c} \dot{\theta}^2 (-I_{xy} w'(0, t) - I_{yy} \phi(0, t) + I_{xz} v'(0, t) - I_{zz} \phi(0, t)) \\ -2\dot{\theta} (-I_{xy} \dot{v}'(0, t) - I_{xz} \dot{w}'(0, t)) \\ +I_{xy} \ddot{w}'(0, t) + I_{yy} \ddot{\phi}(0, t) - I_{xz} \ddot{v}'(0, t) + I_{zz} \ddot{\phi}(0, t) \end{array} \right) \right) = 0
\end{aligned} \tag{4.27}$$

Application of the displacement function solutions Equations (4.3 through 4.5) into (4.27) gives the final form of the equations for torsional displacements prior to application of the displacement function solutions and arrangement into matrices:

$$\begin{aligned}
& \left(\dot{\theta}^2 2\rho I \int_0^L \sum_{i=1}^N \Phi_i(x) \Phi_j(x) q_\phi(t) \{\bar{\mathbf{v}}_i\} dx - 2\rho I \int_0^L \sum_{i=1}^N \Phi_i(x) \Phi_j(x) \ddot{q}_\phi(t) \{\bar{\mathbf{v}}_i\} dx \right. \\
& \quad \left. - GI \int_0^L \Phi_i'(x) \Phi_j'(x) q_\phi(t) \{\bar{\mathbf{v}}_i\} dx \right. \\
& - \Phi_j(L) \left(\begin{array}{c} \dot{\theta}^2 \left(\begin{array}{c} I_{xy} \sum_{i=1}^N Z_i'(L) q_w(t) \{\bar{\mathbf{v}}_i\} - I_{yy} \sum_{i=1}^N \Phi_i(L) q_\phi(t) \{\bar{\mathbf{v}}_i\} \\ -I_{xz} \sum_{i=1}^N Y_i'(L) q_v(t) \{\bar{\mathbf{v}}_i\} - I_{zz} \sum_{i=1}^N \Phi_i(L) q_\phi(t) \{\bar{\mathbf{v}}_i\} \end{array} \right) \\ -2\dot{\theta} \left(\begin{array}{c} I_{xy} \sum_{i=1}^N Y_i'(L) \dot{q}_v(t) \{\bar{\mathbf{v}}_i\} + I_{xz} \sum_{i=1}^N Z_i'(L) \dot{q}_w(t) \{\bar{\mathbf{v}}_i\} \\ -I_{xy} \sum_{i=1}^N Z_i'(L) \ddot{q}_w(t) \{\bar{\mathbf{v}}_i\} + I_{yy} \sum_{i=1}^N \Phi_i(L) \ddot{q}_\phi(t) \{\bar{\mathbf{v}}_i\} \\ +I_{xz} \sum_{i=1}^N Y_i'(L) \ddot{q}_v(t) \{\bar{\mathbf{v}}_i\} + I_{zz} \sum_{i=1}^N \Phi_i(L) \ddot{q}_\phi(t) \{\bar{\mathbf{v}}_i\} \end{array} \right) \end{array} \right) \\
& \left. \right) = 0
\end{aligned} \tag{4.28}$$

$$-\Phi_j(0) \left(\begin{array}{c} \hat{\theta}^2 \left(\begin{array}{c} -I_{xy} \sum_{i=1}^N Z_i'(0) q_w(t) \{\bar{\mathbf{v}}_i\} - I_{yy} \sum_{i=1}^N \Phi_i(0) q_\phi(t) \{\bar{\mathbf{v}}_i\} \\ + I_{xz} \sum_{i=1}^N Y_i'(0) q_v(t) \{\bar{\mathbf{v}}_i\} - I_{zz} \sum_{i=1}^N \Phi_i(0) q_\phi(t) \{\bar{\mathbf{v}}_i\} \end{array} \right) \\ -2\hat{\theta} \left(\begin{array}{c} -I_{xy} \sum_{i=1}^N Y_i'(0) \dot{q}_v(t) \{\bar{\mathbf{v}}_i\} - I_{xz} \sum_{i=1}^N Z_i'(0) \dot{q}_w(t) \{\bar{\mathbf{v}}_i\} \\ + I_{xy} \sum_{i=1}^N Z_i'(0) \ddot{q}_w(t) \{\bar{\mathbf{v}}_i\} + I_{yy} \sum_{i=1}^N \Phi_i(0) \ddot{q}_\phi(t) \{\bar{\mathbf{v}}_i\} \\ - I_{xz} \sum_{i=1}^N Y_i'(0) \ddot{q}_v(t) \{\bar{\mathbf{v}}_i\} + I_{zz} \sum_{i=1}^N \Phi_i(0) \ddot{q}_\phi(t) \{\bar{\mathbf{v}}_i\} \end{array} \right) \end{array} \right) = 0 \quad (4.28) \text{ cont.}$$

4.4.5 Summation Matrices

Equations (4.15, 4.22 and 4.28) can be simplified by the substitution of matrices in lieu of the trial functions. The approximate solutions for the displacement functions determined in Section 4.4.1 are applied. Table 4-1 contains the system matrix substitutions $[A_{ij}]$, $[B_{ij}]$, $[C_{ij}]$, $[D_{ij}]$ and $[E_{ij}]$ matrices by summing and integrating along the length of the shaft and $[F_{0ij}]$, $[F_{Lij}]$, $[G_{0ij}]$, $[G_{Lij}]$, $[H_{0ij}]$, $[H_{Lij}]$, $[I_{0ij}]$ and $[I_{Lij}]$ matrices at the shaft ends ($x=0$, $x=L$).

y plane lateral bending (v):

$$\left(\begin{array}{c} (\hat{\theta}^2 m_0 [A_{ij}] \{q_v(t)\} \{\bar{\mathbf{v}}_i\} + 2\hat{\theta} m_0 [A_{ij}] \{\dot{q}_w(t)\} \{\bar{\mathbf{v}}_i\} - m_0 [A_{ij}] \{\ddot{q}_v(t)\} \{\bar{\mathbf{v}}_i\} \\ - \rho I [B_{ij}] \{\ddot{q}_v(t)\} \{\bar{\mathbf{v}}_i\} - EI [C_{ij}] \{q_v(t)\} \{\bar{\mathbf{v}}_i\} \\ - \left(\begin{array}{c} -\hat{\theta}^2 (I_{xx} [F_{Lij}] \{q_v(t)\} \{\bar{\mathbf{v}}_i\} + I_{xy} - I_{xz} [G_{Lij}] \{q_\phi(t)\} \{\bar{\mathbf{v}}_i\}) \\ -2\hat{\theta} (I_{xx} [F_{Lij}] \{\dot{q}_w(t)\} \{\bar{\mathbf{v}}_i\} - I_{xy} [G_{Lij}] \{\dot{q}_\phi(t)\} \{\bar{\mathbf{v}}_i\}) \\ + I_{yy} [F_{Lij}] \{\ddot{q}_v(t)\} \{\bar{\mathbf{v}}_i\} + I_{yz} [F_{Lij}] \{\ddot{q}_w(t)\} \{\bar{\mathbf{v}}_i\} + I_{xx} [F_{Lij}] \{\ddot{q}_v(t)\} \{\bar{\mathbf{v}}_i\} \\ + I_{xz} [G_{Lij}] \{\ddot{q}_\phi(t)\} \{\bar{\mathbf{v}}_i\} + k [F_{Lij}] \{q_v(t)\} \{\bar{\mathbf{v}}_i\} \end{array} \right) \\ - \left(\begin{array}{c} -\hat{\theta}^2 (I_{xx} [F_{0ij}] \{q_v(t)\} \{\bar{\mathbf{v}}_i\} - I_{xy} + I_{xz} [G_{0ij}] \{q_\phi(t)\} \{\bar{\mathbf{v}}_i\}) \\ -2\hat{\theta} (I_{xx} [F_{0ij}] \{\dot{q}_w(t)\} \{\bar{\mathbf{v}}_i\} + I_{xy} [G_{0ij}] \{\dot{q}_\phi(t)\} \{\bar{\mathbf{v}}_i\}) \\ + I_{yy} [F_{0ij}] \{\ddot{q}_v(t)\} \{\bar{\mathbf{v}}_i\} + I_{yz} [F_{0ij}] \{\ddot{q}_w(t)\} \{\bar{\mathbf{v}}_i\} + I_{xx} [F_{0ij}] \{\ddot{q}_v(t)\} \{\bar{\mathbf{v}}_i\} \\ - I_{xz} [G_{0ij}] \{\ddot{q}_\phi(t)\} \{\bar{\mathbf{v}}_i\} + k [F_{0ij}] \{q_v(t)\} \{\bar{\mathbf{v}}_i\} \end{array} \right) \end{array} \right) = 0 \quad (4.29)$$

z plane lateral bending(w):

$$\begin{aligned}
& (\hat{\theta}^2 m_0 [A_{ij}] \{q_w(t)\} \{\bar{\mathbf{v}}_i\} - 2\hat{\theta} m_0 [A_{ij}] \{\dot{q}_v(t)\} \{\bar{\mathbf{v}}_i\} - m_0 [A_{ij}] \{\ddot{q}_w(t)\} \{\bar{\mathbf{v}}_i\} \\
& \quad - \rho I [B_{ij}] \{\ddot{q}_w(t)\} \{\bar{\mathbf{v}}_i\} - EI [C_{ij}] \{q_w(t)\} \{\bar{\mathbf{v}}_i\} \\
& \quad - \left(\begin{array}{c} -\hat{\theta}^2 (I_{xx} [F_{Lij}] \{q_w(t)\} \{\bar{\mathbf{v}}_i\} + I_{xz} + I_{xy} [G_{Lij}] \{q_\phi(t)\} \{\bar{\mathbf{v}}_i\}) \\ + 2\hat{\theta} (I_{xx} [F_{Lij}] \{\dot{q}_v(t)\} \{\bar{\mathbf{v}}_i\} + I_{xz} [G_{Lij}] \{\dot{q}_\phi(t)\} \{\bar{\mathbf{v}}_i\}) \\ + I_{yz} [F_{Lij}] \{\ddot{q}_v(t)\} \{\bar{\mathbf{v}}_i\} + I_{zz} [F_{Lij}] \{\ddot{q}_w(t)\} \{\bar{\mathbf{v}}_i\} + I_{xx} [F_{Lij}] \{\ddot{q}_w(t)\} \{\bar{\mathbf{v}}_i\} \\ - I_{xy} [G_{Lij}] \{\ddot{q}_\phi(t)\} \{\bar{\mathbf{v}}_i\} + k [F_{Lij}] \{q_w(t)\} \{\bar{\mathbf{v}}_i\} \end{array} \right) \\
& \quad - \left(\begin{array}{c} -\hat{\theta}^2 (I_{xx} [F_{0ij}] \{q_w(t)\} \{\bar{\mathbf{v}}_i\} - I_{xz} - I_{xy} [G_{0ij}] \{q_\phi(t)\} \{\bar{\mathbf{v}}_i\}) \\ + 2\hat{\theta} (I_{xx} [F_{0ij}] \dot{q}_v(t) \{\bar{\mathbf{v}}_i\} - I_{xz} [G_{0ij}] \{\dot{q}_\phi(t)\} \{\bar{\mathbf{v}}_i\}) \\ + I_{yz} [F_{0ij}] \{\ddot{q}_v(t)\} \{\bar{\mathbf{v}}_i\} + I_{zz} [F_{0ij}] \{\ddot{q}_w(t)\} \{\bar{\mathbf{v}}_i\} + I_{xx} [F_{0ij}] \{\ddot{q}_w(t)\} \{\bar{\mathbf{v}}_i\} \\ + I_{xy} [G_{0ij}] \{\ddot{q}_\phi(t)\} \{\bar{\mathbf{v}}_i\} + k [F_{0ij}] \{q_v(t)\} \{\bar{\mathbf{v}}_i\} \end{array} \right) = 0
\end{aligned} \tag{4.30}$$

Torsional Motion(φ):

$$\begin{aligned}
& (\hat{\theta}^2 2\rho I [D_{ij}] \{q_\phi(t)\} \{\bar{\mathbf{v}}_i\} - 2\rho I [D_{ij}] \{\ddot{q}_\phi(t)\} \{\bar{\mathbf{v}}_i\} - GI [E_{ij}] \{q_\phi(t)\} \{\bar{\mathbf{v}}_i\} \\
& \quad - \left(\begin{array}{c} \hat{\theta}^2 (I_{xy} [H_{Lij}] \{q_w(t)\} \{\bar{\mathbf{v}}_i\} - I_{yy} [I_{Lij}] \{q_\phi(t)\} \{\bar{\mathbf{v}}_i\}) \\ - I_{xz} [H_{Lij}] \{q_v(t)\} \{\bar{\mathbf{v}}_i\} - I_{zz} [I_{Lij}] \{q_\phi(t)\} \{\bar{\mathbf{v}}_i\} \\ - 2\hat{\theta} (I_{xy} [H_{Lij}] \{\dot{q}_v(t)\} \{\bar{\mathbf{v}}_i\} + I_{xz} [H_{Lij}] \{\dot{q}_w(t)\} \{\bar{\mathbf{v}}_i\}) \\ - I_{xy} [H_{Lij}] \{\ddot{q}_w(t)\} \{\bar{\mathbf{v}}_i\} + I_{yy} [I_{Lij}] \{\ddot{q}_\phi\} \{\bar{\mathbf{v}}_i\} \\ + I_{xz} [H_{Lij}] \{\ddot{q}_v(t)\} \{\bar{\mathbf{v}}_i\} + I_{zz} [I_{Lij}] \{\ddot{q}_\phi\} \{\bar{\mathbf{v}}_i\} \end{array} \right) \\
& \quad - \left(\begin{array}{c} \hat{\theta}^2 (-I_{xy} [H_{0ij}] \{q_w(t)\} \{\bar{\mathbf{v}}_i\} - I_{yy} [I_{0ij}] \{q_\phi(t)\} \{\bar{\mathbf{v}}_i\}) \\ + I_{xz} [H_{0ij}] \{q_v(t)\} \{\bar{\mathbf{v}}_i\} - I_{zz} [I_{0ij}] \{q_\phi(t)\} \{\bar{\mathbf{v}}_i\} \\ - 2\hat{\theta} (-I_{xy} [H_{0ij}] \{\dot{q}_v(t)\} \{\bar{\mathbf{v}}_i\} - I_{xz} [H_{0ij}] \{\dot{q}_w(t)\} \{\bar{\mathbf{v}}_i\}) \\ + I_{xy} [H_{0ij}] \{\ddot{q}_w(t)\} \{\bar{\mathbf{v}}_i\} + I_{yy} [I_{0ij}] \{\ddot{q}_\phi\} \{\bar{\mathbf{v}}_i\} \\ - I_{xz} [H_{0ij}] \{\ddot{q}_v(t)\} \{\bar{\mathbf{v}}_i\} + I_{zz} [I_{0ij}] \{\ddot{q}_\phi\} \{\bar{\mathbf{v}}_i\} \end{array} \right) = 0
\end{aligned} \tag{4.31}$$

Table 4-1 – Summation matrix substations

MAIN EQUATIONS			
MATRIX	VALID TERMS	ELEMENTS	VALUE
[A _{ij}]	$\int_0^L \sum_{i=1}^N Y_i(x)Y_j(x)dx$	i = j (Diagonal)	$\frac{L}{2}$
	$\int_0^L \sum_{i=1}^N Z_i(x)Z_j(x)dx$	i ≠ j (Off diagonal)	0
[B _{ij}]	$\int_0^L \sum_{i=1}^N Y_i'(x)Y_j'(x)dx$	i = j	$\frac{ij\pi^2}{2L}$
	$\int_0^L \sum_{i=1}^N Z_i'(x)Z_j'(x)dx$	i ≠ j	0
[C _{ij}]	$\int_0^L \sum_{i=1}^N Y_i''(x)Y_j''(x)dx$	i = j	$\frac{i^2j^2\pi^4}{2L^3}$
	$\int_0^L \sum_{i=1}^N Z_i''(x)Z_j''(x)dx$	i ≠ j	0
[D _{ij}]	$\int_0^L \sum_{i=1}^N \Phi_i(x)\Phi_j(x)dx$	i = j	$\frac{L}{2}$
		i ≠ j	0
[E _{ij}]	$\int_0^L \sum_{i=1}^N \Phi_i'(x)\Phi_j'(x)dx$	i = j	$\frac{ij\pi^2}{2L}$
		i ≠ j	0

BOUNDARY CONDITIONS			
MATRIX	VALID TERMS	ELEMENTS	VALUE
$[F_{0ij}]$	$\sum_{i=1}^N Y_i'(0)Y_j'(0)$	ALL	$\frac{ij\pi^2}{L^2}$
	$\sum_{i=1}^N Z_i'(0)Z_j'(0)$		
	$\sum_{i=1}^N Z_i'(0)Y_j'(0)$		
	$\sum_{i=1}^N Y_i'(0)Z_j'(0)$		
$[F_{Lij}]$	$\sum_{i=1}^N Y_i'(L)Y_j'(L)$	$i = j$	$\frac{ij\pi^2}{L^2}$
	$\sum_{i=1}^N Z_i'(L)Z_j'(L)$	$i \neq j$	$\cos i\pi \cos j\pi \left(\frac{ij\pi^2}{L^2}\right)$
	$\sum_{i=1}^N Z_i'(L)Y_j'(L)$		
	$\sum_{i=1}^N Y_i'(L)Z_j'(L)$		
$[G_{0ij}]$	$\sum_{i=1}^N \Phi_i(0)Y_j'(0)$	ALL	$\frac{j\pi}{L}$
	$\sum_{i=1}^N \Phi_i(0)Z_j'(0)$		
$[G_{Lij}]$	$\sum_{i=1}^N \Phi_i(L)Y_j'(L)$	ALL	$\cos i\pi \cos j\pi \left(\frac{j\pi}{L}\right)$
	$\sum_{i=1}^N \Phi_i(L)Z_j'(L)$		
$[H_{0ij}]$	$\sum_{i=1}^N Y_i'(0)\Phi_j(0)$	ALL	$\frac{i\pi}{L}$
	$\sum_{i=1}^N Z_i'(0)\Phi_j(0)$		

MATRIX	VALID TERMS	ELEMENTS	VALUE
$[H_{Lij}]$	$\sum_{i=1}^N Y_i'(L)\Phi_j(L)$	ALL	$\cos i\pi \cos j\pi \left(\frac{i\pi}{L}\right)$
	$\sum_{i=1}^N Z_i'(L)\Phi_j(L)$		
$[I_{0ij}]$	$\sum_{i=1}^N \Phi_i(0)\Phi_j(0)$	ALL	1
$[L_{ij}]$	$\sum_{i=1}^N \Phi_i(L)\Phi_j(L)$	ALL	$\cos i\pi \cos j\pi$

4.4.6 System Matrices

To calculate the free response of the system, the discretised equations of motion are collated into the form of Equation (4.32). Individual components include the additional matrices due to the influence of the eccentric sleeves and torsional spring effects of the flexible elements.

$$\begin{aligned}
& ([M_{sh}] + [M_{sl}])\{\ddot{q}(t)\} + ([C_{corsh}] + [C_{corsl}])\{\dot{q}(t)\} \\
& + ([K_{sh}] + [K_T] + [K_{centsh}] + [K_{centsl}])\{q(t)\}\{\bar{v}_i\} = 0
\end{aligned} \tag{4.32}$$

$[M_{sh}] = \underline{\text{Shaft Mass Matrix}}$

$$= \begin{bmatrix} -m_0[A_{ij}] - \rho I[B_{ij}] & 0 & 0 \\ 0 & -m_0[A_{ij}] - \rho I[B_{ij}] & 0 \\ 0 & 0 & -2\rho I[D_{ij}] \end{bmatrix} \tag{4.33}$$

$[M_{sl}] = \underline{\text{Sleeve Mass Matrix}}$

$$= - \begin{bmatrix} (I_{yy} + I_{xx})([F_{0ij}] + [F_{Lij}]) & I_{yz}([F_{0ij}] + [F_{Lij}]) & I_{xz}([G_{Lij}] - [G_{0ij}]) \\ I_{yz}([F_{0ij}] + [F_{Lij}]) & (I_{zz} + I_{xx})([F_{0ij}] + [F_{Lij}]) & I_{xy}([G_{0ij}] - [G_{Lij}]) \\ I_{xz}([H_{Lij}] - [H_{0ij}]) & I_{xz}([H_{0ij}] - [H_{Lij}]) & (I_{yy} + I_{zz})([I_{0ij}] + [I_{Lij}]) \end{bmatrix} \tag{4.34}$$

$[\mathbf{C}_{\text{corsh}}] = \underline{\text{Shaft Coriolis Force Matrix}}$

$$= 2\dot{\theta} \begin{bmatrix} 0 & m_0[A_{ij}] & 0 \\ -(m_0[A_{ij}]) & 0 & 0 \\ 0 & 0 & 0 \end{bmatrix} \quad (4.35)$$

$[\mathbf{C}_{\text{corsl}}] = \underline{\text{Sleeve Coriolis Matrix}}$

$$= 2\dot{\theta} \begin{bmatrix} 0 & I_{xx}([F_{Lij}] + [F_{Oij}]) & -I_{xy}([G_{Lij}] - [G_{Oij}]) \\ -(I_{xx}([F_{Lij}] + [F_{Oij}])) & 0 & -I_{xz}([G_{Lij}] - [G_{Oij}]) \\ -I_{xy}([H_{Oij}] - [H_{Lij}]) & -I_{xz}([H_{Oij}] - [H_{Lij}]) & 0 \end{bmatrix} \quad (4.36)$$

$[\mathbf{K}_{\text{sh}}] = \underline{\text{Shaft Stiffness Matrix}}$

$$= \begin{bmatrix} -EI[C_{ij}] & 0 & 0 \\ 0 & -EI[C_{ij}] & 0 \\ 0 & 0 & -GI[E_{ij}] \end{bmatrix} \quad (4.37)$$

$[\mathbf{K}_{\text{T}}] = \underline{\text{Torsional Element Stiffness}}$

$$= \begin{bmatrix} -k([F_{Lij}] + [F_{Oij}]) & 0 & 0 \\ 0 & -k([F_{Lij}] + [F_{Oij}]) & 0 \\ 0 & 0 & 0 \end{bmatrix} \quad (4.38)$$

$[\mathbf{K}_{\text{centsh}}] = \underline{\text{Shaft Centrifugal Force Matrix}}$

$$= \dot{\theta}^2 \begin{bmatrix} m_0[A_{ij}] & 0 & 0 \\ 0 & m_0[A_{ij}] & 0 \\ 0 & 0 & 2\rho I[D_{ij}] \end{bmatrix} \quad (4.39)$$

$[K_{\text{centsl}}] = \underline{\text{Sleeve Centrifugal Force Matrix}}$

$$= \dot{\theta}^2 \begin{bmatrix} I_{xx} ([F_{Lij}] + [F_{0ij}]) & 0 & -I_{xz} ([G_{Lij}] - [G_{0ij}]) \\ 0 & I_{xx} ([F_{Lij}] + [F_{0ij}]) & -I_{xy} ([G_{0ij}] - [G_{Lij}]) \\ -I_{xz} ([H_{0ij}] - [H_{Lij}]) & -I_{xy} ([H_{Lij}] - [H_{0ij}]) & (I_{yy} + I_{zz}) ([I_{0ij}] + [I_{Lij}]) \end{bmatrix} \quad (4.40)$$

$\{q(t)\} = \underline{\text{Displacement Vectors}}$

$$= \begin{Bmatrix} q_v(t) \\ q_w(t) \\ q_\phi(t) \end{Bmatrix} \quad (4.41)$$

$\{\dot{q}(t)\} = \underline{\text{Velocity Vectors}}$

$$= \begin{Bmatrix} \dot{q}_v(t) \\ \dot{q}_w(t) \\ \dot{q}_\phi(t) \end{Bmatrix} \quad (4.42)$$

$\{\ddot{q}(t)\} = \underline{\text{Acceleration Vectors}}$

$$= \begin{Bmatrix} \ddot{q}_v(t) \\ \ddot{q}_w(t) \\ \ddot{q}_\phi(t) \end{Bmatrix} \quad (4.43)$$

4.4.7 Numerical Solution

Modal analysis of the free response of the system is obtained by manipulation of Equation (4.32). In its simplest form, this can be converted into two first order differential equations where M, C and K are the global system mass, stiffness and damping matrices, respectively [3], [96]:

$$\begin{bmatrix} C & M \\ M & 0 \end{bmatrix} \frac{d}{dt} \begin{Bmatrix} q(t) \\ \dot{q}(t) \end{Bmatrix} - \begin{bmatrix} K & 0 \\ 0 & -M \end{bmatrix} \begin{Bmatrix} q(t) \\ \dot{q}(t) \end{Bmatrix} \quad (4.44)$$

MATLAB is used to obtain an Eigenvalue solution for the system at chosen values of rotational velocity, $\dot{\theta}$. The eig command solves Equation (4.45) for ω which is the circular natural frequency of a particular mode.

$$\det[K' - \omega^2 M'] = 0 \quad \text{Where } K' = \begin{bmatrix} C & M \\ M & 0 \end{bmatrix} \text{ and } M' = \begin{bmatrix} K & 0 \\ 0 & -M \end{bmatrix} \quad (4.45)$$

4.4.7.1 Convergence

The number of terms in the Galerkin solution is investigated to provide good convergence without significantly impacting on required computational overhead. Table 4-2 contains the parameters for a shaft, without the eccentric sleeves, used for obtaining results of the convergence study. The parameters are representative of the simplifications made to geometry of a full shaft. The flexible element stiffness is determined by finite element analysis using ANSYS Workbench 17.0.

Table 4-2 – Parameters of simplified shaft

Length	920	mm
Spacer shaft diameter (OD/ID)	62/56	mm
Density	7850	kgm ³
Young's Modulus	200	GPa
Flexible Element Stiffness	1x10 ⁴	N/m
Maximum Speed	12000	rpm

The first three bending modes of the shaft are considered: Modes 1 and 2 are first bending mode, Modes 3 and 4 are second bending mode and Modes 5 and 6 are the third bending modes. Convergence is investigated at zero rotational velocity, i.e. where no gyroscopic effects are observed and a high rotational velocity (12000rpm) where significant gyroscopic effects will be observed. Without gyroscopic effects, the terms of the Coriolis and centrifugal matrices will be zero and the obtained frequencies of the pairs of modes for each bending motion will be identical. However, as rotational speed increases, the gyroscopic effects

become more prevalent and a splitting occurs, resulting in forward and backward modes of different frequencies. In a rotating frame, the natural frequencies of forward modes decrease with increasing rotational velocity and backward modes increase [3].

As a first approximation, natural frequencies are obtained using a truncation of three terms in the system matrices. Without increasing the truncation, it is not possible to attest whether or not the first approximation using three terms provides a converged solution. Therefore, truncation of the system matrices is increased until convergence is observed. Convergence error is measured by the relative difference between the obtained natural frequencies as the number of terms is increased. Convergence is determined to be reached once the convergence error reaches a steady state. Table 4-4 provides the convergence error results for the forward and backward motions of the first three bending modes of the shaft as the number of terms is increased from three to thirty.

To assess the computational efficiency of the model, Table 4-3 gives the computation time for calculation of natural frequencies for the Galerkin solutions using three to thirty terms. Figure 4.1 and Figure 4.2 show the convergence error and computation time for three to thirty terms at 0 and 12000rpm. Using up to nine terms, the increase in computation time is largely linear, resulting in an accurate solution being obtained in a relatively short time. However, once the truncation is increased to greater than ten terms, the increase in computation time becomes exponential.

Table 4-3 – Computation time for 3 to 30 term solutions

No. of Terms	3	5	7	9	11	13	15	20	25	30
Time (s)	0.51	1.50	2.60	7.63	31.66	60.90	105.8	281.5	463.1	664.4

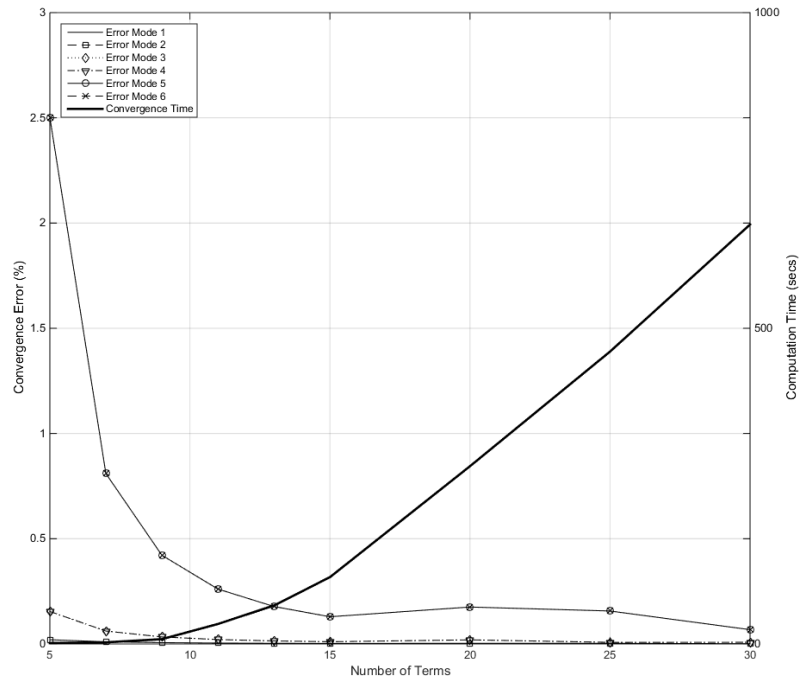


Figure 4.1 – Convergence error and computation time at 0 rpm

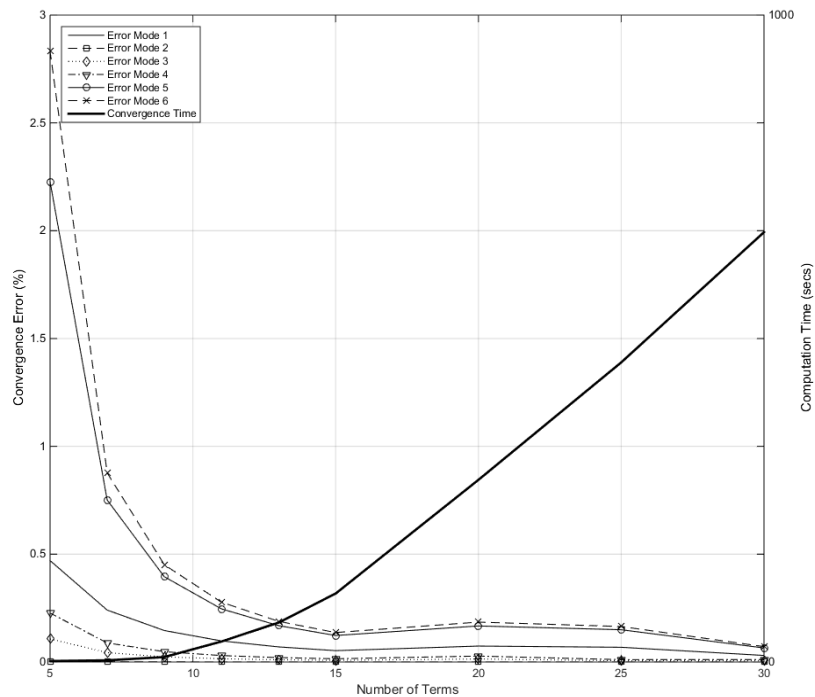


Figure 4.2 – Convergence error and computation time at 12000 rpm

Table 4-4 – Convergence error at 0 and 12000 rpm

No. of Terms	Mode 1	Mode 2	Mode 3	Mode 4	Mode 5	Mode 6
0 rpm						
5	0.020%	0.020%	0.154%	0.154%	2.502%	2.502%
7	0.010%	0.010%	0.062%	0.062%	0.810%	0.810%
9	0.006%	0.006%	0.033%	0.033%	0.422%	0.422%
11	0.004%	0.004%	0.021%	0.021%	0.261%	0.261%
13	0.003%	0.003%	0.015%	0.015%	0.178%	0.178%
15	0.002%	0.002%	0.011%	0.011%	0.129%	0.129%
20	0.003%	0.003%	0.020%	0.020%	0.176%	0.176%
25	0.003%	0.003%	0.008%	0.008%	0.157%	0.157%
30	0.001%	0.001%	0.008%	0.008%	0.068%	0.068%
12000rpm						
5	0.470%	0.003%	0.107%	0.227%	2.227%	2.833%
7	0.241%	0.001%	0.043%	0.088%	0.751%	0.877%
9	0.146%	0.001%	0.024%	0.048%	0.396%	0.451%
11	0.098%	0.001%	0.015%	0.030%	0.246%	0.278%
13	0.070%	0.000%	0.010%	0.021%	0.169%	0.189%
15	0.053%	0.000%	0.008%	0.015%	0.123%	0.137%
20	0.074%	0.000%	0.014%	0.028%	0.167%	0.185%
25	0.068%	0.000%	0.006%	0.011%	0.150%	0.165%
30	0.030%	0.000%	0.006%	0.011%	0.065%	0.071%

From Table 4-4, along with Figure 4.1 and Figure 4.2, the numbers of terms to obtain suitably convergent solutions for each of the bending modes can be identified. At 0 rpm the first bending modes (modes 1 and 2), second bending modes (modes 3 and 4) and third bending modes (modes 5 and 6) show identical convergence errors, due to no gyroscopic effects impacting on the modes. The first bending mode readily converged with five terms, the second bending modes show a slightly larger convergence error with five terms but good convergence with nine, and the third bending mode becomes more consistent with 15 terms but is still considerably greater than the first and second bending modes.

At 12000 rpm, due to considerable gyroscopic effects and splitting of the modes, the pairs of natural frequencies of each bending motion differ, resulting in different convergence errors. The convergence error is particularly high for mode 1 as this is close to a critical speed and the natural frequency of the mode is approaching zero, therefore small changes of critical speed has a large relative effect upon the convergence error. Modes 2 to 4 all show good convergence using 15 terms. Due to the anticipated running speed of the shaft, the third bending mode is not considered as being of importance. Therefore, only converged solutions for the first and second bending modes need to be considered and a maximum of 10 terms is therefore chosen.

4.5 Finite Element Analysis

To assess the validity of the proposed simplified model, a three-dimensional finite element model is developed using ANSYS Workbench 17.0. The full assembly is shown in Figure 4.3 and is a representation of the technical drawing in Appendix D. This shaft conforms to that used later for experimental validation in Chapter 5. The model could be simplified using symmetry, however due to the sleeve geometry, the system is not axisymmetric and has limited symmetry. Furthermore, a full solid model was used to produce the most accurate solution possible and also due to the availability of powerful computational resources.

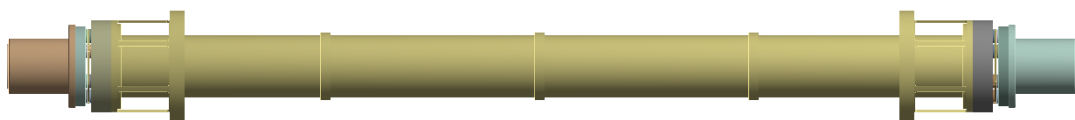


Figure 4.3 – ANSYS shaft geometry

4.5.1 Geometry

The geometry of the full assembly includes 2x hubs, 4x adaptors, 2x flexible element packs, 2x balance sleeves, 1x spacer shaft, 30x bolts and 24 x element/overload washers. Figure 4.4 shows the shaft geometry at one end of the assembly with relevant notation. The following modifications are used to reduce complexity:

- **Bolts removed and replaced with suitable contact regions**

The objective of this is to remove frictional nonlinearities from the analysis. Nonlinearities due to friction occur if the bolts are insufficiently tightened. The bolts in the experimental assembly are tightened to specific torque specifications and unlikely to come loose. Therefore calculating any friction is unnecessary and computationally inefficient.

- **Element washers are left in place**

This provides a link between the flexible elements and adaptors.

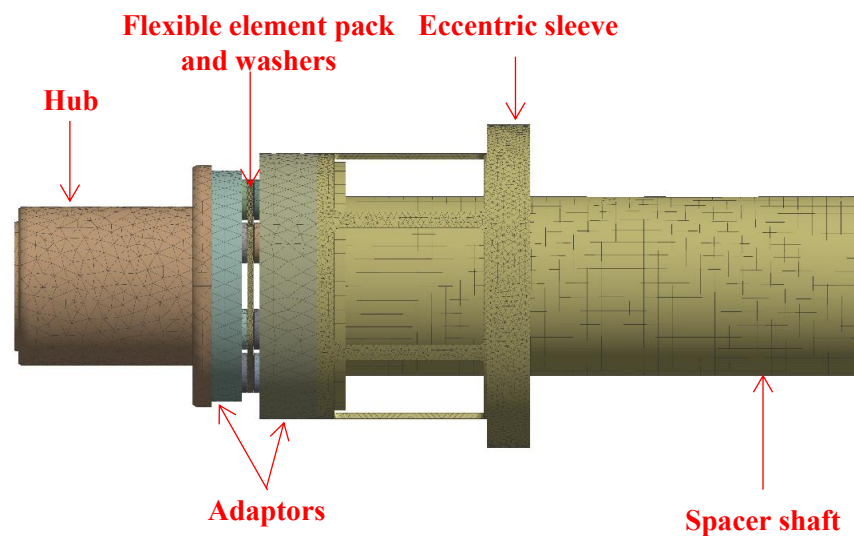


Figure 4.4 – Simplified geometry at shaft end

4.5.2 Materials

The materials used to manufacture the shaft assembly are specified in Appendix D and material properties for the relevant components are listed Table 4-5. These are entered into the engineering data file within ANSYS and the correct material properties applied to the relevant components.

Table 4-5 – Material properties

Material	BS970 817M40T	AISI 301 Stainless	Grade 5 Titanium
Component(s)	Hub, Spacer, Sleeves	Flexible Elements	Adaptors
Modulus of Elasticity (GPa)	205	195	114
Poisson Ratio	0.3	0.3	0.342
Ultimate Tensile Strength (MPa)	850	515	950
Tensile Yield Strength (MPa)	700	205	880
Compressive Yield Strength (MPa)	800	500	970

4.5.3 Connections

Connections between bodies are modelled as special contact regions. As with physical bodies, these regions allow for the transference of forces but prevent the bodies from passing through and penetrating one another. Regions in contact are given ‘contact’ and ‘target’ status. The interaction of these is dependent upon the type of contact region selected. Table 4-6 [98] shows the contact types available in ANSYS Mechanical. Contact types that allow separation and friction constantly change the stiffness matrix of the system and are therefore non-linear.

The technical drawing for the shaft assembly states all fasteners must be tightened to 9Nm. For the size of bolts used, this provides a tightening force of ~7500N—hence it is assumed that the components are fully bonded with no possibility of separation. From consideration of Table 4-6, a bonded contact region suitably replicates this condition. Due to the bonded contact region, additional bolt pretension loads are not required.

Table 4-6 – ANSYS contact types

Contact Type	Description
Bonded	If contact regions are bonded, then no sliding or separation between faces or edges is allowed. Think of the region as <i>glued</i> . This type of contact allows for a linear solution since the contact length/area will not change during the application of the load. If contact is determined on the mathematical model, any gaps will be closed and any initial penetration will be ignored
No Separation	Similar to the Bonded case. It only applies to regions of faces or edges. Separation of the geometries in contact is not allowed.
Frictionless	Models standard unilateral contact; that is, normal pressure equals zero if separation occurs. Thus gaps can form in the model between bodies depending on the loading. This solution is nonlinear because the area of contact may change as the load is applied. A zero coefficient of friction is assumed, thus allowing free sliding. The model should be well constrained when using this contact setting. Weak springs are added to the assembly to help stabilize the model in order to achieve a reasonable solution.
Rough	Similar to the frictionless setting, this setting models perfectly rough frictional contact where there is no sliding. It only applies to regions of faces or edges. By default, no automatic closing of gaps is performed. This case corresponds to an infinite friction coefficient between the contacting bodies
Frictional	In this setting, the two contacting geometries can carry shear stresses up to a certain magnitude across their interface before they start sliding relative to each other. This state is known as "sticking." The model defines an equivalent shear stress at which sliding on the geometry begins as a fraction of the contact pressure. Once the shear stress is exceeded, the two geometries will slide relative to each other. The coefficient of friction can be any nonnegative value

In instances where a relatively small part is in contact with a relatively large area, such as element washers to flexible elements, the face of the smaller component is ‘mapped’ upon the larger face so that only the relevant areas are in contact (see Figure 4.5). Bonded contact regions are used.

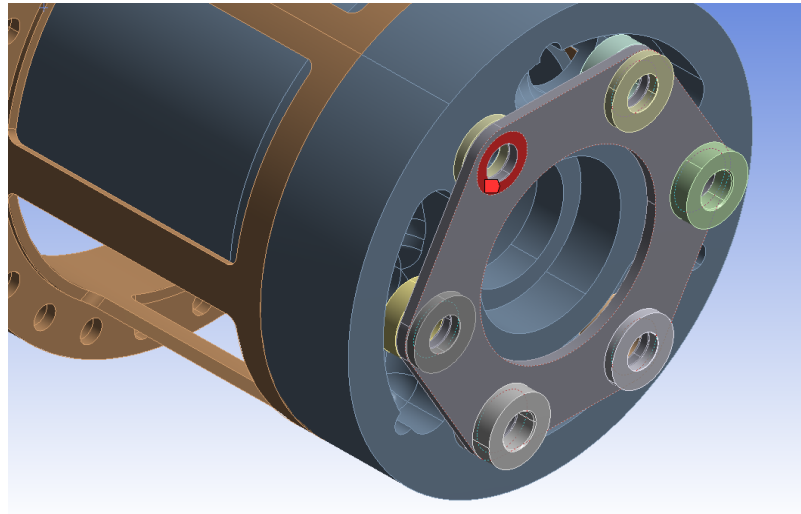


Figure 4.5 – Contact region taken from large area

4.5.4 Element Types

All components are meshed using solid elements SOLID187. These are 10 node higher order 3D elements and are well suited to modelling irregular geometry, Figure 4.6.

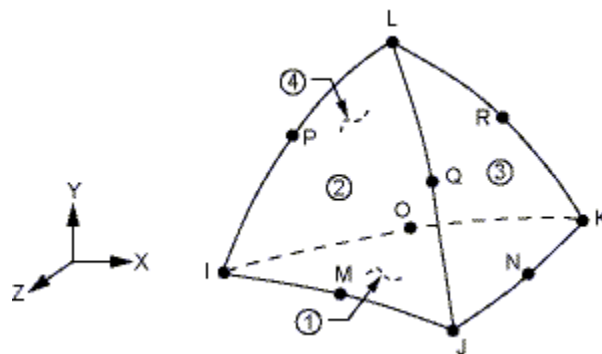


Figure 4.6 – SOLID187 element [98]

Contact regions use the contact/target elements CONTA174 and TARGE170, Figure 4.7. These are 3D elements used to describe the boundary of deformable bodies. CONTA174 and TARGE170 elements are used to represent contact and sliding between deformable bodies. The elements are placed onto the surfaces of 3-D solid elements. The elements have the same degrees of freedom as the solid element face with which they are connected. Contact occurs when the element surface penetrates one of the target segment elements on a specified target surface.

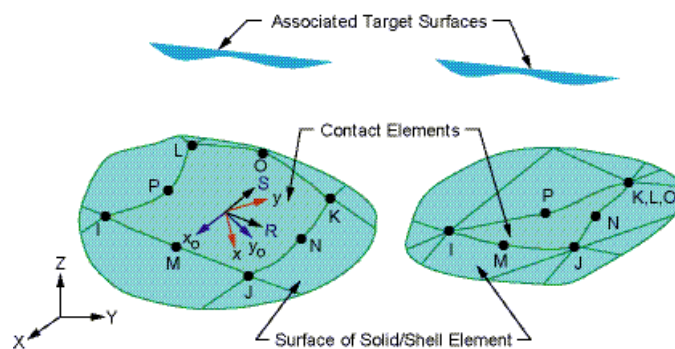


Figure 4.7 – CONTA174 and TARGE170 elements [98]

4.5.5 Meshing

- **Shaft, Hubs, Adaptors, Eccentric Sleeves**

Refinements are made to the mesh to ensure solution convergence. The ‘Body Sizing’ mesh tool is used to apply suitable mesh density to the geometry. Figure 4.8 shows the refined mesh in one hub and the spacer shaft.

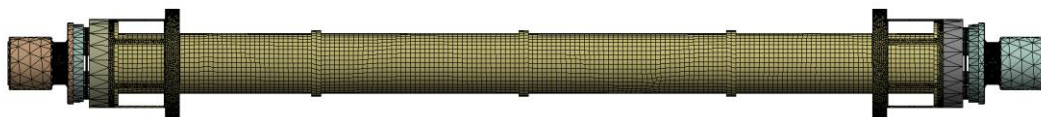


Figure 4.8 – Refined hub and spacer shaft

- **Flexible Element Pack**

The flexible element pack is constructed from eight individual 1mm thick shims. Modelling as a collection of individual layers generates warning messages relating to insufficient elements through the thickness. Refining the mesh such that each flexible element component has sufficient solid elements through the thickness drastically increases the number of elements and increases computation time without improving results. Additional meshing issues become evident when replicating the mesh across all eight elements. As the individual flexible elements are constructed from the same material it is possible to eliminate the meshing problems by replacing all the individual elements with one of equal thickness to the eight. The single element has the same stiffness properties as the eight but imparts a more effective mesh. The individual flexibility of each element is not expected to play any role in the consideration of the lower modes of the shaft assembly. Therefore, in the following analysis, the substitution will not have any significant impact on the results.

The ‘Virtual Topology’ tool is used to ‘clean’ the outside faces of the new flexible element and remove unnecessary edges. A 1mm element size is used with the ‘Body Sizing’ mesh tool. This enables a suitably refined mesh to be developed without significantly increasing computation time, Figure 4.9. Complex contact regions between each flexible element component are removed, thereby further simplifying the model.

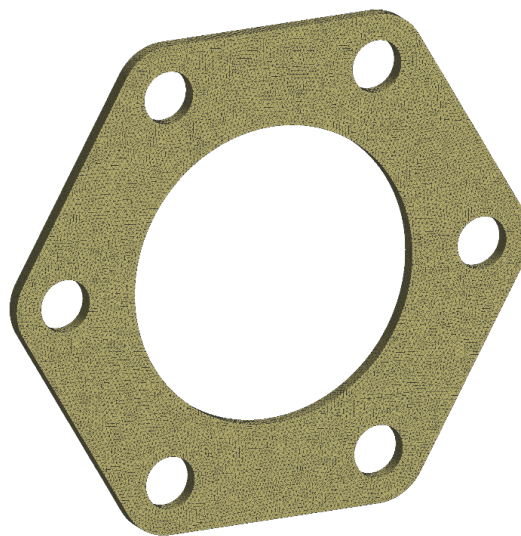


Figure 4.9 – Refined flexible element mesh

4.5.6 Boundary Conditions and Loads

- **Hubs**

The shaft assembly hubs are fitted directly onto two electric motors with short, solid shafts. An interference fit is provided by use of two externally fitted Tollock couplings. It can therefore be assumed that the connection between shaft and motors will be rigid. The boundary conditions must allow for rotation about the x axis, however no other motions will be possible. A 'Remote Displacement' boundary condition that constrains x,y,z translational movement and rotation about the y and z axes, suitably replicates this condition.

- **Shaft Assembly**

The spacer shaft, spacer adaptors and balance sleeves are contained by the flexible element section of the coupling. This allows movement of the spacer shaft that is not fully constrained by the boundary conditions applied to the hubs. There is limited rotation about the y and z axes. Boundary conditions are not applied directly to control movement, however, the use of contact regions between adaptors, washer and the flexible elements replicate the physical connections and allowable movement. Figure 4.10 shows the flexible element region of the geometry.

- **Rotational Velocity** is applied about the x axis.

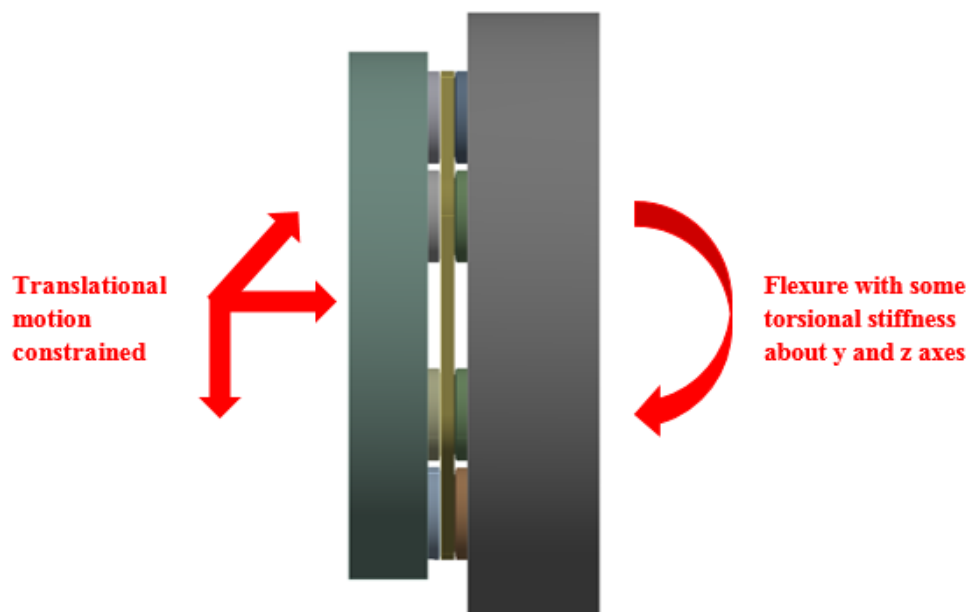


Figure 4.10 – Coupling flexible element connection

4.5.7 Solver Settings

ANSYS uses an Eigenvector solver to determine the free response of a structure. For simple analyses the structure has constant mass and stiffness, no damping and there can be no applied time varying loads. In such cases the equation of motion is given as [98]:

$$[M]\{\ddot{q}\} + [K]\{q\} = \{0\} \quad (4.46)$$

Using a harmonic solution of the form $\{q\} = \{\bar{v}_i\} \cos \omega_i t$, Equation (4.46) becomes:

$$(-\omega^2[M] + [K])\{\bar{v}_i\} = \{0\} \quad (4.47)$$

As is the case when using the eig command in MATLAB, this equality is satisfied when $\det[K - \omega^2 M] = 0$. When using linear models, the system matrices are relatively sparse and contain many zero terms. In such cases the Block Lanczos method, which utilises a sparse matrix solver, can be used. Sparse matrix solvers do not refine a result through a series of iterations until a solution is obtained, but use direct elimination of equations. Direct elimination factorise the sparse matrix into an alternative form for solution which is simpler to solve. For ANSYS, this form is triangular with forwards and backwards substitution. The resulting matrices are typically large, hence the suitability for simple linear models.

When considering spinning structures in rotordynamics, the inclusion of damping is due to gyroscopic or Coriolis effects. These are proportional to rotational velocity and therefore the terms in the damping matrix are none constant. With the inclusion of damping, the eigenvalue/eigenvector solution to Equation (4.46) becomes:

$$[K]\{\bar{v}_i\} + \lambda_i[C]\{\bar{v}_i\} = -\lambda_i^2[M]\{\bar{v}_i\} \quad (4.48)$$

The eigenvalue solution of Equation (4.48) is complex:

$$\lambda_i = \sigma_i \pm j\omega_i \quad (4.49)$$

The real part of the eigenvalue, σ , indicates the stability of the mode whilst the complex, ω , gives the natural frequency. The real part of the eigenvectors dictate the mode shapes of the system.

For completeness, the specific ANSYS solver settings used to generate Campbell diagrams and obtain critical speeds are:

- **Reduced Damped solver (QRDAMP)** – Used for computational efficiency in terms of solution time. Accuracy of results is checked against Full Damped solver
- **Modes are not reused** – The undamped Eigensolution is calculated at each step
- **Complex solutions is stored** – Allows the complex part of the solution to be stored and the natural frequencies extracted for producing Campbell Diagrams

The reduced damped solver uses a two stage process. Firstly, the non-symmetric stiffness and damping matrices that are symmetrised and the undamped Eigensolution is obtained, using the Block Lanczos method. In the subsequent step, the full, non-symmetric matrices are included and transformed with the mode shapes from the eigenvectors obtained from the initial undamped solution.

4.5.8 Comparison of Proposed (Theoretical) and Finite Element Models

For both models, a modal analysis identifies the natural frequencies, with Campbell diagrams used to obtain the critical speeds of the shaft over a defined range of operating speeds. Results from the ANSYS modal analysis are used to visualise the mode shapes of the system. To assess the accuracy of the proposed theoretical model, critical speeds for the rotating shaft have been obtained for four eccentric sleeve configurations viz. no sleeve, short sleeve, medium sleeve and long sleeve.

The specific sleeve lengths considered for this analysis are determined by experimental testing performed in a previous study. A sleeve with an overall length of 76mm (medium sleeve) had a stiffness equal to that of the shaft under consideration, Figure 4.3. Matching the stiffness of the sleeves to the shaft is considered the design configuration for optimal balancing effect. Additionally, lengths 66mm (short sleeve) and 86mm (long sleeve) were selected to investigate the effect of using stiffer and more flexible sleeves on balancing efficacy, Table 4-7:

Table 4-7 – Sleeve lengths used in analysis

Short	Medium	Long
66mm	76mm	86mm

Figure 4.11 and Figure 4.12 show the normalised Campbell diagrams for the theoretical and ANSYS finite element models for the first bending mode of the shaft in each case, normalised against the maximum frequency and rotational speed. Since natural frequencies are obtained in a rotating coordinate system, the critical speeds are determined by the speed at which the frequency of the mode becomes zero.

Table 4-8 gives the normalised critical speeds of each sleeve configuration for the model variants. The critical speeds for each sleeve configuration are normalised with respect to the critical speed of the system with no sleeve attached.

Table 4-8 – Normalised shaft critical speeds

	No sleeve	Short	Medium	Long
Theoretical	1.000	0.9924	0.9923	0.9922
ANSYS	1.000	0.982	0.971	0.942

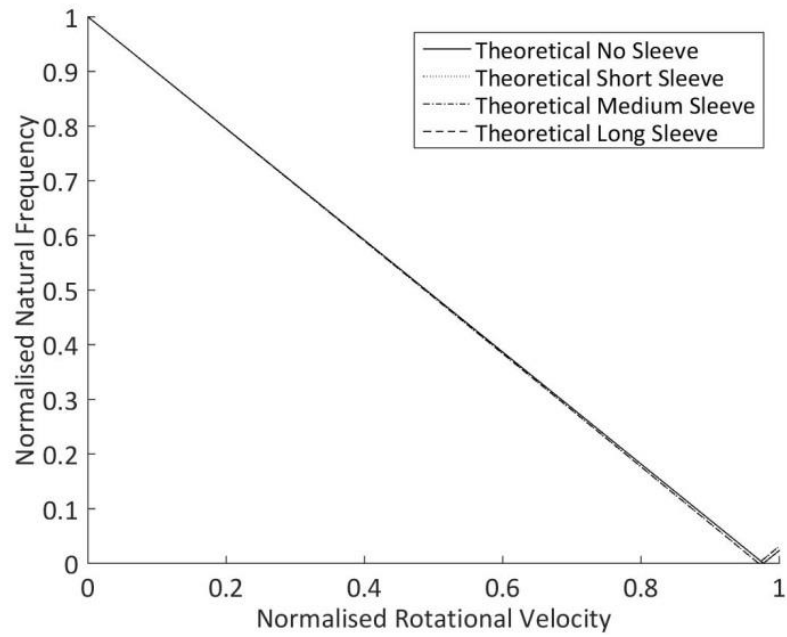


Figure 4.11 – Campbell diagram for theoretical solution

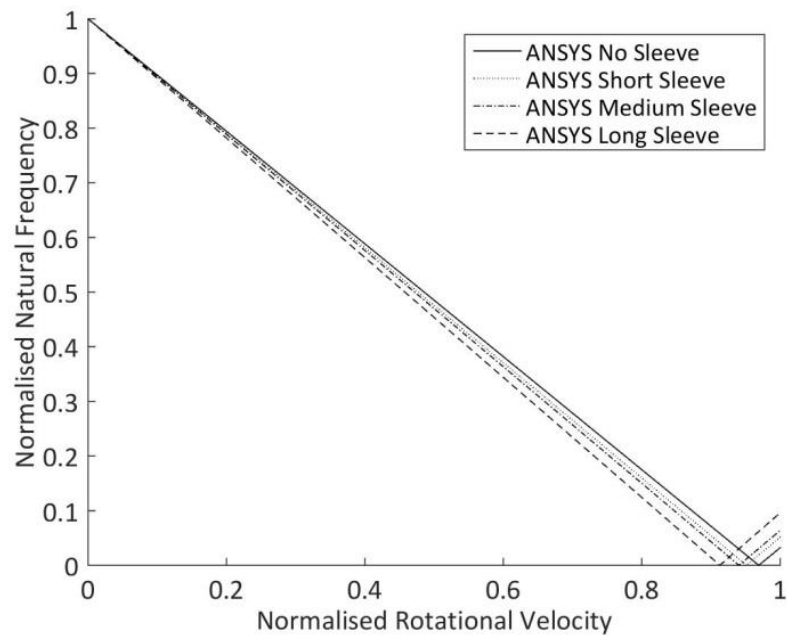


Figure 4.12 – Campbell diagram for finite element mode

Comparison of the Campbell diagrams and results in Table 4-8 show a disparity in the relative change of critical speed between the two models. The theoretical model shows a marked decrease in critical speed with the addition of the short sleeve but no further significant change with the addition of sleeves of increasing length. By contrast, the finite element model shows a continuing decrease in critical speed with the addition of sleeves of increasing length. This can be attributed to the theoretical model only considering mass/inertia effects of the sleeves, as opposed to the finite element model that accommodates for the full geometry of the system. As such, the results presented in Table 4-8 show that mass/inertia effects alone are not sufficient to describe the change in critical speed as the eccentric sleeve length increases. This also follows a degree of intuition, where increasing mass and reducing stiffness decreases the natural frequencies of the system.

The effect of increasing sleeve length on stiffness can be readily observed in the mode shapes of the system under free vibration, as shown in Figure 4.13 to Figure 4.15. For the short sleeve, the deflection of the sleeve is approximately equal to that at the same location on the shaft; essentially it is rigid. However, as the length of the sleeve is increased, the deflection becomes significantly greater than that of the shaft at the same location. This can be rationalized by considering that, as the sleeve increases in length, it becomes more flexible. When considered in conjunction with the normalized critical speeds presented in Table 4-8, this indicates that sleeve flexibility becomes progressively more influential on the dynamics of the system as sleeve length increases and that the assumption of rigid body sleeves is limited.



Figure 4.13 – 1st bending mode of shaft with short sleeve, from FE analysis



Figure 4.14 – 1st bending mode of shaft with medium sleeve, from FE analysis



Figure 4.15 – 1st bending mode of shaft with long sleeve, from FE analysis

4.6 Modifications to the Finite Element Model

To investigate the effect of sleeve flexibility on the dynamics of the system, the geometry of the eccentric sleeves is removed and replaced with a point mass with equivalent inertia properties, as shown in Figure 4.16.

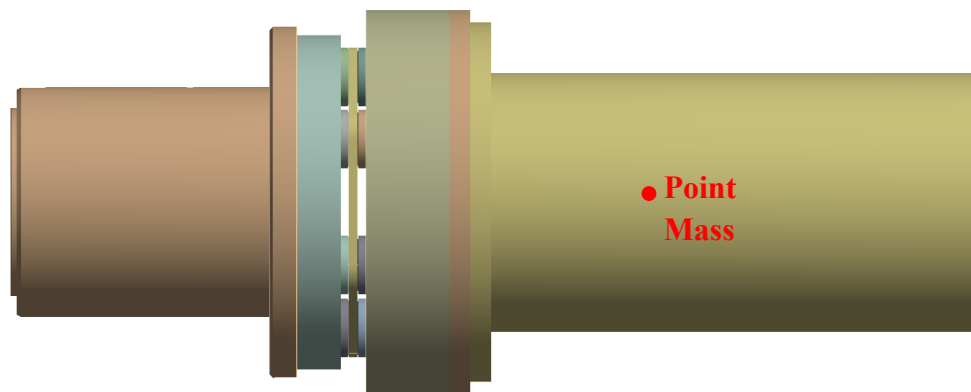


Figure 4.16 – Finite element model of shaft with point mass replacing the sleeve

The effect of sleeve flexibility can be shown through the described modifications to the finite element model. Removing the sleeve geometry, the mass of the sleeve is induced on the system without any stiffness effects. Figure 4.17 shows the normalised Campbell diagram for the ANSYS finite element model with point mass replacement. Normalised critical speeds are included in Table 4-9. Results for the point mass finite element model are comparable to those of the theoretical model—there is an initial decrease in critical speed with the addition of the short sleeve but no further significant change with the addition of the medium and long sleeves.

Table 4-9 – Normalised shaft critical speeds for point mass model

	No sleeve	Short	Medium	Long
ANSYS	1.000	0.991	0.989	0.987

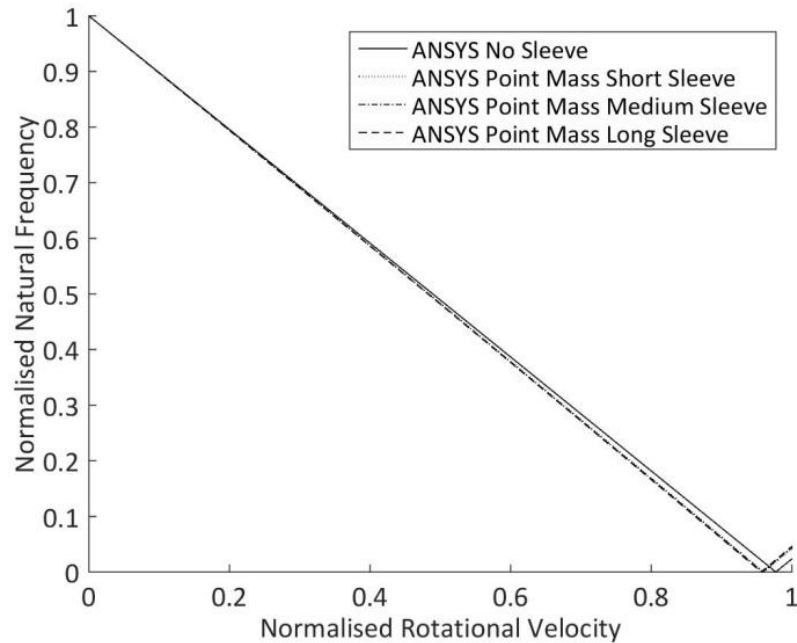


Figure 4.17 – Campbell diagram for finite element model with point masses

Removal of the sleeve geometry has shown that mass alone does not explain the change in critical speed and therefore sleeve stiffness does have a significant impact upon the dynamics of the shaft; this is in contrast to the initial assumptions made in Chapter 3. This is a counterintuitive result given that each sleeve is connected to the shaft at one end and in free space at the other. Although the overall mass of the system has been increased, the stiffness of the sleeve does not directly affect the stiffness of the shaft and would not be expected to alter the natural frequency significantly. This is suggestive that during free vibration, the flexibility of the sleeves is impacting the dynamics of the shaft.

4.7 Conclusions

The equations of motion derived in Chapter 3 are discretised using the Galerkin method. The resulting matrices show that the mass inertia terms of the eccentric sleeves are added to the inertia of the shaft. This is somewhat intuitive as mass is being added to the system. Through consideration of the fundamental equation for natural frequency ($\omega = \sqrt{k/m}$), the addition of the eccentric sleeves is predicted to have a softening effect and reduce the natural frequencies of the shaft.

Solution convergence of the system matrices is used for theoretical determination of the shaft critical speeds through modal analysis using MATLAB. A convergence study shows that using a maximum of 10 terms in the system matrices provides satisfactory convergence without significantly increasing computation time of the solution.

A 3-dimensional finite element model of the full shaft geometry is created using ANSYS Workbench and the results of modal analysis are compared with the theoretical model. The normalised critical speeds of the first bending mode are compared for each model using four different sleeve configurations; a shaft with no sleeve and a short, medium and long sleeve. When considering the relative difference in shaft critical speeds as the sleeve length is changed, a discrepancy is identified between the two approaches. Making modifications to the finite element model to remove the sleeve flexibility but leave the mass/inertia, produces results markedly similar to those of the theoretical model. Sleeve flexibility is therefore found to have a greater than anticipated effect upon the critical speeds of the shaft. Furthermore, sleeve flexibility becomes progressively more important with increasing sleeve length.

The modelling practices have identified potential bounds of applicability for the proposed models. When the eccentric sleeves possess high stiffness, the theoretical model can be used to accurately determine the critical speed of the shaft. However, the magnitude of influence of sleeve stiffness on the change of critical speed of the shaft increases with decreasing sleeve stiffness. As such, the accuracy of the theoretical model is reduced in the latter case, requiring the use of more complex finite element simulations, at the expense of incurring significant computational overhead.

Although sleeve flexibility appears to be a key parameter, experimental validation is required to establish the validity of the results observed here. An experimental procedure and results are therefore discussed in Chapter 5. Moreover, further investigation of the effect of sleeve flexibility is required to fully understand the mechanism of passive control and the effect upon higher modes of the shaft.

Chapter 5 Experimental Validation Study of Rotating Shaft with Eccentric Sleeves

5.1 Summary

Experimental studies are carried out using a custom high-speed test facility which is a dimensionally scaled representation of a coupling shaft from a Siemens SGT-400 MD gas turbine. A detailed description of the high speed rig, is given, including the control and measurement instrumentation. The response of the system is measured at a series of speeds for four different sleeve/shaft configurations; no sleeve, short, medium and long sleeves. The critical speeds of the system are identified through analysis of response plots to determine the speed at which the peak vibration magnitude occurs. Measured data is used to validate the theoretical and finite element models discussed in Chapter 4. Comparison with the proposed models show a similar trend as displayed by the finite element analysis, but with a slight shift in the absolute positions of the critical speeds. This is due to the existence of bearings and support structures within the experimental rig that aren't captured by either model. Identified modifications to improve model accuracy becomes instrumental in proving that sleeve flexibility is an important factor when considering real operating conditions.

5.2 Chapter Highlights

- Critical speeds are identified from scaled experimental test facility
- The results are compared with the theoretical models presented in Chapter 4
- It is shown that the stiffness of the sleeves must be accommodated when considering the passive control characteristics

5.3 Experimental Setup and Description

The high speed test facility was initially designed for concurrent research into the dynamic balancing capabilities of the eccentric sleeve described in Chapter 1. The motivation for the sleeve design is to reduce the amount of unbalance that exists within a rotating shaft. A positive effect of the counterbalance sleeves is considered as identifying a reduction in shaft deflection and reaction loads at the shaft bearings.

For the purposes of this research, using experimental modal analysis would yield the natural frequencies of the shaft but only in a non-rotating state. This provide some validation towards the models but would not account for any rotational effects, nor allow to critical speeds to be determined.

Measuring the natural frequencies whilst the shaft is rotating allows for experimental Campbell diagrams to determine the critical speeds of the shaft with multiple different sleeve lengths attached. From observation of any splitting of the modes, the degree of rotational effects could also be identified. Work presented in [99] and [100] shows methods for measuring the natural frequencies of a rotating shaft by way of on-shaft mounted, wireless accelerometers and telemetry systems. In practice, both methods were complicated and limited to relatively low speed ~ circa 1000rpm.

The critical speeds are therefore inferred from the peak response, as shown in Figure 2.11 and assuming only unbalance excitation.

5.3.1 Test Methodology

- Obtain the critical speed of the shaft without sleeves, as a benchmark case
- Measure the shaft displacement for each sleeve configuration, at 100rpm intervals up to 12000rpm
- Use the maximum peak response of the shaft mid-point to identify the experimental first critical speeds of the shaft for each sleeve configuration
- Obtain critical speed for each sleeve configuration and compare the relative change from the benchmark case
- Compare the results of experiment with the theoretical models in Chapter 4

5.4 Description of Test Rig

The test facility is shown in Figure 5.1. It consists of two Oswald QDI13.2-2F Induction motors. The motors are supplied by a 415V three phase supply and are capable of producing 49kW with a maximum operating speed of 20000 rpm. A Heidenhaim 512 bit PPR TTL 5 V Quadrature encoder provides positional feedback.

The motors are mounted on engine support frames that are bolted to the floor on vibration isolation feet. A test shaft links the motors together. The shaft is dimensionally scaled from a full sized SGT-400 MD coupling shaft – a technical drawing is given in Appendix D.



Figure 5.1 – Experimental set up

5.5 Test Rig Control

Each motor is controlled using a Unidrive SP AC Drive that stores all parameters, to ensure repeatability, and can be interfaced either through software or analogue controller. Control Techniques CT Soft (Figure 5.2) allows the user to programme and monitor all drive parameters. A custom controller demand interface (Figure 5.3) is used to reduce the complexity of operation, allowing the user to control motor spin direction, speed and stop/start without the need for additional software.

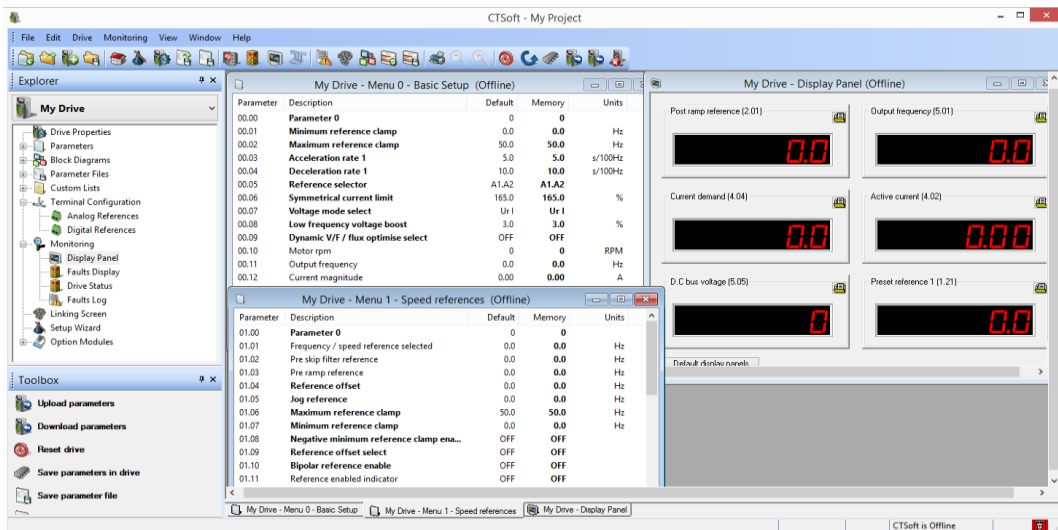


Figure 5.2 – Control software screen shot



Figure 5.3 – Analogue controller

5.6 Shaft Balancing

Shaft balancing was conducted by the manufacturer prior to delivery. Table 5-1 summarises the residual unbalance in each shaft/sleeve configuration as supplied in manufacturer's certificate of conformity.

Table 5-1 – Residual unbalance in test shaft/sleeve configurations

	No Sleeve	Short	Medium	Long
Unbalance (gmm)	4.89	6.24	4.52	7.62

5.7 Shaft Alignment Process

As discussed in Section 2.7, along with a good state of balance, alignment of the test shaft is a critical feature that influences the shaft dynamics and performance. To minimise the any vibration that is not associated with the dynamics of the shaft and sleeves, a tight degree of alignment is required.

Alignment was performed using the Pruftechnik Rotalign laser alignment instrumentation to obtain vertical and horizontal measurements. The degree of offset and parallel alignment was considered for both directions. Modifications to alignment were made, keeping the driving motor fixed and aligning the driven motor to it using adjustment screws.

Alignment tolerances for the test shaft are specified in Appendix D, as $\pm 0.2\text{mm}$ for parallel and offset alignment. Measurements show that the required alignment is readily achievable (as shown in Figure 5.4).

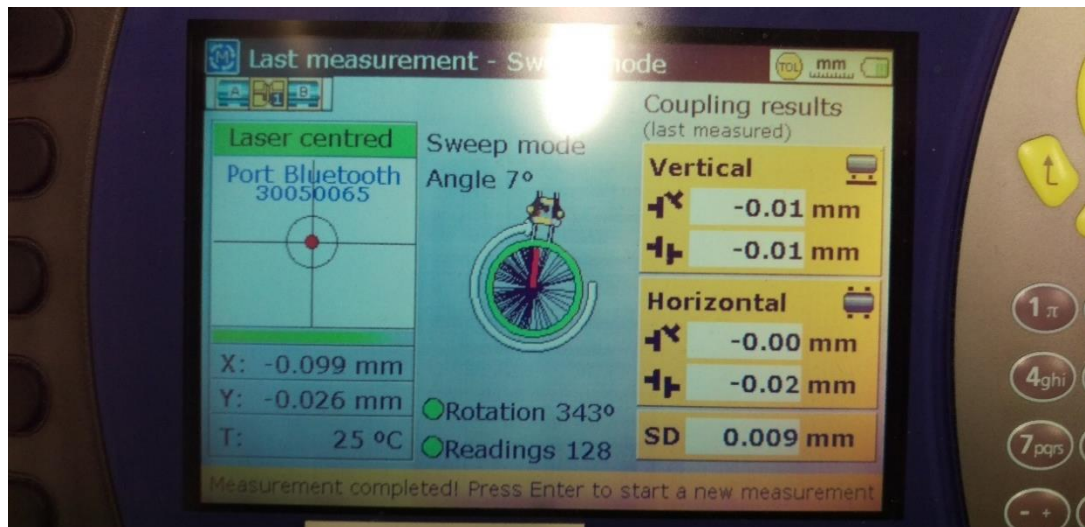


Figure 5.4 – Alignment figures achieved

5.8 Instrumentation

Shaft and sleeve deflections are measured using three laser displacement sensors—see Figure 5.5. The Micro-Epsilon optoNCDT ILD2300-20 allow for high accuracy measurement (1 μ m) with a high sampling rate of up to 50 kHz. Each sensor uses optical triangulation of the transmitted and reflected beams to record an oscillation of positive and negative displacement once per revolution.

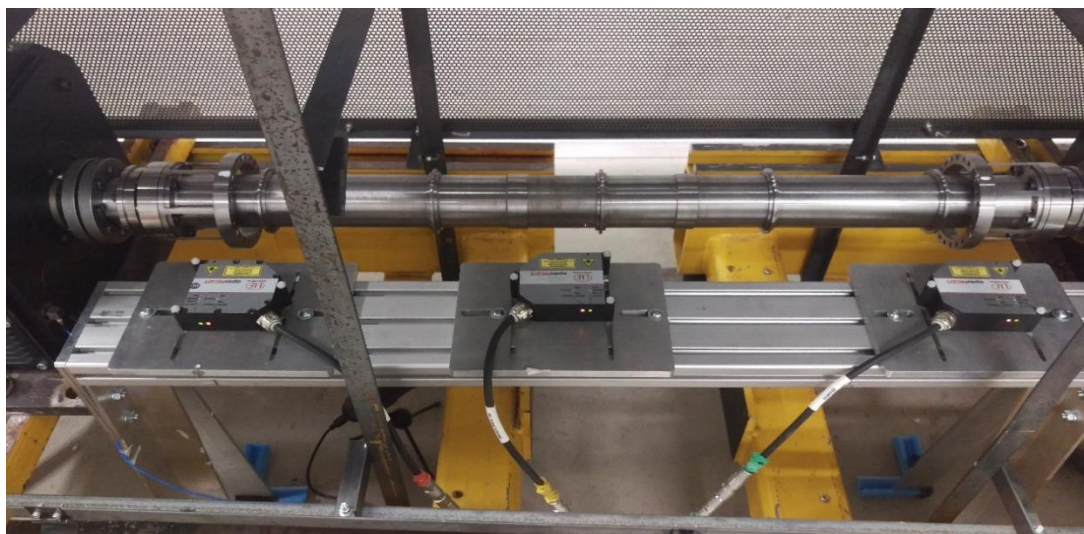


Figure 5.5 – Laser displacement sensors measuring shaft

The displacement measurements are captured directly from the Micro-Epsilon ILD2300 DAQ Tool V.3.1.5 GUI interface, accessed through Ethernet connections, see Figure 5.6. A 10 second record of shaft deflection at steady state speed is taken at 100rpm intervals between 0 and 12000rpm, Figure 5.7 and Figure 5.8.

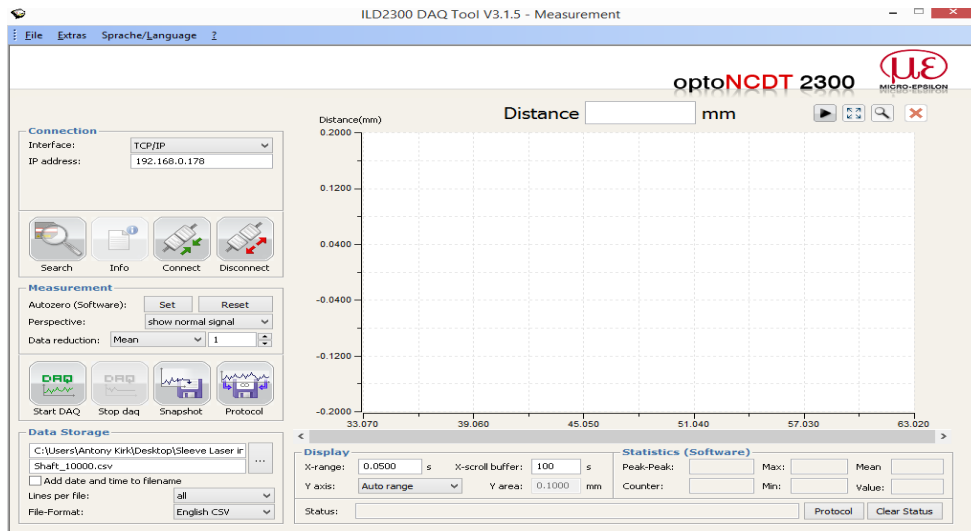


Figure 5.6 – Laser displacement sensors GUI

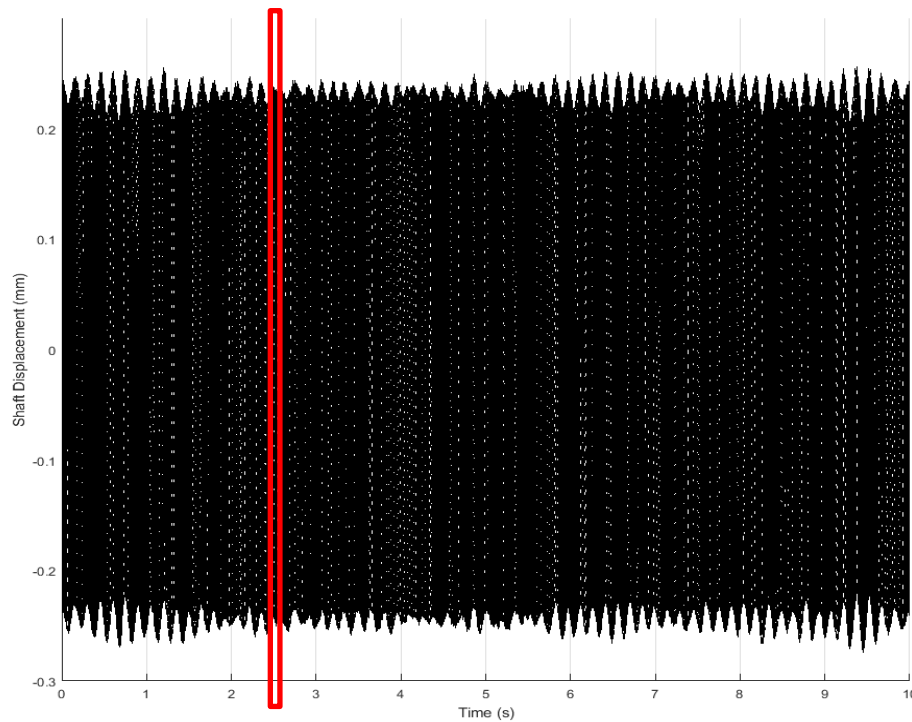


Figure 5.7– Example complete record measurement

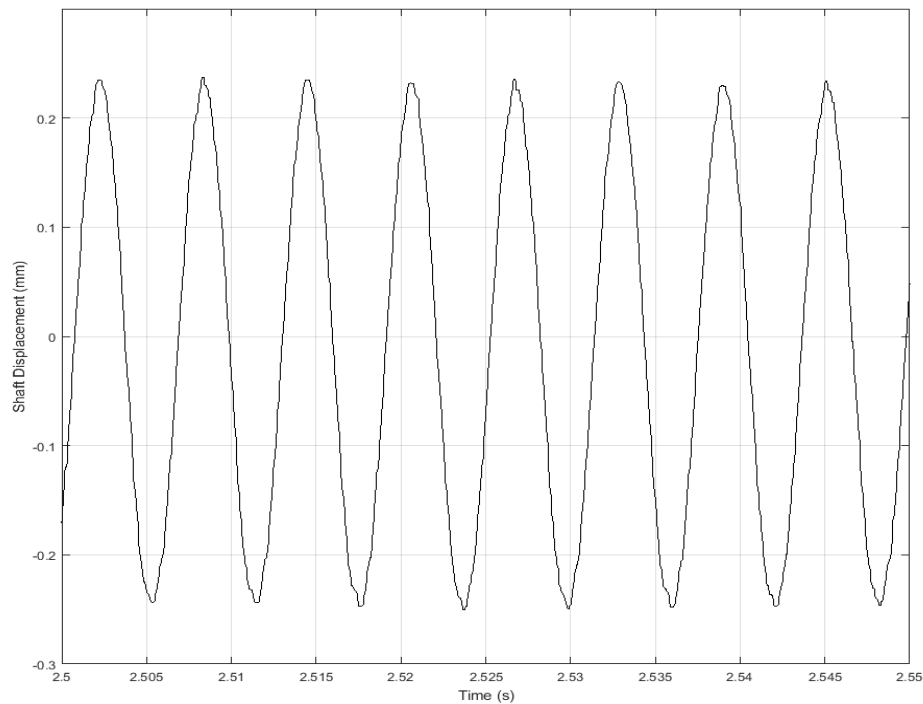


Figure 5.8 – Zoom of data record

5.9 Experimental Results

Figure 5.9 shows example shaft displacement measurements for each of the four sleeve configurations, with respect to rotational speed (8000 to 12000 rpm). Each data point is obtained from MATLAB analysis (the *findpeaks* command) of the raw data from the laser displacement sensors.

Symmetry of orbit and centring of shaft displacement is checked and a mean displacement is obtained for each data set. Following the data analysis, three separate peaks can be observed in Figure 5.9 which correspond to the maximum deflection of the shaft mid-point for the non-sleeve, short and medium configurations. Operation of the long sleeve (86mm) was stopped at 8600rpm due to high levels of shaft and base vibration.

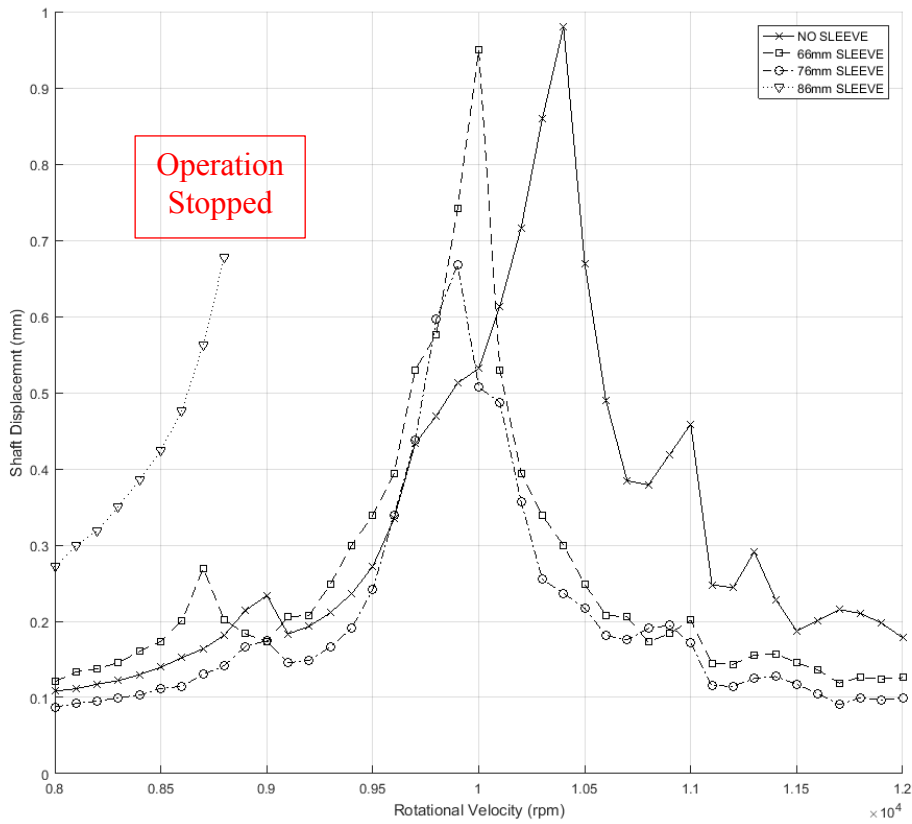


Figure 5.9 – Raw displacement data from shaft for different sleeve configurations

Experimentally measured critical speeds are summarised in Table 5-2. Results with the long sleeve were not considered a robust representation due to significant vibrations occurring at low speed. The resolution of the data allows the determination of the experimental critical speeds to within a tolerance of ± 100 rpm. The resolution of critical speeds is the key error from the experimental data. Due to the averaging process, there are some error in determination of the absolute shaft displacement values, however this is insignificant as it is the speed at which peak displacement occurs that is of importance.

Table 5-2 – Experimental critical speeds

	No sleeve	Short	Medium	Long
Raw	10400	10000	9900	
Normalised	1.00	0.962	0.952	

5.10 Modifications to FE Model

Comparison of the data in Table 5-2 with the critical speeds in Table 4-8 shows similar characteristics as those from the finite element model, albeit over a different speed range: the experimental critical speeds are all lower than those predicted by the finite element model. This is due to the increased length of the entire drive train when the electric motor rotor shafts are included and the existence of bearings within the motors that have a softening effect on the natural frequencies of the shaft. Thus, to consider the degree of correlation between experimental and theoretical results, the influence of the support structures also requires investigation.

Modifications are therefore made to the finite element model to include the effects of the support structures. Physical examination of the motors allows for approximations of the rotor geometry and bearing locations to be determined. The internal motor rotor shafts are determined to be 250mm long. The rotor shaft is supported by two bearings, one mounted at the front edge of the motor casing, with the other at the opposite ends of the shafts. The remainder of the motor casing is empty to aid ventilation and prevent overheating. Appendix E does not give specific bearing data but specifies the type as ‘spindle’. Figure 5.11 shows the shaft with the motor shafts and bearings modelled and Figure 5.11 an internal schematic of the motors.

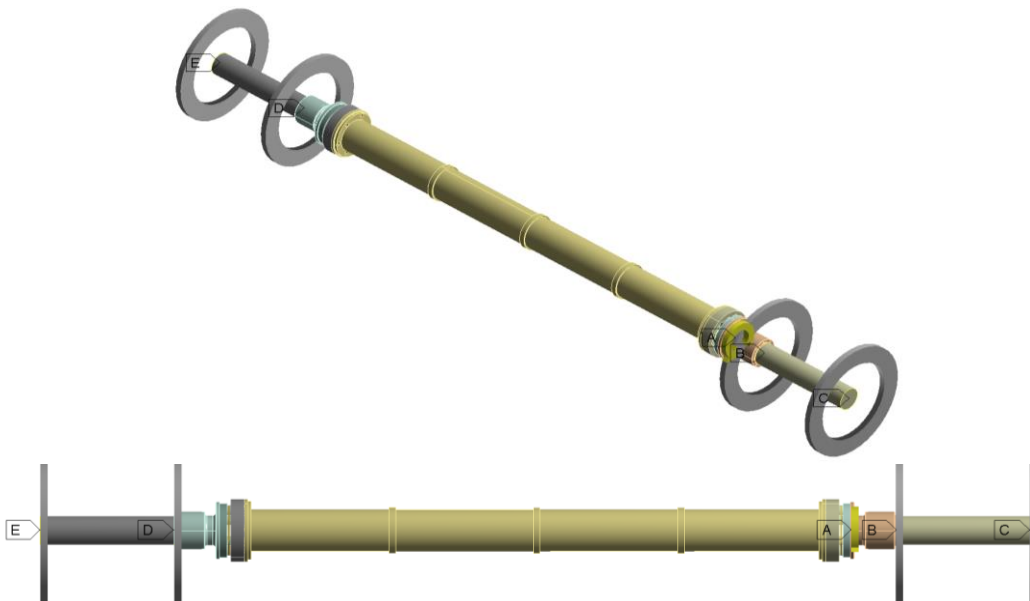


Figure 5.10 – Modifications to finite element model to include support structure effects

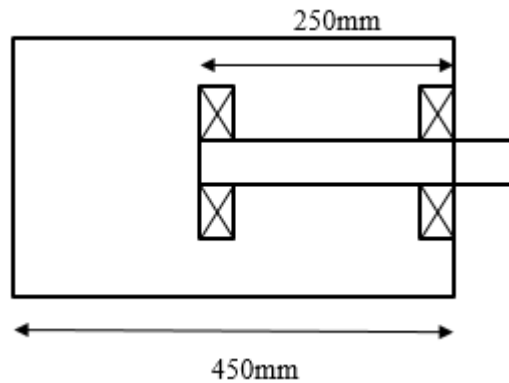


Figure 5.11 – Internal layout of Modifications to finite element model to include support structure effects

Based on the work conducted in [23], a parametric study is conducted whereby the lateral stiffness of the bearings is altered and the critical speed of the first bending mode recorded. Damping and cross coupling terms are not included. A critical speed map is shown in Figure 5.12.

For the no-sleeve configuration, the experimental critical speed of the first mode is determined to be 10400 rpm. To obtain a matched critical speed in the modified ANSYS finite element model, the critical speed map indicates that a bearing stiffness of 3.5×10^7 N/m should be incorporated. A nominal stiffness for the type of bearings used (spindle) is in the region of 1×10^7 to 1×10^8 N/m, which provides a degree of support for the calculated value [101].

The bearing stiffness is applied to the models for the short, medium and long sleeves and the critical speeds compared with the experimental results. From Table 5-3, it can be seen that there exists a good correlation between the modified ANSYS model and experiment values displayed in Table 5-2.

Table 5-3 – Modified finite element critical speeds

	No sleeve	Short	Medium	Long
Raw	10392	10106	9993	9779
Normalised	1.00	0.972	0.962	0.941

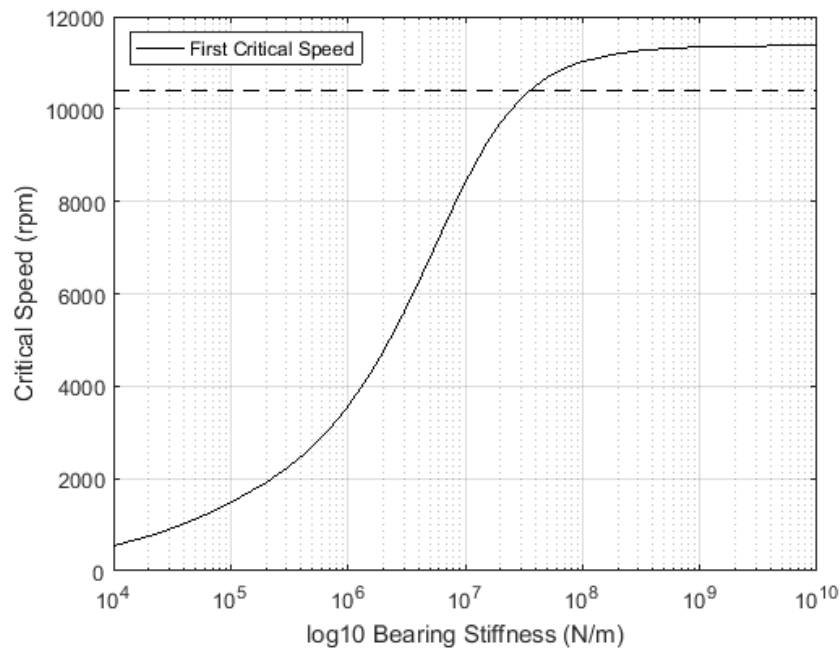


Figure 5.12 – Critical speed map for first bending mode for no-sleeve configuration

5.11 Comparison of Experimental and Theoretical Results

Results from the theoretical and experimental investigations are summarised in Figure 5.13, and normalised against the non-sleeve case in Figure 5.14. Error bars are included to account for the ± 100 rpm tolerance in determining the experimental critical speeds from the experimental data.

The ANSYS finite element models, both with and without the bearings, also follow the underlying trend of the experimental data, although there is a greater relative change of critical speed as the sleeve length increases for the case including bearings. For both the absolute and normalised results, the ANSYS finite element model that includes the bearings lies within the 100rpm tolerance.

However, when compared with results from both the theoretical and ANSYS point mass models, the characteristics are outside the 100rpm margin of error and do not show a significant correlation with the experimental data. It is concluded therefore, that these models do not accurately represent the true dynamics of the system, as shown by the experimental data.

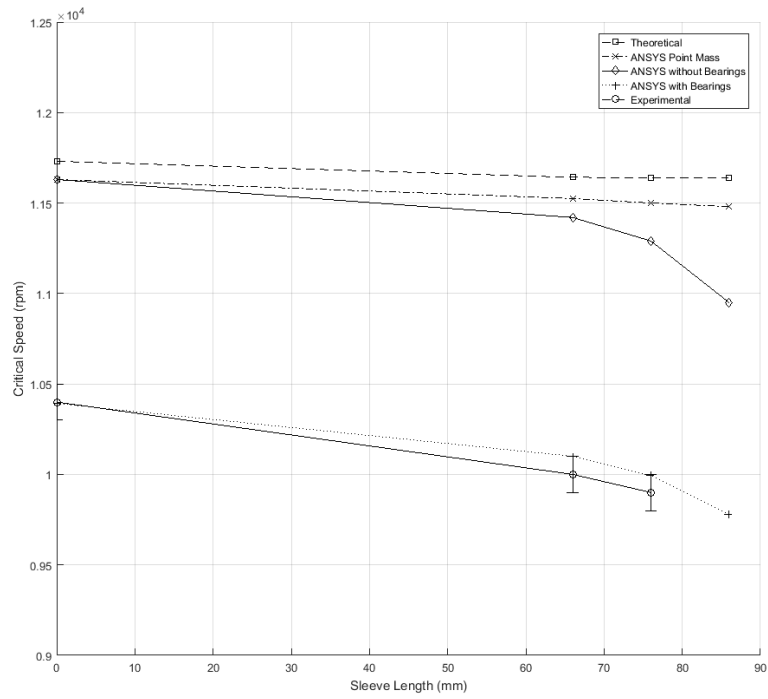


Figure 5.13 – Absolute critical speeds for all modelling approaches and experimental

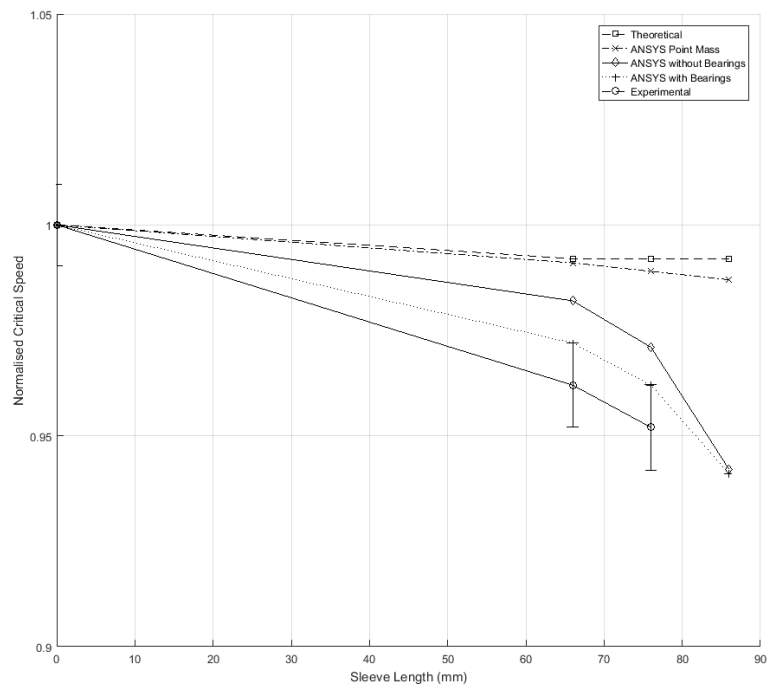


Figure 5.14 – Normalised critical speeds for all modelling approaches and experimental

The models which include sleeve flexibility therefore provide the best qualitative correspondence with the experimental measurements, and as the conclusion in Chapter 4 suggest, confirm that the inclusion of sleeve flexibility is an important factor in identifying the critical speeds of the combined shaft system.

5.12 Relative Sleeve Flexibility

To investigate the flexibility of each test sleeve, displacement measurements are taken on the edge of each sleeve and at the same position on the shaft, over a small range of subcritical shaft speeds, as shown in Figure 5.15. The measured displacements of each sleeve are normalised against the same position on the shaft, and shown in Figure 5.16

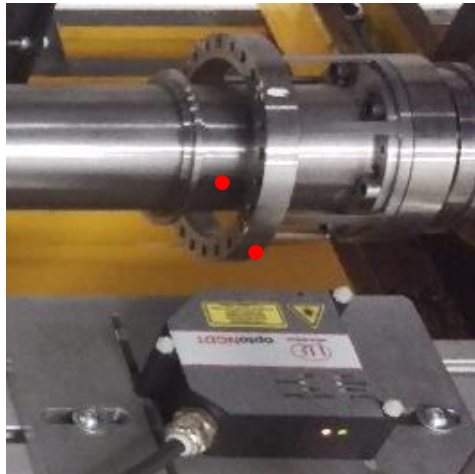


Figure 5.15 – Measurements on sleeve and shaft

It can be seen that the 76mm sleeve has approximately the same mean displacement as that of the shaft. This is in keeping with the initial design of this sleeve to have matched flexibility to the shaft. The 66mm and 86mm sleeves have, respectively, moderately lower and greater relative displacement than the shaft, indicating stiffer and more flexible characteristics, as originally anticipated. The greater flexibility of the long sleeve raises concerns about possible stability issues and the effect of unbalance in operation, particularly if the sleeve length is increased further.

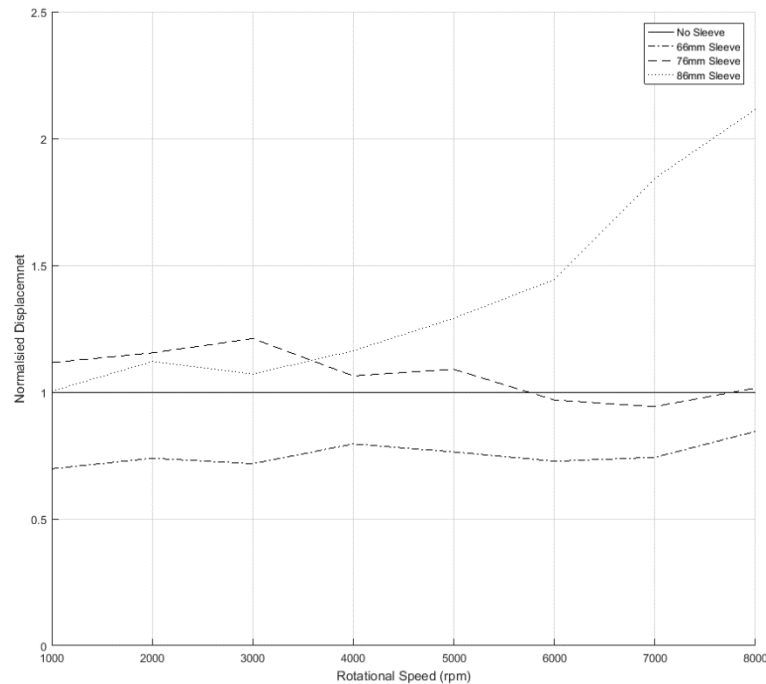


Figure 5.16– Relative sleeve flexibilities

5.13 Conclusions

An experimental test facility using high speed induction motors to replicate a gas turbine and a piece of driven equipment is used to experimentally validate the theoretical and finite element models presented in Chapter 4. A full scale coupling shaft is dimensionally scaled and designed to incorporate a range of eccentric sleeves. Motor control software is utilised to develop an analogue controller for simpler motor speed control. Measurements of shaft and sleeve deflection are carried out using laser displacement sensors.

The experimental results show a good qualitative match with those of the finite element solutions of the full shaft geometry; however, modifications to the model are required to gain a better comparison with the measured critical speeds. The inclusion of approximate support structure geometry and bearing stiffness yield finite element results that are within a 100rpm margin of error.

The results of the theoretical model and finite element model that neglect sleeve flexibility show poor correlation with experimental measurements. Combined with the results from the full geometry finite element models, with and without support structures, it is concluded that sleeve flexibility is an important parameter in the passive control of the shaft critical speeds.

The included support structures only give an indication of the effect upon the shaft critical speed and cannot be fully relied upon without additional specific information of the motor internal layout. As the results of both finite element models with and without the support structures show a similar relative effect with increasing sleeve length for proceeding parametric studies, it is possible to neglect support structure effects to reduce model complexity and increase computational efficiency.

Measurements of the relative sleeve and shaft displacement show that initial assumptions regarding the predicted stiffness (Chapter 4) of the sleeves prove to be correct.

Chapter 6 Effect of Variance Study on Critical Speeds of Shaft with Eccentric Sleeves

6.1 Summary

Having confirmed (in Chapter 5) that sleeve flexibility has a substantial effect on the critical speeds of a shaft, here the investigation considers the wider effect of sleeve length on the shaft critical speeds, including up to the third bending mode of the shaft. Observation of modes shapes show that for short sleeve lengths the mode shapes of the shaft are dominated by shaft bending. However, with increasing sleeve length the shaft modes become dominated by the sleeves. Concurrently, the modes that initially appear to be sleeve dominated at short lengths become dominated by the shaft as sleeve length increases.

For each of the three shaft modes, it is shown that specific sleeve lengths exist that incur a sharp increase in the shaft critical speed. Away from these specified sleeve lengths the overall effect on the modes is to reduce the critical speeds, which is qualitatively similar to the effect of adding mass. The sharp increases in critical speed coincide with lengths of sleeve that have the same natural frequencies as each of the modes of the shaft. Moreover, when the flexibility of the sleeve is neglected and the sleeve mass is added to the shaft alone, these increases do not occur. Thus, the mechanism of passive control is reliant on sleeve flexibility as well as the modal interaction of the sleeve and shaft modes that occur when the shaft and sleeve natural frequencies are coincident. Away from these specific sleeve lengths the overall effect is softening due to added mass.

6.2 Chapter Highlights

- Effect of varying sleeve length upon higher mode critical speeds is investigated
- By changing sleeve length it is possible to change the critical speeds of the shaft by up to +10% and -15 % away from the non-sleeve case
- The mechanism by which passive control occurs is a combination of mass damping and coherence of shaft and sleeve natural frequencies
- Whilst in theory it is possible to increase the critical speed of the shaft to be beyond the non-sleeve case, the sleeve modes must be traversed which may have detrimental consequences for the integrity of the shaft

6.3 Introduction

Previous chapters have discussed the construction and validation of a finite element model for the modal analysis of a rotating shaft with eccentric sleeves. Specifically, it has been shown that increasing the length of the attached sleeves decreases the first critical speed of the shaft. The observed change is greater than if the equivalent sleeve mass and inertia was added to the shaft alone. Therefore, from the definition of natural frequency, the stiffness of the sleeves must have a significant influence upon natural frequencies of the shaft, which is characterised by a change in the first critical speed.

However, the analysis in the previous chapters has been experimentally limited to a small number of sleeve lengths and only considers the first bending mode of the shaft. Consequently, only a limited degree of passive control has been demonstrated. Furthermore, the mechanism by which the eccentric sleeves affect the shaft critical speed has yet to be explored. To obtain an improved understanding of the full passive control characteristics of the sleeve, therefore, a parametric study is now undertaken to:

- Expand the range of sleeve lengths considered
- Investigate the effects upon higher shaft modes
- Identify the mechanism by which passive control occurs
- Consider the individual effects of sleeve stiffness and mass

Consideration of a greater range of sleeve lengths allows for the bounds of applicability of the passive control characteristics of the sleeve to be determined, and to identify the mechanism by which passive control occurs through the sleeves. Having a wider understanding of the magnitude and mechanism of effect will determine the viability of the sleeve as a credible passive control device for the future.

6.4 Mode Classification

A clear definition is now made regarding which modes are considered as part of this analysis. An ANSYS 17.0 modal analysis is used to produce visualisation of the mode shapes of the system in terms of relative displacements. For the system of the shaft with attached eccentric sleeves, the observed mode shapes are a combination of the relative displacements of both components of the system, with different degrees of dominance: some shaft dominated, others dominated by the sleeve. As the length of the sleeve changes, its flexibility and relative displacement also change. Therefore, the order in which the modes are produced may change, in which case, it is important to be able to distinguish between each characteristic mode shape.

To initially categorise the mode shapes, they are displayed for the sleeve length with matched flexibility to the shaft: 76mm. This length of sleeve provides a benchmark of displacement subject to free vibration relative to the shaft prior to making any modifications to the sleeve length and flexibility.

Mode shapes that are dominated by the shaft, designated MODE 1, MODE 2 and MODE 3, are presented in Figure 6.1 to Figure 6.3. These modes take fundamental bending mode shapes of the shaft:

- **MODE 1**, the first shaft mode (Figure 6.1), shows first order bending of the shaft with both sleeves bending in the same direction and in phase with each other.
- **MODE 2**, the second shaft mode (Figure 6.2) shows second order shaft bending with the sleeves opposing the shaft peaks and out of phase with each other.
- **MODE 3**, the third shaft mode (Figure 6.3) shows third order shaft bending with the sleeves opposing the outer peaks, but with the sleeves in phase with each other.

An illustrative measure of the particular dominance of a mode is determined by the ratio of maximum shaft and sleeve displacements; the displacement ratio (DR). A low DR, typically less than 1, indicates that a particular mode has the shaft with the greatest relative displacement, whereas a mode with a higher DR has the sleeve with the greatest relative displacement.



Figure 6.1 – MODE 1: Shaft dominated 1st bending mode (DR = 0.61)

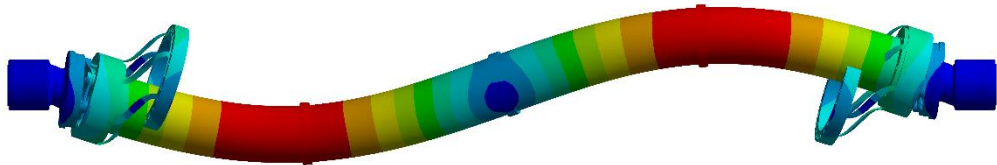


Figure 6.2 – MODE 2: Shaft dominated 2nd bending mode (DR = 0.43)

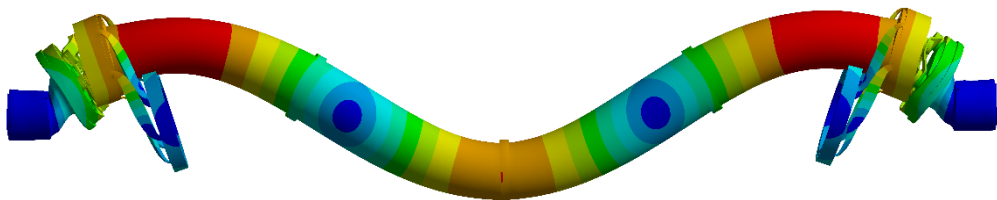


Figure 6.3 – MODE 3: Shaft dominated 3rd bending mode (DR = 0.86)

Sleeve dominated modes are shown in Figure 6.4 and Figure 6.5:

- **MODE 4**, the first sleeve dominated mode (Figure 6.4), shows large relative displacement of the sleeves with negligible deflection of the shaft. The sleeves are bending out of phase with each other.
- **MODE 5**, the second sleeve dominated mode (Figure 6.5), shows a minor first order bending motion of the shaft with significant relative displacement of the sleeves in the opposing direction. In this case both sleeves are bending in phase with each other.



Figure 6.4 – Mode 4: 1st sleeve dominated mode (DR = 22.3)



Figure 6.5 – Mode 5: 2nd sleeve dominated mode (DR = 4.79)

Several methods exist for the tracking and comparison of modes. Mode correlation criteria use matrices filled with terms between 0 and 1 (1 being a perfect match, 0 a poor match) [102]; the Modal Assurance Criterion (MAC) [103] is a commonly used method. The Normalised Cross Orthogonality (NCO) [104] and [105] uses mass or stiffness matrices to compare the orthogonality of modes. In this instance, however, it is the dominance of shaft or sleeve upon the deformed shape of the structure that is of interest. Therefore the dominance ratio and classification of ‘shaft’ or ‘sleeve’ mode is sufficient for this study.

6.5 Bounds of the Parametric Study

The bounds of the parametric study are chosen from observation of the mode shapes of the system. With a 26mm sleeve length it becomes possible to readily distinguish MODES 4 and 5. With shorter sleeve lengths, the sleeve has insufficient flexibility to bend and essentially acts as a rigid disk, and therefore clear sleeve modes are difficult to identify. Similarly, 136mm is the longest sleeve length where it is still possible to identify distinct sleeve mode shapes. At length greater than this the sleeve is so flexible it is difficult to identify shapes resembling MODE 4 or 5. Increments of 10mm between 26mm and 136mm are chosen for the study. In each case, the geometry of the sleeves is modified to the correct length using Design Modeller within the ANSYS Workbench suit. Table 6-1 shows the sleeve lengths used in the parametric study, with those previously used in Chapter 4 highlighted.

Table 6-1 – Sleeve lengths used for parametric study

26	36	46	56	66	76	86	96	106	116	126	136
x	x	x	x	✓	✓	✓	x	x	x	x	x

6.6 Modal Behaviour

Investigating the effects that a change in sleeve length has on the dynamics of the system, in particular the mode shapes, can be accomplished without considering the critical speeds of the system. Obtaining the natural frequencies and modes shapes at 0 rpm is computationally efficient as there are no rotational effects to accommodate. Therefore, a damped solver is not required and a faster Block Lanczos solver is used here. Neglecting rotational effects remove the splitting of modes and reduces the number of modes that need to be considered.

From the parametric sweep, Figure 6.6 shows the natural frequencies of MODES 1 to 5. Specifically, Figure 6.6(a) shows the natural frequencies of MODES 4 and 5 decrease with an exponential trend as sleeve length increases. Moreover, consideration of first shaft mode in Figure 6.6(b) shows the natural frequency converging with the first sleeve mode. This is suggestive of a mode that is initially dominated by the shaft eventually becoming dominated

by (only) one of the sleeve modes. This appears at odds with normal expectations, particularly when the natural frequency of sleeve bending is also considered.

The individual natural frequencies of the non-sleeve shaft and the sleeves themselves are obtained by conducting a modal analysis of the isolated sleeve and shaft bodies. The sleeve is analysed whilst clamped on its flange faces, as shown in Figure 6.8. The frequency of the bending is obtained for each of the sleeve lengths in Table 6-1. The shaft is analysed without the attached sleeves and the natural frequency of the first three bending modes recorded. The natural frequencies of each sleeve length and the three shaft bending modes are shown in Figure 6.7.

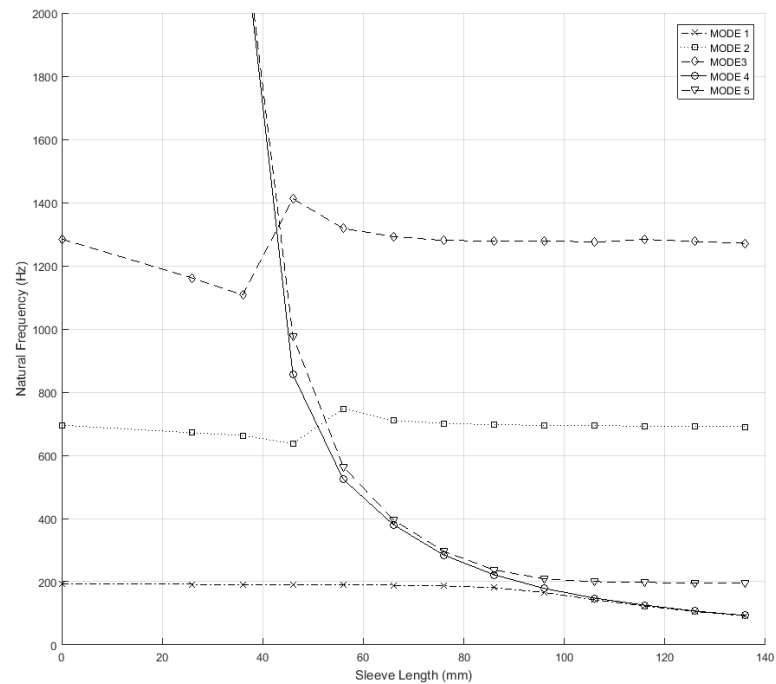


Figure 6.6 (a) – Natural frequencies of all modes against sleeve length

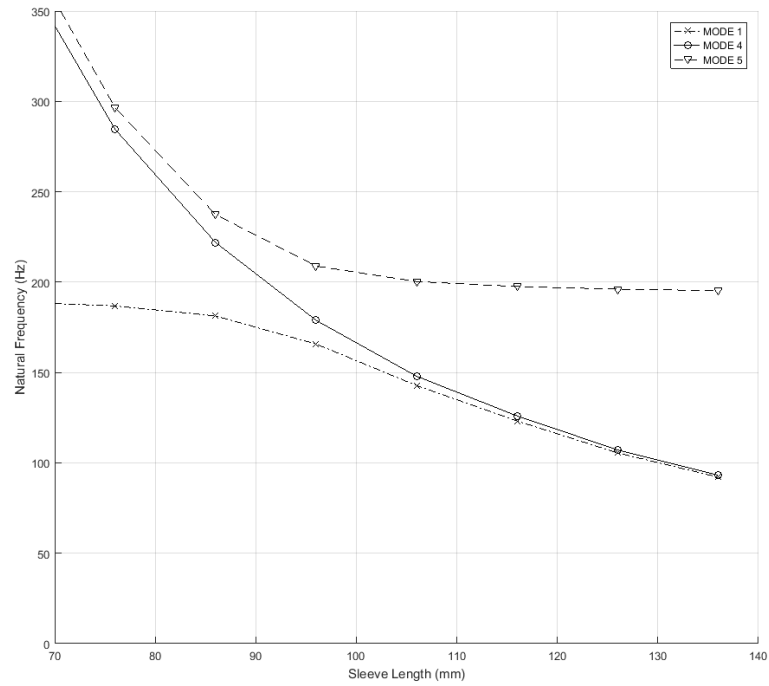


Figure 6.6 (b) – Natural frequencies of MODEs 1, 4 and 5 against sleeve length

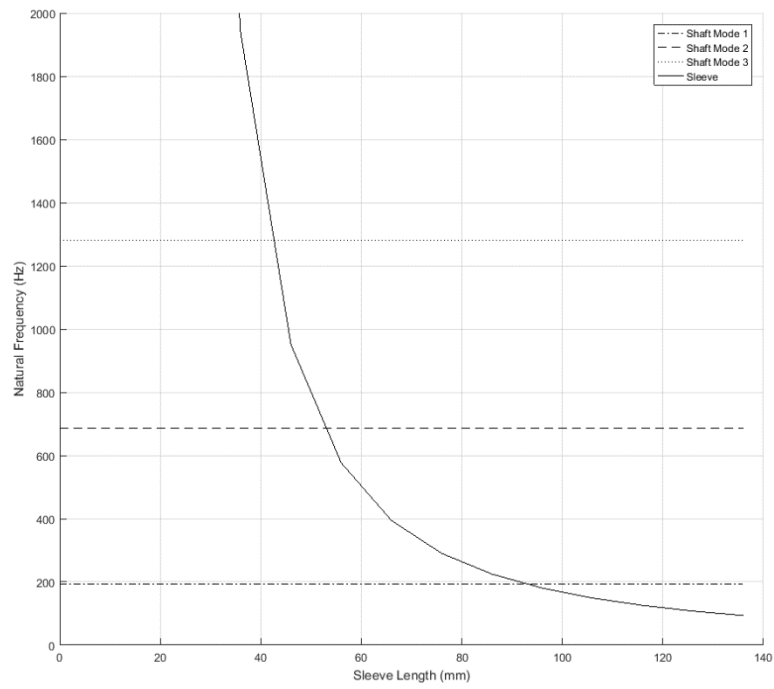


Figure 6.7 – Natural frequencies of bending for isolated shaft and sleeve

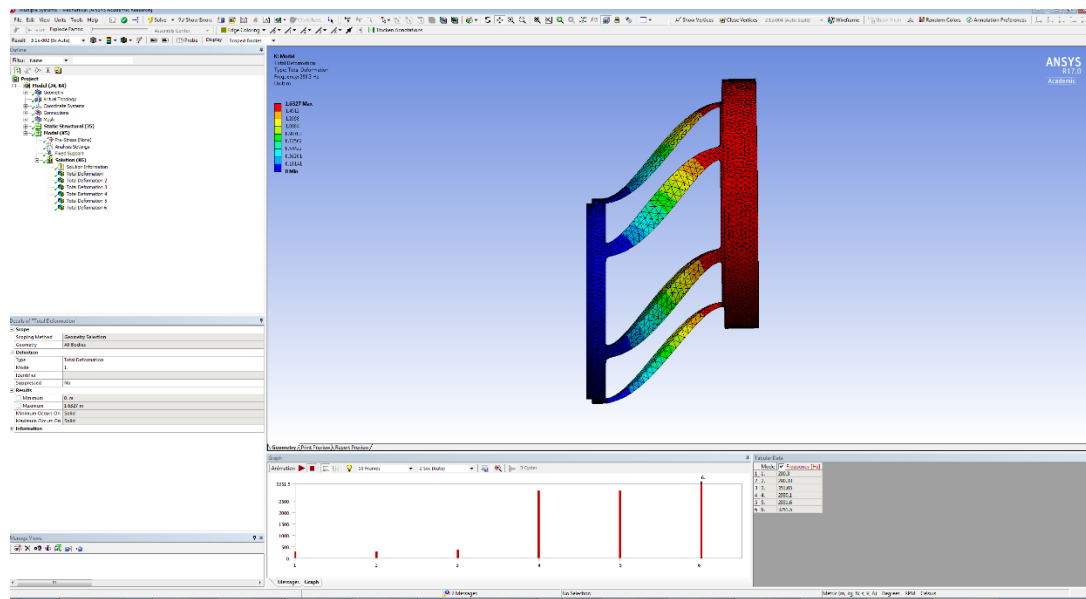


Figure 6.8 – Modal analysis of isolated sleeve

The sleeve natural frequency of bending decreases with an exponential trend with increasing sleeve length. By inspection of Figure 6.4 and Figure 6.5, both modes are dominated by sleeve bending, albeit with opposite phase. Therefore, it stands to reason that it is both the sleeve-dominated modes of the system that should follow the trend and not a mode that was initially dominated by the shaft.

With some ambiguity being identified around the natural frequencies associated with each mode, the mode shapes in the region where MODE 1 and MODE 4 converge, in Figure 6.6(b), are now more closely inspected. The mode shapes and displacement ratios for 76, 86, 96, 106 and 116mm sleeve lengths for MODES 1, 4 and 5 are presented, respectively, Table 6-2 to 6-4.

Table 6-2 shows MODE 1 is initially dominated by the shaft, but since sleeve flexibility increases with length, the mode shape becomes increasingly dominated by the sleeve. In particular, with a 116mm sleeve length the displacement of the shaft is negligible in comparison to that of the sleeve. Since this mode becomes dominated by the sleeve it is expected that it is more influenced by the bending of the sleeve, and therefore its natural frequency should decrease in concordance with Figure 6.7.

Table 6-3 shows that the shape of MODE 4 is very consistent with increasing sleeve length. There is a continuous increase in displacement ratio in favour of the sleeve whilst the shaft displacement remains negligible for all the sleeve lengths considered. As this mode remains dominated by the sleeve, the frequency of the mode should decrease in line with the frequency of the sleeve itself. It is concluded, therefore, that this mode is not interacting with the MODE 1 and it is correctly displayed in Figure 6.6.

Table 6-4 shows a similar but inverse pattern to Table 6-2 i.e. the sleeve is initially dominant but the shaft displacement surpasses it with increasing sleeve length. Despite the flexibility of the sleeve increasing with sleeve length, the mode shape becomes dominated by the displacement of the shaft itself. It would be expected that MODE 5 would follow the first natural frequency of the shaft.

Comparison of modes shapes for MODE 1 and MODE 5 show that they remain constant but a switch over in dominance appears between the shaft and the sleeve at a particular sleeve length. The displacement ratios in Figure 6.9 show this happens at approximately 92mm sleeve length. This coincides with the sleeve length at which the natural frequencies of sleeve bending and the first shaft mode are equal, in Figure 6.7.

Table 6-2 – MODE 1 displacement ratios and mode shapes






Sleeve Length (mm)	DR	Mode Shape
76	0.61	
86	1.08	
96	2.64	
106	5.68	
116	9.36	

Table 6-3 – MODE 4 displacement ratios and mode shapes











Sleeve Length (mm)	DR	Mode Shape
76	22.30	
86	35.78	
96	51.80	
106	70.59	
116	82.02	

Table 6-4 – MODE 5 displacement ratios and mode shapes

Sleeve Length (mm)	DR	Mode Shape
76	4.79	
86	2.69	
96	1.12	
106	0.56	
116	0.38	

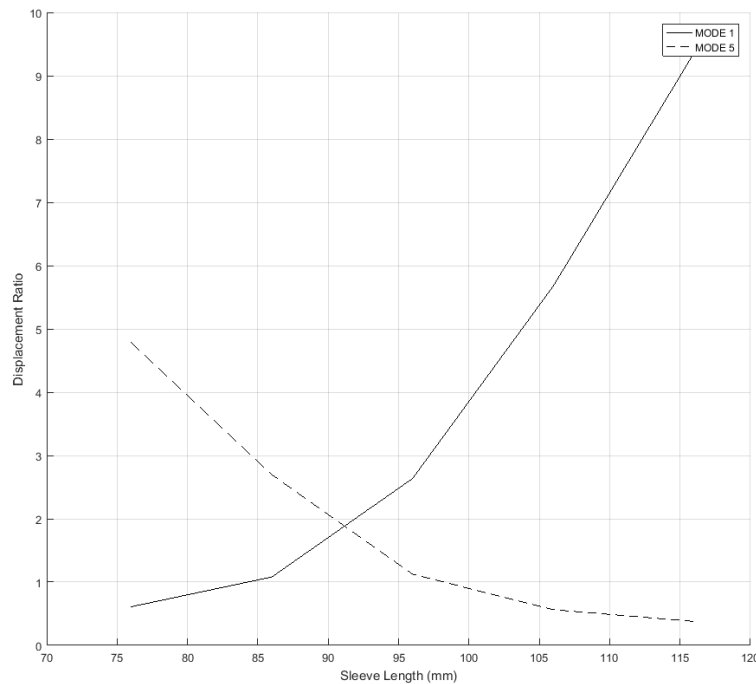


Figure 6.9 – Displacement ratio (DR) of MODE 1 and MODE 5 for sleeve lengths 76 to 116mm

6.7 Participation Factor and Effective Mass

The effective modal mass of a structure ($M_{i\text{eff}}$) is a measure of the significance of an individual mode of vibration with respect to the entire response of a structure [98]:

$$M_{i\text{eff}} = \frac{\gamma_i^2}{\{\bar{\mathbf{v}}_i\}^T [\mathbf{M}] \{\bar{\mathbf{v}}_i\}} \quad (6.1)$$

An individual mode with a high effective mass fraction has a significant proportion of the total mass of the system participating in the vibration, and will therefore be readily excitable. Conversely, a mode with a low effective mass will not be as readily excited. The participation factor, γ_i is the square root of effective mass and provides quantitative measure of comparing the significance of individual modes.

Participation factors are directly produced by ANSYS modal analysis. The participation factor results of the modal analysis are normalised against the mode with the largest participation factor. Figure 6.10 shows the normalised participation factors for the MODE 1 and MODE 5 for the range of sleeve lengths, 76 to 116mm.

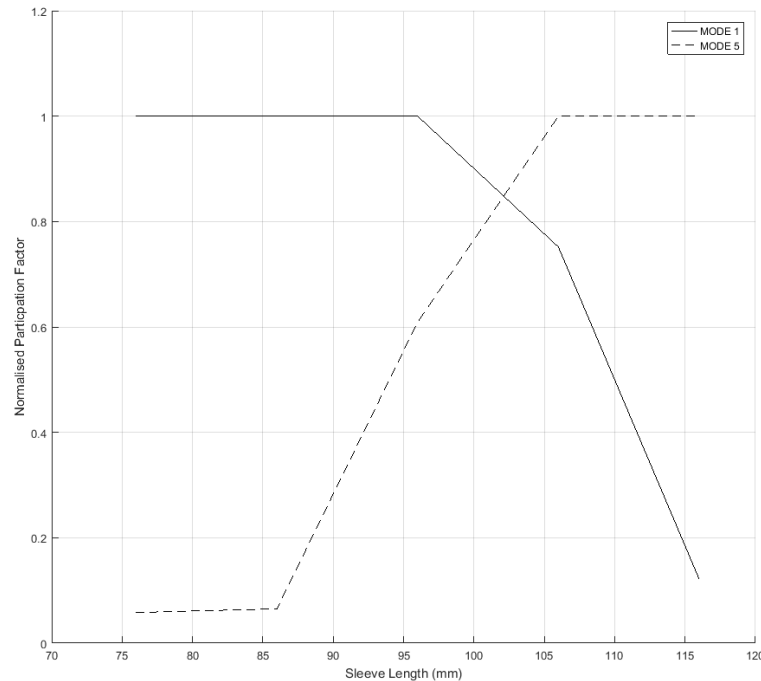


Figure 6.10 – Normalised participation factors for sleeve lengths 76 to 116mm

Figure 6.10 shows that the participation factor, and by definition effective mass, of the system shifting from MODE 1 to MODE 5. When coupled with the mode shapes displayed in Table 6-2 and Table 6-4, and the displacement ratios in Figure 1.1, this confirms that the dominance of the shaft is shifting from MODE 1 to MODE 5.

It is notable that the displacement ratios and participation factors for MODE1 and MODE 5 both allude to similar conclusions. However, there is a discrepancy between the two. Specifically, the DR shows a changeover in relative displacement at approximately 92mm, but the participation factors does not switch over until ~102mm. A possible explanation is that the relative displacement of the sleeves becomes greater at 92mm, but the full effective mass of the shaft does not move across modes until a slightly longer sleeve length is considered.

6.8 Revised Mode Classification

With increasing length, the structure is fundamentally being changed, therefore the modes shapes are not strictly identical. Since the dominance of the shaft is shown to shift from one mode shape to another with increasing sleeve length, the classification of a ‘shaft’ or ‘sleeve’ mode remains sufficient in this instance, however further analysis, using methods such as the mode assurance criteria, would give a better and statistical comparison of how the modes change with increasing sleeve length.

With the shifting dominance of the shaft between modes with increasing sleeve length, the definition of a ‘shaft’ mode now requires further clarification for these scenarios. To avoid confusion in classification of shaft and sleeve modes, *the n^{th} shaft mode is referred to as the lowest frequency mode dominated by shaft’s n^{th} order bending behaviour*. With this definition in mind, Figure 6.6(b) can now be displayed with greater clarity:

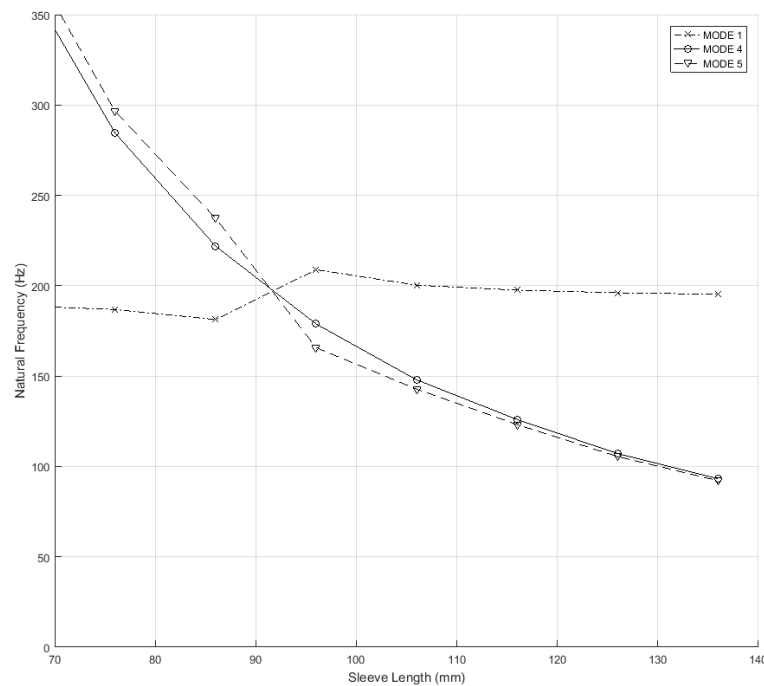


Figure 6.11 – Corrected natural frequencies of MODES 1, 4 and 5 against sleeve length

6.9 Higher Order Modes

For MODE 2 and MODE 3, Figure 6.6(a) shows a similar effect on the natural frequencies as that described for MODE 1, whereby there is an increase in shaft mode at a given sleeve length. The increase is observed for both modes in regions where the natural frequency of the shaft is close to that of the sleeve; 42 and 54mm respectively in this case.

MODE 2 and MODE 4 are shown in Table 6-5 and Table 6-6 respectively, for 36, 46, 56 and 66mm sleeve lengths. The now recognisable pattern of shifting shaft dominance from MODE 2 to MODE 4 is observed as sleeve length increases. Figure 6.12 shows the shaft dominance changing from MODE 2 to MODE 4 at approximately 48mm sleeve length in this case.

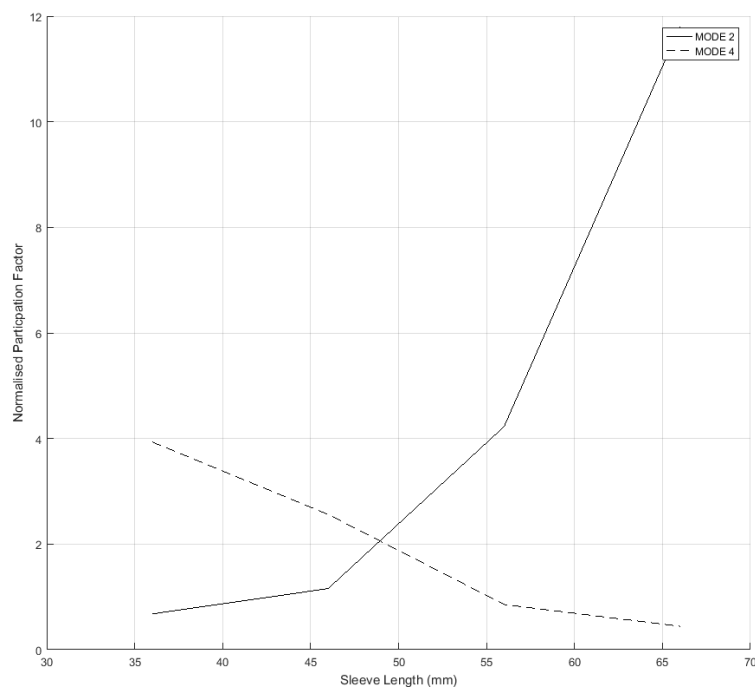


Figure 6.12 – Displacement ratio (DR) of MODE 2 and MODE 4 for sleeve lengths 36 to 66mm

Table 6-5 – MODE 2 displacement ratios and mode shapes

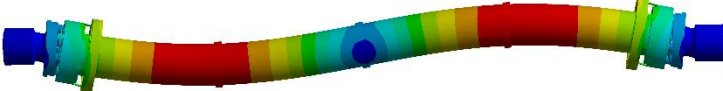
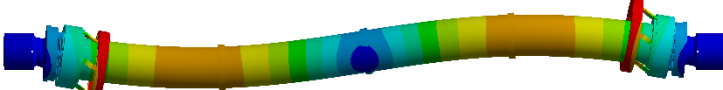



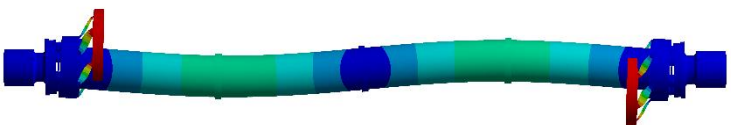
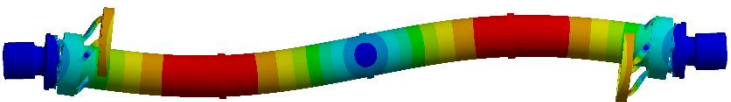
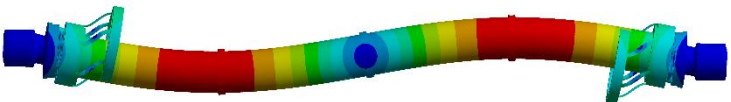
Sleeve Length (mm)	DR	Mode Shape
36	0.68	
46	1.16	
56	4.23	
66	11.81	

Table 6-6 – MODE 4 displacement ratios and mode shapes

Sleeve Length (mm)	DR	Mode Shape
36	3.93	
46	2.56	
56	0.86	
66	0.44	

Similarly, MODE 3 and MODE 5 are shown in Table 6.7 and Table 6.8, respectively, for 26, 36, 46 and 56mm sleeve lengths. The shape of MODE 5 for the 26mm sleeve shows influence of a much higher order mode than third order shaft bending, namely the fifth order. On closer inspection, the sleeves are deforming in the opposite direction to the shaft. Due to the short length of the sleeves, they are effectively rigid disks with an extremely high natural frequency. It is reasonable to assume that the high natural frequency is interacting with a higher order mode of the shaft, hence the observed mode shape. As the sleeve length is increased, the shifting dominance of the shaft is repeated from MODE 3 to MODE 5. Figure 6.13 shows the shaft dominance changing from MODE 3 to MODE 5 at approximately 48mm sleeve length.

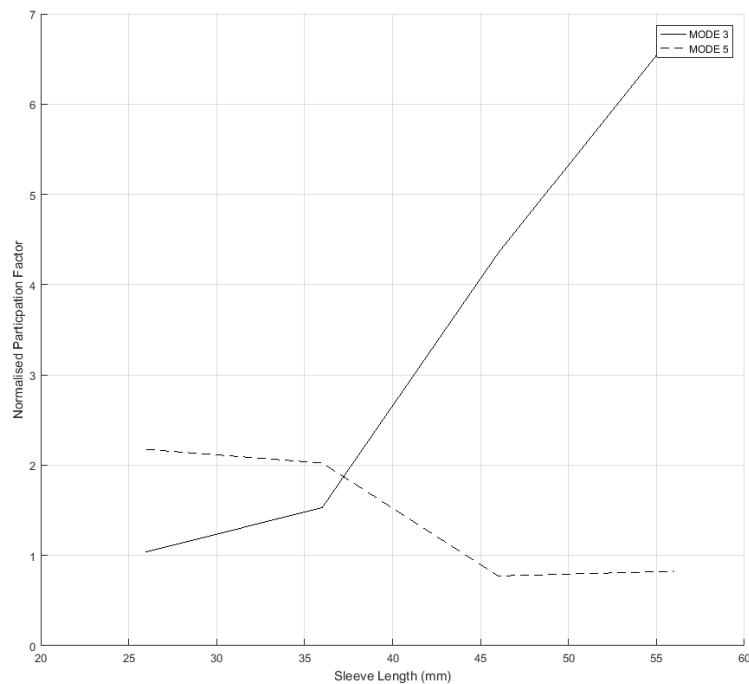


Figure 6.13 – Displacement ratio (DR) of MODE 3 and MODE 4 for sleeve lengths 26 to 56mm

Table 6-7 – MODE 3 displacement ratios and mode shapes


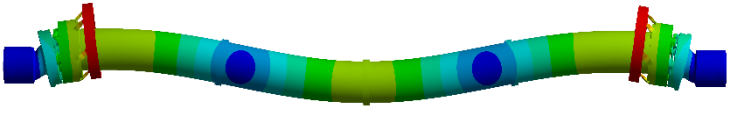


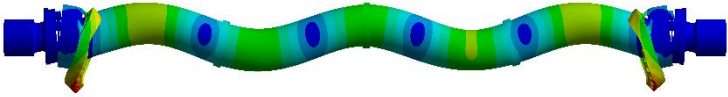



Sleeve Length (mm)	DR	Mode Shape
26	1.04	
36	1.53	
46	4.35	
56	6.78	

Table 6-8 – MODE 5 displacement ratios and mode shapes

Sleeve Length (mm)	DR	Mode Shape
26	2.17	
36	2.02	
46	0.77	
56	0.82	

The response of the structure is dominated by the first bending mode of the shaft (MODE 1) and therefore the participation factors for the other higher modes are low, and it is therefore difficult to derive meaningful information from the data. However, the presented mode shapes and displacement ratios offer sufficient evidence to confirm that there is an interaction between shaft and sleeve for each of the initially shaft dominated modes, that shifts the shaft motion, resulting in an effectual increasing of natural frequencies of the shaft.

6.10 Passive Control of Critical Speeds

From the non-rotating natural frequencies of the system, the modes have been correctly identified and classified. Rotational effects are applied to the model viz. Section 4.5.7, and Campbell diagrams used to extract the forward whirling critical speeds of the shaft for sleeve lengths from 0 to 136mm. Figure 6.14 shows the absolute critical speeds for the first three modes of the shaft. Figure 6.15 shows the critical speeds of each of the three shaft modes, normalised against the non-sleeve critical speed for each.

All three shaft modes show an initial decrease in critical speed with added sleeve length, followed by a sharp increase in the regions where the natural frequency of the sleeves coincide with each mode of the shaft, followed by another steady decrease beyond this region. The critical speed of the first shaft mode never decreases below those of either of the sleeve modes.

The effect of increasing critical speeds is classified as positive passive control and the reduction of critical speeds, of negative passive control. The point at which each mode changes from negative to positive control occurs at shorter lengths for increasing mode number. From Figure 6.7, this occurs due to the exponential increase in natural frequency of the sleeve as it approaches the natural frequencies of the higher modes of the shaft.

The normalised data shows the maximum positive increase of critical speeds is relatively consistent (but not exact) for all modes, at approximately +10%. There is an increasing maximum reduction in critical speed with higher modes: from 5% on the first mode, 7% for the second and up to 15% for the third shaft mode.

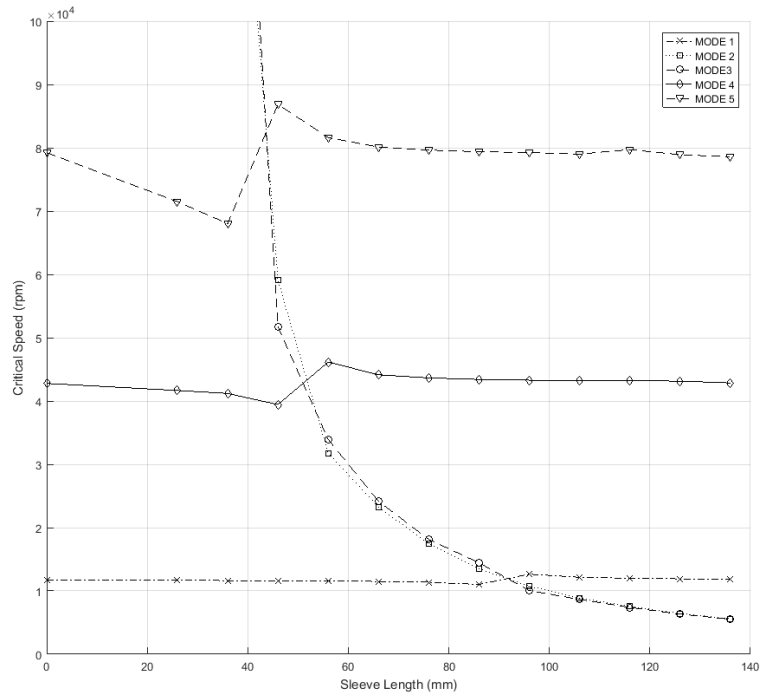


Figure 6.14 – Critical speeds of all considered modes for sleeve lengths 0 to 136mm

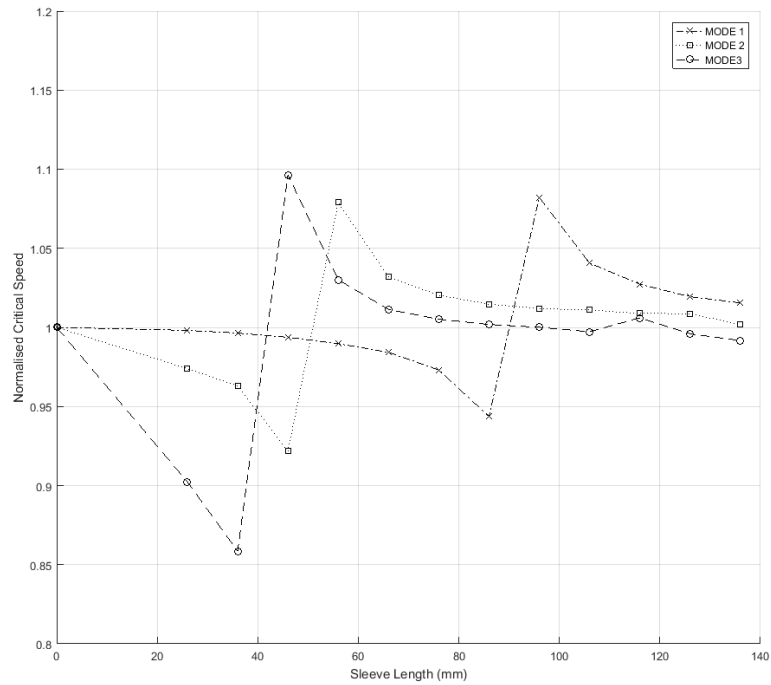


Figure 6.15 – Normalised critical speeds of shaft bending modes for sleeve lengths 0 to 136mm

6.11 Effect of Stiffness and Mass

To investigate the individual effects of sleeve mass and stiffness, the process for replacing sleeve geometry with equivalent mass and inertia, viz Section 4.6, is applied to all the sleeve lengths under consideration; 26 to 136mm. Figure 6.16 to Figure 6.18 show the critical speeds for the full geometry and point mass models for each of the three shaft modes respectively.

When sleeve flexibility is neglected, each of the three shaft modes do not show the expected change over from positive to negative passive control. With the exception of the third mode, which shows a significant decrease with the addition of the shortest sleeve length, for each mode increasing sleeve length has an increasing softening effect on the critical speeds.

For sleeve lengths away from the region of changeover, e.g. 0-70 and 110-140 mm for the first mode, the full geometry model shows a similar softening effect as the non-flexibility case. Therefore, in these regions the passive control mechanism is due to added mass of the sleeve.

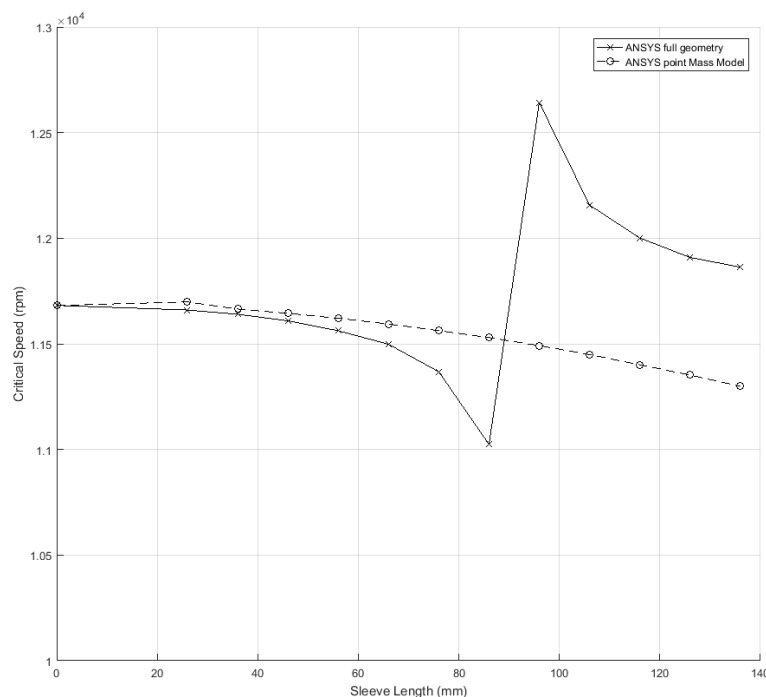


Figure 6.16 – First critical speeds including point mass model for sleeve lengths 0 to 136mm

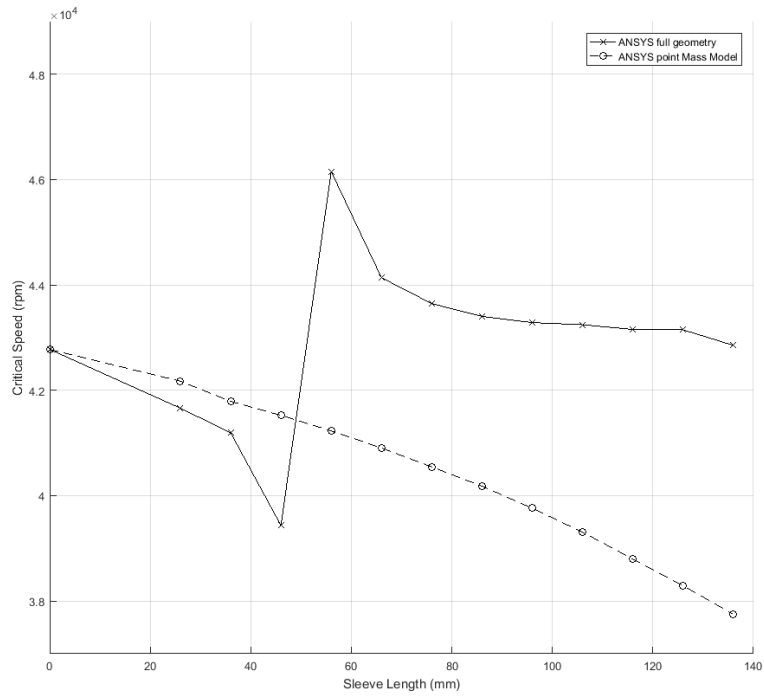


Figure 6.17 – Second critical speeds including point mass model for sleeve lengths 0 to 136mm

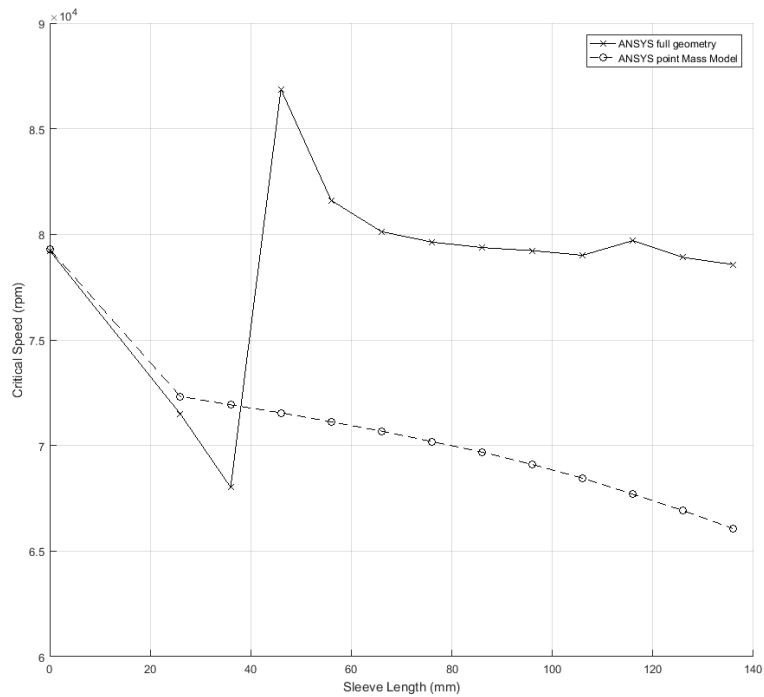


Figure 6.18 – Third critical speeds including point mass model for sleeve lengths 0 to 136mm

6.12 Conclusions

A parametric study to expand the range of sleeve lengths analysed, has been conducted. Using the validated finite element model from Chapters 4 and 5, modal analysis on a combination of shaft, sleeve and shaft and sleeve together have shown that the effective mass of the shaft is dominant in its first mode. This dominance shifts between two mode shapes of the system, resulting in an effective increase in shaft critical speed. This phenomenon occurs at sleeve lengths where the natural frequency of the sleeve is close to that of each of the modes of the shaft. Finally, by neglecting the flexibility of the sleeves, it is shown that for sleeve lengths that do not have natural frequencies that match any of the modes of the shaft, the critical speeds are reduce progressively.

Based on the conducted analysis, it is concluded that the mechanism of passive control is a combination of softening due to added mass of the sleeves and coherence of the individual modes of the shaft and sleeves.

Without consideration of sleeve flexibility it is not possible to increase the critical speed of any of the three shaft modes. It is shown for very short sleeve lengths that they are essentially rigid bodies with high natural frequencies and do not interact with the lower modes of the shaft.

Sleeve lengths at which the natural frequency does not coincide with one of the modes of the shaft, reduce the critical speeds of all modes, with progressively increasing effect with higher modes. Dependant on the desired method of control, selection of a specific sleeve length will offer either positive or negative passive control.

In this manner, the sleeves are not dissimilar to a tuned mass damper. When comparing a fixed operational speed with and without attached sleeves, if the natural frequency of the sleeve is matched to one of the modes of the shaft, it would be anticipated that the critical speed would increase and the amount of vibration at that speed would reduce.

The defined mechanism offers the opportunity to increase the critical speed margin in practical applications and reduce unwanted lateral vibrations. However, users must be mindful that as sleeve length is increased, the corresponding critical speeds decrease and may become more detrimental than those of the shaft that are intended for control.

Chapter 7 Conclusions and Recommendations

This thesis has presented a new method for controlling the critical speeds of a rotating shaft using attached eccentric sleeves. This chapter draws together the various elements undertaken in the course of this thesis. The main conclusions are discussed, with recommendations for future work presented.

7.1 Research Contributions

- The mechanism by which passive control occurs is a combination of mass damping and coherence of shaft and sleeve natural frequencies
- The effect of adding eccentric balancing sleeves upon the dynamics of a rotating shaft is similar to that of a tuned mass damper
- Sleeve stiffness must be considered as part of the analysis as it has a significant effect upon the critical speeds of the shaft.

7.2 Conclusions

All mechanical systems have an infinite number of frequencies which when excited will cause it to resonate. When the natural frequencies of rotating systems are excited, usually through unbalanced forces, the speed at which these vibrations occur are called a critical speed. The standard techniques for mitigating vibration in rotating structures are split into three main categories; Careful design and manufacture, correct installation and effective control strategies.

The eccentric sleeves were developed as a ‘semi active’ method of vibration control to improve the state of balance of dynamically unstable coupling shafts. However, adding the sleeves affects inherent dynamics of the shaft, requiring detailed analysis to understand and

quantify the effects. As a first approximation, the sleeves are modelled theoretically as part of a simplified representation of a full coupling shaft using the Extended Hamilton's Principle.

Initial simulations suggest that the flexibility of the sleeves has little impact upon the dynamics of the system and can therefore be neglected. Generally, to obtain an approximate solution for a continuous system it must first be discretised into a finite number of packages or elements. Ergo, the derived equations of motion are discretised using the Galerkin method and the resulting matrices solved numerically. Comparison with computational finite element methods for a small number of different sleeve lengths identifies a discrepancy between the two.

Experimental validation using a purpose built high speed test facility gives good indication that the difference is due to the lack of sleeve flexibility in the theoretical model. Therefore in order to understand the mechanism of the sleeve dynamics, the full geometry of the system must be analysed using finite element simulations.

A broader parametric study of sleeve lengths shows that the definition of a 'shaft mode' is fluid due to the effective mass of the shaft shift from an initially shaft dominated mode shape to a initially sleeve dominated mode shape. The phenomenon occurs at sleeve lengths where the natural frequency of the sleeve is close to those of the shaft. Based upon the conducted analysis, it is concluded that the mechanism of passive control is a combination of softening due to added mass of the sleeves and coherence of the individual modes of the shaft and sleeves. In this manner, the sleeves are not dissimilar to a tuned mass damper.

The defined mechanism offers the opportunity to increase the critical speed margin in practical applications and reduce unwanted lateral vibrations. However, potential users must be mindful that as sleeve length is increased, the corresponding critical speeds decrease and may become more detrimental than those of the shaft that are intended for control.

7.3 Recommendations for Further Work

This work identified the possible mechanism by which the chosen design of sleeve can passively control the critical speeds of a rotating shaft. Although some degree of parametric study has been conducted to broaden the scope of the investigation, additional work could open this out further and help to obtain an even better understanding of the dynamics.

The discrepancy between the theoretical and finite element models was attributed to the lack of consideration of sleeve flexibility in the theoretical model. The neglected higher order terms in the theoretical derivation may warrant further investigation to identify if these have any effect upon the coherence of the two modelling approaches.

Using the current range of sleeve lengths already considered, response analysis could be carried out using finite element simulations. Using the no-sleeve case as a benchmark with a small and fixed amount of unbalance excitation, the effect of changing the sleeve length (and therefore shaft critical speed) would demonstrate if the observed levels of vibration produced are mitigated or increased.

During observation of the long sleeve (86mm) configuration, high levels of vibration were observed and the test was aborted. The reason for these high levels of vibration are unknown. They could potentially be due to high levels of unbalance in the sleeve itself but may be due to, so far, unidentified stability issues. Further theoretical analysis of the design along with additional experimental testing could identify the cause of the vibration. Some of the sleeve lengths identified do have a significant, positive and usable impact upon the shaft dynamics but would require operation at speeds above the sleeve critical speeds. If significant instabilities can be identified with thorough analysis, this would prevent significant damage and disregard these particular sleeve lengths from consideration.

This investigation has been limited to the geometry of the sleeve as it was designed for balancing purposes, with slight modifications to the length. Investigating the individual effects of mass and stiffness of the sleeve upon the shaft critical speed would decouple the passive control characteristics away from the existing geometry and lead to other potential designs, for example a high stiffness/low mass tube without the heavy ring seen in Figure 1.5

With an alternative configuration identified, further experimental validation could be undertaken to include elements of active control. If the stiffness of the geometry is identified as the key factor in passive control, a sleeve with variable stiffness could be designed. This could be 'tuned' to suit the shaft which it is connected, even during operation where the effect on vibration levels is monitored.

References

- [1] “Industrial Gas Turbines”, *Siemens Gas Turbines*, [Online] Available: <http://www.energy.siemens.com/hq/en/powergeneration/gas-turbines>
- [2] M. P. Boyce, *Gas turbine engineering handbook*, 2nd ed., Gulf Professional publishing, 2002.
- [3] M. I. Friswell, J. E. Penney, S. D. Garvey and A. W. Lees, *Dynamics of rotating structures*, New York, NY: Cambridge University Press, 2010.
- [4] M. L. Adams Jr, *Rotating machinery vibration*. 2nd ed., Boca Raton, FL: CRC Press, 2010.
- [5] Y. Batrak, “Lateral Vibration Prediction Issues”, Shaftdesigner, The Netherlands, 2010.
- [6] *Special Purpose Couplings for Petroleum, Chemical and Gas Industry Services*, API 617, 2007.
- [7] G. Knowles, “Apparatus comprising a shaft and a balancing sleeve”, U.S. Patent 8556738 B2, 24 Feb 2010
- [8] W. Rankine, “On the Centrifugal Force of Rotating Shafts”, *Engineer*, 27, pp.247:249, 1869.

- [9] S. Dunkerley, "On the Whirling and Vibration of Shafts", *Philosophical Transactions of the Royal Society of London, Series A*, vol. 185, part I, pp.279, 1894.
- [10] W. Weaver, *Theory of the vibration of rotating shafts*, University of Wisconsin, 1917.
- [11] H.H. Jeffcott, "The lateral vibration of loaded shafts in the neighbourhood of a whirling speed - The effect of want of balance", *Philosophical Magazine*, series. 6, vol. 37, pp. 304-314, 1919.
- [12] S. Timoshenko, D. H. Young, W. Weaver Jr, *Vibration problems in engineering*, John Wiley and Sons, 1974.
- [13] R. Bishop, "The Vibration of Rotating Shafts", *IMEchE Part C: J Mechanical Engineering Science*, vol.1, pp. 50-65, 1959.
- [14] R. Bishop and G. Gladwell, "The vibration and balancing of an unbalanced flexible rotor", *IMEchE Part C: J Mechanical Engineering Science*, vol.1, pp. 66-77, 1959.
- [15] G. Gladwell and R. Bishop, "The vibration of rotating shafts in flexible bearings", *IMEchE Part C: J Mechanical Engineering Science*, vol.1, pp. 195- 206, 1959.
- [16] A. Foppl, "Das problem das Laval'schen turbinewelle", *Civilingenieur* vol. 41, pp. 248-250, 1895.
- [17] C. Chree, "The whirling and transverse vibrations of rotating shafts", *Philosophical Magazine*, vol. 19, pp. 504-542, 1903.
- [18] J.S. Rao, *History of rotordynamics*, *History of Mechanism and Machine Science* 20, Springer, 2011.
- [19] R.B. Green, "Gyroscopic effects on the critical speeds of flexible rotors", *Transactions of the American Society of Mechanical Engineers*, vol. 70, pp. 369-376, 1948.

- [20] M. I. Friswell, S. D. Garvey, J. E. T. Penny and M. G. Smart, "Computing critical speeds for rotating machines with speed dependent bearing properties", *Journal of Sound and Vibration*, vol. 213(1), pp. 139-158, 1998.
- [21] ANSYS Mechanical APDL Rotordynamic Analysis Guide. Version 17.0
- [22] E. Swanson, C. D. Powell and S. A. Weissman, "A practical review of rotating machinery critical speeds and modes", *Sound and Vibration*, pp. 10-17, May 2005.
- [23] R. Tiwari, A. W. Lees and M. I. Friswell, "Identification of Dynamic Bearing Parameters", *The Shock and Vibration Digest*, vol. 36(2), pp. 99-124, 2004.
- [24] F. Lewis, "Vibration during acceleration through a critical speed" *Journal of Applied Mechanics*, vol.54, pp. 253-257, 1932.
- [25] A. Srinivasan and T. Thurston, "GT2012 2012 - The limited torque acceleration through critical speed phenomenon in rotating machinery", *Proceedings of ASME Turbo Expo, Copenhagen, Denmark, 2012*.
- [26] D. Combescure and A. Lazarus, "Refined finite element modelling for the vibration analysis of large rotating machines: Application to the gas turbine modular helium reactor power conversion unit", *Journal of Sound and Vibration*, vol. 318, pp. 1262-1280, 2008.
- [27] G. Genta and M. Silvagni, "On Centrifugal Softening in Finite Element Method Rotordynamics", *Journal of Applied Mechanics*, vol. 81, 2014.
- [28] E. Downham, "The critical whirling speeds and natural vibrations of a shaft carrying a symmetrical rotor", *Ministry of Supply, ARC R&M No 2854, 1954*.
- [29] D. Inman, *Engineering vibrations*, 3rd ed., Pearson, 2008.

- [30] L. M. Greenhill and G. A. Cornejo, "Critical speeds resulting from unbalance excitation of backward whirl modes", ASME Design Engineering Technical Conferences, vol. 3, part. B, 1995.
- [31] J. Vance J, F. Zeidan and B. Murphy, *Machinery vibration and rotordynamics*, John Wiley & Sons, 2010.
- [32] D. G. Huang, "Characteristics of torsional vibrations of a shaft with unbalance", Journal of Sound and Vibration, vol. 308, pp. 692-698, 2007.
- [33] B.O. Al-Bedoor, "Modelling the coupled torsional and lateral vibrations of unbalanced rotors", Computer Methods in Applied Mechanics and Engineering vol. 190, pp. 5999-6008, 2000.
- [34] J. Wu and I. Yang, "Computer method for torsion and flexure coupled forced vibration of shafting system damping", Journal of Vibration and Control 1995, vol; 180: pp. 417-435, 1995.
- [35] Q. H. Qin and C. X. Mao, "Coupled torsional-flexural vibration of shaft systems in mechanical engineering 1 - Finite element model", Computers and Structures, vol. 58, no.4, pp. 835-843, 1996.
- [36] D. G. Huang, "Characteristics of torsional vibrations of a shaft system with parallel misalignment", IMechE Part C: J Mechanical Engineering Science vol. 219, pp. 1219-1224, 2005.
- [37] M. Li and L. Yu, "Analysis of the coupled lateral torsional vibration of a rotor bearing system with a misaligned gear coupling", Journal of Sound and Vibration, vol. 243, pp. 283-300. 2001.
- [38] Z. Gorsiewski, "Analysis of coupling mechanism in lateral-torsional rotor vibrations", Journal of Theoretical and Applied Mechanics, 46(4), pp. 829-844, 2008.

- [39] K. V. S. Seshendra Kumar and B. S. K. SundaraSiva Rao, "An experimental study of whirling characteristics of gear pinion rotor system", *International Journal of Mechanics and Applications*, 2(2), pp. 10-13, 2012.
- [40] M. Ananda Rao, J. Srinivas, V. Rama Raju and K. Mumar, "Coupled torsional lateral vibration analysis of geared shaft systems using mode synthesis", *Journal of Sound and Vibration*, vol.261, pp. 359-364, 2003.
- [41] A.S. Lee, J. W. Ha and D.H. Choi, "Coupled lateral and torsional characteristics of a speed increasing geared rotor system", *Journal of Sound and Vibration*, vol. 263, pp. 725-742, 2003.
- [42] C. A. Papadopoulos and A. D. Diamarogonas, "Coupled longitudinal and bending vibrations of a rotating shaft with an open crack", *Journal of Sound and Vibration*, vol.117, pp. 81-93, 1987.
- [43] C.A. Papadopoulos and A. D. Diamarogonas, "Stability of cracked rotors in the coupled vibration mode", *Journal of Vibration, Acoustics, Stress and Reliability in Design*, vol. 110, pp. 356-359, 1988.
- [44] M. Behzad and A. R. Bastami, "Effect of centrifugal force on natural frequency of lateral vibration of rotating shafts", *Journal of Sound and Vibration*, vol. 274, pp. 985-995, 2004.
- [45] Z. Lua and X. Sun, "Coupled torsional-lateral-axial vibration analysis of a geared shaft system using substructure synthesis", *Mechanism and Machine Theory*, 31(3), pp. 345-352, 1996.
- [46] A.K. Darpe, K. Gupta and A. Chawla, "Coupled bending, longitudinal and torsional vibrations of a cracked rotor", *Journal of Sound and Vibration*, vol. 269, pp. 33-60, 2004.
- [47] ANSYS Training Material. Lecture 2: Modal Analysis – Introduction to Rotordynamics. Version 14.5

- [48] D.J. Ewins, *Modal Testing: Theory, Practice and Application, Second Edition*, Research Studies Press Ltd, 2000.
- [49] Brüel & Kjær, *Sound & Vibration Measurement, A/S*.
- [50] A. Vollen and L. Komzsik, *Computational Techniques of Rotor Dynamics with the Finite Element Method*, CRC Press, 2012.
- [51] A. W. Lees, J. K. Sinha and M. I. Friswell, "Model-based identification of rotating machines", *Mechanical Systems and Signal Processing*, vol. 23, pp. 1884-1893, 2009.
- [52] J.J Yu, "On two plane balancing of symmetric rotors", *Proceedings of ASME Turbo Expo*, Copenhagen, Denmark, 2012.
- [53] P.G. Morton, "Modal balancing of flexible shafts without trial weights", *IMechE Part C: J Mechanical Engineering Science*, vol. 199, pp.71-78, 1985.
- [54] A. G. Parkinson, "Balancing of rotating machinery", *IMechE Part C: J Mechanical Engineering Science*, vol. 205, pp. 53-66, 1991.
- [55] D. J. Rodrigues, A. R. Champneys, M.I. Friswell and R.E. Wilson, "Automatic balancing of a rigid rotor with misaligned shaft", *Applied Mechanics and Materials*, 5(6), pp. 231-236, 2006.
- [56] S.D. Garvey, M.I Friswell, E.J. Williams and I. D. Care, "Robust balancing for rotating machines", *IMechE Part C: J Mechanical Engineering Science*, vol. 216, pp. 1117-1130, 2002.
- [57] "An engineer's guide to shaft alignment, vibration analysis, dynamic balancing and wear debris analysis", *Pruftechnik*, 2002.
- [58] H. P. Bloch, "Update your shaft-alignment knowledge", *Chemical Week Publishing Llc*, 111(9), pp 68-72, September 2004

- [59] S. Prabhakar, A.S. Sekhar and A. R. Mohanty, "Vibration analysis of a misaligned rotor-coupling-bearing system passing through critical speed", *IMEchE Part C: J Mechanical Engineering Science*, vol. 215, pp. 1417-1428, 2001.
- [60] P. N. Saavedra and D. E. Ramirez, "Vibration analysis of rotors for the identification of shaft misalignment - Part 1 Theoretical Analysis", *IMEchE Part C: J Mechanical Engineering Science*, vol. 218, pp. 971-985, 2004.
- [61] P. N. Saavedra and D. E. Ramirez, "Vibration analysis of rotors for the identification of shaft misalignment - Part 2 Experimental validation", *IMEchE Part C: J Mechanical Engineering Science*, vol. 218, pp. 987-999, 2004.
- [62] T. H Patel, M. J. Zuo and A. K. Darpe, "Vibration response of coupled rotor systems with crack and misalignment", *IMEchE Part C: J Mechanical Engineering Science*, vol. 225, pp. 700-713, 2011.
- [63] S. Ganesan and C. Padmanabhan, "Modelling of parametric excitation of a flexible coupling-rotor system due to misalignment", *IMEchE Part C: J Mechanical Engineering Science*, vol. 225, pp. 2907-2918, 2011.
- [64] Y. A. Wang and D. Inman, "Comparison of Control Laws for Vibration Suppression Based on Energy Consumption", *Journal of Intelligent Material Systems and Structures*, vol. 22, pp. 795-809, 2011.
- [65] M. O. T. Cole, P. S. Keogh and C. R. Burrows, "Control of multi-frequency rotor vibration components", *IMEchE Part C: J Mechanical Engineering Science*, vol. 216, pp. 165-177, 2002.
- [66] S. Zhou S and J. Shi, "Active Balancing and Vibration Control of Rotating Machinery: A Survey", *The Shock and Vibration Digest*, vol. 33, pp. 361-371, 2001.
- [67] C. R. Burrows, P. S. Keogh and M. NSahinkaya, "Progress towards smart rotating machinery through the use of active bearings", *IMEchE Part C: J Mechanical Engineering Science*, vol. 223, pp. 2849-2859, 2009.

- [68] J. M. Hale, J. R. White, R. Stephenson and F. Liu, "Development of piezoelectric paint thick-film vibration sensors", *IMechE Part C: J Mechanical Engineering Science*, vol. 219, pp. 1-9, 2005.
- [69] M. N. Ghasemi-Nejhad, S. Pourjalali, M. Uyema and A. Yousefpour, "Finite Element Method for active vibration suppression of smart composite structures using piezoelectric materials", *Journal of Thermoplastic Composite Materials*, vol. 19, pp. 309-352, 2006.
- [70] V. Sethi, M. A. Franchek and G. Song, "Active multimodal vibration suppression of a flexible structure with piezoceramic sensor and actuator by using loop shaping", *Journal of Vibration and Control* vol. 17, pp. 1994-2006, 1994.
- [71] N. D. Sims, P. V. Bayly and K. A. Young, "Piezoelectric sensors and actuators for milling tool stability lobes", *Journal of Sound and Vibration*, vol. 281, pp. 743-762, 2005.
- [72] H. G. Horst and P. Wolfel, "Active Vibration Control of a high speed rotor using PZT patches on the shaft surface. *Journal of Intelligent Material Systems and Structures*, vol. 15 pp. 721-728, 2004.
- [73] P. J. Sloetjes and A. De Boer, "Vibration reduction and power generation with piezoceramic sheets mounted to a flexible shaft", *Journal of Intelligent Material Systems and Structures*, vol. 19, pp. 25-34, 2008.
- [74] A. B Palazzolo, R. R. Lin, R. M Alexander, A. F. Kascak and J. Montague, "Test and theory for piezoelectric actuator active vibration control of rotating machinery", *Journal of Vibration and Acoustics*, vol. 113, pp. 167-175, 1991.
- [75] Z. Abduljabbar, M. M. Elmadany and A. A. AlAbdulwahab, "Active vibration control of a flexible rotor. *Computers & Structures*, vol. 58, pp. 499-511, 1996.
- [76] G. Pinte, S. Devos, W. Symens, B. Stallaert, J. Swevers and P. Sas, "A modular bearing with internal piezoshunt damping"

- [77] G. Pinte, S. Devos, B. Stallaert, W. Symens, J. Swevers and P. Sas, "A piezo-bearing for the active structural acoustic control of rotating machinery", *Journal of Sound and Vibration*, vol. 329, pp. 1235-1253, 2010.
- [78] D. Wang, M. I. Friswell and Y. Lei, "Maximising the natural frequency of a beam with an intermediate elastic support", *Journal of Vibration and Sound*, vol. 291, pp. 1229-1238, 2006.
- [79] M. I. Friswell and D. Wang, "The minimum support stiffness required to raise the fundamental natural frequency of plate structures", *Journal of Sound and Vibration*, vol. 301, pp. 665-677, 2007.
- [80] S. Suherman and R. H. Plaut, "Use of a flexible internal support to suppress vibrations of a rotating shaft passing through critical speed", *Journal of Vibration and Control*, vol. 3, no. 2, pp. 213-233, 1997.
- [81] A. Delgado and L. San Andrés, "Identification of Force Coefficients in a Squeeze Film Damper with a Mechanical Seal: Large Contact Force", *ASME Journal of Tribology*, vol. 132, pp. 1-7, 2010.
- [82] Y. Y. Lin, C.M. Cheng and C.H. Lee, "A tuned mass damper for suppressing the coupled flexural and torsional buffeting response of long span bridges", *Engineering Structures*, vol. 22, pp. 1195-1204, 2000.
- [83] T. Hanzawa and K. Isoda, "Vibration control by a TMD using a rotational inertial mass", 15th World Conference on Earthquake Engineering, Lisbon, 2012.
- [84] P. Borghesani, T. Argentini, M. Belloli and F. C. Robustelli, "Dynamic Absorbers for Rotation Machinery" in *Proceedings of the 9th IFToMM International Conference on Rotordynamics*, pp. 1703-1714, Springer, 2015.
- [85] K. P. Duffy, R. L. Bagley and O. Mehmed, "On a Self-Tuning Impact Vibration Damper for Rotating Turbomachinery", NASA, USA, AIAA-2000-3100, 2000

- [86] L. Hoeks, M. Schwab and C. Felchner, "Tuned Mass Damper for Rotating Shafts", U.S. Patent 20100285892 A1, 11 Nov 2010.
- [87] S. Venugopal, J. R. Jain, H. Reckmann and B. Meyer-Heye, "Mitigation of rotational vibration using a torsional tuned mass damper", U.S. Patent 20140151122 A1, 5 Jun 2014.
- [88] S. A. A. Hosseini and S. E. Khadem, "Free vibration analysis with nonlinearities in curvature and inertia", *Mechanism and Machine Theory*, vol. 44 pp.272-288, 2009.
- [89] J. P. Corcoran, "What is an acceptable coupling lateral critical speed?" *Turbomachinery International*, pp. 18-21, 2003.
- [90] P. Lou, G-L Dai and Q-Y Zeng, "Finite-element analysis of a Timoshenko beam subjected to a moving mass", *IMEchE Part C: J Mechanical Engineering Science*, vol. 220, pp. 669-678, 2005.
- [91] L. Librescu and S. Ohseop, *Thin-Walled Composite Beams Theory and Application*, Springer, 2006.
- [92] A. H. Nayfeh and P. F. Pai, *Linear and Nonlinear Structural Mechanics*, Wiley, 2004.
- [93] S. S. Rao, *The Finite Element Method in Engineering*, 5th ed., Butterworth-Heinemann, 2011.
- [94] A. Nandi and S. Neogy, "Modelling rotors with three dimensional solid finite elements", *Journal of Strain Analysis*, vol. 36(4), pp. 359-371, 2001.
- [95] V. Ruffini, W. Schwingshackl and J. S. Green, "Prediction Capabilities of Coriolis and Gyroscopic Effects in Current Finite Element Software" in *Proceedings of the 9th IFToMM International Conference on Rotordynamics*, pp. 1853-1862, Springer, 2015.

- [96] L. Meirovitch, *Computational methods in structural dynamics*, Sijthoff and Noordhoof, 1980.
- [97] L. Meirovitch, *Elements of Vibration Analysis*, McGraw Hill, 1986.
- [98] ANSYS Help. Version 17.0
- [99] A. Lufti, J. Gu, A. Ball and F. Gu, "Investigation of a Rotating Shaft with a Novel Integrated Wireless Accelerometer", The Seventh International Conference on Conditional Monitoring and Machinery Failure Prevention Technologies, Stratford upon Avon, 2010.
- [100] M. E. Elnady, J. K. Sinha and S. O Oyadiji, "Identification of Critical Speeds of Rotating Machines Using On-Shaft Wireless Vibration Measurement", Journal of Physics: Conference Series, vol. 364, 2012.
- [101] NSK Motion and Control, *Rolling Bearings CAT. No. E140c*, 2008.
- [102] G. Mogenier, T. Baranger, G. Ferraris, R. Dufour and L. Durantay, "A criterion for mode shape tracking: application to Campbell diagrams", Journal of Vibration and Control, vol. 20,(2), pp. 179-190, 2014.
- [103] R. Allemang and D. Brown, "A correlation coefficient for modal vector analysis", 1st International Modal Analysis Conference (IMAC), Orlando, 1982.
- [104] N. Lieven, "Error location using normalised orthogonality", 12th International Modal Analysis Conference (IMAC), New York, 1994.
- [105] C. Morales, "Comments on the MAC and the NCO and a linear modal correlation coefficient", Journal of Sound and Vibration, vol. 282(1-2), pp. 529-537, 2005.

Appendices

Appendix A Transformation Matrix Derivatives

The derivatives of the transformation matrix $[A]$ used for determining velocities and accelerations in the rotating frame for the shaft in Section 3.5 Derivation of Simply Supported Rotating Shaft Dynamics pp.47 and sleeve in Section 0

Derivation of Eccentric Sleeve Dynamics pp. 67 are obtained via product rule differentiation:

$$[A] = \begin{bmatrix} 1 & 0 & 0 \\ 0 & \cos \theta & -\sin \theta \\ 0 & \sin \theta & \cos \theta \end{bmatrix}$$

$$[\dot{A}] = \dot{\theta} \begin{bmatrix} 0 & 0 & 0 \\ 0 & -\sin \theta & -\cos \theta \\ 0 & \cos \theta & -\sin \theta \end{bmatrix}$$

$$[\ddot{A}] = \dot{\theta} \dot{\theta} \begin{bmatrix} 0 & 0 & 0 \\ 0 & -\cos \theta & \sin \theta \\ 0 & -\sin \theta & -\cos \theta \end{bmatrix} + \ddot{\theta} \begin{bmatrix} 0 & 0 & 0 \\ 0 & -\sin \theta & -\cos \theta \\ 0 & \cos \theta & -\sin \theta \end{bmatrix}$$

Appendix B Integration Coefficients

B.1 Inertia Coefficients

The inertia coefficients in Table 3-1 pp. 59, are obtained by integration of the tubular cross section of the shaft:

$$\begin{aligned} \iint \rho_0 dA &= \rho_0 \int_{r_i}^{r_o} \int_0^{2\pi} r dr d\theta = \rho_0 \left[\frac{r^2}{2} \right]_{r_i}^{r_o} [\theta]_0^{2\pi} \\ &= \rho_0 \left[\frac{r_o^2 - r_i^2}{2} \right] [2\pi - 0] = \pi \rho_0 (r_o^2 - r_i^2) \end{aligned}$$

$$\begin{aligned} \iint \rho_0 y dA &= \rho_0 \int_{r_i}^{r_o} \int_0^{2\pi} r \cos \theta r dr d\theta = \rho_0 \left[\frac{r^3}{3} \right]_{r_i}^{r_o} [\sin \theta]_0^{2\pi} \\ &= \rho_0 \left(\frac{r_o^3 - r_i^3}{3} \right) (\sin 2\pi - \sin 0) = \mathbf{0} \end{aligned}$$

$$\begin{aligned} \iint \rho_0 z dA &= \rho_0 \int_{r_i}^{r_o} \int_0^{2\pi} r \sin \theta r dr d\theta = \rho_0 \left[\frac{r^3}{3} \right]_{r_i}^{r_o} [-\cos \theta]_0^{2\pi} \\ &= \rho_0 \left(\frac{r_o^3 - r_i^3}{3} \right) (-\cos 2\pi + \cos 0) = \mathbf{0} \end{aligned}$$

$$\begin{aligned}
\iint \rho_0 yz \, dA &= \rho_0 \int_{r_i}^{r_o} \int_0^{2\pi} r \sin \theta \, r \cos \theta \, r dr d\theta && \left(\sin \theta \cos \theta = \frac{\sin 2\theta}{2} \right) \\
&= \rho_0 \int_{r_i}^{r_o} \int_0^{2\pi} r^2 \frac{\sin 2\theta}{2} \, r dr d\theta = \rho_0 \left[\frac{r^4}{4} \right]_{r_i}^{r_o} \left[\frac{-\cos 2\theta}{4} \right]_0^{2\pi} \\
&= \rho_0 \left(\frac{r_o^4 - r_i^4}{4} \right) \left(\frac{-\cos 4\pi}{4} + \frac{\cos 0}{4} \right) = \mathbf{0}
\end{aligned}$$

$$\begin{aligned}
\iint \rho_0 y^2 \, dA &= \rho_0 \int_{r_i}^{r_o} \int_0^{2\pi} (r \cos \theta)^2 \, r dr d\theta && \left(\int \cos^2 \theta = \frac{\theta}{2} + \frac{\sin 2\theta}{4} \right) \\
&= \rho_0 \int_{r_i}^{r_o} \int_0^{2\pi} r^2 \cos^2 \theta \, r dr d\theta = \rho_0 \left[\frac{r^4}{4} \right]_{r_i}^{r_o} \left[\frac{\theta}{2} + \frac{\sin 2\theta}{4} \right]_0^{2\pi} \\
&= \rho_0 \left(\frac{r_o^4 - r_i^4}{4} \right) \left(\frac{2\pi - 0}{2} + \frac{\sin 4\pi - \sin 0}{4} \right) = \boldsymbol{\pi \rho_0 \left(\frac{r_o^4 - r_i^4}{4} \right)}
\end{aligned}$$

$$\begin{aligned}
\iint \rho_0 z^2 \, dA &= \rho_0 \int_{r_i}^{r_o} \int_0^{2\pi} (r \sin \theta)^2 \, r dr d\theta && \left(\int \sin^2 \theta = \frac{\theta}{2} - \frac{\sin 2\theta}{4} \right) \\
&= \rho_0 \int_{r_i}^{r_o} \int_0^{2\pi} r^2 \sin^2 \theta \, r dr d\theta = \rho_0 \left[\frac{r^4}{4} \right]_{r_i}^{r_o} \left[\frac{\theta}{2} - \frac{\sin 2\theta}{4} \right]_0^{2\pi} \\
&= \rho_0 \left(\frac{r_o^4 - r_i^4}{4} \right) \left(\frac{2\pi - 0}{2} - \frac{\sin 4\pi - \sin 0}{4} \right) = \boldsymbol{\pi \rho_0 \left(\frac{r_o^4 - r_i^4}{4} \right)}
\end{aligned}$$

B.2 Stiffness Coefficients

The stiffness coefficients in Table 3-2 pp. 64, are obtained by integration of the tubular cross section of the shaft:

$$\begin{aligned} \iint E dA &= E \int_{r_i}^{r_o} \int_0^{2\pi} r dr d\theta = E \left[\frac{r^2}{2} \right]_{r_i}^{r_o} [\theta]_0^{2\pi} \\ &= E \left[\frac{r_o^2 - r_i^2}{2} \right] [2\pi - 0] = \mathbf{E\pi(r_o^2 - r_i^2)} \end{aligned}$$

$$\begin{aligned} \iint Ey dA &= E \int_{r_i}^{r_o} \int_0^{2\pi} r \cos \theta r dr d\theta = E \left[\frac{r^3}{3} \right]_{r_i}^{r_o} [\sin \theta]_0^{2\pi} \\ &= E \left(\frac{r_o^3 - r_i^3}{3} \right) (\sin 2\pi - \sin 0) = \mathbf{0} \end{aligned}$$

$$\begin{aligned} \iint Ez dA &= E \int_{r_i}^{r_o} \int_0^{2\pi} r \sin \theta r dr d\theta = E \left[\frac{r^3}{3} \right]_{r_i}^{r_o} [-\cos \theta]_0^{2\pi} \\ &= E \left(\frac{r_o^3 - r_i^3}{3} \right) (-\cos 2\pi + \cos 0) = \mathbf{0} \end{aligned}$$

$$\begin{aligned} \iint Eyz dA &= E \int_{r_i}^{r_o} \int_0^{2\pi} r \sin \theta r \cos \theta r dr d\theta \\ &= E \int_{r_i}^{r_o} \int_0^{2\pi} r^2 \frac{\sin 2\theta}{2} r dr d\theta = E \left[\frac{r^4}{4} \right]_{r_i}^{r_o} \left[\frac{-\cos 2\theta}{4} \right]_0^{2\pi} \\ &= E \left(\frac{r_o^4 - r_i^4}{4} \right) \left(\frac{-\cos 4\pi}{4} + \frac{\cos 0}{4} \right) = \mathbf{0} \end{aligned}$$

$$\begin{aligned} \iint Ey^2 dA &= E \int_{r_i}^{r_o} \int_0^{2\pi} (r \cos \theta)^2 r dr d\theta \\ &= E \int_{r_i}^{r_o} \int_0^{2\pi} r^2 \cos^2 \theta r dr d\theta = E \left[\frac{r^4}{4} \right]_{r_i}^{r_o} \left[\frac{\theta}{2} + \frac{\sin 2\theta}{4} \right]_0^{2\pi} \\ &= E \left(\frac{r_o^4 - r_i^4}{4} \right) \left(\frac{2\pi - 0}{2} + \frac{\sin 4\pi - \sin 0}{4} \right) = \mathbf{E\pi \left(\frac{r_o^4 - r_i^4}{4} \right)} \end{aligned}$$

$$\begin{aligned}
\iint E z^2 dA &= E \int_{r_i}^{r_o} \int_0^{2\pi} (r \sin \theta)^2 r dr d\theta \\
&= E \int_{r_i}^{r_o} \int_0^{2\pi} r^2 \sin^2 \theta r dr d\theta = E \left[\frac{r^4}{4} \right]_{r_i}^{r_o} \left[\frac{\theta}{2} - \frac{\sin 2\theta}{4} \right]_0^{2\pi} \\
&= E \left(\frac{r_o^4 - r_i^4}{4} \right) \left(\frac{2\pi - 0}{2} - \frac{\sin 4\pi - \sin 0}{4} \right) = \mathbf{E\pi \left(\frac{r_o^4 - r_i^4}{4} \right)}
\end{aligned}$$

As above:

$$\iint G y^2 dA = \mathbf{G\pi \left(\frac{r_o^4 - r_i^4}{4} \right)}$$

$$\iint G z^2 dA = \mathbf{G\pi \left(\frac{r_o^4 - r_i^4}{4} \right)}$$

Appendix C Derivation of Sleeve Kinetic Energies

C.1 Kinetic Energy of 1st Sleeve

The generalised coordinates to determine the kinetic energy of the sleeve are v' , w' , ϕ and θ .

Therefore the variation and the derivatives of r_1 are:

$$\delta r_1 = \frac{\partial r_1}{\partial v'} \delta v' + \frac{\partial r_1}{\partial w'} \delta w' + \frac{\partial r_1}{\partial \phi} \delta \phi + \frac{\partial r_1}{\partial \theta} \delta \theta \quad (C1)$$

$$\frac{\partial r_1}{\partial v'} = \begin{Bmatrix} \bar{r}_y \\ -\bar{r}_x \cos \theta \\ -\bar{r}_x \sin \theta \end{Bmatrix} \quad \frac{\partial r_1}{\partial w'} = \begin{Bmatrix} \bar{r}_z \\ \bar{r}_x \sin \theta \\ -\bar{r}_x \cos \theta \end{Bmatrix} \quad \frac{\partial r_1}{\partial \phi} = \begin{Bmatrix} 0 \\ \bar{r}_y \sin \theta + \bar{r}_z \cos \theta \\ -\bar{r}_y \cos \theta + \bar{r}_z \sin \theta \end{Bmatrix}$$

$$\frac{\partial r_1}{\partial \theta} = \begin{Bmatrix} 0 \\ \bar{r}_x(w'(0, t) \cos \theta + v'(0, t) \sin \theta) - \bar{r}_y(\sin \theta - \phi \cos \theta) - \bar{r}_z(\cos \theta + \phi \sin \theta) \\ -\bar{r}_x(-w'(0, t) \sin \theta + v'(0, t) \cos \theta) + \bar{r}_y(\cos \theta + \phi \sin \theta) - \bar{r}_z(\sin \theta + \phi \cos \theta) \end{Bmatrix} \quad (C2 \text{ a-d})$$

In matrix form, $\{\ddot{r}_1\}^T \delta r_1$ is equivalent to:

$$\{\ddot{r}_1\}^T \frac{\partial r_1}{\partial v'} \delta v' + \{\ddot{r}_1\}^T \frac{\partial r_1}{\partial w'} \delta w' + \{\ddot{r}_1\}^T \frac{\partial r_1}{\partial \phi} \delta \phi + \{\ddot{r}_1\}^T \frac{\partial r_1}{\partial \theta} \delta \theta \quad (C3)$$

$\{\ddot{r}_1\}$ is broken down into components to produce four individual vectors corresponding to centrifugal, non-constant rotation, Coriolis and translational acceleration. (The vectors now have the designations $\{\ddot{r}_{11}\}^T$, $\{\ddot{r}_{12}\}^T$, $\{\ddot{r}_{13}\}^T$, $\{\ddot{r}_{14}\}^T$). The individual components of $\{\ddot{r}_1\}^T \delta r_1$ are obtained through multiplication of Equations 3.45 and C2 (a-d):

$\delta v'$

$$\begin{aligned} & \{\ddot{r}_{11}\}^T \frac{\partial r_1}{\partial v'} \delta v' \\ &= \dot{\theta}^2 \left\{ \begin{array}{c} 0 \\ \bar{r}_x(v'(0,t) \cos \theta - w' \sin \theta) + \bar{r}_y(-\phi \sin \theta - \cos \theta) + \bar{r}_z(-\phi \cos \theta + \sin \theta) \\ \bar{r}_x(w'(0,t) \cos \theta + v' \sin \theta) + \bar{r}_y(\phi \cos \theta - \sin \theta) + \bar{r}_z(-\phi \sin \theta - \cos \theta) \end{array} \right\}^T \\ & \quad \times \left\{ \begin{array}{c} \bar{r}_y \\ -\bar{r}_x \cos \theta \\ -\bar{r}_x \sin \theta \end{array} \right\} \delta v' = \dot{\theta}^2 (-\bar{r}_x^2 v'(0,t) + \bar{r}_x \bar{r}_y + \bar{r}_x \bar{r}_z \phi) \delta v' \end{aligned}$$

$$\begin{aligned} & \{\ddot{r}_{12}\}^T \frac{\partial r_1}{\partial v'} \delta v' \\ &= -\ddot{\theta} \left\{ \begin{array}{c} 0 \\ -\bar{r}_x(v'(0,t) \sin \theta + w'(0,t) \cos \theta) - \bar{r}_y(\phi \cos \theta - \sin \theta) - \bar{r}_z(-\phi \sin \theta - \cos \theta) \\ \bar{r}_x(-w'(0,t) \sin \theta + v'(0,t) \cos \theta) + \bar{r}_y(-\phi \sin \theta - \cos \theta) - \bar{r}_z(\phi \cos \theta - \sin \theta) \end{array} \right\}^T \\ & \quad \times \left\{ \begin{array}{c} \bar{r}_y \\ -\bar{r}_x \cos \theta \\ -\bar{r}_x \sin \theta \end{array} \right\} \delta v' = -\ddot{\theta} (\bar{r}_x^2 w'(0,t) + \bar{r}_x \bar{r}_y \phi - \bar{r}_x \bar{r}_z) \delta v' \end{aligned}$$

$$\begin{aligned} & \{\ddot{r}_{13}\}^T \frac{\partial r_1}{\partial v'} \delta v' \\ &= -2\dot{\theta} \left\{ \begin{array}{c} 0 \\ -\bar{r}_x(\dot{v}'(0,t) \sin \theta + \dot{w}'(0,t) \cos \theta) - \bar{r}_y \dot{\phi} \cos \theta + \bar{r}_z \dot{\phi} \sin \theta \\ \bar{r}_x(-\dot{w}'(0,t) \sin \theta + \dot{v}'(0,t) \cos \theta) - \bar{r}_y \dot{\phi} \sin \theta - \bar{r}_z \dot{\phi} \cos \theta \end{array} \right\}^T \\ & \quad \times \left\{ \begin{array}{c} \bar{r}_y \\ -\bar{r}_x \cos \theta \\ -\bar{r}_x \sin \theta \end{array} \right\} \delta v' = -2\dot{\theta} (\bar{r}_x^2 \dot{w}'(0,t) + \bar{r}_x \bar{r}_y \dot{\phi}) \delta v' \end{aligned}$$

$$\begin{aligned} & \{\ddot{r}_{14}\}^T \frac{\partial r_1}{\partial v'} \delta v' \\ &= \left\{ \begin{array}{c} \bar{r}_y \ddot{v}'(0,t) + \bar{r}_z \ddot{w}'(0,t) \\ -\bar{r}_x(\ddot{v}'(0,t) \cos \theta - \ddot{w}'(0,t) \sin \theta) + \bar{r}_y \ddot{\phi} \sin \theta + \bar{r}_z \ddot{\phi} \cos \theta \\ -\bar{r}_x(\ddot{w}'(0,t) \cos \theta + \ddot{v}'(0,t) \sin \theta) - \bar{r}_y \ddot{\phi} \cos \theta + \bar{r}_z \ddot{\phi} \sin \theta \end{array} \right\}^T \\ & \quad \times \left\{ \begin{array}{c} \bar{r}_y \\ -\bar{r}_x \cos \theta \\ -\bar{r}_x \sin \theta \end{array} \right\} \delta v' = \bar{r}_y^2 \ddot{v}'(0,t) + \bar{r}_y \bar{r}_z \ddot{w}'(0,t) + \bar{r}_x^2 \ddot{v}'(0,t) - \bar{r}_x \bar{r}_z \ddot{\phi} \delta v' \end{aligned}$$

$$\begin{aligned}
\therefore \{\bar{\mathbf{r}}_1\}^T \delta \mathbf{v}' &= \dot{\theta}^2 (-\bar{r}_x^2 \mathbf{v}'(\mathbf{0}, t) + \bar{r}_x \bar{r}_y + \bar{r}_x \bar{r}_z \Phi) \\
&\quad - \ddot{\theta} (\bar{r}_x^2 \mathbf{w}'(\mathbf{0}, t) + \bar{r}_x \bar{r}_y \Phi - \bar{r}_x \bar{r}_z) - 2\dot{\theta} (\bar{r}_x^2 \dot{\mathbf{w}}'(\mathbf{0}, t) + \bar{r}_x \bar{r}_y \dot{\Phi}) \\
&\quad + \bar{r}_y^2 \dot{\mathbf{v}}'(\mathbf{0}, t) + \bar{r}_y \bar{r}_z \dot{\mathbf{w}}'(\mathbf{0}, t) + \bar{r}_x^2 \dot{\mathbf{v}}'(\mathbf{0}, t) - \bar{r}_x \bar{r}_z \dot{\Phi} \delta \mathbf{v}'
\end{aligned} \tag{C4}$$

$\delta \mathbf{w}'$

$$\begin{aligned}
&\{\ddot{\mathbf{r}}_{11}\}^T \frac{\partial r_1}{\partial \mathbf{w}'} \delta \mathbf{w}' \\
&= \dot{\theta}^2 \left\{ \begin{array}{l} \bar{r}_x (\mathbf{v}'(0, t) \cos \theta - \mathbf{w}'(0, t) \sin \theta) + \bar{r}_y (-\Phi \sin \theta - \cos \theta) + \bar{r}_z (-\Phi \cos \theta + \sin \theta) \\ \bar{r}_x (\mathbf{w}'(0, t) \cos \theta + \mathbf{v}'(0, t) \sin \theta) + \bar{r}_y (\Phi \cos \theta - \sin \theta) + \bar{r}_z (-\Phi \sin \theta - \cos \theta) \end{array} \right\}^T \\
&\quad \times \left\{ \begin{array}{l} \bar{r}_z \\ \bar{r}_x \sin \theta \\ -\bar{r}_x \cos \theta \end{array} \right\} \delta \mathbf{w}' = \dot{\theta}^2 (-\bar{r}_x^2 \mathbf{w}'(0, t) - \bar{r}_x \bar{r}_y \Phi + \bar{r}_x \bar{r}_z) \delta \mathbf{w}'
\end{aligned}$$

$$\begin{aligned}
&\{\ddot{\mathbf{r}}_{12}\}^T \frac{\partial r_1}{\partial \mathbf{w}'} \delta \mathbf{w}' \\
&= -\ddot{\theta} \left\{ \begin{array}{l} -\bar{r}_x (\mathbf{v}'(0, t) \sin \theta + \mathbf{w}'(0, t) \cos \theta) - \bar{r}_y (\Phi \cos \theta - \sin \theta) - \bar{r}_z (-\Phi \sin \theta - \cos \theta) \\ \bar{r}_x (-\mathbf{w}'(0, t) \sin \theta + \mathbf{v}'(0, t) \cos \theta) + \bar{r}_y (-\Phi \sin \theta - \cos \theta) - \bar{r}_z (\Phi \cos \theta - \sin \theta) \end{array} \right\}^T \\
&\quad \times \left\{ \begin{array}{l} \bar{r}_z \\ \bar{r}_x \sin \theta \\ -\bar{r}_x \cos \theta \end{array} \right\} \delta \mathbf{w}' = -\ddot{\theta} (-\bar{r}_x^2 \mathbf{v}'(0, t) + \bar{r}_x \bar{r}_y + \bar{r}_x \bar{r}_z \Phi) \delta \mathbf{w}'
\end{aligned}$$

$$\begin{aligned}
&\{\ddot{\mathbf{r}}_{13}\}^T \frac{\partial r_1}{\partial \mathbf{w}'} \delta \mathbf{w}' \\
&= -2\dot{\theta} \left\{ \begin{array}{l} -\bar{r}_x (\dot{\mathbf{v}}'(0, t) \sin \theta + \dot{\mathbf{w}}'(0, t) \cos \theta) - \bar{r}_y \dot{\Phi} \cos \theta + \bar{r}_z \dot{\Phi} \sin \theta \\ \bar{r}_x (-\dot{\mathbf{w}}'(0, t) \sin \theta + \dot{\mathbf{v}}'(0, t) \cos \theta) - \bar{r}_y \dot{\Phi} \sin \theta - \bar{r}_z \dot{\Phi} \cos \theta \end{array} \right\}^T \\
&\quad \times \left\{ \begin{array}{l} \bar{r}_z \\ \bar{r}_x \sin \theta \\ -\bar{r}_x \cos \theta \end{array} \right\} \delta \mathbf{w}' = -2\dot{\theta} (-\bar{r}_x^2 \dot{\mathbf{v}}'(0, t) + \bar{r}_x \bar{r}_z \dot{\Phi}) \delta \mathbf{w}'
\end{aligned}$$

$$\begin{aligned}
& \{\ddot{r}_{14}\}^T \frac{\partial r_1}{\partial w'} \delta w' \\
&= \left\{ \begin{array}{c} \bar{r}_y \dot{v}'(0, t) + \bar{r}_z \dot{w}'(0, t) \\ -\bar{r}_x (\dot{v}'(0, t) \cos \theta - \dot{w}'(0, t) \sin \theta) + \bar{r}_y \ddot{\phi} \sin \theta + \bar{r}_z \ddot{\phi} \cos \theta \\ -\bar{r}_x (\dot{w}'(0, t) \cos \theta + \dot{v}'(0, t) \sin \theta) - \bar{r}_y \ddot{\phi} \cos \theta + \bar{r}_z \ddot{\phi} \sin \theta \end{array} \right\}^T \\
&\quad \times \left\{ \begin{array}{c} \bar{r}_z \\ \bar{r}_x \sin \theta \\ -\bar{r}_x \cos \theta \end{array} \right\} \delta w' = \bar{r}_y \bar{r}_z \dot{v}'(0, t) + \bar{r}_y^2 \dot{w}'(0, t) + \bar{r}_x^2 \dot{w}'(0, t) + \bar{r}_x \bar{r}_y \ddot{\phi} \delta w'
\end{aligned}$$

$$\begin{aligned}
\therefore \{\ddot{r}_1\}^T \delta w' &= \dot{\theta}^2 (-\bar{r}_x^2 w'(0, t) - \bar{r}_x \bar{r}_y \phi + \bar{r}_x \bar{r}_z) \\
&\quad - \ddot{\theta} (-\bar{r}_x^2 v'(0, t) + \bar{r}_x \bar{r}_y + \bar{r}_x \bar{r}_z \phi) \\
&\quad - 2\dot{\theta} (-\bar{r}_x^2 \dot{v}'(0, t) + \bar{r}_x \bar{r}_z \dot{\phi}) + \bar{r}_y \bar{r}_z \dot{v}'(0, t) + \bar{r}_z^2 \dot{w}'(0, t) \\
&\quad + \bar{r}_x^2 \dot{w}'(0, t) + \bar{r}_x \bar{r}_y \ddot{\phi} \delta w' \tag{C5}
\end{aligned}$$

$\delta \phi$

$$\begin{aligned}
& \{\ddot{r}_{11}\}^T \frac{\partial r_1}{\partial \phi} \delta \phi \\
&= \dot{\theta}^2 \left\{ \begin{array}{c} 0 \\ \bar{r}_x (v'(0, t) \cos \theta - w'(0, t) \sin \theta) + \bar{r}_y (-\phi \sin \theta - \cos \theta) + \bar{r}_z (-\phi \cos \theta + \sin \theta) \\ \bar{r}_x (w'(0, t) \cos \theta + v'(0, t) \sin \theta) + \bar{r}_y (\phi \cos \theta - \sin \theta) + \bar{r}_z (-\phi \sin \theta - \cos \theta) \end{array} \right\}^T \\
&\quad \times \left\{ \begin{array}{c} 0 \\ \bar{r}_y \sin \theta + \bar{r}_z \cos \theta \\ -\bar{r}_y \cos \theta + \bar{r}_z \sin \theta \end{array} \right\} \delta \phi = \dot{\theta}^2 (-\bar{r}_x \bar{r}_y w'(0, t) - \bar{r}_y^2 \phi + \bar{r}_x \bar{r}_z v'(0, t) - \bar{r}_z^2 \phi) \delta \phi
\end{aligned}$$

$$\begin{aligned}
& \{\ddot{r}_{12}\}^T \frac{\partial r_1}{\partial \phi} \delta \phi \\
&= -\ddot{\theta} \left\{ \begin{array}{c} 0 \\ -\bar{r}_x (v'(0, t) \sin \theta + w'(0, t) \cos \theta) - \bar{r}_y (\phi \cos \theta - \sin \theta) - \bar{r}_z (-\phi \sin \theta - \cos \theta) \\ \bar{r}_x (-w'(0, t) \sin \theta + v'(0, t) \cos \theta) + \bar{r}_y (-\phi \sin \theta - \cos \theta) - \bar{r}_z (\phi \cos \theta - \sin \theta) \end{array} \right\}^T \\
&\quad \times \left\{ \begin{array}{c} 0 \\ \bar{r}_y \sin \theta + \bar{r}_z \cos \theta \\ -\bar{r}_y \cos \theta + \bar{r}_z \sin \theta \end{array} \right\} \delta \phi = -\ddot{\theta} (-\bar{r}_x \bar{r}_y v'(0, t) + \bar{r}_y^2 - \bar{r}_x \bar{r}_z w'(0, t) + \bar{r}_z^2) \delta \phi
\end{aligned}$$

$$\begin{aligned}
& \{\ddot{r}_{13}\}^T \frac{\partial r_1}{\partial \phi} \delta \phi \\
&= 2\dot{\theta} \left\{ \begin{array}{c} 0 \\ -\bar{r}_x(\dot{v}'(0,t)\sin\theta + \dot{w}'(0,t)\cos\theta) - \bar{r}_y\dot{\phi}\cos\theta + \bar{r}_z\dot{\phi}\sin\theta \\ \bar{r}_x(-\dot{w}'(0,t)\sin\theta + \dot{v}'(0,t)\cos\theta) - \bar{r}_y\dot{\phi}\sin\theta - \bar{r}_z\dot{\phi}\cos\theta \end{array} \right\}^T \\
&\quad \times \left\{ \begin{array}{c} 0 \\ \bar{r}_y\sin\theta + \bar{r}_z\cos\theta \\ -\bar{r}_y\cos\theta + \bar{r}_z\sin\theta \end{array} \right\} \delta \phi = -2\dot{\theta}(-\bar{r}_x\bar{r}_y\dot{v}'(0,t) - \bar{r}_x\bar{r}_z\dot{w}'(0,t))\delta \phi
\end{aligned}$$

$$\begin{aligned}
& \{\ddot{r}_{14}\}^T \frac{\partial r_1}{\partial \phi} \delta \phi \\
&= \left\{ \begin{array}{c} \bar{r}_y\dot{v}'(0,t) + \bar{r}_z\dot{w}'(0,t) \\ -\bar{r}_x(\dot{v}'(0,t)\cos\theta - \dot{w}'(0,t)\sin\theta) + \bar{r}_y\ddot{\phi}\sin\theta + \bar{r}_z\ddot{\phi}\cos\theta \\ -\bar{r}_x(\dot{w}'(0,t)\cos\theta + \dot{v}'(0,t)\sin\theta) - \bar{r}_y\ddot{\phi}\cos\theta + \bar{r}_z\ddot{\phi}\sin\theta \end{array} \right\}^T \\
&\quad \times \left\{ \begin{array}{c} 0 \\ \bar{r}_y\sin\theta + \bar{r}_z\cos\theta \\ -\bar{r}_y\cos\theta + \bar{r}_z\sin\theta \end{array} \right\} \delta \phi = \bar{r}_x\bar{r}_y\dot{w}'(0,t) + \bar{r}_y^2\ddot{\phi} - \bar{r}_x\bar{r}_z\dot{v}'(0,t) + \bar{r}_z^2\ddot{\phi} \delta \phi
\end{aligned}$$

$$\begin{aligned}
\therefore \{\ddot{r}_1\}^T \delta \phi &= \dot{\theta}^2(-\bar{r}_x\bar{r}_y\dot{w}'(0,t) - \bar{r}_y^2\ddot{\phi} + \bar{r}_x\bar{r}_z\dot{v}'(0,t) - \bar{r}_z^2\ddot{\phi}) \\
&\quad - \ddot{\theta}(-\bar{r}_x\bar{r}_y\dot{v}'(0,t) + \bar{r}_y^2\ddot{\phi} - \bar{r}_x\bar{r}_z\dot{w}'(0,t) + \bar{r}_z^2\ddot{\phi}) \\
&\quad - 2\dot{\theta}(-\bar{r}_x\bar{r}_y\dot{v}'(0,t) - \bar{r}_x\bar{r}_z\dot{w}'(0,t)) + \bar{r}_x\bar{r}_y\dot{w}'(0,t) + \bar{r}_y^2\ddot{\phi} \quad (C6) \\
&\quad - \bar{r}_x
\end{aligned}$$

$\delta\theta$ (Neglecting higher order terms)

$$\begin{aligned}
& \{\ddot{r}_{11}\}^T \frac{\partial r_1}{\partial \theta} \delta \theta \\
&= \dot{\theta}^2 \left\{ \begin{array}{c} 0 \\ \bar{r}_x(\dot{v}'(0,t)\cos\theta - \dot{w}'(0,t)\sin\theta) + \bar{r}_y(-\dot{\phi}\sin\theta - \cos\theta) + \bar{r}_z(-\dot{\phi}\cos\theta + \sin\theta) \\ \bar{r}_x(\dot{w}'(0,t)\cos\theta + \dot{v}'(0,t)\sin\theta) + \bar{r}_y(\dot{\phi}\cos\theta - \sin\theta) + \bar{r}_z(-\dot{\phi}\sin\theta - \cos\theta) \end{array} \right\}^T \\
&\quad \times \left\{ \begin{array}{c} 0 \\ \bar{r}_x(\dot{w}'(0,t)\cos\theta + \dot{v}'(0,t)\sin\theta) - \bar{r}_y(\sin\theta - \dot{\phi}\cos\theta) - \bar{r}_z(\cos\theta + \dot{\phi}\sin\theta) \\ -\bar{r}_x(-\dot{v}'(0,t)\sin\theta + \dot{w}'(0,t)\cos\theta) + \bar{r}_y(\cos\theta + \dot{\phi}\sin\theta) - \bar{r}_z(\sin\theta + \dot{\phi}\cos\theta) \end{array} \right\} \delta \theta = 0
\end{aligned}$$

$$\begin{aligned}
& \{\ddot{\mathbf{r}}_{12}\}^T \frac{\partial \mathbf{r}_1}{\partial \theta} \delta \theta \\
&= -\ddot{\theta} \left\{ \begin{array}{c} 0 \\ -\bar{r}_x(v'(0,t)\sin\theta + w'(0,t)\cos\theta) - \bar{r}_y(\phi\cos\theta - \sin\theta) - \bar{r}_z(-\phi\sin\theta - \cos\theta) \\ \bar{r}_x(-w'(0,t)\sin\theta + v'(0,t)\cos\theta) + \bar{r}_y(-\phi\sin\theta - \cos\theta) - \bar{r}_z(\phi\cos\theta - \sin\theta) \end{array} \right\}^T \\
&\quad \times \left\{ \begin{array}{c} 0 \\ \bar{r}_x(w'(0,t)\cos\theta + v'(0,t)\sin\theta) - \bar{r}_y(\sin\theta - \phi\cos\theta) - \bar{r}_z(\cos\theta + \phi\sin\theta) \\ -\bar{r}_x(-w'(0,t)\sin\theta + v'(0,t)\cos\theta) + \bar{r}_y(\cos\theta + \phi\sin\theta) - \bar{r}_z(\sin\theta + \phi\cos\theta) \end{array} \right\} \delta \theta \\
&\quad = -\ddot{\theta}(\bar{r}_y^2 + \bar{r}_z^2 - 2(\bar{r}_x\bar{r}_y v'(0,t) + \bar{r}_x\bar{r}_z w'(0,t)) - \bar{r}_y\bar{r}_z\phi)\delta\theta
\end{aligned}$$

$$\begin{aligned}
& \{\ddot{\mathbf{r}}_{13}\}^T \frac{\partial \mathbf{r}_1}{\partial \theta} \delta \theta \\
&= -2\dot{\theta} \left\{ \begin{array}{c} 0 \\ -\bar{r}_x(\dot{v}'(0,t)\sin\theta + \dot{w}'(0,t)\cos\theta) - \bar{r}_y\dot{\phi}\cos\theta + \bar{r}_z\dot{\phi}\sin\theta \\ \bar{r}_x(-\dot{w}'(0,t)\sin\theta + \dot{v}'(0,t)\cos\theta) - \bar{r}_y\dot{\phi}\sin\theta - \bar{r}_z\dot{\phi}\cos\theta \end{array} \right\}^T \\
&\quad \times \left\{ \begin{array}{c} 0 \\ \bar{r}_x(w'(c,t)\cos\theta + v'(c,t)\sin\theta) - \bar{r}_y(\sin\theta - \phi\cos\theta) - \bar{r}_z(\cos\theta + \phi\sin\theta) \\ -\bar{r}_x(-w'(c,t)\sin\theta + v'(c,t)\cos\theta) + \bar{r}_y(\cos\theta + \phi\sin\theta) - \bar{r}_z(\sin\theta + \phi\cos\theta) \end{array} \right\} \delta \theta \\
&\quad = -2\dot{\theta}(\bar{r}_x\bar{r}_y\dot{v}'(0,t) + \bar{r}_x\bar{r}_z\dot{w}'(0,t))\delta\theta
\end{aligned}$$

$$\begin{aligned}
& \{\ddot{\mathbf{r}}_{14}\}^T \frac{\partial \mathbf{r}_1}{\partial \theta} \delta \theta \\
&= \left\{ \begin{array}{c} \bar{r}_y\ddot{v}'(0,t) + \bar{r}_z\ddot{w}'(0,t) \\ -\bar{r}_x(\ddot{v}'(0,t)\cos\theta - \ddot{w}'(0,t)\sin\theta) + \bar{r}_y\ddot{\phi}\sin\theta + \bar{r}_z\ddot{\phi}\cos\theta \\ -\bar{r}_x(\ddot{w}'(0,t)\cos\theta + \ddot{v}'(0,t)\sin\theta) - \bar{r}_y\ddot{\phi}\cos\theta + \bar{r}_z\ddot{\phi}\sin\theta \end{array} \right\}^T \\
&\quad \times \left\{ \begin{array}{c} 0 \\ \bar{r}_x(w'(c,t)\cos\theta + v'(c,t)\sin\theta) - \bar{r}_y(\sin\theta - \phi\cos\theta) - \bar{r}_z(\cos\theta + \phi\sin\theta) \\ -\bar{r}_x(-w'(c,t)\sin\theta + v'(c,t)\cos\theta) + \bar{r}_y(\cos\theta + \phi\sin\theta) - \bar{r}_z(\sin\theta + \phi\cos\theta) \end{array} \right\} \delta \theta \\
&\quad = \bar{r}_x\bar{r}_y\ddot{w}'(0,t) - \bar{r}_x\bar{r}_z\ddot{v}'(0,t) + \bar{r}_y^2\ddot{\phi} + \bar{r}_z^2\ddot{\phi}\delta\theta
\end{aligned}$$

$$\begin{aligned}
\therefore \{\ddot{\mathbf{r}}_1\}^T \delta \theta &= -\ddot{\theta}(\bar{r}_y^2 + \bar{r}_z^2 - \bar{r}_y\bar{r}_z\phi - 2(\bar{r}_x\bar{r}_y v'(0,t) + \bar{r}_x\bar{r}_z w'(0,t))) \\
&\quad - 2\dot{\theta}(\bar{r}_x\bar{r}_y\dot{v}'(0,t) + \bar{r}_x\bar{r}_z\dot{w}'(0,t)) + \bar{r}_x\bar{r}_y\dot{w}'(0,t) \\
&\quad - \bar{r}_x\bar{r}_z\dot{v}'(0,t) + \bar{r}_y^2\ddot{\phi} + \bar{r}_z^2\ddot{\phi}\delta\theta
\end{aligned} \tag{C7}$$

Summing together Equations C4 to C7, the variation of kinetic energy in the first sleeve can be obtained once suitable inertia coefficients are derived and substitutes into (C8):

$$\begin{aligned}
\{\ddot{r}_1\}^T \delta r_1 = & (\dot{\theta}^2 (-\bar{r}_x^2 v'(0, t) + \bar{r}_x \bar{r}_y + \bar{r}_x \bar{r}_z \phi) - \ddot{\theta} (\bar{r}_x^2 w'(0, t) + \bar{r}_x \bar{r}_y \phi - \bar{r}_x \bar{r}_z)) \\
& - 2\dot{\theta} (\bar{r}_x^2 \dot{w}'(0, t) + \bar{r}_x \bar{r}_y \dot{\phi}) + \bar{r}_y^2 \ddot{v}'(0, t) + \bar{r}_y \bar{r}_z \ddot{w}'(0, t) \\
& + \bar{r}_x^2 \ddot{v}'(0, t) - \bar{r}_x \bar{r}_z \ddot{\phi} \delta v') \\
& + (\dot{\theta}^2 (-\bar{r}_x^2 w'(0, t) - \bar{r}_x \bar{r}_y \phi + \bar{r}_x \bar{r}_z)) \\
& - \ddot{\theta} (-\bar{r}_x^2 v'(0, t) + \bar{r}_x \bar{r}_y + \bar{r}_x \bar{r}_z \phi) - 2\dot{\theta} (-\bar{r}_x^2 \dot{v}'(0, t) + \bar{r}_x \bar{r}_z \dot{\phi}) \\
& + \bar{r}_y \bar{r}_z \ddot{v}'(0, t) + \bar{r}_z^2 \ddot{w}'(0, t) + \bar{r}_x^2 \ddot{w}'(0, t) + \bar{r}_x \bar{r}_y \ddot{\phi} \delta w') \\
& + (\dot{\theta}^2 (-\bar{r}_x \bar{r}_y w'(0, t) - \bar{r}_y^2 \phi + \bar{r}_x \bar{r}_z v' - \bar{r}_z^2 \phi) \\
& - \ddot{\theta} (-\bar{r}_x \bar{r}_y v'(0, t) + \bar{r}_y^2 - \bar{r}_x \bar{r}_z w'(0, t) + \bar{r}_z^2) \\
& - 2\dot{\theta} (-\bar{r}_x \bar{r}_y \dot{v}'(0, t) - \bar{r}_x \bar{r}_z \dot{w}'(0, t)) + \bar{r}_x \bar{r}_y \ddot{w}'(0, t) + \bar{r}_y^2 \ddot{\phi} \\
& - \bar{r}_x \bar{r}_z \ddot{v}'(0, t) + \bar{r}_z^2 \ddot{\phi} \delta \phi) \\
& + (-\ddot{\theta} (\bar{r}_y^2 + \bar{r}_z^2 - \bar{r}_y \bar{r}_z \phi - 2 (\bar{r}_x \bar{r}_y v'(0, t) + \bar{r}_x \bar{r}_z w'(0, t))) \\
& - 2\dot{\theta} (\bar{r}_x \bar{r}_y \dot{v}'(0, t) + \bar{r}_x \bar{r}_z \dot{w}'(0, t)) + \bar{r}_x \bar{r}_y \ddot{w}'(0, t) - \bar{r}_x \bar{r}_z \ddot{v}'(0, t) \\
& + \bar{r}_y^2 \ddot{\phi} + \bar{r}_z^2 \ddot{\phi} \delta \theta)
\end{aligned} \tag{C8}$$

C.2 Kinetic Energy of 2nd Sleeve

The same generalised coordinates (v', w', ϕ and θ) apply for the second sleeve; however to determine its kinetic energy the variation derivatives of r_2 must be considered:

$$\delta r_2 = \frac{\partial r_2}{\partial v'} \delta v' + \frac{\partial r_2}{\partial w'} \delta w' + \frac{\partial r_2}{\partial \phi} \delta \phi + \frac{\partial r_2}{\partial \theta} \delta \theta \quad (C9)$$

$$\frac{\partial r_2}{\partial v'} = \begin{Bmatrix} \bar{r}_y \\ \bar{r}_x \cos \theta \\ \bar{r}_x \sin \theta \end{Bmatrix} \quad \frac{\partial r_2}{\partial w'} = \begin{Bmatrix} \bar{r}_z \\ -\bar{r}_x \sin \theta \\ \bar{r}_x \cos \theta \end{Bmatrix} \quad \frac{\partial r_2}{\partial \phi} = \begin{Bmatrix} 0 \\ \bar{r}_y \sin \theta + \bar{r}_z \cos \theta \\ -\bar{r}_y \cos \theta + \bar{r}_z \sin \theta \end{Bmatrix}$$

$$\frac{\partial r_2}{\partial \theta} = \begin{Bmatrix} 0 \\ -\bar{r}_x(w'(L, t) \cos \theta + v'(L, t) \sin \theta) - \bar{r}_y(\sin \theta - \phi \cos \theta) - \bar{r}_z(\cos \theta + \phi \sin \theta) \\ \bar{r}_x(-w'(L, t) \sin \theta + v'(L, t) \cos \theta) + \bar{r}_y(\cos \theta + \phi \sin \theta) - \bar{r}_z(\sin \theta + \phi \cos \theta) \end{Bmatrix} \quad (C10 \text{ a-d})$$

$\{\ddot{r}_2\}^T \delta r_2$ is obtained using the individual vector components of $\{\ddot{r}_2\}$ and through multiplication of Equations (3.46) and (C10 a-d)

$\delta v'$

$$\begin{aligned} & \{\ddot{r}_{21}\}^T \frac{\partial r_2}{\partial v'} \delta v' \\ &= \dot{\theta}^2 \begin{Bmatrix} 0 \\ -\bar{r}_x(v'(L, t) \cos \theta - w'(L, t) \sin \theta) + \bar{r}_y(-\phi \sin \theta - \cos \theta) + \bar{r}_z(-\phi \cos \theta + \sin \theta) \\ -\bar{r}_x(w'(L, t) \cos \theta + v'(L, t) \sin \theta) + \bar{r}_y(\phi \cos \theta - \sin \theta) + \bar{r}_z(-\phi \sin \theta - \cos \theta) \end{Bmatrix}^T \\ & \quad \times \begin{Bmatrix} \bar{r}_y \\ \bar{r}_x \cos \theta \\ \bar{r}_x \sin \theta \end{Bmatrix} \delta v' = \dot{\theta}^2 (-\bar{r}_x^2 v'(L, t) - \bar{r}_x \bar{r}_y - \bar{r}_x \bar{r}_z \phi) \delta v' \end{aligned}$$

$$\begin{aligned}
& \{\ddot{r}_{22}\}^T \frac{\partial r_2}{\partial v'} \delta v' \\
&= -\ddot{\theta} \left\{ \begin{array}{c} 0 \\ \bar{r}_x(v'(L, t)\sin\theta + w'(L, t)\cos\theta) - \bar{r}_y(\phi\cos\theta - \sin\theta) - \bar{r}_z(-\phi\sin\theta - \cos\theta) \\ -\bar{r}_x(-w'(L, t)\sin\theta + v'(L, t)\cos\theta) + \bar{r}_y(-\phi\sin\theta - \cos\theta) - \bar{r}_z(\phi\cos\theta - \sin\theta) \end{array} \right\}^T \\
&\quad \times \begin{pmatrix} \bar{r}_y \\ \bar{r}_x \cos\theta \\ \bar{r}_x \sin\theta \end{pmatrix} \delta v' = -\ddot{\theta}(\bar{r}_x^2 w'(L, t) - \bar{r}_x \bar{r}_y \phi + \bar{r}_x \bar{r}_z) \delta v'
\end{aligned}$$

$$\begin{aligned}
& \{\ddot{r}_{23}\}^T \frac{\partial r_2}{\partial v'} \delta v' \\
&= -2\dot{\theta} \left\{ \begin{array}{c} 0 \\ \bar{r}_x(\dot{v}'(L, t)\sin\theta + \dot{w}'(L, t)\cos\theta) - \bar{r}_y\dot{\phi}\cos\theta + \bar{r}_z\dot{\phi}\sin\theta \\ -\bar{r}_x(-\dot{w}'(L, t)\sin\theta + \dot{v}'(L, t)\cos\theta) - \bar{r}_y\dot{\phi}\sin\theta - \bar{r}_z\dot{\phi}\cos\theta \end{array} \right\}^T \\
&\quad \times \begin{pmatrix} \bar{r}_y \\ \bar{r}_x \cos\theta \\ \bar{r}_x \sin\theta \end{pmatrix} \delta v' = -2\dot{\theta}(\bar{r}_x^2 \dot{w}'(L, t) - \bar{r}_x \bar{r}_y \dot{\phi}) \delta v'
\end{aligned}$$

$$\begin{aligned}
& \{\ddot{r}_{24}\}^T \frac{\partial r_2}{\partial v'} \delta v' \\
&= \left\{ \begin{array}{c} \bar{r}_y \ddot{v}'(L, t) + \bar{r}_z \ddot{w}'(L, t) \\ \bar{r}_x(\ddot{v}'(L, t)\cos\theta - \ddot{w}'(L, t)\sin\theta) + \bar{r}_y \ddot{\phi}\sin\theta + \bar{r}_z \ddot{\phi}\cos\theta \\ \bar{r}_x(\ddot{w}'(L, t)\cos\theta + \ddot{v}'(L, t)\sin\theta) - \bar{r}_y \ddot{\phi}\cos\theta + \bar{r}_z \ddot{\phi}\sin\theta \end{array} \right\}^T \\
&\quad \times \begin{pmatrix} \bar{r}_y \\ \bar{r}_x \cos\theta \\ \bar{r}_x \sin\theta \end{pmatrix} \delta v' = \bar{r}_y^2 \ddot{v}'(L, t) + \bar{r}_y \bar{r}_z \ddot{w}'(L, t) + \bar{r}_x^2 \ddot{v}'(L, t) + \bar{r}_x \bar{r}_z \ddot{\phi} \delta v'
\end{aligned}$$

$$\begin{aligned}
\therefore \{\ddot{r}_2\}^T \delta v' &= \dot{\theta}^2(-\bar{r}_x^2 v'(L, t) - \bar{r}_x \bar{r}_y - \bar{r}_x \bar{r}_z \phi) \\
&\quad - \ddot{\theta}(\bar{r}_x^2 w'(L, t) - \bar{r}_x \bar{r}_y \phi + \bar{r}_x \bar{r}_z) - 2\dot{\theta}(\bar{r}_x^2 \dot{w}'(L, t) - \bar{r}_x \bar{r}_y \dot{\phi}) \\
&\quad + \bar{r}_y^2 \ddot{v}'(L, t) + \bar{r}_y \bar{r}_z \ddot{w}'(L, t) + \bar{r}_x^2 \ddot{v}'(L, t) + \bar{r}_x \bar{r}_z \ddot{\phi} \delta v' \quad (C11)
\end{aligned}$$

$\delta w'$

$$\begin{aligned} & \{\ddot{r}_{21}\}^T \frac{\partial r_2}{\partial w'} \delta w' \\ &= \dot{\theta}^2 \left\{ \begin{array}{c} 0 \\ -\bar{r}_x(v'(L, t)\cos\theta - w'(L, t)\sin\theta) + \bar{r}_y(-\phi\sin\theta - \cos\theta) + \bar{r}_z(-\phi\cos\theta + \sin\theta) \\ -\bar{r}_x(w'(L, t)\cos\theta + v'(L, t)\sin\theta) + \bar{r}_y(\phi\cos\theta - \sin\theta) + \bar{r}_z(-\phi\sin\theta - \cos\theta) \end{array} \right\}^T \\ & \quad \times \left\{ \begin{array}{c} \bar{r}_z \\ -\bar{r}_x\sin\theta \\ \bar{r}_x\cos\theta \end{array} \right\} \delta w' = \dot{\theta}^2 (-\bar{r}_x^2 w'(L, t) + \bar{r}_x \bar{r}_y \phi - \bar{r}_x \bar{r}_z) \delta w' \end{aligned}$$

$$\begin{aligned} & \{\ddot{r}_{22}\}^T \frac{\partial r_2}{\partial w'} \delta w' \\ &= -\ddot{\theta} \left\{ \begin{array}{c} 0 \\ \bar{r}_x(v'(L, t)\sin\theta + w'(L, t)\cos\theta) - \bar{r}_y(\phi\cos\theta - \sin\theta) - \bar{r}_z(-\phi\sin\theta - \cos\theta) \\ -\bar{r}_x(-w'(L, t)\sin\theta + v'(L, t)\cos\theta) + \bar{r}_y(-\phi\sin\theta - \cos\theta) - \bar{r}_z(\phi\cos\theta - \sin\theta) \end{array} \right\}^T \\ & \quad \times \left\{ \begin{array}{c} \bar{r}_z \\ -\bar{r}_x\sin\theta \\ \bar{r}_x\cos\theta \end{array} \right\} \delta w' = -\ddot{\theta} (-\bar{r}_x^2 v'(L, t) - \bar{r}_x \bar{r}_y - \bar{r}_x \bar{r}_z \phi) \delta w' \end{aligned}$$

$$\begin{aligned} & \{\ddot{r}_{23}\}^T \frac{\partial r_2}{\partial w'} \delta w \\ &= -2\dot{\theta} \left\{ \begin{array}{c} 0 \\ \bar{r}_x(\dot{v}'(L, t)\sin\theta + \dot{w}'(L, t)\cos\theta) - \bar{r}_y\dot{\phi}\cos\theta + \bar{r}_z\dot{\phi}\sin\theta \\ -\bar{r}_x(-\dot{w}'(L, t)\sin\theta + \dot{v}'(L, t)\cos\theta) - \bar{r}_y\dot{\phi}\sin\theta - \bar{r}_z\dot{\phi}\cos\theta \end{array} \right\}^T \\ & \quad \times \left\{ \begin{array}{c} \bar{r}_z \\ -\bar{r}_x\sin\theta \\ \bar{r}_x\cos\theta \end{array} \right\} \delta w' = -2\dot{\theta} (-\bar{r}_x^2 \dot{v}'(L, t) - \bar{r}_x \bar{r}_z \dot{\phi}) \delta w' \end{aligned}$$

$$\begin{aligned} & \{\ddot{r}_{24}\}^T \frac{\partial r_2}{\partial w'} \delta w' \\ &= \left\{ \begin{array}{c} \bar{r}_y \ddot{v}'(L, t) + \bar{r}_z \ddot{w}'(L, t) \\ \bar{r}_x(\ddot{v}'(L, t)\cos\theta - \ddot{w}'(L, t)\sin\theta) + \bar{r}_y \ddot{\phi}\sin\theta + \bar{r}_z \ddot{\phi}\cos\theta \\ \bar{r}_x(\ddot{w}'(L, t)\cos\theta + \ddot{v}'(L, t)\sin\theta) - \bar{r}_y \ddot{\phi}\cos\theta + \bar{r}_z \ddot{\phi}\sin\theta \end{array} \right\}^T \\ & \quad \times \left\{ \begin{array}{c} \bar{r}_z \\ -\bar{r}_x\sin\theta \\ \bar{r}_x\cos\theta \end{array} \right\} \delta w' = \bar{r}_y \bar{r}_z \ddot{v}'(L, t) + \bar{r}_z^2 \ddot{w}'(L, t) + \bar{r}_x^2 \ddot{w}'(L, t) - \bar{r}_x \bar{r}_y \ddot{\phi} \delta w' \end{aligned}$$

$$\begin{aligned}
\therefore \{\ddot{\mathbf{r}}_2\}^T \delta \mathbf{w}' &= \dot{\theta}^2 (-\bar{r}_x^2 \mathbf{w}'(\mathbf{L}, t) + \bar{r}_x \bar{r}_y \dot{\phi} - \bar{r}_x \bar{r}_z) \\
&- \ddot{\theta} (-\bar{r}_x^2 \mathbf{v}'(\mathbf{L}, t) - \bar{r}_x \bar{r}_y - \bar{r}_x \bar{r}_z \dot{\phi}) \\
&- 2\dot{\theta} (-\bar{r}_x^2 \dot{\mathbf{v}}'(\mathbf{L}, t) - \bar{r}_x \bar{r}_z \dot{\phi}) + \bar{r}_y \bar{r}_z \ddot{\mathbf{v}}'(\mathbf{L}, t) + \bar{r}_z^2 \dot{\mathbf{w}}'(\mathbf{L}, t) \\
&+ \bar{r}_x^2 \dot{\mathbf{w}}'(\mathbf{L}, t) - \bar{r}_x \bar{r}_y \ddot{\phi} \delta \mathbf{w}'
\end{aligned} \tag{C12}$$

 $\delta \phi$

$$\begin{aligned}
&\{\ddot{\mathbf{r}}_{21}\}^T \frac{\partial r_2}{\partial \phi} \delta \phi \\
&= \dot{\theta}^2 \left\{ \begin{array}{c} 0 \\ -\bar{r}_x (v'(\mathbf{L}, t) \cos \theta - w'(\mathbf{L}, t) \sin \theta) + \bar{r}_y (-\phi \sin \theta - \cos \theta) + \bar{r}_z (-\phi \cos \theta + \sin \theta) \\ -\bar{r}_x (w'(\mathbf{L}, t) \cos \theta + v'(\mathbf{L}, t) \sin \theta) + \bar{r}_y (\phi \cos \theta - \sin \theta) + \bar{r}_z (-\phi \sin \theta - \cos \theta) \end{array} \right\}^T \\
&\quad \times \left\{ \begin{array}{c} 0 \\ \bar{r}_y \sin \theta + \bar{r}_z \cos \theta \\ -\bar{r}_y \cos \theta + \bar{r}_z \sin \theta \end{array} \right\} \delta \phi = \dot{\theta}^2 (\bar{r}_x \bar{r}_y w'(\mathbf{L}, t) - \bar{r}_y^2 \phi - \bar{r}_x \bar{r}_z v'(\mathbf{L}, t) - \bar{r}_z^2 \phi) \delta \phi
\end{aligned}$$

$$\begin{aligned}
&\{\ddot{\mathbf{r}}_{22}\}^T \frac{\partial r_2}{\partial \phi} \delta \phi \\
&= -\ddot{\theta} \left\{ \begin{array}{c} 0 \\ \bar{r}_x (v'(\mathbf{L}, t) \sin \theta + w'(\mathbf{L}, t) \cos \theta) - \bar{r}_y (\phi \cos \theta - \sin \theta) - \bar{r}_z (-\phi \sin \theta - \cos \theta) \\ -\bar{r}_x (-w'(\mathbf{L}, t) \sin \theta + v'(\mathbf{L}, t) \cos \theta) + \bar{r}_y (-\phi \sin \theta - \cos \theta) - \bar{r}_z (\phi \cos \theta - \sin \theta) \end{array} \right\}^T \\
&\quad \times \left\{ \begin{array}{c} 0 \\ \bar{r}_y \sin \theta + \bar{r}_z \cos \theta \\ -\bar{r}_y \cos \theta + \bar{r}_z \sin \theta \end{array} \right\} \delta \phi = -\ddot{\theta} (\bar{r}_x \bar{r}_y v'(\mathbf{L}, t) + \bar{r}_y^2 + \bar{r}_x \bar{r}_z w'(\mathbf{L}, t) + \bar{r}_z^2) \delta \phi
\end{aligned}$$

$$\begin{aligned}
&\{\ddot{\mathbf{r}}_{23}\}^T \frac{\partial r_2}{\partial \phi} \delta \phi \\
&= -2\dot{\theta} \left\{ \begin{array}{c} 0 \\ \bar{r}_x (\dot{v}'(\mathbf{L}, t) \sin \theta + \dot{w}'(\mathbf{L}, t) \cos \theta) - \bar{r}_y \dot{\phi} \cos \theta + \bar{r}_z \dot{\phi} \sin \theta \\ -\bar{r}_x (-\dot{w}'(\mathbf{L}, t) \sin \theta + \dot{v}'(\mathbf{L}, t) \cos \theta) - \bar{r}_y \dot{\phi} \sin \theta - \bar{r}_z \dot{\phi} \cos \theta \end{array} \right\}^T \\
&\quad \times \left\{ \begin{array}{c} 0 \\ \bar{r}_y \sin \theta + \bar{r}_z \cos \theta \\ -\bar{r}_y \cos \theta + \bar{r}_z \sin \theta \end{array} \right\} \delta \phi = -2\dot{\theta} (\bar{r}_x \bar{r}_y \dot{v}'(\mathbf{L}, t) + \bar{r}_x \bar{r}_z \dot{w}'(\mathbf{L}, t)) \delta \phi
\end{aligned}$$

$$\begin{aligned}
& \{\ddot{r}_{24}\}^T \frac{\partial r_2}{\partial \phi} \delta \phi \\
&= \left\{ \begin{array}{c} \bar{r}_y \ddot{v}'(L, t) + \bar{r}_z \ddot{w}'(L, t) \\ \bar{r}_x (\ddot{v}'(L, t) \cos \theta - \ddot{w}'(L, t) \sin \theta) + \bar{r}_y \ddot{\phi} \sin \theta + \bar{r}_z \ddot{\phi} \cos \theta \\ \bar{r}_x (\ddot{w}'(L, t) \cos \theta + \ddot{v}'(L, t) \sin \theta) - \bar{r}_y \ddot{\phi} \cos \theta + \bar{r}_z \ddot{\phi} \sin \theta \end{array} \right\}^T \\
&\quad \times \left\{ \begin{array}{c} 0 \\ \bar{r}_y \sin \theta + \bar{r}_z \cos \theta \\ -\bar{r}_y \cos \theta + \bar{r}_z \sin \theta \end{array} \right\} \delta \phi = -\bar{r}_x \bar{r}_y \ddot{w}'(L, t) + \bar{r}_y^2 \ddot{\phi} + \bar{r}_x \bar{r}_z \ddot{v}'(L, t) + \bar{r}_z^2 \ddot{\phi} \delta \phi
\end{aligned}$$

$$\begin{aligned}
\therefore \{\ddot{r}_2\}^T \delta \phi &= \dot{\theta}^2 (\bar{r}_x \bar{r}_y w'(L, t) - \bar{r}_y^2 \phi - \bar{r}_x \bar{r}_z v'(L, t) - \bar{r}_z^2 \phi) \\
&\quad - \ddot{\theta} (\bar{r}_x \bar{r}_y v'(L, t) + \bar{r}_y^2 + \bar{r}_x \bar{r}_z w'(L, t) + \bar{r}_z^2) \\
&\quad - 2\dot{\theta} (\bar{r}_x \bar{r}_y v'(L, t) + \bar{r}_x \bar{r}_z w'(L, t)) - \bar{r}_x \bar{r}_y \ddot{w}'(L, t) + \bar{r}_y^2 \ddot{\phi} \\
&\quad + \bar{r}_x \bar{r}_z \ddot{v}'(L, t) + \bar{r}_z^2 \ddot{\phi} \delta \phi(L, t) + \bar{r}_x^2 \ddot{w}'(L, t) - \bar{r}_x \bar{r}_y \ddot{\phi} \delta w'
\end{aligned} \tag{C13}$$

$\delta \theta$ (Neglecting higher order terms)

$$\begin{aligned}
& \{\ddot{r}_{21}\}^T \frac{\partial r_2}{\partial \theta} \delta \theta \\
&= \dot{\theta}^2 \left\{ \begin{array}{c} 0 \\ -\bar{r}_x (v'(L, t) \cos \theta - w'(L, t) \sin \theta) + \bar{r}_y (-\phi \sin \theta - \cos \theta) + \bar{r}_z (-\phi \cos \theta + \sin \theta) \\ -\bar{r}_x (w'(L, t) \cos \theta + v'(L, t) \sin \theta) + \bar{r}_y (\phi \cos \theta - \sin \theta) + \bar{r}_z (-\phi \sin \theta - \cos \theta) \end{array} \right\}^T \\
&\quad \times \left\{ \begin{array}{c} 0 \\ -\bar{r}_x (w'(L, t) \cos \theta + v'(L, t) \sin \theta) - \bar{r}_y (\sin \theta - \phi \cos \theta) - \bar{r}_z (\cos \theta + \phi \sin \theta) \\ \bar{r}_x (-w'(L, t) \sin \theta + v'(L, t) \cos \theta) + \bar{r}_y (\cos \theta + \phi \sin \theta) - \bar{r}_z (\sin \theta + \phi \cos \theta) \end{array} \right\} \delta \theta = 0
\end{aligned}$$

$$\begin{aligned}
& \{\ddot{r}_{22}\}^T \frac{\partial r_2}{\partial \theta} \delta \theta \\
&= -\ddot{\theta} \left\{ \begin{array}{c} 0 \\ \bar{r}_x (v'(L, t) \sin \theta + w'(L, t) \cos \theta) - \bar{r}_y (\phi \cos \theta - \sin \theta) - \bar{r}_z (-\phi \sin \theta - \cos \theta) \\ -\bar{r}_x (-w'(L, t) \sin \theta + v'(L, t) \cos \theta) + \bar{r}_y (-\phi \sin \theta - \cos \theta) - \bar{r}_z (\phi \cos \theta - \sin \theta) \end{array} \right\}^T \\
&\quad \times \left\{ \begin{array}{c} 0 \\ -\bar{r}_x (w'(L, t) \cos \theta + v'(L, t) \sin \theta) - \bar{r}_y (\sin \theta - \phi \cos \theta) - \bar{r}_z (\cos \theta + \phi \sin \theta) \\ \bar{r}_x (-w'(L, t) \sin \theta + v'(L, t) \cos \theta) + \bar{r}_y (\cos \theta + \phi \sin \theta) - \bar{r}_z (\sin \theta + \phi \cos \theta) \end{array} \right\} \delta \theta \\
&= -\ddot{\theta} (-\bar{r}_y^2 - \bar{r}_z^2 - 2(\bar{r}_x \bar{r}_y v'(L, t) + \bar{r}_x \bar{r}_z w'(L, t)) + \bar{r}_y \bar{r}_z \phi) \delta \theta
\end{aligned}$$

$$\begin{aligned}
& \{\ddot{r}_{23}\}^T \frac{\partial r_2}{\partial \theta} \delta \theta \\
&= -2\dot{\theta} \left\{ \begin{array}{c} 0 \\ \bar{r}_x(\dot{v}'(L, t)\sin\theta + \dot{w}'(L, t)\cos\theta) - \bar{r}_y\dot{\phi}\cos\theta + \bar{r}_z\dot{\phi}\sin\theta \\ -\bar{r}_x(-\dot{w}'(L, t)\sin\theta + \dot{v}'(L, t)\cos\theta) - \bar{r}_y\dot{\phi}\sin\theta - \bar{r}_z\dot{\phi}\cos\theta \end{array} \right\}^T \\
&\quad \times \left\{ \begin{array}{c} 0 \\ -\bar{r}_x(w'(L, t)\cos\theta + v'(L, t)\sin\theta) - \bar{r}_y(\sin\theta - \phi\cos\theta) - \bar{r}_z(\cos\theta + \phi\sin\theta) \\ \bar{r}_x(-w'(L, t)\sin\theta + v'(L, t)\cos\theta) + \bar{r}_y(\cos\theta + \phi\sin\theta) - \bar{r}_z(\sin\theta + \phi\cos\theta) \end{array} \right\} \delta \theta \\
&\quad = -2\dot{\theta} \left(-\bar{r}_x\bar{r}_y\dot{v}'(0, t) - \bar{r}_x\bar{r}_z\dot{w}'(0, t) \right) \delta \theta
\end{aligned}$$

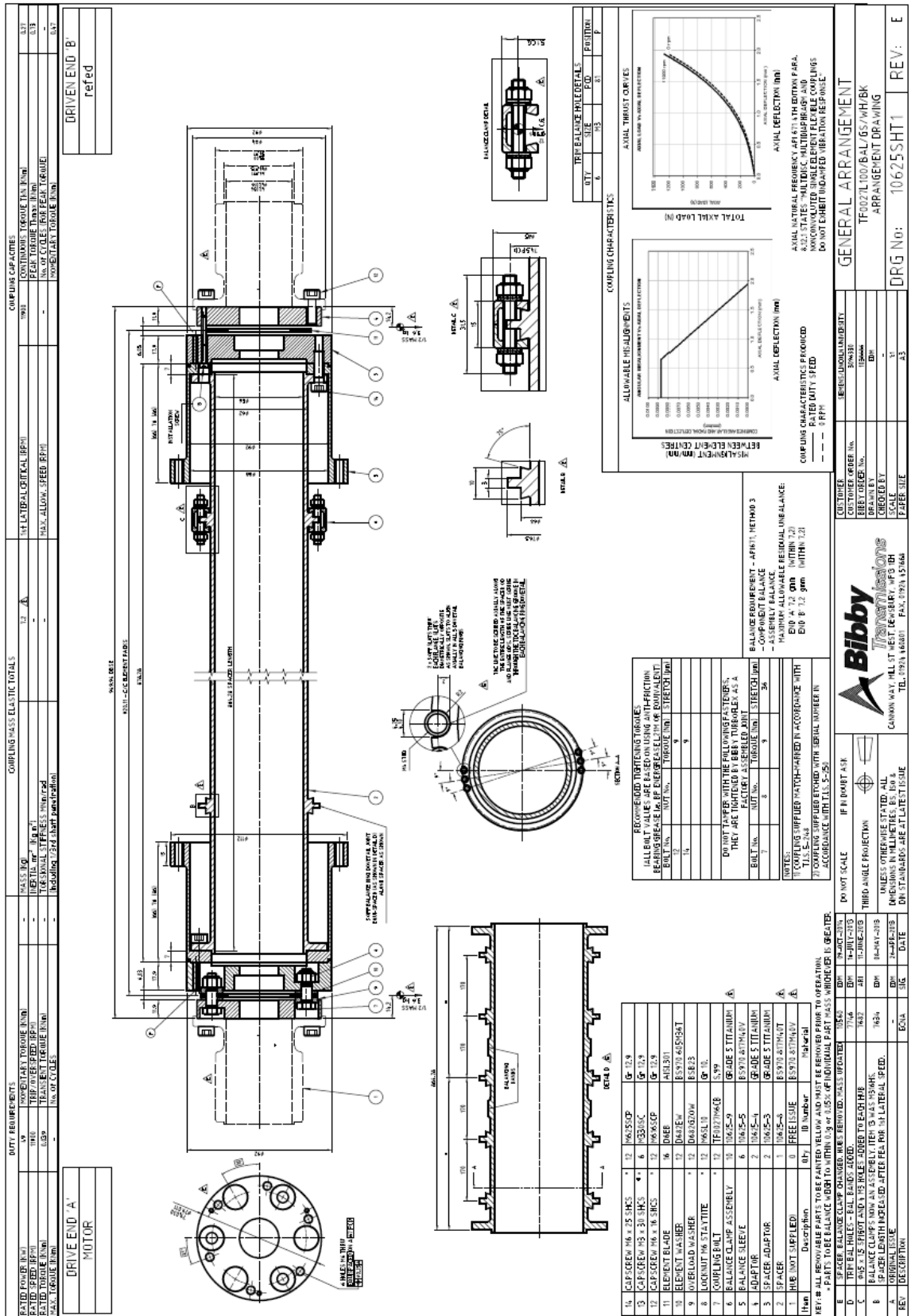
$$\begin{aligned}
& \{\ddot{r}_{24}\}^T \frac{\partial r_2}{\partial \theta} \delta \theta \\
&= \left\{ \begin{array}{c} \bar{r}_y\ddot{v}'(L, t) + \bar{r}_z\ddot{w}'(L, t) \\ \bar{r}_x(\ddot{v}'(L, t)\cos\theta - \ddot{w}'(L, t)\sin\theta) + \bar{r}_y\ddot{\phi}\sin\theta + \bar{r}_z\ddot{\phi}\cos\theta \\ \bar{r}_x(\ddot{w}'(L, t)\cos\theta + \ddot{v}'(L, t)\sin\theta) - \bar{r}_y\ddot{\phi}\cos\theta + \bar{r}_z\ddot{\phi}\sin\theta \end{array} \right\}^T \\
&\quad \times \left\{ \begin{array}{c} 0 \\ -\bar{r}_x(w'(L, t)\cos\theta + v'(L, t)\sin\theta) - \bar{r}_y(\sin\theta - \phi\cos\theta) - \bar{r}_z(\cos\theta + \phi\sin\theta) \\ \bar{r}_x(-w'(L, t)\sin\theta + v'(L, t)\cos\theta) + \bar{r}_y(\cos\theta + \phi\sin\theta) - \bar{r}_z(\sin\theta + \phi\cos\theta) \end{array} \right\} \delta \theta \\
&\quad = \bar{r}_x\bar{r}_y\ddot{w}'(L, t) - \bar{r}_x\bar{r}_z\ddot{v}'(L, t) - \bar{r}_y^2\ddot{\phi} - \bar{r}_z^2\ddot{\phi}\delta\theta
\end{aligned}$$

$$\begin{aligned}
\therefore \{\ddot{r}_2\}^T \delta \theta &= -\ddot{\theta} \left(\bar{r}_y^2 + \bar{r}_z^2 - \bar{r}_y\bar{r}_z\phi + 2 \left(\bar{r}_x\bar{r}_y\dot{v}'(L, t) + \bar{r}_x\bar{r}_z\dot{w}'(L, t) \right) \right) \\
&\quad - 2\dot{\theta} \left(-\bar{r}_x\bar{r}_y\dot{v}'(L, t) - \bar{r}_x\bar{r}_z\dot{w}'(L, t) \right) + \bar{r}_x\bar{r}_y\ddot{w}'(L, t) \\
&\quad - \bar{r}_x\bar{r}_z\ddot{v}'(L, t) - \bar{r}_y^2\ddot{\phi} - \bar{r}_z^2\ddot{\phi} \delta \theta
\end{aligned} \tag{C14}$$

Summing together Equations (C11) through (C14), the variation of kinetic energy in the second sleeve can be obtained once suitable inertia coefficients have been derived:

$$\begin{aligned}
\{\ddot{r}_z\}^T \delta r_z = & (\dot{\theta}^2 (-\bar{r}_x^2 v'(L, t) - \bar{r}_x \bar{r}_y - \bar{r}_x \bar{r}_z \phi) \\
& - \ddot{\theta} (\bar{r}_x^2 w'(L, t) - \bar{r}_x \bar{r}_y \phi + \bar{r}_x \bar{r}_z) - 2\dot{\theta} (\bar{r}_x^2 \dot{w}'(L, t) - \bar{r}_x \bar{r}_y \dot{\phi}) \\
& + \bar{r}_y^2 \ddot{v}'(L, t) + \bar{r}_y \bar{r}_z \ddot{w}'(L, t) + \bar{r}_x^2 \ddot{v}'(L, t) + \bar{r}_x \bar{r}_z \ddot{\phi} \delta v') \\
& + (\dot{\theta}^2 (-\bar{r}_x^2 w'(L, t) + \bar{r}_x \bar{r}_y \phi - \bar{r}_x \bar{r}_z) \\
& - \ddot{\theta} (-\bar{r}_x^2 v'(L, t) - \bar{r}_x \bar{r}_y - \bar{r}_x \bar{r}_z \phi) \\
& - 2\dot{\theta} (-\bar{r}_x^2 \dot{v}'(L, t) - \bar{r}_x \bar{r}_z \dot{\phi}) + \bar{r}_y \bar{r}_z \ddot{v}'(L, t) + \bar{r}_z^2 \ddot{w}'(L, t) \\
& + \bar{r}_x^2 \ddot{w}'(L, t) - \bar{r}_x \bar{r}_y \ddot{\phi} \delta w') \\
& + (\dot{\theta}^2 (\bar{r}_x \bar{r}_y w'(L, t) - \bar{r}_y^2 \phi - \bar{r}_x \bar{r}_z v' - \bar{r}_z^2 \phi) \\
& - \ddot{\theta} (\bar{r}_x \bar{r}_y v'(L, t) + \bar{r}_y^2 + \bar{r}_x \bar{r}_z w'(L, t) + \bar{r}_z^2) \\
& - 2\dot{\theta} (\bar{r}_x \bar{r}_y \dot{v}'(L, t) + \bar{r}_x \bar{r}_z \dot{w}'(L, t)) - \bar{r}_x \bar{r}_y \ddot{w}'(L, t) + \bar{r}_y^2 \ddot{\phi} \\
& + \bar{r}_x \bar{r}_z \ddot{v}'(L, t) + \bar{r}_z^2 \ddot{\phi} \delta \phi) \\
& + (-\ddot{\theta} (-\bar{r}_y^2 - \bar{r}_z^2 + \bar{r}_y \bar{r}_z \phi - 2 (\bar{r}_x \bar{r}_y v'(L, t) + \bar{r}_x \bar{r}_z w'(L, t))) \\
& - 2\dot{\theta} (-\bar{r}_x \bar{r}_y \dot{v}'(L, t) - \bar{r}_x \bar{r}_z \dot{w}'(L, t)) + \bar{r}_x \bar{r}_y \ddot{w}'(L, t) \\
& - \bar{r}_x \bar{r}_z \ddot{v}'(L, t) - \bar{r}_y^2 \ddot{\phi} - \bar{r}_z^2 \ddot{\phi} \delta \theta)
\end{aligned} \tag{C15}$$

Appendix D Technical Drawing of Test Shaft



Appendix E Technical Specifications of Oswald QDI13.2-2FI Motors



Maschinenspezifische Dokumentation

für regelbare AC-Kompaktmotoren

Machine specific documentation

for variable speed AC compact motors

Baureihe / Series

QDI

Typ / Type: QDI13.2-2FI

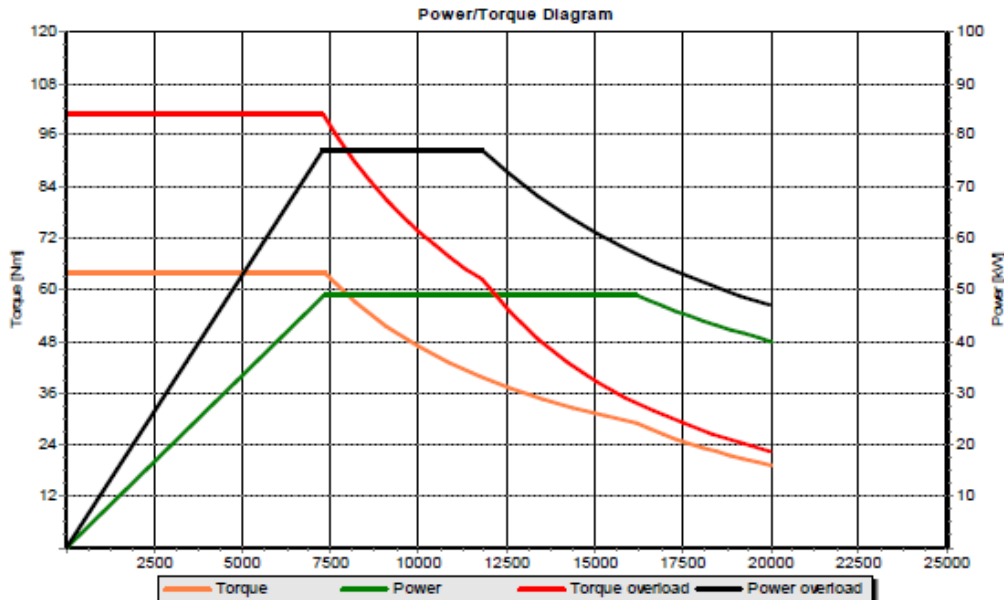
Kunde / Customer:	Control Techniques Drives Ltd. Stafford Park 4 Telford TF3 3BA, United Kingdom	
Kunden-Projekt-Nr. / Customer project no.:		
Bestell-Nr. / Order no.:	427637/620943 dated 25-Jul-2011	
Hersteller-Auftrags-Nr. / Manufacturer order no.:	27262-1	
Hersteller-Bau-Nr. / Manufacturer model no.:	4210-000004	
Maschinen-Serien-Nr. / Machine serial no.:	160896	

Die zur Erfassung der hier angegebenen Daten verwendeten Meßgeräte werden in regelmäßigen Abständen kalibriert, wodurch eine eindeutige Rückführbarkeit gewährleistet ist.

The measuring instruments used for the collection of the data indicated here will be calibrated in regular intervals whereby a clear returnability is ensured.



Technical data sheet



Driving Data

		Rated				Overload			
		P _{red.}	P	Fw P _{oon.}	Fw P _{red.}	P _{red.}	P	Fw P _{oon.}	Fw P _{red.}
Voltage	U [V]		440	440	440		440	440	440
Power mech.	P [kW]		49	49	40		77	77	47
Current	I [A]		77				120		
Magn. Current	I _{mag} [A]		29				29		
Frequency	f [Hz]		123,0	272,0	336,0		123,0	199,5	336,0
Speed	n [min ⁻¹]		7320	16160	20000		7285	11780	19970
Torque	M [Nm]		64	29	19		101	62	22
Power Factor	cos φ [-]		0,88				0,91		
Efficiency	η [%]		96,0				95,5		
M _{breakd./M_{rated}}			4,2	2,0	2,0		2,7	1,7	1,7

Poles	2
Connection	Star
Duty	S1
allowed Inverter Freq. ≥	3 kHz
Pulse Rise Time ≥	0,3 μs

Equivalent Circuit (each single phase values)

R1	26,0 mΩ	X1σ	166,0 mΩ
R2'	16,0 mΩ	X2σ'	115,0 mΩ
Xm	8,30 Ω	f	123,0 Hz

Resistance R at room temperature (20°C/68°F).
 Calculation to operating temp.: R_{hot} = R_{20°C/68°F} x 1,4.
 Reactance at rated frequency f.
 Calculation of inductance: L = X / (2 x π x f).

Protection:

Temperature Sensors		Protection IP	23
3 x PT100 (Winding)		Insulation Class	H
2 x PT100 (Bearing)		Winding Insul. max.	1,57 kV peak



Cooling:	IC	06	internally cooled with external blower
	1	Type: Radial blower D060/M, Voltage: 208-265/360-460 +/- 5% V, Current: 2.4-3.1/1.4-1.8 A, Power: 550 W, Speed: 2860 1/min, Frequency: 50 Hz, Housing position: Dr, with filter: NDE, Mounting position: on top NDE,	
	2		
	3		

Mechanical Design:			gr	hrs
Bearing DE	Spindle bearing, current insulated	Regreasing DE	without	
Bearing NDE	Spindle bearing, current insulated	Regreasing NDE	without	
Shaft DE	D42k6 x 50mm, plain shaft without spline	Torque Flange DE		
Shaft NDE		Torque Flange NDE		
Mounting	B3	Terminal Box	right	regarding B3
Balancing		Cable Outlet	down	regarding B3
		Cable Gland	1 x M63; 5 x M16	
Vibration Level	R			

Options:	
-----------------	--

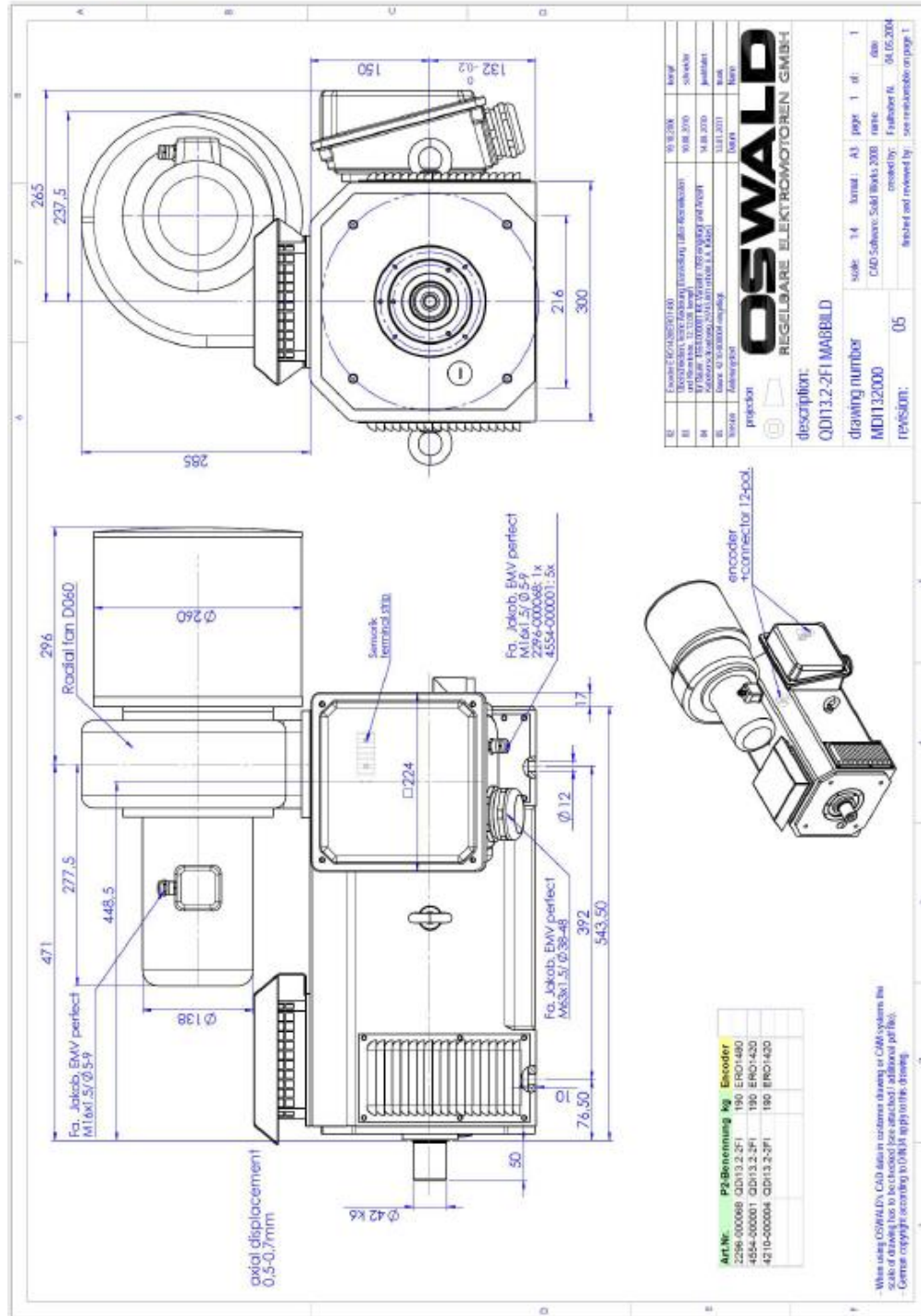
Encoder:	1	Type: Incremental encoder ERO1420, No. of pulses: 512 ppr, Voltage: 5 V, Signal: TTL, Connection: cable 1m, Design hollow shaft (H) / shaft (W): H, Diameter hole / shaft: ø8 mm, Protection: IP40, incl. plug + mating plug,
	2	

Brake:	
---------------	--

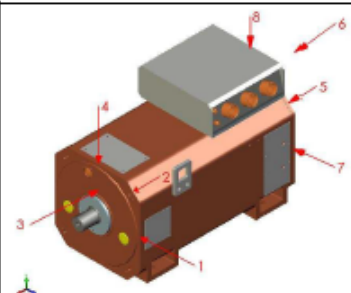
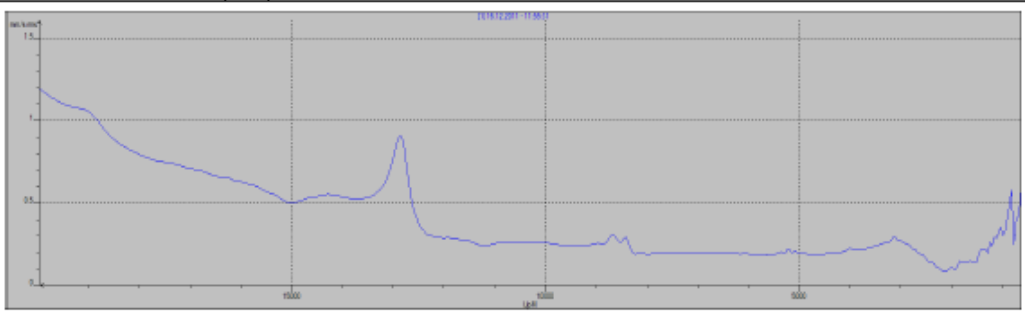
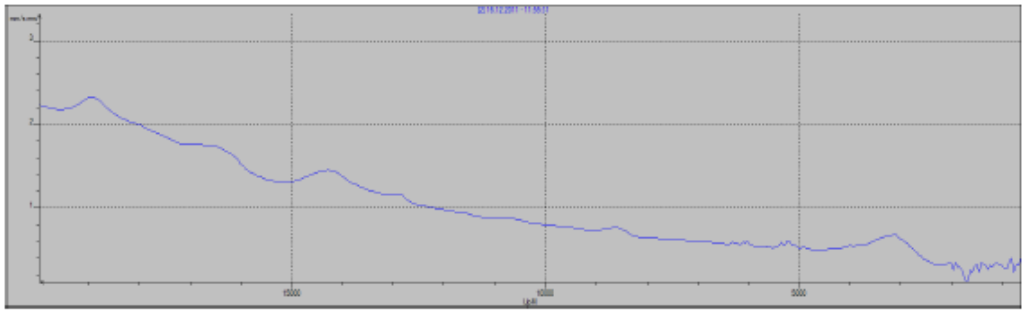
Misc.:			
Dimen. Sheet	MDI132000-05	Inertia	0,05 kg m ²
Paint	RAL 9005 black	max Altitude ≤	1000 m
Weight	180 kg	max Ambient Temperature ≤	40 °C

Comment:	Fixed bearing NDE
	values after testing

Rev | Text | Name | Date | valid SerNo.



OSWALD
REGELBARE ELEKTROMOTOREN

Prüfprotokoll Schwingungsmessung				
Test report vibration measurements				
Prüffeld / test rig			Rev. 1/2005	
Kom.-Nr. / order no.:	27262-1	Bau-Nr. / part no.:	4210-000004	
Typ / type:	QDI13.2-2FI			
Schwingstärke / vibration level:	R	Umgebungstemperatur / ambient temperature:	21°C	
Gültige Normen + Vorgaben / applicable standards + specifications:		EN 60034-14:2004-09 / PA470-22 / BN100-01		
1	A-Lager horizontal		1	DE bearing horizontal
2	A-Lager 45°		2	DE bearing 45°
3	A-Lager axial		3	DE bearing axial
4	A-Lager vertikal		4	DE bearing vertical
5	B-Lager 45°		5	NDE bearing 45°
6	B-Lager axial		6	NDE bearing axial
7	B-Lager horizontal		7	NDE bearing horizontal
8	B-Lager vertikal		8	NDE bearing vertical
Meßpunkt / test point:	2	A-Lager / DE bearing		
				
Meßpunkt / test point:	5	B-Lager / NDE bearing		
				
Bemerkungen / remarks: -				
Schwingwerte gemäß Vorgabe erfüllt / vibrations according to specification?			<input checked="" type="checkbox"/> ja / yes <input type="checkbox"/> nein / no	
Datum / date:	16.12.11	Prüfer / checked by:	C. Eck, Prüfstandsmitarbeiter / test rig assistant	



Lagereinlauf bearing running-in				
Prüffeld / test rig				Rev. 1/2005
Kom.-Nr. / order no.:	27262-1	Bau-Nr. / part no.:	4210-000004	Ser.-Nr. / serial no.: 160896
Typ / type:	QDI13.2-2FI			
Gültige Normen + Vorgaben / applicable standards + specifications:	PA 470-21			
Umgebungstemperatur / ambient temperature:	21°C			
Bemerkungen / remarks: -				
Lagereinlauf gemäß Vorgabe erfüllt / bearing running-in according to specification?				<input checked="" type="checkbox"/> ja / yes <input type="checkbox"/> nein / no
Datum / date:	16.12.11	Prüfer / checked by:	C. Eck, Prüfstandsmitarbeiter / test rig assistant	